CZECH TECHNICAL UNIVERSITY IN PRAGUE

FACULTY OF NUCLEAR SCIENCES AND PHYSICAL ENGINEERING

Department of Physics

DOCTORAL THESIS

Open Charm Production at STAR

Prague 2023

Ing. Lukáš Kramárik

ČESKÉ VYSOKÉ UČENÍ TECHNICKÉ V PRAZE

FAKULTA JADERNÁ A FYZIKÁLNĚ INŽENÝRSKÁ

Katedra fyziky

DISERTAČNÍ PRÁCE

Produkce otevřeného půvabu na experimentu STAR

Praha 2023 Ing. Lukáš Kramárik

Bibliografický záznam

Autor	Ing. Lukáš Kramárik Katedra fyziky Fakulta jaderná a fyzikálně inženýrská České vysoké učení technické v Praze
Název práce	Produkce otevřeného půvabu na experimentu STAR
Studijní program	Aplikace přírodních věd
Studijní obor	Jaderné inženýrství
Školitel	doc. Mgr. Jaroslav Bielčík, Ph.D. Katedra fyziky Fakulta jaderná a fyzikálně inženýrská České vysoké učení technické v Praze
Školitel specialista	Xin Dong, Ph.D. Lawrence Berkeley National Laboratory
Akademický rok	2023/2024
Počet stran	167
Klíčová slova	mezony s otevřeným půvabem, proton-deuteron srážky, studená jaderná hmota

Bibliographic entry

Author	Ing. Lukáš Kramárik Physics Department Faculty of Nuclear Sciences and Physical Engineering Czech Technical University in Prague
Title	Open Charm Production at STAR
Degree programme	Application of natural sciences
Field of study	Nuclear engineering
Supervisor	doc. Mgr. Jaroslav Bielčík, Ph.D. Physics Department Faculty of Nuclear Sciences and Physical Engineering Czech Technical University in Prague
Supervisor specialist	Xin Dong, Ph.D. Lawrence Berkeley National Laboratory
Academic year	2023/2024
Number of pages	167
Key words	open charm mesons, proton-deuteron collisions, cold nuclear matter

Acknowledgement

I extend my deepest gratitude to my supervisor, Jaroslav Bielčík, for his unwavering support and guidance throughout my academic journey in particle physics. From the inception of my research, he has been a constant source of inspiration, providing invaluable insights that have shaped the trajectory of my work. Furthermore, I am profoundly grateful for his mentorship, patience, and dedication to my intellectual and professional growth. His encouragement has been a driving force behind the successful completion of this PhD thesis.

Special thanks are due to Xin Dong, whose expertise in technical matters and innovative ideas played a pivotal role in the success of this research. He not only offered crucial technical guidance but also provided novel perspectives on decision-making in the analysis process.

In addition to my academic mentors, I extend my heartfelt thanks to my family—my pillar of strength. My wife and children have been my greatest supporters, offering understanding, and a nurturing environment that allowed me to focus on my studies. My wife's encouragement and sacrifices have been instrumental, and this thesis is a testament to her support. A special, heartfelt mention goes to my parents. Their support, encouragement, and belief in my abilities have been a constant source of strength throughout this challenging journey.

In closing, while specific names are omitted to avoid unintentional omissions, I express my heartfelt appreciation to the numerous individuals who have been part of my academic journey. To the countless colleagues, friends, and mentors who have generously shared insights, offered assistance, and contributed to the rich tapestry of my experience, your collective influence has been immeasurable.

Abstract

One of the main goals of experiments at the Large Hadron Collider in CERN and the Relativistic Heavy Ion Collider (RHIC) in BNL is to study hot and dense nuclear matter, quark-gluon plasma (QGP), that could be created in collisions of heavy ions. The QGP is expected to be present in the first phases of the Big Bang, where all of the matter in the Universe was created. Furthermore, its studies give insight into the various aspects of quantum-chromodynamics (QCD). It mainly helps exploit various phase transitions in the nuclear matter phase diagram. At RHIC energies, heavy-flavor (charm and beauty) quarks are primarily produced in the hard partonic scatterings in the initial stages of heavy-ion collisions. Thanks to this, they are an excellent probe of the whole evolution of the created QGP. However, the particle production measurements in heavy-ion collisions, compared to those in the collisions of protons (p+p), are also affected by the Cold Nuclear Matter (CNM) effects. The CNM effects arise from the dense nuclear environment in the collisions, not from the hot medium presence. Small collision systems, such as collisions of protons or deuterons with heavy ions, are a great tool for investigating CNM effects.

In 2014–2016, the Heavy Flavor Tracker (HFT) silicon detector was installed in the STAR detector at RHIC. Its track-pointing resolution enabled the precise and detailed studies of open heavy-flavor production in the collisions of gold ions (Au+Au) at energy per colliding nucleon $\sqrt{s_{\mathrm{NN}}} = 200$ GeV. Modification of the production compared to the p+p collisions, accessed via nuclear modification factor measurements, was studied for D^0, $\mathrm{D}^{\pm}$ mesons and electrons from beauty and charm decays. Open heavy-flavor elliptic flow (v_2) and directed flow (v_1) were also measured.

This thesis studies the production of D^0 meson in deuteron-gold (d+Au) collisions at $\sqrt{s_{\mathrm{NN}}} = 200$ GeV, measured in 2016. This measurement complements the studies done in the Au+Au collisions and aims to help isolate the CNM effect from the effects of the QGP. Thanks to the excellent impact parameter resolution provided by the HFT, $\mathrm{D}^0(\overline{\mathrm{D}^0})$ mesons are reconstructed from their hadronic decay to kaon and pion, $\mathrm{D}^0(\overline{\mathrm{D}^0}) \rightarrow \mathrm{K}^-\pi^+(\mathrm{K}^+\pi^-)$. Topological properties of D^0 mesons decays are used to extract D^0 meson raw yield.

The performance of the three classification machine learning algorithms, boosted decision trees (BDT), random forest, and deep neural network, was studied on the simulated data. The BDT was selected to separate the signal from the background in the correct-sign pairs of kaons and pions, and the D^0 meson peak significance at the level of 7σ was achieved. Statistics allowed us to reconstruct D^0 meson in the three transverse momentum intervals: 1–2, 2–3, and 3–5 GeV/c.

Measured D^0 meson production is compared to the previous measurements done in 2003. Furthermore, it was compared to the results from p+p collisions in the form of the nuclear modification factor. Within uncertainties, the measured nuclear modification factor agrees with the results from light hadrons in d+Au collisions and, for low transverse momentum, D^0 mesons in the Au+Au collisions.

Abstrakt

Jedným z hlavných cieľov experimentov na Veľkom hadrónovom urýchľovači (Large Hadron Collider, LHC) v CERNe a Relativistickom urýchľovači ťažkých jadier (Relativistic Heavy Ion Collider, RHIC) v BNL je štúdium horúcej a hustej jadrovej hmoty, kvark gluónovej plazmy (quark-gluon plasma, QGP), ktorá môže vznikať v zrážkach ťažkých iontov. Predpokladá sa, že QGP bola prítomná v prvých fázach veľkého tresku, kedy vznikla všetka hmota vo vesmíre. Naviac, vďaka štúdiu jej vlastností, je možné nahliadať na rôzne aspekty kvantovej chromodynamiky popisujúcej silnú interakciu elementárnych častíc. Jedným z nich je aj popis fázových prechodov jadrovej hmoty. Pri energiách dosahovaných na RHICu, kvarky ťažkých vôní (krásny a pôvabný) sú vytvárané najmä v tvrdých partónových interakciách v počiatočných fázach zrážok ťažkých iontov. Vďaka tomu sú jedinečnou sondou celej evolúcie vzniknutej QGP. Avšak produkcia častíc v zrážkach ťažkých jadier je v porovnaní so zrážkami protónov (p+p) ovplyvnená aj efektami studenej jadrovej hmoty (Cold Nuclear Matter, CNM). CNM efekty sú dôsledkom hustého prostredia v zrážajúcich sa jadrách a nie sú dôsledkom prítomnosti horúcej jadrovej hmoty. Malé zrážkové systémy, ako sú zrážky protónov alebo deuterónov s ťažkými iónmi, sú výborným nástrojom na skúmanie CNM efektov.

V rokoch 2014–2016 bol v detektore STAR na RHICu nainštalovaný kremíkový detektor s názvom Heavy Flavor Tracker (HFT). Jeho rozlíšenie rekonštrukcie dráh častíc umožnilo presné a detailné štúdie produkcie ťažkých kvarkov v kolíziách iónov zlata (Au+Au) pri energii na jeden zrážaný nukleón $\sqrt{s_{\mathrm{NN}}} = 200$ GeV. Modifikácia produkcie v porovnaní s kolíziami p+p, ktorá bola prístupná prostredníctvom meraní faktora jadrovej modifikácie, bola študovaná pre D^0, $\mathrm{D}^{\pm}$ mezóny a elektróny z rozpadov krásnych a pôvabných kvarkov. Bol tiež meraný eliptický anizotropný tok (v_2) a priamy tok (v_1) otvorených ťažkých mezónov.

Táto dizertačná práca študuje produkciu D^0 mezónov v zrážkach deuterón-zlato (d+Au) pri $\sqrt{s_{\mathrm{NN}}} = 200$ GeV meraných v roku 2016. Toto meranie dopĺňa štúdie vykonané v Au+Au a má za cieľ pomôcť izolovať CNM efekty od efektov QGP. Vďaka vynikajúcemu rozlíšeniu merania vzdialenosti častíc od miesta zrážky poskytovaného HFT, sú D^0 mezóny rekonštruované z ich hadronického rozpadu na kaón a pión, $\mathrm{D}^0(\overline{\mathrm{D}^0}) \rightarrow \mathrm{K}^-\pi^+(\mathrm{K}^+\pi^-)$. Topologické vlastnosti rozpadov D^0 mezónov sa používajú na získanie produkcie D^0 mezónov.

Výkon troch klasifikačných algoritmov strojového učenia, a to posilnených stromov rozhodovania (boosted decision trees, BDT), náhodných lesov (random forest) a hlbokých neurónových sietí, bol študovaný na simulovaných dátach. BDT bol vybraný na separáciu signálu od pozadia v pároch kaónov a piónov s opačným nábojom. Meraný výťažok D^0 mezónov dosiahol štatistickú signifikanciu na úrovni 7σ. Množstvo nameraných zrážok nám umožnilo rekonštruovať D^0 mezóny v troch intervaloch priečnej hybnosti: 1–2, 2–3, a 3–5 GeV/c.

Nameraná produkcia D^0 mezónov bola porovnaná s predchádzajúcimi meraniami z roku 2003. Ďalej sa porovnávala s výsledkami z p+p vo forme faktora jadrovej modifikácie. V rámci neistôt sa nameraný faktor jadrovej modifikácie zhodoval s výsledkami pre ľahké hadróny v d+Au a D^0 mezóny s nízkou priečnou hybnosťou v Au+Au.

Contents

Introduction

In the 1970s, the new state of nuclear matter, the quark-gluon plasma (QGP), was predicted. This hot and dense state most likely existed shortly after the Big Bang, and it is investigated by laboratories that can detect collisions of heavy ions since enormous energy is needed for its creation. Its presence in central heavy-ion collisions in particle accelerators was finally confirmed in 2004 by the Relativistic Heavy Ion Collider (RHIC) experiments. Understanding the properties of the QGP could also result in a more precise theoretical description of the strong interaction of elementary particles in the Standard Model and their creation. In the QGP, the large temperature and energy densities cause the melting of bound hadrons. Therefore, their constituent quarks, and gluons, become quasi-free particles. Since 2004, multiple probes of the QGP creation have been measured by experiments in both RHIC and the Large Hadron Collider (LHC). These probes are mainly collectivity of the particles in heavy-ion collisions, suppression of particle's production compared with the one in proton-proton (p+p) collisions, where QGP is not expected to be created, or different hadronization (hadron forming) processes in heavy-ion and p+p collisions.

Heavy-flavor (charm and bottom) quarks are produced primarily in the early stages of collisions [1] and thus experience their entire evolution. The study of open-charm meson yields probes the quark mass dependence of energy loss in the QGP and hadronization in the heavy-ion collisions. Furthermore, understanding the sensitivity of heavy quarks to the collective motion of the system, reflected in the elliptic flow of heavy mesons, can provide information on the degree of their thermalization in the QGP and help to constrain the heavy quark diffusion coefficient. The Solenoidal Tracker at RHIC (STAR) experiment at the Relativistic Heavy Ion Collider (RHIC) performed extensive studies of heavy-flavor hadron production in gold-gold (Au+Au) collisions at $\sqrt{s_{\mathrm{NN}}} = 200$ GeV recorded in years 2014–2016. In this period, the Heavy Flavor Tracker (HFT) [2], the high-precision silicon vertex detector, was installed at the center of the STAR apparatus. Significant suppression of D^0 and $\mathrm{D}^{\pm}$ meson production in these collisions compared to p+p collisions at the same energy was measured. Furthermore, the STAR measured significant D^0 meson collectivity in Au+Au collisions.

However, it is crucial to separate various processes affecting the hot medium probes to study QGP properties in the relativistic collisions at accelerators quantitatively. These are initial state effects before QGP creation and final state effects after QGP cooldown. The most significant ones are caused by the heavy nuclei in the collisions and dense environment after the hadronization. Collectively, these are called cold nuclear matter (CNM) effects. They include mainly modification of parton distribution functions of nucleons in colliding nuclei, multiple scatterings of the partons by the dense target, and parton scatterings in the nucleus, resulting in their energy loss and the broadening of the transverse momentum distribution (Cronin effect). The CNM effects are studied mainly in asymmetric proton-nucleus or deuteron-nucleus (p/d+A) collisions. At RHIC, these are proton-gold (p+Au) and deuteron-gold (d+Au) col-

lisions at various energies. In 2016, the STAR measured d+Au collisions at $\sqrt{s_{\mathrm{NN}}} = 200$ GeV with the HFT installed. The primary analysis in this thesis aims to study D^0 mesons production in these collisions and its comparison with the one in p+p collisions. Thanks to the excellent HFT spatial resolution, topological reconstruction of the hadronic decay of D^0 meson to K^- and π^+ with branching ratio 3.89 ± 0.04 % [3] is used. This measurement results aim to constraint models predicting the CNM effects that would better control charm quark behavior in the QGP measured in Au+Au collisions.

To further improve the separation of D^0 meson signal and combinatorial background $\mathrm{K}\pi$ pairs, the Boosted Decision Trees (BDT) machine learning algorithm from the Toolkit for Multivariate Data Analysis (TMVA) package [4] is applied. The performance of other machine-learning methods, deep neural network, and random forest are compared to the BDT on the simulated data. The architecture of methods is carefully designed to maximize the classification performance of signal from background separation. Such comparison proves the decision to use the BDT. Furthermore, it shows that other methods, not only the widely used BDT, should be considered for the signal extraction in the high-energy physics. Together with my colleagues, we missed detailed description of the machine-learning algorithm setup and individual steps in their application on the high-energy data, thus we decided to publish it for D^0 meson signal extraction in the Journal of Instrumentation (JINST).

This thesis is organized as follows. The first chapter overviews the physics background for D^0 measurements in heavy-ion and p/d+A collisions and published measurements of open-charm connected to it. Next, an introduction to supervised machine-learning methods and their application to the experimental data is presented in the second chapter. The third chapter introduces the STAR detector apparatus, mainly as it operated in 2014–2016 when the data for the primary analysis were recorded. The last chapter demonstrates all steps in D^0 meson reconstruction, its efficiency corrections, and systematic uncertainties calculations done by the author of this thesis. All figures in the last chapter are for this thesis. Although the analysis was discussed within the STAR heavy-flavor analytics team, they were not officially approved and published by the STAR collaboration.

Author's contribution

Machine-learning methods for D^0 meson signal extraction

I am a co-author of the article (J. Bielčík, K. Hladká, L. Kramárik and V. Kůs, *Machine learning classification for D^0 meson signal extraction in d+Au collisions*, JINST 17 (2022) 02, P02017) that describes in detail the application of machine-learning methods on the data. The simulation of the d+Au collisions, which setup I tested, is used to demonstrate the configuration of the algorithms. We designed the parameters of the random forest and deep neural network classifiers to compare with the typical BDT setup. Application of the BDT on the STAR data to reconstruct invariant mass peaks was also published in a separate article (L. Kramárik, for the STAR Collaboration, *Reconstruction of D^0 meson in d+Au collisions at 200 GeV by the STAR experiment*, 2020 Phys. Scr. 95 074010). These articles are in App. B.

Data analysis at the STAR experiment

As a member of the STAR collaboration, my work during my Ph.D. studies mainly aimed to study D^0 meson production in d+Au collisions. All heavy flavor analyses at STAR are consulted within the Heavy-Flavor Physics Working Group. Regular updates on the D^0 meson analysis were discussed at the phone meetings of this group. Usually, several analyzers work on the same dataset to optimize analysis and results. I was leading the efforts related to D^0 meson production in d+Au collisions since most of the analysis steps were done solely by me.

In addition, I participated in several analysis and collaboration meetings of the STAR experiment, where I discussed the current status of my work with more STAR collaboration members. Details of the D meson reconstruction were also discussed during the one-month-long internship at Lawrence Berkeley National Laboratory. In addition, I performed preliminary reconstruction and analysis of D^0 mesons in p+Au collisions, which is not presented in this thesis. Furthermore, I contributed with the trigger and tracking efficiencies in the measurement of D^0 and D^* meson in p+p collisions at $\sqrt{s_{\mathrm{NN}}} = 500$ GeV, recorded in 2011. The article with these results, titled *Measurements of D^0 and D^* production in p+p collisions at $\sqrt{s_{NN}} = 500$ GeV*, is in the STAR collaboration review and will be published soon in the Physical Review D journal. I am one of its primary authors. A list of my public presentations and posters on the topic of this thesis is in App. B. Most of them were presented for the STAR collaboration, resulting in the publications of the proceedings.

Zero Degree Calorimeter maintenance

Zero Degree Calorimeter (ZDC) is one of the STAR's subdetectors. It was built to detect particles in very forward rapidities. In addition, the signal from ZDC is a part of the STAR trigger system and Relativistic Heavy Ion Collider (RHIC) luminosity measurements. Thus, monitoring ZDC during the data taking and tuning it before and during the run is essential. As a service task, I worked as an expert on the ZDC detector, monitoring its performance and calibrating the supply voltage of photomultipliers. I was a member of ZDC experts from 2017 to 2020. During data taking in 2019 and 2020, I was the on-call for critical support escalations of the ZDC.

Furthermore, before data taking in the year 2018, together with my colleagues, we disassembled ZDC and tested installed photomultipliers. For this, we assembled the special testing kit. We also tested STAR's spare photomultiplier tubes (PMT) to choose those with the best performance. As a result of this work, two PMTs in the ZDC were replaced. During the data taking, it was concluded that the detector's performance improved. Finally, we established the ZDC documentation with all of the software and hardware information needed for future experts and regularly updated it.

Last but not least, I participated in data-taking shifts as the detector operator. The main goal of these shifts is to turn on and monitor STAR subdetectors directly in the STAR detector control room during the data taking. In total, I spent together approx. 10 weeks in this position.

Student advisory

As a part of my work, I helped supervise students during their bachelor's and master's degrees. These students worked on different open charm analyses at the STAR experiment. I

was a consultant to Tomáš Truhlář, who finished his bachelor thesis on multivariate analysis of D^0 in d+Au collisions [5]. Then, it was Zuzana Moravcová. In her bachelor thesis and during master studies, she worked on the training of Boosted Decision Trees machine learning method for reconstruction of $D^{\pm}$ mesons in Au+Au collisions [6]. Furthermore, I consulted her D^0 elliptic flow studies in d+Au collisions in her diploma thesis [7]. Finally, I was a consultant to Robert Líčeník in applying the BDT to calculate invariant yields of $D^{\pm}$ meson in Au+Au collisions [8].

Chapter 1

Cold nuclear matter effects

1.1 Elementary particles and interactions

The Universe is expected to be created from a hot and dense singularity 14 billion years ago. This singularity was a hot and dense matter, the quark-gluon plasma (QGP), which was present 10^{-10} to 10^{-6} s after the Big Bang. In the current Universe, visible matter comprises protons, neutrons, and electrons, forming atoms. However, according to Lambda Cold Dark Matter (λCDM) cosmology model [9], this ordinary matter makes only approx. 5 % of the energy density in the Universe. The rest includes dark energy (approx. 68 %) and dark matter (approx. 27 %).

The Standard Model is a theory that describes elementary particles of ordinary matter and their interaction via three fundamental forces: electromagnetic, weak, and strong. Fundamental forces are described by the exchange of gauge bosons with integer spin. Particles carrying electromagnetic interaction, described by Quantum Electrodynamics (QED), are photons. They have no mass and are charge neutral. Electrically charged bosons $W^{\pm}$, possessing mass of 80.377 ± 0.012 GeV/c^2 [3], and neutral Z^0, with mass 91.1876 ± 0.0021 GeV/c^2 [3], mediate weak interaction. Finally, gluons are massless carriers of the strong interaction, described by the theory called Quantum Chromodynamics (QCD). This interaction pertains to the color charge that both gluons and quarks possess.

Quarks and leptons are elementary particles forming matter. All of them are fermions since they have half-integer spin. Quarks carry both color and electric charge, while leptons do not have the color charge. Electrons, muons, tauons, and their antiparticles carry an electric charge, unlike neutrinos that remain neutral. This is why neutrinos have a lower chance of interaction. Although the original Standard Model predicts that neutrinos have no mass, it was experimentally proved that neutrinos oscillate between their flavors, so they should have very low but non-zero mass [10,11]. This oscillation was firstly measured by experiments detecting neutrinos in cosmic rays. The current goal of the neutrino experiments is to measure neutrino mass precisely or to detect new, so-called sterile neutrino that would help theoretically explain their non-zero mass in the Standard Model [12].

Last but not least, another fundamental principle of the Standard Model is the Higgs mechanism. It describes observed masses of gauge bosons in the Standard Model via breaking the electroweak force symmetry. This mechanism is assured by the Higgs boson, the last experimentally confirmed particle of the Standard Model [13]. Higgs boson is a scalar particle and posses mass of 125.22 ± 0.14 GeV/c^2 [14].

Nowadays, multiple supersymmetry theories predict new elementary particles. These models are based on the new symmetry, causing that every matter particle (fermion) of the Standard Model has its boson counterpart and vice versa [15]. Dark matter in the Universe might be composed of such exotic particles. Despite the significant effort to measure them, they are yet to be observed. Dark matter particles are expected to not interact via strong or electromagnetic interaction and have very low mass. These particles are known in most models as weakly interacting massive particles (WIMPs) [16].

Dark matter could be detected by its gravitational effects. However, the Standard Model does not describe the gravitational force. General relativity predicts that massive objects cause the warping of spacetime. Acceleration of such objects disrupts this spacetime and propagates as gravitational waves with the speed of light. Einstein predicted this phenomenon in 1916 [17]. In 2016, the first measurement of gravitational waves was announced by LIGO and Virgo collaborations [18]. The particle that might be a carrier of the gravitation, graviton, has not yet been measured or observed, but it might be imagined as the smallest gravitational wave possible. Due to the infinite range of the gravitational force, it would have zero mass and, because of the general relativity properties, spin 2.

Despite the success of the Standard Model in describing matter around us, more is needed to provide a successful description of the matter-antimatter asymmetry. If the physics processes obeyed the Standard Model theory during the Universe's creation, the amount of matter and antimatter in the Universe would be the same. This symmetry was broken during the early phases of the Universe in the process called baryogenesis. It still needs to be clarified how exactly this process occurred. The matter-antimatter asymmetry might be caused by a violation of the charge-conjugation parity-reversal (CP) symmetry, which predicts the same behavior of a particle and its antiparticle in the mirror image of its spatial coordinates. Strong and electromagnetic interactions are CP invariant, but the violation was measured in weak decays. It was first observed in 1964 in K^0 decay at Alternating Gradient Synchrotron (AGS) accelerator in Brookhaven National Laboratory (BNL) [19]. This discovery was awarded the Nobel Prize in 1980. From then, CP violation was studied in the weak decays of charm and beauty mesons [3].

Another baryogenesis scenarios describe the transition between the high-temperature electroweak symmetric phase of matter to the low-temperature matter with broken symmetry. This transition has yet to be measured. However, the planned Future Circular Collider (FCC) in CERN may allow studying such theories via new interactions at mass scale at the level of 100 TeV [12].

1.2 Phase diagram of the QCD matter

Gluons, carriers of the strong interaction, contrary to photons carrying electromagnetic interactions described by the QED, have a color charge. The color charge results in self-interactions of the gluon field, bringing several new features to the QCD compared to the QED. In the QED, negatively charged electrons in the vacuum emit virtual photons that could transform to electron-positron pairs. Because of this virtual pair creation and annihilation, the electron is surrounded by the polarized medium, or the cloud of photons, electrons, and positrons. Because of the electron's negative charge, positrons are attracted by the bare charge and thus are close to the center of the cloud. This distribution of the electric charge around the electron naturally causes so-called screening of the electric charge– the measured electric

charge depends on how far from the center of the cloud it is tested. The measured charge is higher if the test probe penetrates the cloud. In the QED, electric charge is calculated as the combination of all the possible variations of the cloud. Such calculation consists of summating all the possible vacuum polarization loops, bringing divergent intervals. These integrals are then regularized, and the theory is renormalized to describe physically measurable quantities.

However, if the same procedure is applied in QCD, additional self-interaction of gluons (carrying color charge) should be taken into account. This leads to the formation of a cloud of gluons with the same color and corresponding anticolor as the quark they surround and quarks of the same color. If the quark in the center of the cloud is tested the same way as it is done for electrons, a probe that penetrates the color cloud charge measures a lower color charge. This antiscreening of the color charge causes the so-called asymptotic freedom. Quarks close to each other are free, noninteracting particles. However, the larger the distance from the bare quark, the stronger the interaction is. If more energy is fed to a quark-antiquark pair bind, their distance could be larger. However, at a large enough distance, generating quark-antiquark pair from the vacuum is energetically more favorable.

In the 1970s, Hagedron first predicted that at sufficiently high temperatures, a QCD matter phase transition occurs [20]. Hagedron's statistical model is based on the thermodynamics of strong interactions at large temperatures. At the critical temperature, hadrons are melted, and quarks become deconfined and quasi-free particles. Created hot and dense nuclear matter is the quark-gluon plasma (QGP). Energy densities and temperatures sufficiently high to create the QGP are accessed in collisions of heavy ions at accelerator experiments.

One of the first measured observable of the QGP was the strangeness enhancement in sulfur-sulfur collisions, measured by the NA35 Collaboration in CERN [21]. However, in studies of asymmetric proton-ion collisions in 1992, such enhancement was not measured [22]. These differences in the strangeness productions indicated the different particle production processes in heavy-ion and p-A collisions. Creation of the QGP in heavy-ion collisions [23] was finally confirmed by the experiments at Relativistic Heavy Ion Collider (RHIC) in 2004 [24–27]. One of the main QGP observables is the collectivity of the particles produced in heavy-ion collisions. It is accessed via momentum anisotropy of the final state particles (anisotropic flow) and is caused by initial spatial anisotropy in the overlap region of colliding hadrons.

Furthermore, other probes of the QGP in the collisions are both distribution and modification of produced particle jets (collimated sprays of particles). If the pair of jets (di-jet) is created in the collision, where no hot medium is expected, both of the jets are observed with nearly the same energy, but the opposite direction. In the case of heavy-ion collision, di-jet asymmetry is observed. Thus one of the observed jets has lower energy and a more distorted shape than its counterpart [28, 29].

Another striking evidence of the QGP creation is the suppression of quarkonia states[1] in heavy-ion collisions compared to the p+p. The confinement inside quarkonia is expected to be screened by the free color charges (quarks and gluons) in the hot medium. This phenomenon is the so-called color Debye screening [30]. If the screening is strong enough, quarkonia are "melted", and their production is suppressed. The Debye screening depends on the medium temperature and the binding energy of quarkonia. Therefore, with known binding energy, a comparison of quarkonia measurements probes the temperature and energy density reached in the QGP.

[1] Quarkonium is meson with valence quark and antiquark having the same flavor.

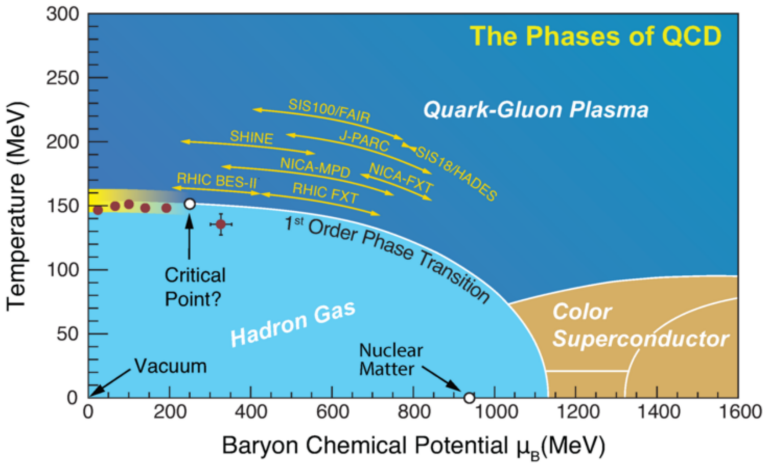

Figure 1.1: Sketch of the QCD phase diagram indicating the range in baryon chemical potential μ_B and temperature that different experiments cover. Taken from Ref. [31].

Figure 1.1 displays the so-called QCD phase diagram, representing states of QCD matter for given baryochemical potential (energy needed to add one baryon to the system) and temperature of the system. There are three different states of the QCD matter. Quarks and gluons are confined in the hadron gas and deconfined in the QGP phase. For high baryon chemical potential and low temperature, there is a color superconductor state [32]. There are two predicted transitions from hadrons to the QGP. For low baryochemical potential and high temperature, lattice QCD calculations predict rapid cross-over transition [33]. On the other hand, for higher baryochemical potential and low temperatures, the first-order transition is predicted [34]. There is a so-called critical point between these two types of transitions. The search for this point is one of the goals for heavy-ions physics since its precise position in the phase diagram still needs to be discovered. When cross-over transition occurs for zero baryon chemical potential, the critical temperature is currently calculated to be 154 ± 9 MeV [35].

In the collisions in experiments, firstly, there are inelastic collisions between colliding nucleons. The QGP might be created if the energy density is high enough and the system becomes nearly stable. The system starts to expand, lowering its temperature. Thus, as seen in the QCD diagram in Fig. 1.1, the confined nuclear matter starts forming in a process called hadronization. After that, inelastic collisions between hadrons occur. When the system cools down enough, it freeze-out and there are no inelastic collisions between hadrons.

Additionally, Fig. 1.1 shows the coverage of the experiments measuring properties of the QCD matter. One of the most crucial experimental programs that study the QCD phase diagram is the Beam Energy Scan (BES) at the STAR experiment, which first phase was measured mainly in years 2010–2011 [36] and the second in 2019–2020 [37]. Collecting data from Au+Au collisions with different energies allows covering baryon chemical potential from 20 to 400 MeV.

1.3 Cold nuclear matter effects in p/d+A collisions

In heavy-ion collisions, the created hot matter is expected to modify the particle spectra. Various observables, such as described collectivity of produced particles, di-jet asymmetry,

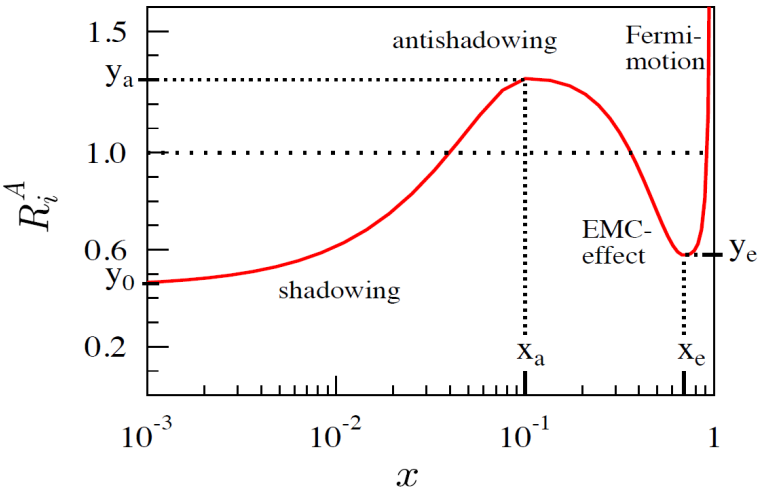

Figure 1.2: Modification of parton distribution functions in colliding nuclei, expressed as dependency of shadowing factor R_i^A on the parton momentum fraction x in the nucleus, with different regimes indicated. Taken from Ref. [38].

and suppression of particle production, could help calculate the QGP properties. However, to study these QGP effects, a quantitative understanding of the effects of the heavy nuclei in the initial stages of collisions is needed. Asymmetric collisions are studied to isolate these so-called cold nuclear matter (CNM) effects. These asymmetric collisions are mainly proton-lead (p+Pb) collisions at the Large Hadron Collider (LHC) in CERN, proton-gold (p+Au) and deuteron-gold (d+Au) collisions at the RHIC in BNL. At RHIC, the maximum energy of the collision is $\sqrt{s_{\mathrm{NN}}} = 200$ GeV. Therefore, the energy density in such collisions is expected to be too low to create the thermalized medium. Nevertheless, a dense nuclear environment could alter colliding nucleons. At LHC, p+Pb collisional energies go up to $\sqrt{s_{\mathrm{NN}}} = 8.16$ TeV.

Parton distribution functions (PDF) describe the probability to find a given parton (quark or gluon) with parton momentum fraction x (fraction of the nucleon momentum carried by the parton) in a nucleon. The dynamics of partons and mainly PDF are expected to differ for free protons and nucleons in colliding nuclei. In relativistic heavy ions, the density of partons could largely grow. Nuclear modification of PDF depends on the x regime and on the scale of parton-parton interaction Q^2. In the case of deep inelastic scattering, the process of the probing nucleon by lepton, Q^2 is the square of momentum transfer between the nucleon and the probe. Generally, it could be considered as a resolution scale of the process. The nuclear modification factor of the PDF could be expressed by a shadowing factor

$$R_i^A(x, Q^2) = \frac{f_i^A(x, Q^2)}{A f_i^{\mathrm{nucleon}}(x, Q^2)}, \tag{1.1}$$

where f_i^A is the bound nucleon PDF (nPDF) for parton flavor i and f_i^{nucleon} is the free nucleon PDF. The value of R_i^A for different x is shown in Fig. 1.2. Four different regions of nuclear modifications are shown.

At small x, there is a so-called nuclear shadowing regime [39]. The number of partons in the nucleon saturates, and sea quarks and gluons dominate PDF. At sufficiently high energy, called saturation scale, the gluon radiation probability is lower than the probability of the gluon fusion. A low number of gluons induces lower particle production cross-section. This

phenomenon is described by the color glass condensate (CGC) theoretical framework [40]. Additionally, due to the saturation, interactions with the target nucleus are limited to the nucleons on its surface since the inner ones are shadowed.

Multiple soft interactions of the partons in the initial stages of the collisions result in the so-called nuclear broadening of the initial beam parton transverse momentum (k_{T}-broadening). Such broadening is the source of another CNM effect, the Cronin effect [41], also called antishadowing, discovered in 1974. When first observed, the particle production in proton-nucleus collisions was enhanced compared to the p+p case for hadron transverse momentum $2 < p_{\mathrm{T}} < 6$ GeV/c. Generally, it is observed as an enhancement of the particle production in the intermediate p_{T} region that increases with the mass of the measured hadron.

Additionally, the interactions of the hadrons in the final state might contribute to the CNM effects. Bound states, especially quarkonium, could be absorbed when passing through the nucleons [42]. Furthermore, quarkonia could be dissociated by comovers— partons or hadrons created or moving in their proximity. Since quarkonia suppression is considered an essential probe of the QGP created in heavy-ion collisions, measuring how much of this suppression is caused by the final state interactions with the cold matter is crucial.

Finally, to properly evaluate the effects of the hot medium, it is important to compare particle yields in proton-proton (p+p) and the heavy-ion (A+A), proton-nucleus (p+A) or deuteron-nucleus (d+A) collisions. Nuclear modification factor measurements could quantify such a comparison of particle production in different collisional systems. In case of a comparison of given particle yield $\mathrm{d}N/\mathrm{d}p_{\mathrm{T}}$ in d+A and in p+p collisions, it is defined as

$$R_{\mathrm{p+A}} = \frac{\left.\dfrac{\mathrm{d}N}{\mathrm{d}p_{\mathrm{T}}}\right|_{\mathrm{p+A}}}{\langle N_{\mathrm{coll}}\rangle \left.\dfrac{\mathrm{d}N}{\mathrm{d}p_{\mathrm{T}}}\right|_{\mathrm{p+p}}}, \tag{1.2}$$

where $\langle N_{\mathrm{coll}}\rangle$ is the average number if binary nucleon-nucleon collisions in p+A collision, usually obtained with the Glauber model [43]. The nuclear modification factor is similarly defined for A+A collision or any collision type if $\langle N_{\mathrm{coll}}\rangle$ is calculated accordingly. N_{coll} depends on the overlap of the colliding nucleus and nucleon (nucleus in the case of A+A collisions). Figure 1.3 shows the schematic view of the collision in the collider, where the projectile and target could be nucleon or nucleus. Nucleons participating in the collisions are those in the region where projectile and target overlap. The higher the distance of their centers (size of the impact parameter vector $\mathbf{b}$), the lower the number of participants and thus lower N_{coll}. Every collision system could be divided into centrality classes, from those with the lowest (central collisions) to those with the highest impact parameter size (peripheral collisions). For the studies separated into centrality classes, N_{coll} is averaged for the collisions in the given centrality interval. Impact parameter, number of participants, and N_{coll} could not be directly measured, so the simulated collisions are matched to the observables, such as the collision multiplicity (number of tracks detected in the mid-rapidity region) or the signal in the detectors situated at high rapidities, measuring the signal from non-participating nucleons.

If the p+p reference is unavailable, particle production modification could be studied with the ratio of yields in central and peripheral collisions. Additionally, if the detector acceptance allows for p/d+A collisions, forward production could be compared with the backward one. Nuclear modification factor equal to unity means that production in compared collision types

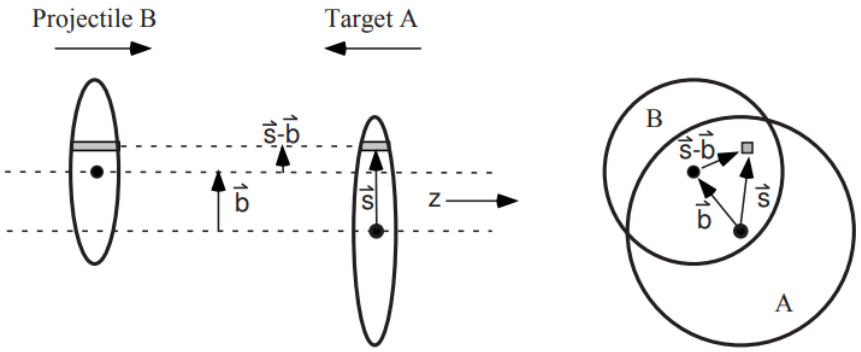

Figure 1.3: Schematic representation of the collision geometry (used in the Optical Glauber Model), with transverse (left) and longitudinal (right) views. Impact parameter **b** is the vector between the projectile and the target centers. Taken from Ref. [43].

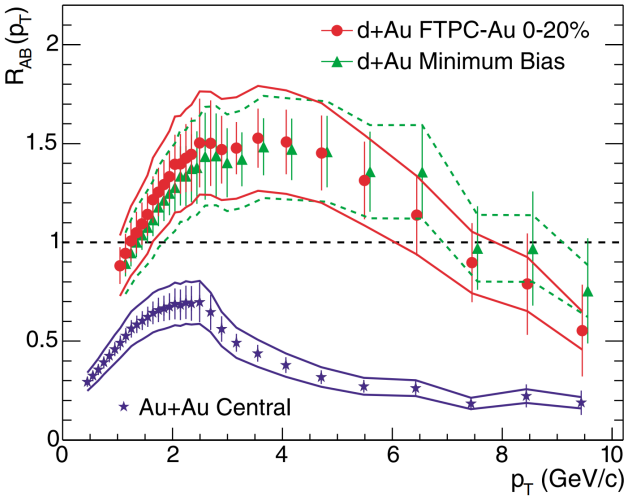

Figure 1.4: Nuclear modification factor R_{AB} vs. transverse momentum p_{T} for inclusive hadrons, measured in minimum-bias and central d+Au and central Au+Au collisions at $\sqrt{s_{\mathrm{NN}}} = 200$ GeV by the STAR experiment. Taken from Ref. [44].

is equivalent and that the p+A or A+A collision is a superposition of $\langle N_{\mathrm{coll}} \rangle$ p+p collisions. However, for example, the production of light particles is suppressed in the central A+A collisions at sufficiently high energies, thus $R_{\mathrm{A+A}} < 1$.

Figure 1.4 shows the nuclear modification factor of inclusive hadrons as a function of their transverse momentum p_{T} in minimum-bias and central d+Au and central Au+Au collisions at $\sqrt{s_{\mathrm{NN}}} = 200$ GeV.[2] Hadron production is suppressed in Au+Au collisions, since for p_{T} larger than 5 GeV/c $R_{\mathrm{Au+Au}}$ is at the level of 0.3. For lower p_{T}, a clear peak is mainly caused by the Cronin effect. In d+Au collisions, this effect is even more evident. The Cronin peak is much broader, and $R_{\mathrm{d+Au}}$ goes up to 1.5. As can be seen, it is important to measure nuclear modification factors in p/d+A collisions to separate initial state and hot-medium-induced effects properly.

In the same d+Au collisions, the PHENIX experiment measured the $R_{\mathrm{d+Au}}$ for identified

[2] $p_{\mathrm{T}} = \sqrt{p_{\mathrm{x}}^2 + p_{\mathrm{y}}^2}$, where particle momentum vector $\mathbf{p} = (p_{\mathrm{x}}, p_{\mathrm{y}}, p_{\mathrm{z}})$, while p_{z} denotes momentum in the direction of beam (colliding nucleons).

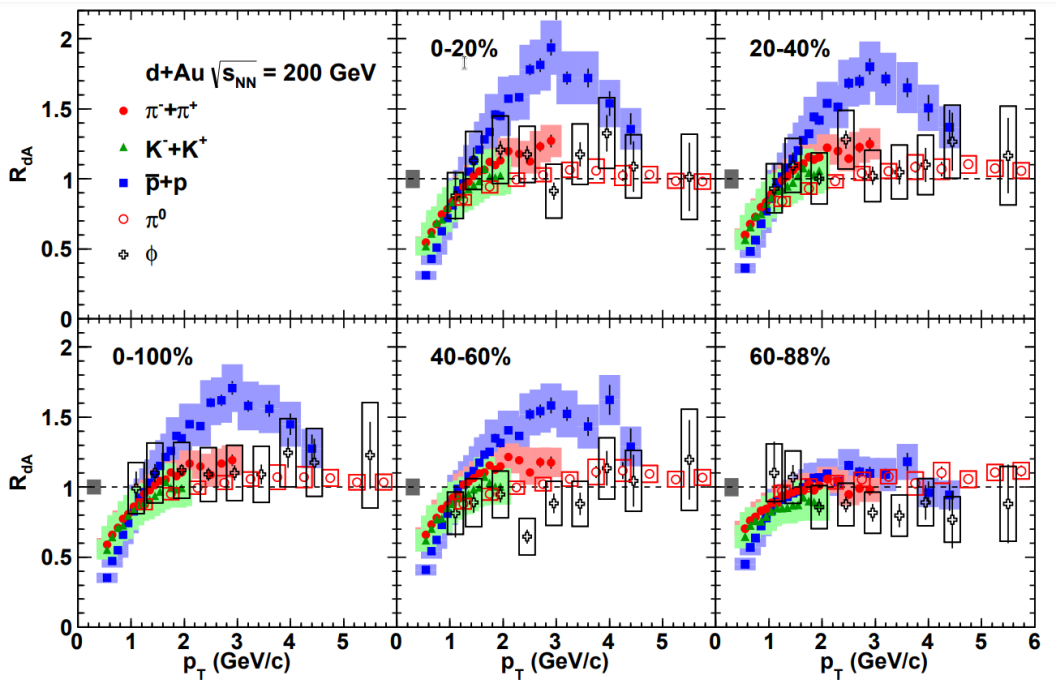

Figure 1.5: Nuclear modification factor R_{dA} vs. transverse momentum p_{T} for identified hadrons, measured in d+Au collisions centralities and at $\sqrt{s_{\mathrm{NN}}} = 200$ GeV by the PHENIX experiment. Taken from Ref. [46].

particles and various collision centralities. Results are shown in Fig. 1.5. As can be seen, the Cronin peak enhancement disappears in more peripheral collisions. In the central d+Au collisions, for pions and kaons, the maximum $R_{\mathrm{d+Au}}$ is at the level of 1.2. However, for protons, it goes up to 2. This baryon enhancement (also referenced as baryon anomaly) was also observed in Au+Au collisions [45], and it is another effect that needs to be studied in p/d+A collisions.

To summarize, measurements of the asymmetric collisions thus have crucial importance in the QGP studies. Anisotropic flow and the suppression observed in heavy-ion collisions have been the main proofs of the QGP creation. However, it is essential to measure these observables in the small collisional systems to isolate different sources of these effects, which might be initial-state interactions, multiple light scatterings of the colliding partons, possible modification of the hot QCD matter, different hadronization processes, or the final-state interactions.

1.4 Measurement of open-charm hadrons

Thanks to their large mass, heavy (charm c with mass of 1.27 ± 0.02 GeV/c^2 and beauty b with mass of $4.18^{+0.03}_{-0.02}$ GeV/c^2 [3]) quarks are created mainly in the initial stages of heavy-ion collisions and then travel through the hot and dense matter. Thus, they are excellent probes of the properties of the QGP, such as its temperature, the density of the partons, and their hadronization process. Measurements of charm meson production in heavy-ion collisions also allow studies of the charm quark energy loss in the hot medium, which is directly related to the transport coefficients of the QGP. There are two main sources of energy loss of quark

in the medium. One is collisional energy loss, which is important for traversing parton with low transverse momentum. The other one is inelastic energy loss via gluon radiation, which is expected to depend on the quark color and mass [47]. The mass ordering is expected in this energy loss, so for gluons and light quarks, it is higher than for charm quarks, and for them, it is higher than for b quarks. Furthermore, the collective behavior of charm quarks in the QGP is sensitive to the degree of thermalization in the medium. It can be used to constrain the heavy-flavor quark spatial diffusion coefficient.

Charm quark was discovered in 1974 when J/ψ, the bound state of c quark and its antiparticle $\overline{\mathrm{c}}$ was measured by experiments in SLAC [48] and at AGS accelerator in BNL [49]. This discovery was awarded the 1976 Nobel Prize. In 1976, in SLAC, the first mesons with one c quark were reconstructed via their decays to kaons and pions [50,51]. Mesons that have one c or $\overline{\mathrm{c}}$ quark are D mesons. This thesis aims to study the production of D^0 mesons formed of c and $\overline{\mathrm{u}}$ quarks. D^0 meson antiparticle, $\overline{\mathrm{D}^0}$, is composed of u and $\overline{\mathrm{c}}$ quarks and is usually studied together with D^0 meson. Invariant mass of D^0 meson is measured to be 1864.83 ± 0.05 MeV/c^2 and its lifetime τ is $(410.1 \pm 1.5) \times 10^{-15}$ s, that corresponds to $c\tau = 122.90 \pm 0.45$ μm [3].

In analyzing data from collisions of heavy ions, if the detector resolution of the primary vertex and track position is sufficient, hadronic decays of D mesons are used to reconstruct them and measure their production invariant yield. Charged D^+ meson (composed of valence c and $\overline{\mathrm{d}}$ quarks) is reconstructed via its decay to K^- and two π^+ with branching ratio 8.98 ± 0.28 % and $c\tau = 311.8 \pm 2.1$ μm [3]. D^{*+} meson, that has resonance width 83.4 ± 1.8 keV [3], decays in the primary vertex and is reconstructed via its decay to D^0 meson and π^+ with branching ratio 67.7 ± 0.5 % [3]. In the main analysis of this thesis, decay channel $\mathrm{D}^0(\overline{\mathrm{D}^0}) \rightarrow \mathrm{K}^-\pi^+(\mathrm{K}^+\pi^-)$ with branching ratio 3.89 ± 0.04 % [3] is used. Kaons and pions could be directly detected at experiments, which allows full reconstruction of D mesons.

1.4.1 D^0 meson topological reconstruction

The STAR detector can track charged particles with great precision. Thanks to this, topological properties of D^0 meson decay are used to reconstruct this meson. In this section, topological decay variables used in the main analysis of this thesis, reconstruction of D^0 meson in d+Au collisions at $\sqrt{s_{\mathrm{NN}}} = 200$ GeV, are described. These variables are common for open-charm hadron analyses across high-energy physics experiments. Figure 1.6 shows schematic decay of D^0 meson together with used variables:

- primary vertex (PV) is the reconstructed place of the collision, where D^0 meson is created;
- kaon and pion distance of the closest approach (DCA) to PV, $\mathrm{DCA_K}$ and DCA_π;
- DCA between daughter particles (K and π), $\mathrm{DCA_{daughters}}$;
- D^0 meson decay vertex (SV, secondary vertex), reconstructed as the midpoint of the line corresponding to $\mathrm{DCA_{daughters}}$;
- decay length of D^0 meson candidate corresponding to the lifetime of D^0 meson, calculated as the distance between PV and SV;
- reconstructed D^0 meson distance of the closest approach to primary vertex, $\mathrm{DCA_{D^0}}$;
- angle θ between reconstructed D^0 (Kπ pair) momentum $p_{\mathrm{K}\pi}$ and decay length vector;
- angle ζ between reconstructed $p_{\mathrm{K}\pi}$ and kaon momentum.

Since origins of kaons and pions tracks coming from D^0 meson decays are expected to be shifted from PV, $\mathrm{DCA_K}$ and DCA_π are expected to be larger than 0 μm and thus have

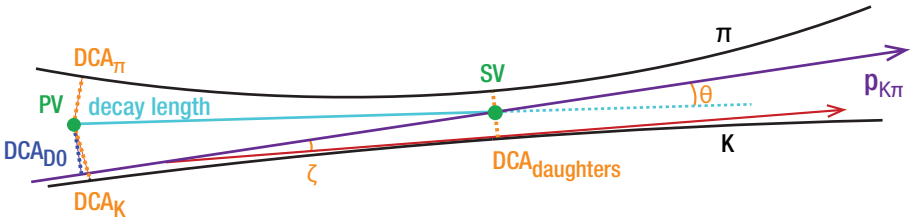

Figure 1.6: Schematic representation of D^0 meson decay. D^0 is created in the primary vertex (PV) and decays in the secondary vertex (SV) to kaon and pion, whose distances of closest approach (DCA) to PV (DCA_K and DCA_π) and between them ($DCA_{daughters}$), together with reconstructed decay length and D^0 meson distance of closest approach to PV (DCA_{D^0}) are used for D^0 meson topological reconstruction. Curvatures of K and π tracks are exaggerated.

significant classification power. Thanks to the great HFT spatial resolution, the reconstructed decay length is also expected to be shifted from 0 μm, even after the smearing caused by finite detector resolution. Omitting detector smearing effects, the momentum of D^0 before the decay has the same direction as the momentum of the Kπ pair. Therefore, the cosine of θ is expected to be close to the unity. It is expected that most of the D^0 mesons in d+Au collisions at $\sqrt{s_{NN}} = 200$ GeV are produced relatively close to the PV. Reconstructed Kπ pairs with high DCA_{D^0} are mainly from the combinatorial background because at such energies, non-prompt (coming from B meson decays) D^0 production is minimal. Generally, machine-learning algorithms significantly profit from uncorrelated variables. Because of this and to further suppress combinatorial background, we also decided to use the cosine of angle ζ.

1.4.2 Open-charm results from the STAR

STAR measured D^0 and D^* meson production in p+p collision at $\sqrt{s_{NN}} = 200$ GeV, recorded in 2009 [52]. D mesons were reconstructed via their hadronic decays to kaons and pions. From D meson production, overall charm production in these collisions was calculated. Together with theoretical calculations, the resulting charm production cross section is shown in Fig. 1.7 (left). In Fig. 1.7 (left top), measurements are compared with Fixed-Order Next-to-Leading-Log (FONLL) perturbative QCD calculations limits [53]. As can be seen, the results are on the model's upper limits, consistent with CDF and ALICE experiments results [52]. Figure 1.7 (left bottom) displays a comparison of the results with three different PYTHIA tunes. PHENIX tune was used in charm contribution estimation from dielectron measurements. PYTHIA configuration modified to match measured heavy-flavor production in low transverse momentum region is labeled as "this tune". This was the first direct D meson measurement for such low transverse momentum, so it helped with models' constraints.

Additionally, STAR studied D^0 and D^* in p+p at $\sqrt{s_{NN}} = 500$ GeV, recorded in 2011. Analysis steps and results in progress are described in detail in [54]. Resulting charm production calculated using various D mesons is shown in Fig. 1.7 (right), together with comparison to the FONLL calculations. Charm production results accessed via D mesons reconstruction in p+p at $\sqrt{s_{NN}} = 500$ GeV are in the STAR publication committee review and will be published soon. The author of this thesis is one of the primary authors of this future article. The main contribution is in the calculations of the trigger-bias efficiency (described for the D^0 in d+Au analysis in Sec. 4.6.7). Efficiencies of individual triggers and their impact on the calculated D^0 meson spectra were estimated from simulated collisions embedded in the

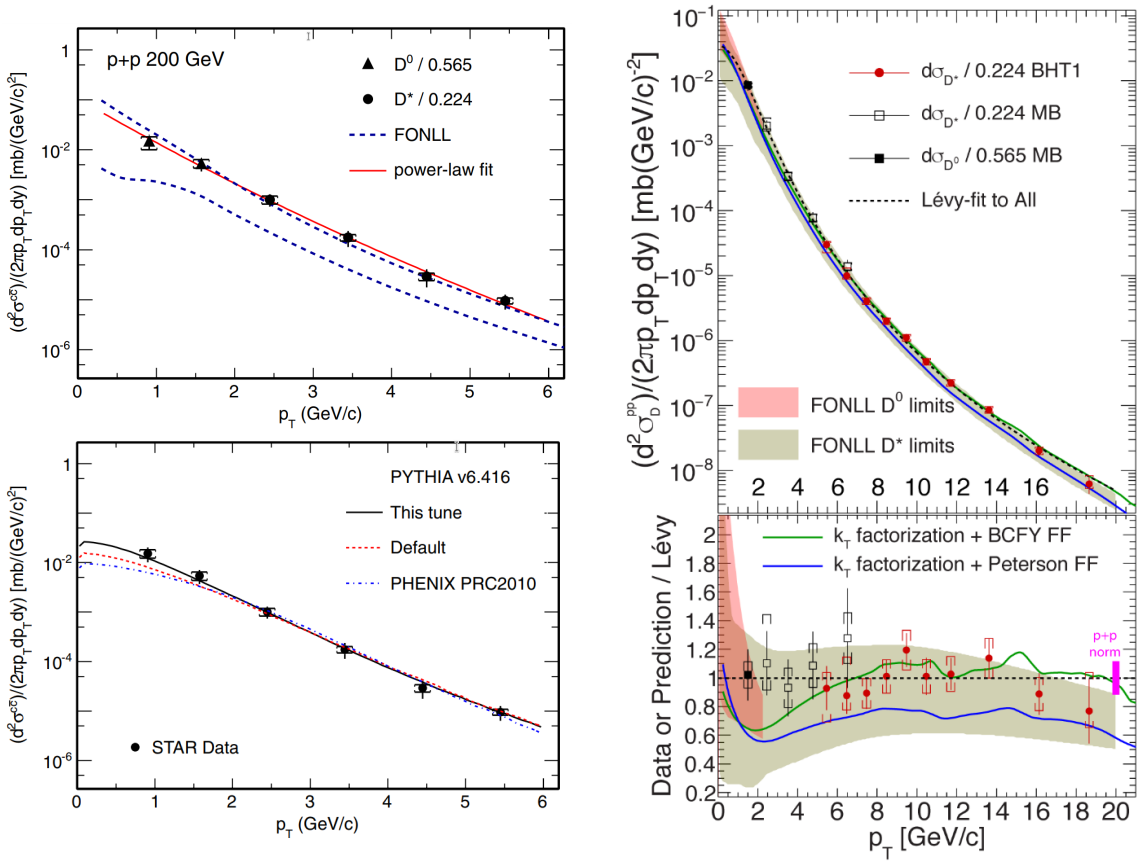

Figure 1.7: Charm productions cross section calculated from D^0 and D^* production in p+p collisions at $\sqrt{s_{NN}} = 200$ GeV (left plots) and $\sqrt{s_{NN}} = 500$ GeV (right), compared with FONL calculation [53] (left) and various PYTHIA tunes (right). Taken from Ref. [52] and [54].

recorded data. Resulting corrections are used to correct the D^0 and D^* mesons raw yields.

Furthermore, high transverse momentum electrons produced from heavy-flavor decays were measured in p+p collisions at $\sqrt{s_{NN}} = 200$ GeV in STAR [55]. Results are again consistent with FONLL calculations with uncertainties. To conclude the open heavy-flavor measurements in p+p collisions at STAR, models describe the measurements of both charm cross-section and electron from the open-charm decays. Therefore, open charm and mainly D^0 meson production is well understood in this collision system.

In the years 2014–2016, a detector built from precise silicon sensors, Heavy Flavor Tracker (HFT) (further described in Sec. 3.2.4), was installed at STAR, which enabled detailed measurements of the open-charm hadrons in Au+Au and d+Au collisions at $\sqrt{s_{NN}} = 200$ GeV. An overview of results from these measurements was presented by the author of the thesis at the International Conference in High Energy Physics [56] (proceedings are in App.B). D^0, $D^{\pm}$, D_s mesons and Λ_c baryon were reconstructed using the topological reconstruction of their decays to kaons, pions, and protons in a similar way as described in Sec. 1.4.1. Additionally, measurements of electrons coming from the decays of the heavy-flavor hadrons are enabled using template fitting of their DCA distributions.

Energy loss in Au+Au collisions is accessed via measurements of the nuclear modification factor R_{AA}. R_{AA} was measured for D^0 [57] and (for the first time at the STAR) $D^{\pm}$ [58] mesons using their hadronic decays for various collision centralities. Results for both mesons are consistent with each other. R_{AA} of D^0 meson is shown in Fig. 1.8. D meson production is suppressed at high transverse momentum $p_T > 3$ GeV/c and for central collisions. Figure 1.8 (right) shows that this suppression is similar to the one measured for light hadrons and to the D^0 mesons measured at the LHC in Pb+Pb collisions at $\sqrt{s_{NN}} - 2.76$ TeV. Towards more peripheral collisions, suppression at high p_T is lower. For low p_T, there is no significant collision centrality dependence.

Thanks to the excellent DCA resolution of the HFT, R_{AA} of electrons from both charm and beauty decays was measured, and it is shown in Fig. 1.9 (left). Charm-decayed electrons show suppression at high p_T, consistent with the measurements of D mesons. Measured beauty-decayed electrons suppression is smaller than charm-decayed electrons with significance $> 3\sigma$, as can be seen in Fig. 1.9 (right) when comparing the data with the null hypothesis. From this, it can be concluded that the energy loss of beauty is smaller than for charm hadrons.

Both D^0 meson and heavy-flavor decay electron R_{AA} results are compared to the theoretical calculations. R_{AA} of D^0 meson comparison to the Duke model [59] and the Linearized Boltzmann Transport (LBT) model [60] is shown in Fig. 1.8 (right). Figure 1.9 shows comparison of heavy-flavor electron R_{AA} with the Duke and Parton-Hadron-String-Dynamic (PHSD) model [61, 62]. These models use the same approach for hadronization modeling, combining coalescence and fragmentation mechanisms. Furthermore, they include heavy quark diffusion in the deconfined medium and mass-dependent energy loss mechanisms in the QGP. The Duke model uses a Langevin stochastic simulation to trace the charm quark propagation inside the QGP medium and incorporates collisional and radiative energy losses. The medium parameters have been constrained by fitting the previous experimental data. In the LBT, the transport calculation includes elastic scattering processes for collisional energy loss and the higher-twist formalism for medium-induced radiative energy loss. The heavy quark transport is coupled with a 3D viscous hydrodynamic evolution tuned for light-flavor hadron data.

The collectivity of particles produced in collisions is measured through angular anisotropies in the final-state momentum distributions and is described by Fourier expansion of the third

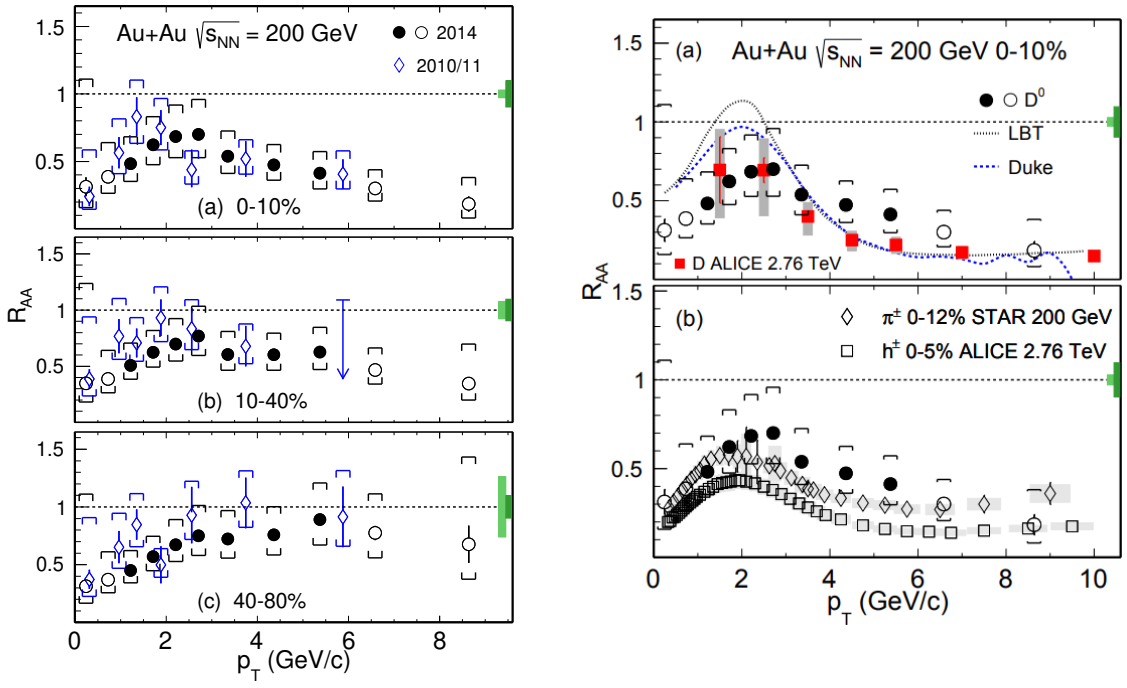

Figure 1.8: Left: the nuclear modification factor R_{AA} of D^0 meson as a function of transverse momentum p_{T} in different centrality classes measured with (year 2014) and without (years 2010/11) the HFT detector installed in Au+Au collisions at $\sqrt{s_{\mathrm{NN}}} = 200$ GeV. Right: R_{AA} of D^0 mesons measured in central collisions, compared to the R_{AA} of pions and to the ALICE results in Pb+Pb collisions at $\sqrt{s_{\mathrm{NN}}} = 2.76$ TeV. Taken from Ref. [57].

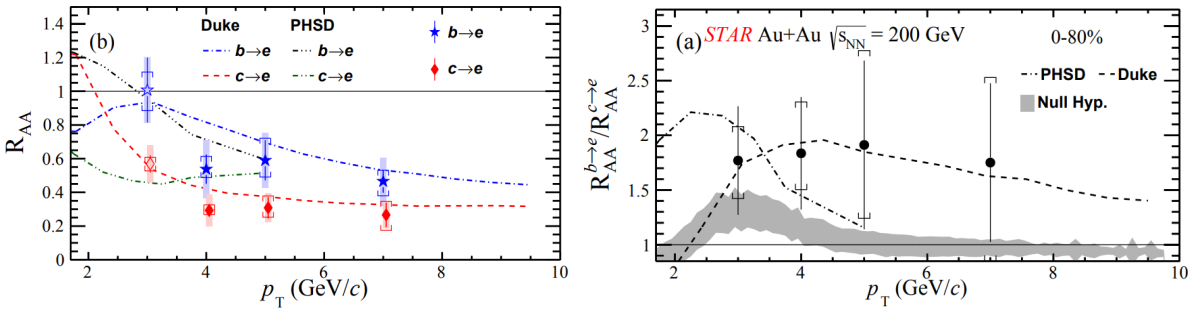

Figure 1.9: The nuclear modification factor R_{AA} of charm and bottom decay electron as a function of transverse momentum p_{T} (left) and their ratio (right), compared to the DUKE [59] and PHSD [61, 62] model predictions. Taken from Ref. [63].

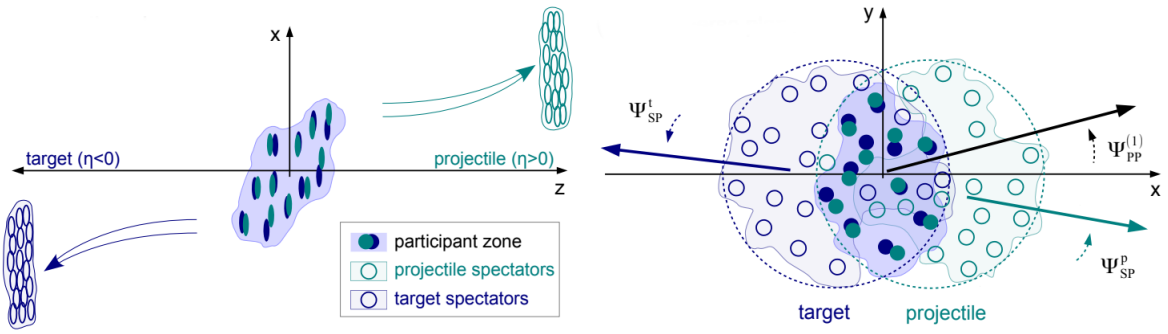

Figure 1.10: Schema of the non-central heavy-ion collision in the reaction (left) and transverse (right) plane. Taken from Ref. [66]

derivation of the particle distribution,

$$E\frac{\mathrm{d}^3N}{\mathrm{d}^3p} = \frac{1}{2\pi}\frac{\mathrm{d}^2N}{p_\mathrm{T}\mathrm{d}p_\mathrm{T}\mathrm{d}y}\left(1+2\sum_{n=1}^{\infty}v_n\cos\left[n(\phi-\psi_\mathrm{RP})\right]\right), \qquad (1.3)$$
$$v_n(p_\mathrm{T},y) = \langle\cos\left[n(\phi-\psi_\mathrm{RP})\right]\rangle,$$

where E is energy, p is momentum, p_T is transverse momentum, ϕ is azimuthal angle, y rapidity of produced particle and ψ_RP denotes the reaction plane angle. The reaction plane is defined by the beam axis and impact parameter of colliding nuclei. Figure 1.10 shows the schema of the non-central heavy-ion collision in the reaction plane (left) and transverse plane (right). Spectators are nucleons not participating in the collision. As seen in Fig. 1.10 (left), the spectators are deflected from the beam line. This deflection is significant for measurements at forward rapidities further from the place of the collision. Measurements of produced particles' v_1 enable quantitative studies of initial fields created by the spectator's and participant's matter. Contrarily, v_2 measurements probe the effects of high energy density in the participant zone, where colliding nuclei overlap. As displayed in Fig. 1.10 (right), this overlap region has an elliptical (almond) shape. Due to the large number of nucleons in this region, for high collisional energies, the energy density in this region causes the creation of a hot medium with high internal pressure. The expansion of this medium is sufficiently high to induce the collectivity of the produced particles. Experimentally, ψ_RP is usually approximated independently for each term of the series in Eq. 1.3, ψ_n. Several methods can be used. For example, for v_1 measurements, ψ_1 could be approximated using the azimuthal distribution of spectators in the forward rapidity [64]. For v_2 studies, ψ_2 could be, e.g., reconstructed using all prompt particles expected to be created in the collisions. More details on methods for flow analyses are in [65].

At STAR, D^0 meson collectivity measurements were done for the first two coefficients in Eq. 1.3, v_1 [64] and v_2 [67]. These results are shown in Fig. 1.11. Furthermore, v_1 and v_2 were also studied for electrons from charm hadrons decays. The elliptic flow v_2 of these electrons and for D^0 mesons is similar to the one measured for light hadrons. D^0 meson results are shown in Fig. 1.11 (left). Thus, charm quarks gain significant flow in the QGP and may achieve local thermal equilibrium. Directed flow v_1 studies access the constraints of initial conditions of the heavy-ion collisions. Furthermore, the initial electromagnetic field is predicted to induce larger v_1 for charm quarks than light flavor quarks due to the early production of charm quarks. It gives opposite contributions to charm and anti-charm quarks. Measured D^0 meson v_1 are shown in Fig. 1.11 (right). Measured v_1 is significantly larger for D^0 meson than for

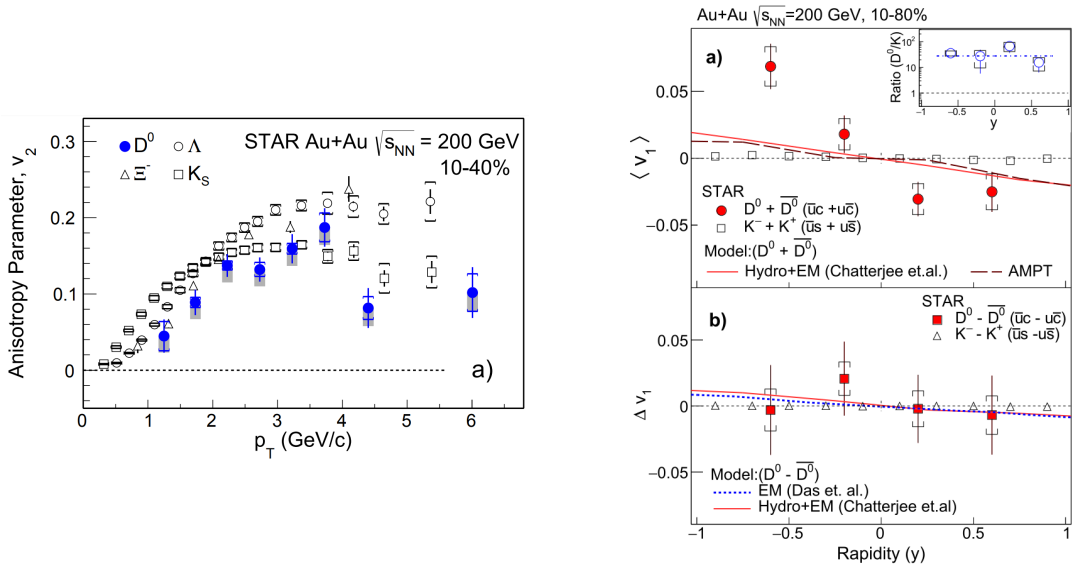

Figure 1.11: Elliptic v_2 (left, taken from Ref. [67]) and directed v_1 (right, taken from Ref. [64]) flow of D^0 meson. D^0 v_2 transverse momentum p_T dependency is displayed together with results for light hadrons. Directed flow v_1 results are rapidity dependent and calculated for D^0 with $p_T > 1.5$ GeV/c, compared to that of kaons for $p_T > 0.2$ GeV/c. Additionally, the bottom left plot displays v_1 particle-antiparticle difference.

light hadrons. Additionally, the magnitude of v_1 of charm-decayed electrons is consistent with D^0 mesons.

The charm quark hadronization properties are studied by measuring the yield ratios of charm hadrons. At STAR, baryon-to-meson ratio for charm quark is accessed with Λ_c/D^0 measurements [68]. The resulting yield ratio is shown in Fig. 1.12 (left). As seen in Fig. 1.12 (left top), it is comparable with the baryon-to-meson ratios for light and strange flavor hadrons. Additionally, this ratio increases towards more central collisions, which is consistent with the prediction of the coalescence hadronization model calculations. Comparison of the measurement with various model predictions is shown in Fig. 1.12. Models differ mainly in the charm quark hadronization mechanism and QGP medium properties. The model that best describes the data is the Catania model, which includes coalescence and fragmentation hadronization of charm quarks [69].

To probe both strangeness enhancement and coalescence of charm quarks with strange quarks in the QGP, D_s^+/D^0 yield ratio was measured [70]. As can be seen in Fig. 1.12 (right top), this ratio has no significant centrality dependence. Moreover, it is significantly larger than the fragmentation baseline, represented by a PYTHIA8 calculation. Figure 1.12 (right bottom) shows the comparison with the ALICE measurements in central Pb+Pb collisions at $\sqrt{s_{NN}} = 5.02$ TeV. The results from both experiments are consistent in the overlapping region.

The mentioned measurements in Au+Au collisions at $\sqrt{s_{NN}} = 200$ GeV are combined to calculate total open charm hadron production and compare with the one in p+p. This calculation is described in more detail in [58]. In Au+Au collision with 10–40% centrality, STAR measured open-charm hadron production cross section per binary collision as $113.3 \pm 6.2(\text{stat}) \pm 27.2(\text{sys})$ μb. In p+p collisions, charm quark production results have

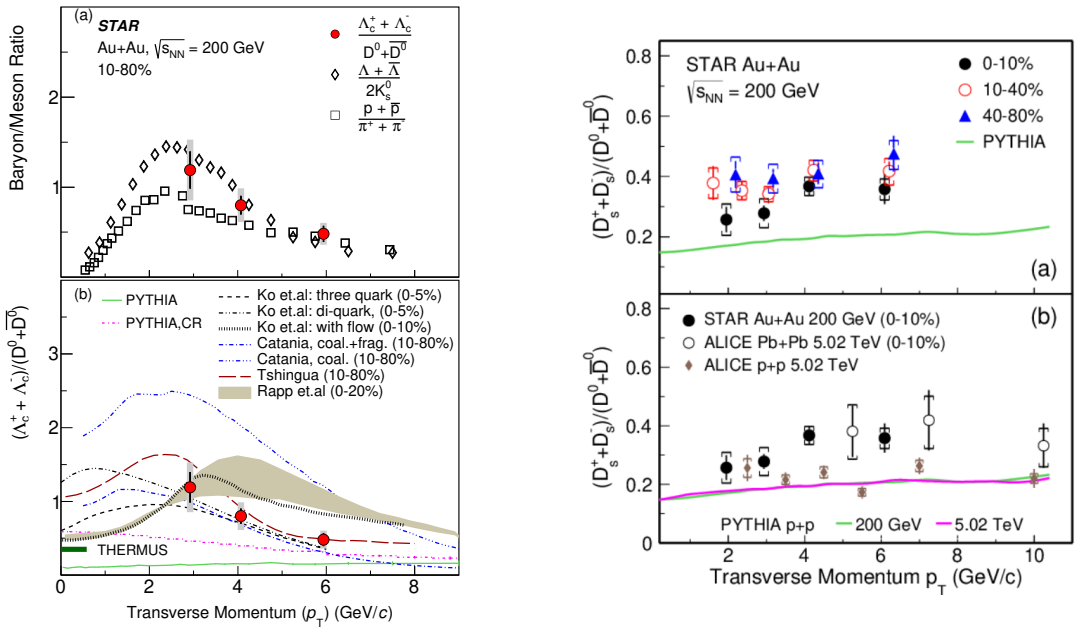

Figure 1.12: Left: Λ_c^+/D^0 yield ratio as a function of p_T compared to light-hadron results (top) and different model calculations (bottom). Taken from Ref. [68]. Right: $\mathrm{D}_\mathrm{s}^+/\mathrm{D}^0$ yield ratio as a function of p_T in different centralities of Au+Au collisions compared to PYTHIA p+p calculations and to an ALICE measurement [71, 72]. Taken from Ref. [70].

the consistent value of $130 \pm 30(\mathrm{stat}) \pm 26(\mathrm{sys})$ µb. Such agreement, together with D meson suppression measured with R_AA and yield ratios differing in p+p and Au+Au collisions, suggests different distribution of charm quarks among open-charm hadron species in Au+Au and p+p collisions. Furthermore, these results indicate that the charm quark participates in the coalescence hadronization in the QGP.

In 2016, STAR recorded d+Au collisions at $\sqrt{s_\mathrm{NN}} = 200$ GeV with the HFT installed. However, open-charm measurement results from these collisions have yet to be published. Such results would complement the open-charm studies and help to compare different physics effects in d+Au, Au+Au, and p+p collisions. This thesis presents measurement of D^0 meson production in these d+Au collisions.

1.5 Open charm measurements in p/d+A collisions

High-energy physics experiments extensively measure D^0 meson. In addition to the STAR measurements in heavy-ion collisions, the nuclear modification factor was measured in Pb+Pb collisions by CMS [73] and ALICE experiment [74]. ATLAS extensively studied D^0 meson production in p+Pb collisions at $\sqrt{s_\mathrm{NN}} = 8.16$ TeV [75]. The LHCb collaboration published detailed studies of the D^0 meson production dependency on the rapidity in p+Pb collisions at $\sqrt{s_\mathrm{NN}} = 5.02$ TeV [76]. Furthermore, elliptic flow of D^0 meson was published by CMS in p+Pb collisions at $\sqrt{s_\mathrm{NN}} = 5.02$ and 8.16 TeV [77].

The ALICE experiment also measured D meson species in p+Pb collisions at $\sqrt{s_\mathrm{NN}} = 5.02$ TeV using the topological reconstruction similar as described in Sec. 1.4.1. Results of the nuclear modification R_pPb for D^0, $\mathrm{D}^\pm$ and D^* are shown in Fig. 1.13 (left). For $p_\mathrm{T} > 3$ GeV/c,

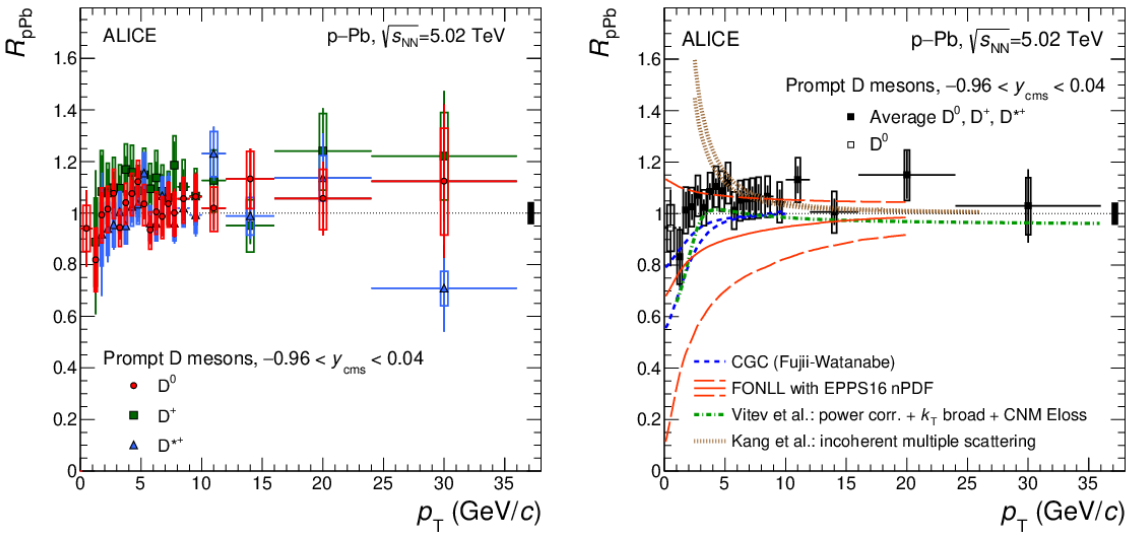

Figure 1.13: Nuclear modification factor vs. transverse momentum p_{T} of D^0 mesons in p+Pb collisions at $\sqrt{s_{\mathrm{NN}}} = 5.02$ TeV measured by the ALICE. The left figure separately displays results for D^0, $\mathrm{D}^{\pm}$, and D$*$. The results for D meson species are averaged on the right plot, and one D^0 meson point at low p_{T} is displayed. Results are compared with various theoretical predictions. Taken from Ref. [78].

R_{pPb} is consistent with unity for all measured D mesons. For lower p_{T}, R_{pPb} decreases, and there is a hint of modification by the CNM. Figure 1.13 (right) compares the species-averaged R_{pPb} with the model calculations incorporating various CNM effects. All models except the one by Kang et al., consisting of incoherent multiple scatterings, describe data within uncertainties. Successful models are based on the CGC theory, then k_{T}-broadening combined with nuclear shadowing, energy loss of the charm in the CNM, and various nPDF parametrizations.

Figure 1.14 shows transverse momentum dependence of nuclear modification factor in d+Au collisions at PHENIX for leptons from heavy flavor decays in two centrality classes (central and peripheral) and for three rapidity intervals (midrapidity, forward and backward rapidity). In this figure and other following figures, forward (positive) rapidity is in the direction of the colliding proton (deuteron). As it could be seen in Fig. 1.14 (right), the nuclear modification factor for leptons from heavy-flavor decays is consistent with unity for all of the three shown rapidity ranges in peripheral collision (centrality 60-88%). However, for the central collisions shown in Fig. 1.14 (left), nuclear modification factors in forward and backward rapidities strongly deviate from each other and unity. As described in [79], although the measurements at forward rapidity are described both by the model considering nPDFs, k_{T}-broadening and the CNM energy loss (ELOSS model) or by nPDFs alone, nuclear modification factor at backward rapidity cannot be described considering only the nPDFs.

In the measurements, it is also possible to distinguish leptons from beauty hadron decays and others. Nuclear modification factors of leptons from beauty decays in p+Pb collisions R_{pPb} at $\sqrt{s_{\mathrm{NN}}} = 5.02$ TeV and in Pb+Pb collisions at $\sqrt{s_{\mathrm{NN}}} = 2.76$ TeV, both measured by ALICE, is displayed in Fig. 1.15. Within uncertainties, R_{pPb} is consistent with unity. Thus, the production of electrons from beauty hadrons in p+Pb scales with that in p+p collisions. This measurement confirms that initial-state effects due to the presence of CNM are minor in

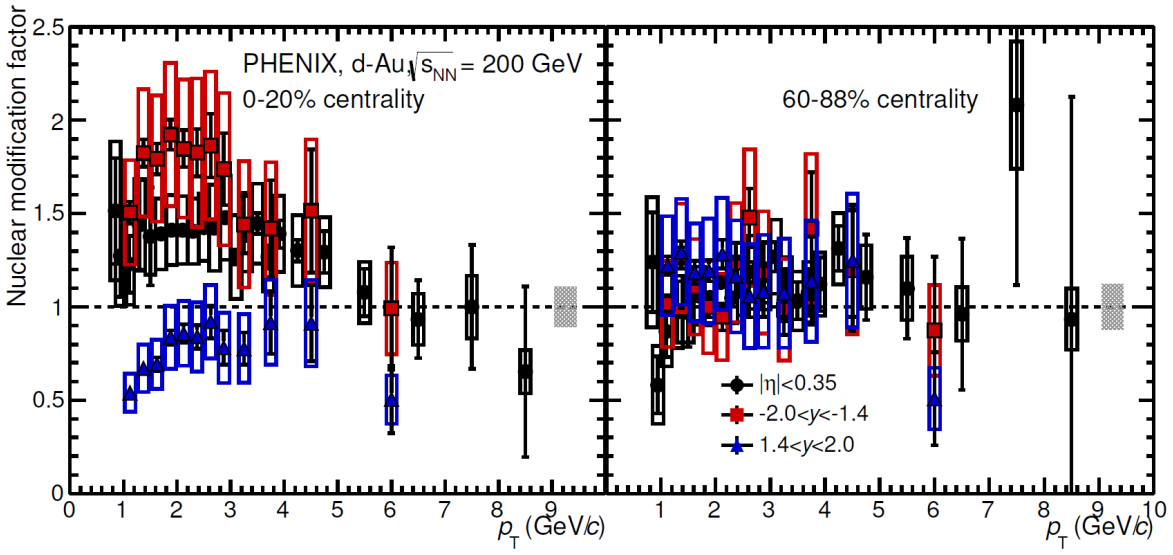

Figure 1.14: Nuclear modification factor of leptons from heavy flavor decays in d+Au collisions at $\sqrt{s_{\mathrm{NN}}} = 200$ GeV as a function of transverse momentum in the 0–20% (left) and 60–88% (right) centrality classes, measured by PHENIX. Taken from Ref. [79].

the measured transverse momentum range at LHC energies.

The STAR experiment recently published J/ψ measurements in p+Au collisions at $\sqrt{s_{\mathrm{NN}}} =$ 200 GeV recorded in 2015. Resulting nuclear modification factor R_{pA} is displayed in Fig. 1.16 (top) together with results from d+Au collisions measured by PHENIX and central Au+Au collisions measured by STAR, both at $\sqrt{s_{\mathrm{NN}}} = 200$ GeV. For $p_{\mathrm{T}} < 3$ GeV/c, the R_{pA} is consistent with unity, indicating no CNM effects in this region. For lower p_{T}, it drops to 0.7, contributing significantly to the nuclear modification factor in central Au+Au collisions. The new measurement in p+Au is consistent with the previously measured d+Au results. However, the precision of the new measurement is higher. The bottom plot of Fig. 1.16 compares p+Au results with the theoretical model predictions. All models agree with the measurements, except the comover model for $p_{\mathrm{T}} > 3.5$ GeV/c [81]. The ICEM and Lansberg calculations include the effects of nuclear modification of the PDF. The TAMU model extends the transport model for heavy-ion collisions to p+Au collisions [82].

Figure 1.17 shows the STAR measurement of D^0 meson production from the data recorded in 2003. D^0 mesons were reconstructed using reconstruction of Kπ pairs, but the detector resolution was significantly worse than in runs recorded with the HFT. Together with D^0 meson spectra, Fig. 1.17 shows results from non-photonic electrons. These were calculated by subtracting photonic spectra from the inclusive ones. Additionally, Fig. 1.17 displays fits of both D^0 and non-photonic electrons. Furthermore, the dotted line shows the electron fit results divided by the number of binary collisions in d+Au collisions. For lower transverse momentum p_{T}, the results in d+Au are consistent with those in p+p. For $p_{\mathrm{T}} > 2.5$ GeV/c, these lines are at the upper bound of uncertainty in p+p measurement.

The CNM effects on D^0 production were extensively measured in p+Pb collisions at LHC at $\sqrt{s_{\mathrm{NN}}} = 5.02$ and 8.16 TeV. At RHIC, where the energy of the p/d+Au collisions is much smaller, $\sqrt{s_{\mathrm{NN}}} = 200$ GeV, only measured D^0 meson spectra in d+Au collisions were recorded in 2003. However, the precision of these measurements did not allow us to study CNM effects in more detail. In order to study all regimes of the nuclear modification of initial PDF in

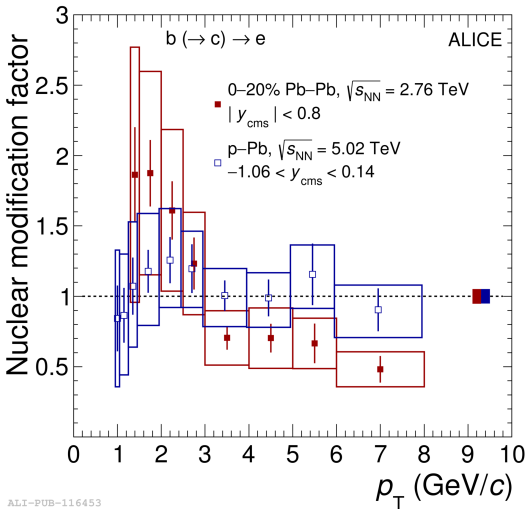

Figure 1.15: Nuclear modification factors R_{pPb} and R_{PbPb} of electrons from beauty-hadron decays at mid-rapidity as a function of transverse momentum for minimum-bias p+Pb collisions at $\sqrt{s_{\mathrm{NN}}} = 5.02$ TeV and 20% most central Pb+Pb collisions at $\sqrt{s_{\mathrm{NN}}} = 2.76$ TeV, measured by ALICE. The data points of the p+Pb analysis were shifted by 0.05 GeV/c to the left along the p_{T} axis for better visibility. Taken from Ref. [80].

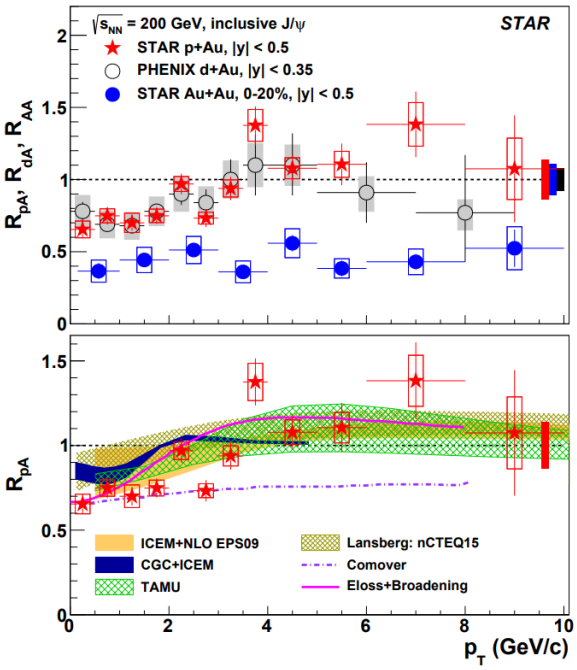

Figure 1.16: Top: nuclear modification factor of J/ψ $R_{\mathrm{pA/dA/AA}}$ as a function of transverse momentum p_{T}, measured in p+Au, d+Au and central Au+Au collisions at $\sqrt{s_{\mathrm{NN}}} = 200$ GeV. Bottom: J/ψ R_{pA} in p+Au collisions compared the various theoretical model calculations. Taken from Ref. [83].

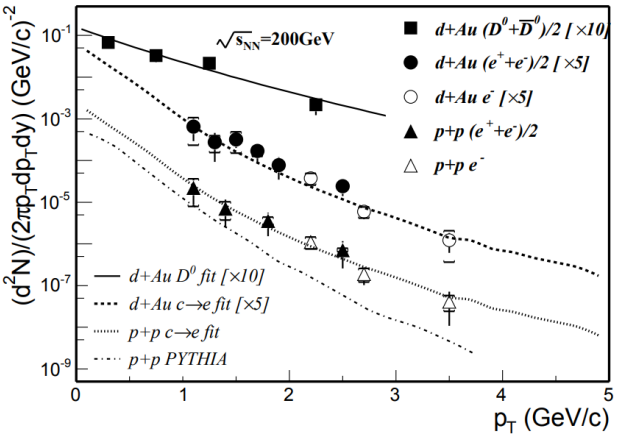

Figure 1.17: D^0 transverse momentum p_T distributions from d+Au collisions at $\sqrt{s_{NN}}$ = 200 Gev, measured in 2003, together with non-photonic electron p_T distributions in p+p collisions and d+Au collisions. Solid and dashed lines are the fit results from both D^0 and electron spectra in d+Au collisions. The dotted line is scaled down by a factor of $N_{bin} = 7.5 \pm 0.4$ from d+Au to p+p collisions. Taken from Ref. [84].

collisions where the QGP is not created, it is necessary to complement LHC results with the results at the RHIC energies. Furthermore, to complement measurements of CNM effects on the J/ψ production in p+Au collisions, results of D^0 meson in either p+Au or d+Au collisions at the same energy are needed. At STAR in 2016, d+Au collisions were recorded with the high-precision HFT detector, which allows for studying D^0 meson in more detail.

Chapter 2

Supervised machine-learning methods for signal extraction

This chapter will introduce machine learning methods and typical steps involved in their application. The references in this chapter contain a more detailed description of the methods and their further mathematical proofs. To learn the machine-learning and the data analytics workflow, it is suggested to directly try to implement various tests on data known to an analyzer after understanding the basics mentioned in this chapter.

Supervised statistical machine-learning methods are generally used to predict a target based on the relations between variables and the target observed in the training data. The training data consists of multiple samples composed of the variables, also known as features, whose values are known in the prediction, and the target, whose values are known only for the training sample. Generally, these methods are separated into classifiers and regressors. As the name suggests, classifiers classify input data into two or more classes. For each sample, they either directly predict a class where it most-likely belongs or a probability-like value (score) that might be used to decide the sample class further. An example of a classifier algorithm problem might be a method that separates collisions into central and peripheral based on the input variables, such as the signal in the forward detectors, the multiplicity of the event, or the signal in the calorimeters. On the other hand, regressors are used to predict a continuous value. The regressor model would be used in the aforementioned example to predict the centrality value using the same features.

Various machine-learning methods might be used to solve a given problem. From the most basic ones, such as the linear methods, to the most complex deep neural networks, each method has its pros and cons. For the given problem, the best performance might not be obtained with the most sophisticated methods, and the basic linear model might provide satisfying results. Each algorithm has a different structure and, thus, parameters optimised in training. Parameters that are set before the model training and that are not generally optimized byt the model are so-called hyperparameters. They set the method's structure, optimization function, or how the algorithm should approach its intermediate results. These parameters significantly influence the method performance, so they must be chosen carefully. The most common way of choosing the hyperparameters is the grid search. The grid is the set of hyperparameters and their values intended to be tested. Then, the model is trained for each hyperparameter combination, and its performance is evaluated. Finally, the analyzer chooses the model with the best results or refines the hyperparameter grid.

2.1 D^0 meson decay simulated data

Based on the published article, which the author of this thesis co-authored [85], individual steps and methods discussed in this chapter will be demonstrated on the D^0 meson reconstruction. This article presents the detailed description of the machine-learning algorithms setup and individual steps in their application on the high-energy data. Furthermore, it concludes that not only the widely used BDT, but also other methods should be tested for the signal extraction analyses.

Data from the full d+Au at $\sqrt{s_{\mathrm{NN}}} = 200$ GeV event simulation are used. The d+Au events generated with the HIJING [86] simulator are fed to the GEANT [87] simulation of the STAR detector response. Next, resulting tracks are reconstructed similarly and with a comparable detector response as in the recorded data. Additionally, collision evolution is known. Thus to each reconstructed track, its origin is well-known. Further technical details of the implementation of this simulation are in Sec. 4.2.2.

The resulting reconstructed kaon and pion tracks are within each event combined into like-sign (correct) charge and unlike-sign (wrong) charge combination $\mathrm{K}\pi$ pairs. Pairs with invariant mass from 1.7 GeV/c^2 to 2 GeV/c^2 are further analyzed. Thanks to the information from the simulation, for each correct-charge $\mathrm{K}\pi$ pair, it is known if it comes from D^0 meson decay or not. $\mathrm{K}\pi$ pairs from the D^0 meson are tagged as the signal, while others are the background. The goal of D^0 meson reconstruction analysis in the recorded data is to construct a method that will take correct-charge $\mathrm{K}\pi$ and classify them to signal and background. Wrong-charge pairs are used to estimate the combinatorial background left after such classification. The study presented in this chapter aims to evaluate the performance of various machine learning methods on the such signal from background separation.

In tested classification models, D^0 meson topological decay properties, shown in Sec. 1.4.1 are calculated for all $\mathrm{K}\pi$ pairs and used as features. The target is the simulation information, whether or not the $\mathrm{K}\pi$ pair comes from D^0 meson. Only correct-charge pairs are used in training. Distributions of topological variables in the simulated data are shown in Fig. 2.1 for correct-charge and wrong-charge pairs with transverse momentum $1 < p_{\mathrm{T,K}\pi} < 2$ GeV/c. Differences between correct-charge signal and background distributions are observed from which the algorithm might benefit. However, distributions of all correct charge pairs, correct-charge background and wrong-charge background are very close and overlapping. In the recorded data, there is only a tiny fraction of signal pairs in the correct-charge pairs, and the signal distribution is unknown. Thus, correct-charge and wrong-charge pair distributions have a nearly similar shape. Furthermore, as it could be observed from shown background ratios, there is no significant distributional difference between correct-charge background pairs that are not coming from D^0 meson decay in our data and wrong-charge pairs.

All methods are tested separately in 5 $\mathrm{K}\pi$ transverse momentum intervals $p_{\mathrm{T,K}\pi}$: 0–1, 1–2, 2–3, 3–5, and 5–8 GeV/c. $\mathrm{K}\pi$ transverse momentum corresponds to the reconstructed D^0 meson transverse momentum $p_{\mathrm{T,D^0}}$. In what follows, classification performance is evaluated using the area under the receiver operating characteristic curves (ROC), AUC. ROC represents the dependency of signal efficiency on background efficiency for different thresholds on the output of the classification predictions.

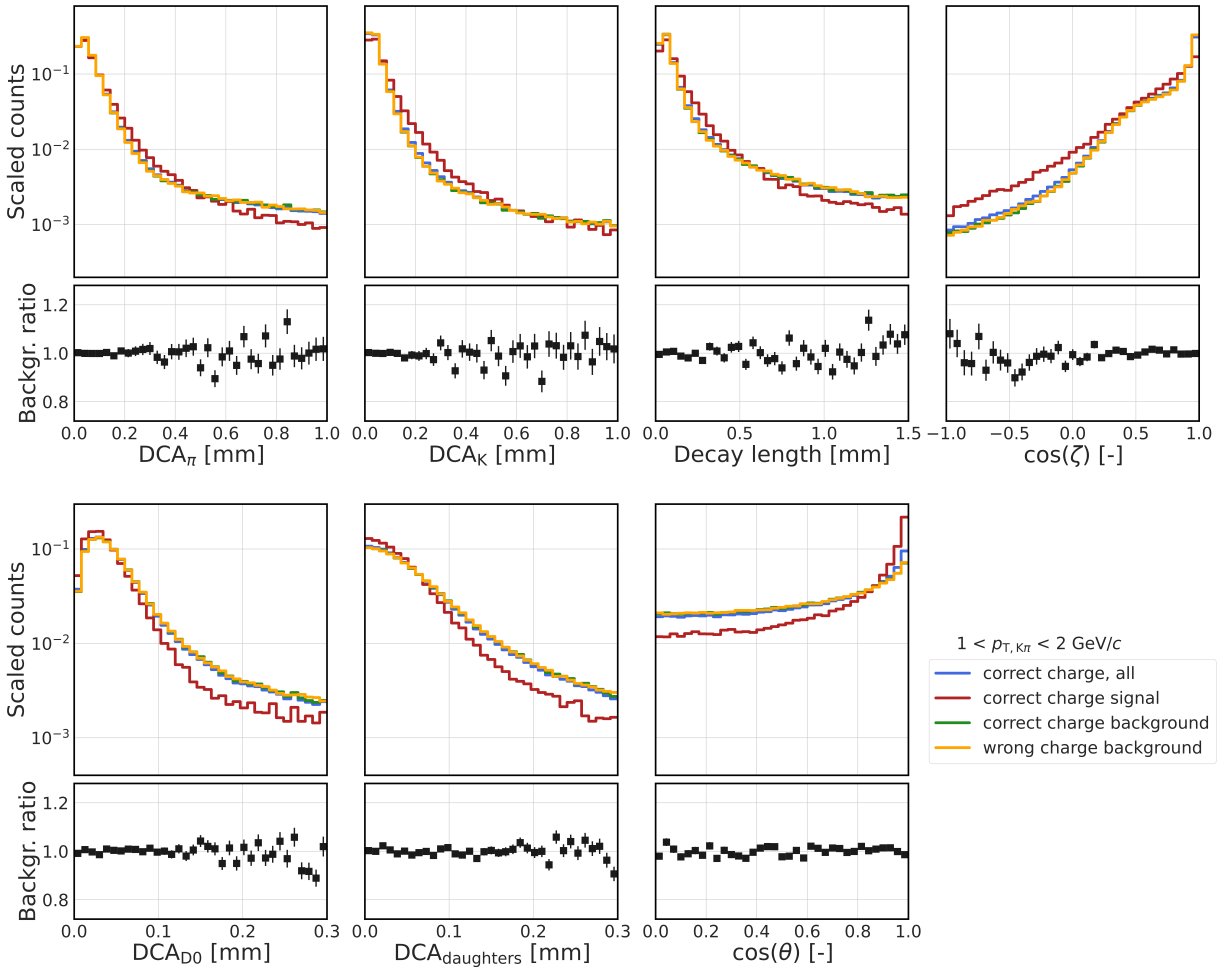

Figure 2.1: Distributions of topological variables for Kπ pair transverse momentum $1 < p_{\mathrm{T,K\pi}} < 2$ GeV/c and for correct-charge and wrong-charge Kπ pairs, together with corresponding ratios of correct-charge and wrong-charge backgrounds Kπ pairs distributions. Kπ pairs are from data simulated with HIJING and GEANT, and have invariant mass from 1.7 GeV/c^2 to 2 GeV/c^2. Taken from Ref. [85].

2.2 Train, test and validation set preparation

For the model's training and proper evaluation, input data must be split into train and test sets. Additionally, some algorithms require a so-called validation data set. As the name suggests, the training sample is used to train the model - optimize all parameters. The other two sets are often called hold-out sets. Samples in these sets are not used to build a model.

Since the method is trained on the training set, predictions calculated on the same samples might be significantly better than for the unseen data. For example, a very trivial algorithm that would remember all training data would have the maximum score but will not reflect the actual performance on the unseen data. Because of this, the test set, unseen in the model training, is used. The trained model generates its predictions, which are evaluated using the known target. Some implementations also require a validation sample of data. This set is used in training, e.g., to evaluate intermediate results during the fitting of the method. For example, thanks to this, training could stop to avoid overfitting the training sample. The validation sample indirectly influences selected parameters in such a case. Thus, it needs to be split apart from the test sample.

Composition of features and targets in the three sets must be similarly balanced to train and evaluate the model correctly. Additionally, for each dataset to work appropriately, the number of samples in each set must be large enough for its function. A small number of samples in the hold-out sets might not represent the data statistically correctly and thus lead to the wrong evaluation results (bias). On the other hand, too many samples reserved as hold-out can limit the size of the train set and, thus, decrease the performance of the trained model.

2.3 Input data engineering

Before the training, the input dataset, consisting of all the features and corresponding target values, should be carefully engineered. Outliers, samples with significantly lower or higher values of features or targets, should be checked, and their removal from the training set should be considered. Additionally, irrelevant or unimportant samples might be removed or their weight in training lowered. Such analyses can help the model to learn the relations between the features and the target that are more probable in the unseen data in the prediction.

In particle reconstruction analyzes, it is not essential to identify all signal samples. However, any selection (classification) should lead to a set samples with a statistically significant signal-to-background ratio. By cutting out the feature-space subset with low signal density, signal-searching algorithms are forced to focus on the region where the signal number is high on the one hand but, on the other hand, hard to set apart from the background. In the study done with the simulated D^0 meson pairs, the decay properties of the meson and our detector's known resolution can hint at the region where the D^0 meson signal could not be observed. Based on this knowledge, various precuts sets on the training data are tested to find the ones that suppress background significantly more than signal. Signal and background efficiencies are calculated for three sets of rectangular cuts on D^0 meson decay properties. These cuts are shown in Table 2.1 and are similar in all p_{T,D^0} intervals. Signal and background efficiencies corresponding to these cuts are in Fig. 2.2. As can be seen, the background efficiencies of loose

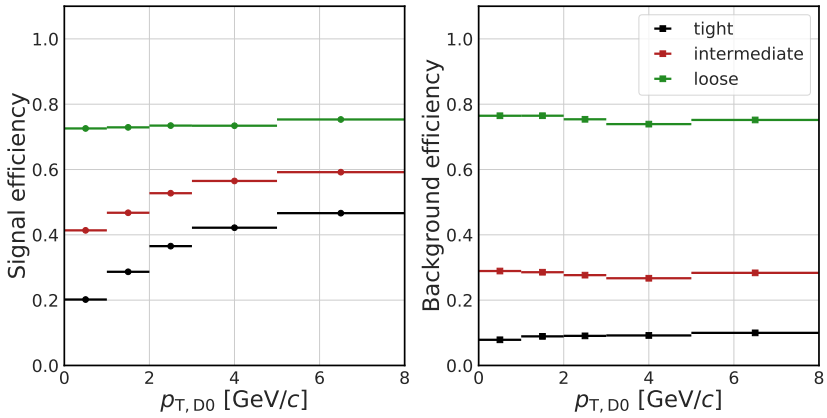

Figure 2.2: Signal (left) and background (right) efficiencies vs. reconstructed transverse momentum of Kπ pairs (D^0 meson candidates) p_{T,D^0} for selection cuts listed in Table 2.1.

cuts are nearly similar to the signal ones'. However, tighter cuts suppress the background significantly more than the signal. It is expected to obtain algorithms precise in higher signal density regions using tight precuts. In what follows, all steps are done separately for two data sample scenarios - one with no preselection cuts applied and another with tight precuts.

Table 2.1: Sets of preselection cuts applied to topological variables of D^0 meson decay before classification methods have been trained.

	Loose cuts		Intermediate cuts		Tight cuts	
Variable	Min.	Max.	Min.	Max.	Min.	Max.
$DCA_{K,\pi}$ [mm]	0.0	10.0	0.0	1.0	0.002	2.0
$DCA_{daughters}$ [mm]	0.0	5.0	0.0	0.3	0.0	0.2
decay length [mm]	0.0	5.0	0.0	1.5	0.005	2.0
DCA_{D0} [mm]	0.0	5.0	0.0	0.3	0.0	0.5
$\cos\theta$ [-]	-1.0	1.0	0.0	1.0	0.7	1.0

Some methods benefit from the standardization and the normalization of the input sets. The normalization converts the numerical variable x to x_{norm}, which has values in the range $[0, 1]$, as

$$x_{\text{norm}} = \frac{x - x_{\text{min}}}{x_{\text{max}} - x_{\text{min}}}, \tag{2.1}$$

where x_{min} and x_{max} are minimum and maximum values of x.

The standardization rescales the data so that the distribution of every rescaled feature has zero mean and standard deviation equal to one to align feature ranges. It transforms the value of variable x to x_{stand} as

$$x_{\text{stand}} = \frac{x - \mu}{\sigma}, \tag{2.2}$$

where μ is the mean of the feature original distribution and σ is its standard deviation.

2.4 Linear optimization methods

After the input data are prepared, the selected machine-learning method is applied. Linear methods are one of the most fundamental groups of models on the market. Linear regression is a model to predict the continuous target. On the other hand, logistic regression, despite the name suggests, is a classification model. The optimization of parameters done in the model training will be presented in the example of these two methods.

2.4.1 Linear regression

Linear regression model prediction is calculated as

$$f(\boldsymbol{x}, \boldsymbol{w}, b) = \sum_{i=1}^{d} x_i w_i + b = \boldsymbol{x}\boldsymbol{w} + b, \tag{2.3}$$

where $\boldsymbol{x}$ is a feature vector of dimension d, $\boldsymbol{w}$ are weights and b is bias. Bias b is usually considered and optimized as another weight, so in what follows, $\boldsymbol{w}$ will note all weights together with b. Model training is a series of steps that aim to calculate the weights with the best precision, which is done by minimizing an objective function. In machine learning, the objective function that reflects the uncertainty of the model predictions compared to the known model targets is called the cost function. The most common cost function for regression models is the mean squared error (MSE), defined as

$$E_{\mathrm{MSE}}(\boldsymbol{w}) = \frac{1}{N} \sum_{i=1}^{N} \left(f(\boldsymbol{x_i}, \boldsymbol{w}) - y_i\right)^2, \tag{2.4}$$

where N is the number of samples in the train set, and y is the model target. Usually, the sum of squares, the minor modification of MSE that results in the same minimizing, is used,

$$E_{\mathrm{SS}}(\boldsymbol{w}) = \frac{1}{2} \sum_{i=1}^{N} \left(f(\boldsymbol{x_i}, \boldsymbol{w}) - y_i\right)^2. \tag{2.5}$$

Generally, $f(\boldsymbol{x_i}, \boldsymbol{w})$ can be any regression model prediction. The term $\left(f(\boldsymbol{x_i}, \boldsymbol{w}) - y_i\right)^2$ is called the loss function, and it calculates the error of the single data sample prediction. The cost function aggregates these losses in a desired way. In the case of MSE, it calculates their mean. However, a more complex model penalty might be necessary to regularize (generalize) the model.

In training, the machine learning method optimizes the parameters by iterating through training samples and minimizing the cost function. Mathematically, the minimum of a function is a point where the derivation is equal to zero. The gradient descent is one of the algorithms for finding these minimums. After each training iteration step, it measures the change in all weights regarding the difference in the cost function for the whole training sample. Using the gradient of the cost function, E, from iteration i to $(i+1)$, parameters $\boldsymbol{w}$ are updated as

$$\boldsymbol{w_{i+1}} = \boldsymbol{w_i} - \gamma \nabla E(\boldsymbol{w_i}), \tag{2.6}$$

where γ is the learning rate, which defines how big the parameters change between iterations should be. Gradient calculation for each sample in the training set and in each update of the

weights might require significant resources. Thus, update of the weights might be calculated iteratively for smaller batch of the training data, or for a singly randomly chosen sample. In the case, the minimizing method is called stochastic gradient descent (SGD). Stochastic gradient descent requires more iteration steps, but it significantly speeds up convergence for large datasets.

The learning rate is one of the hyperparameters set by the analyzer. If it is set too high, gradient descent might miss the minimum of the cost function, overshoot it, and the training might not converge. If the training converges too quickly, it could also indicate a too-big learning rate. Small learning rate results in long training. Usually, it is hard to estimate what is the ideal learning rate. In practice, cost function evaluation is observed after each training epoch (one pass through all training samples), and, based on its evolution, the analyzer decides if the learning rate is set satisfyingly. Additionally, some optimizers (Adam, AdaMax [88]) implement the adaptive learning rate, which makes the big steps in gradient descent far from the global minima and small steps close to it. Adaptive change of learning rate enables the optimizer to recognize and escape local minima of the loss function more efficiently. More detailed explanations of different gradient descent and learning rate strategies are in [89].

As can be seen, there are many setup options that an analyzer may use to test. The linear regression can be easily replaced by the polynomial regression by adding polynomial terms in Eq. 2.3. Various cost and loss functions might be used, and different optimization algorithms to find their minima. Generally, the cost and loss functions and minimizer are the basic building block of any machine learning algorithm.

2.4.2 Logistic regression

Logistic regression is a linear classification model that predicts the class's probability. In the case of binomial classification, the logistic regression modifies the linear regression prediction equation (Eq. 2.3) with a sigmoid function, defined as

$$S(x) = \frac{1}{1 + e^{-x}}, \tag{2.7}$$

The resulting probabilities for the feature vector (sample) to be in class A and B are then defined as

$$\begin{aligned} p(A|\boldsymbol{x}) &= S\left(\sum_{i=1}^{d} x_i w_i + b\right) \\ p(B|\boldsymbol{x}) &= 1 - p(A|\boldsymbol{x}). \end{aligned} \tag{2.8}$$

Figure 2.3 shows how the sigmoid function modifies the input function to range from 0 to 1. As can be seen, there is some decision boundary ($f(x) = 0$), where the probability is 0.5. Around this boundary is a region where the probability is rapidly growing. For the analyzer, following the slope of this linear part is essential. Sometimes, a big slope, and thus a model with too confident predictions in the training data, might hint at an overtraining issue.

Since the target is a class (value 0 or 1) and the prediction is continuous, the cost function for classification algorithms differs from those used in the regression. In the classification problems, model performance is evaluated as a product of likelihoods for each sample prediction $f_{\boldsymbol{w}}(\boldsymbol{x}_i)$ according to the target y, so the cost function is

$$E_{\mathrm{L}}(\boldsymbol{w}) = \prod_{i=1}^{N} f_{\boldsymbol{w}}(\boldsymbol{x}_i)^{y_i}(1 - f_{\boldsymbol{w}}(\boldsymbol{x}_i))^{1-y_i}. \tag{2.9}$$

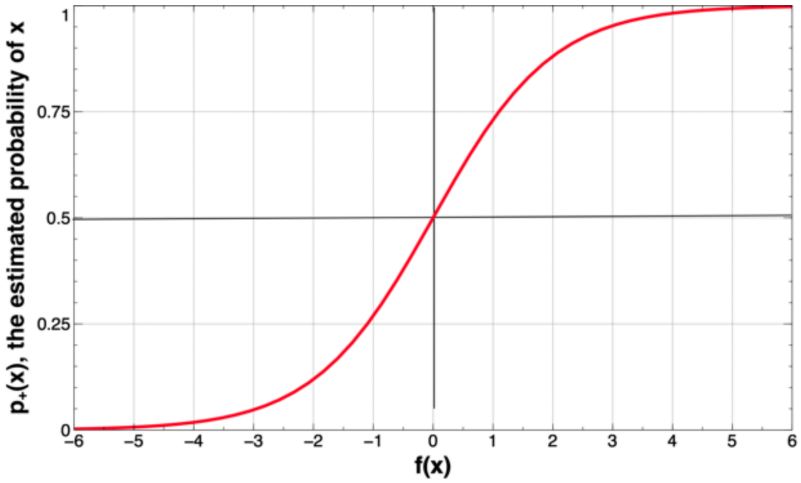

Figure 2.3: Example of the sigmoid function shape–estimated probability calculated with the logistic regression. Taken from Ref. [90].

The algorithm aims to maximize this function (or minimize $-E_{\mathrm{L}}(\boldsymbol{w})$), that's why this criterion is called maximum likelihood.

The logistic regression model has an exponential function in the definition, so mathematically, using log-likelihood is more convenient. It is defined as

$$E_{\mathrm{logL}}(\boldsymbol{w}) = \ln E_{\mathrm{L}}(\boldsymbol{w}) = \sum_{i=1}^{N} y_i \ln f_{\boldsymbol{w}}(\boldsymbol{x}_i) + (1 - y_i) \ln(1 - f_{\boldsymbol{w}}(\boldsymbol{x}_i)). \tag{2.10}$$

2.5 Overfitting and underfitting of the model

After the model is trained, predictions might be generated for all three data sets (train, test, validate) and compared with the real target. In the ideal hyperparameter setup, performance is similar for all three sets. Suppose the performance on the training set is significantly better than on the testing data. In that case, the model is overtrained (remember the example of the model that only remembers all training data). Overtraining is caused by, e.g., too many iterations of model fitting, too complicated model architecture compared to the complexity of the problem to be solved, or relatively many features compared to the size of the training data. Overtraining might also be observed in individual steps in training. If the model error is evaluated after each training iteration, the training error and error on the test set (so-called generalization error) get smaller after every new iteration. After multiple iterations, the generalization error stops decreasing and, on the contrary, starts to get larger, and the model is in the overfitting regime. At this stage, the algorithm is sensitive and learns irrelevant noise, losing its ability to generalize predictions. Another problem is the underfitting regime when the model's performance is relatively low due to the wrong hyperparameter setup. However, low performance might also be caused just by the complexity of the problem, and, of course, the best score that could be achieved for the given problem is hard to estimate. Thus underfitting in training is generally hard to detect.

The same training and generalization error behavior is observed with the increasing model capacity, and the corresponding schema is shown in Fig. 2.4. The model capacity is the

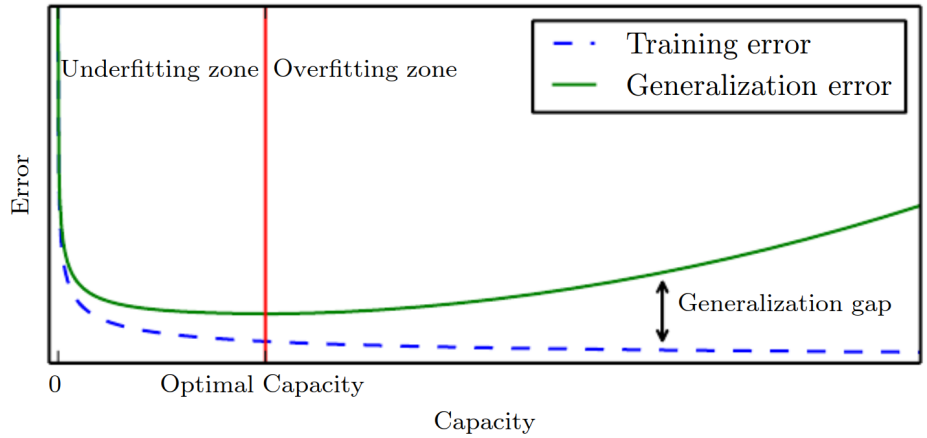

Figure 2.4: Schema of training and generalization error vs. model capacity with underfitting and overfitting zones displayed. Taken from Ref. [91].

ability of the model to find more sophisticated dependencies in the training set. This ability is given by the set of functions from which to model can choose in the optimization. For example, linear regression has a smaller capacity than polynomial regression, and the higher the degree of the polynomial, the higher the model capacity. However, the model will not always find the best-suiting function from its options. Selection is undoubtedly limited by the selected hyperparameters (such as optimization method, learning rate, etc.), the quality and the quantity of the data, which can lead fit to converge into non-ideal conditions. Usually, the model selection with the appropriate capacity results from the analyzer's knowledge of the problem and input dataset and the expected quality of the output prediction. More details on the model capacity, underfitting, and overfitting are in [91].

2.6 Cross-validation

Properly constructing training, validation, and test sets is essential to evaluate the model performance and estimate the fitting procedure's correctness. The generalization error, calculated on the validation or the test set and used to decide the model quality, should be calculated on a large enough sample of the data. Additionally, these data should adequately represent the whole dataset in terms of the distributions of features and targets. A common technique to ensure reliable evaluation is cross-validation. The schema of the cross-validation steps is in Fig. 2.5. In the training phase, cross-validation first splits the dataset into multiple folds. Then, one of the folds is the hold-out set, and the model is trained on the rest of the sample. Afterward, the trained model calculates the predictions on the hold-out set to compute the test performance. This train and predict process is repeated until all folds are the hold-out sets and the validation (test) predictions are calculated for the whole dataset. Finally, the model performance and the generalization error are calculated by comparing the test predictions and the target values.

Since the models trained in the different folds might converge to various parameters, the test performance is more reliable with more folds. However, the number of samples in one training should not limit the model capacity. Usually, the cross-validation is done with at least three and less than ten folds. The number of folds setup is chosen by the analyzers.

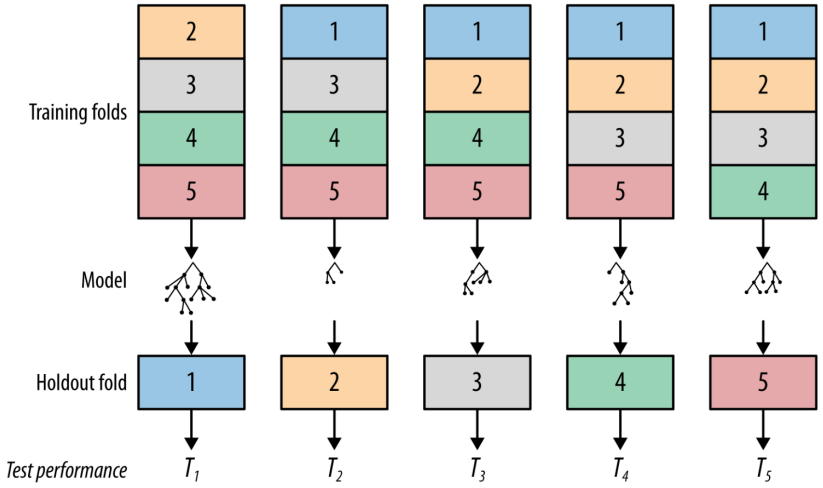

Figure 2.5: Cross-validation schema for input dataset split to five folds. Five model trainings are done, each with different fold as the hould-out set to evaluate the model performance. Taken from Ref. [90].

Cross-validation is commonly used in grid search to find the optimal model hyperparameters.

2.7 Decision tree

The decision tree is a graph-like structure that partitions the input data space and, thanks to this, tries solving the problem in each subregion using a simpler model. An example of a single decision tree and its splitting of the two-dimensional input dataset is in Fig. 2.6. Data in the root node correspond to the whole (training) dataset t_0. Then, a decision on one of the features is made. In the example shown, data are split into those having X_1 larger than 0.7 and others. Two new nodes are created and further split dataset, according to different criteria on features. The terminal nodes split the input dataset into three sets, t_2, t_3, and t_4. These terminal nodes are then tagged based on the target values in them. In the case of classification targets, these are tagged based on the major class in the node–c_1 or c_2. For regression, nodes are tagged by the target's mean value in the terminal node. In the prediction phase, the data sample goes through the decision process from the root to the terminal node. The final prediction is the value based on the tag from the training. The decision tree's depth is the maximum number of decisions taken between the root and the terminal node. The decision tree in Fig. 2.6 thus has a depth equal to two.

In constructing a decision tree, it is essential how the method chooses the best split s of the node to maximize its information gain. Information gain of the split of the node t_0 with N_{t_0} samples to nodes t_1 and t_2 is the impurity decrease Δi_s, defined as

$$\Delta i_s = i(t_0) - i(t_1)\frac{N_{t_1}}{N_{t_0}} - i(t_2)\frac{N_{t_2}}{N_{t_0}}, \tag{2.11}$$

where i are the nodes impurities, N_{t_1} and N_{t_2} are number of samples in the nodes t_1 and t_2. Different methods are used to calculate the impurity of the node. These methods differ for classification and regression problems.

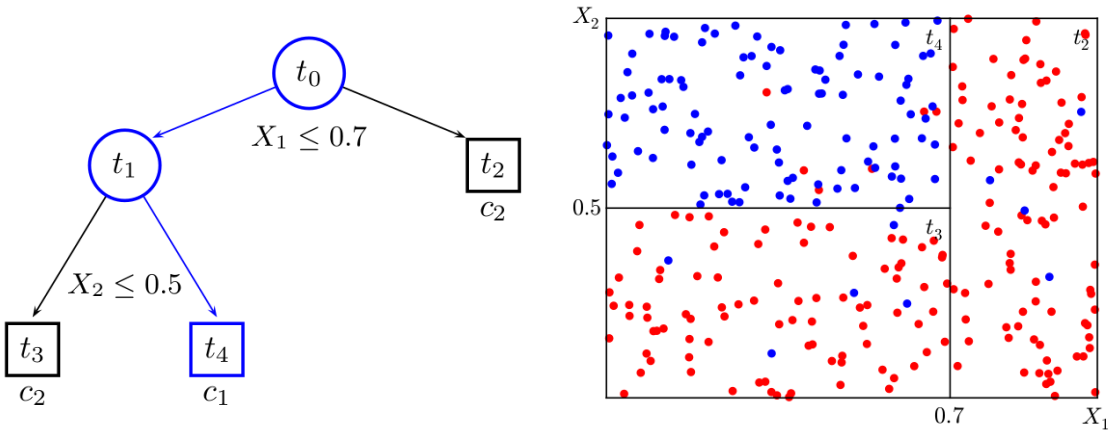

Figure 2.6: Example of the decision tree (left) and the corresponding partitioning of the input feature space (right). In the root node, all of the input data t_0 are split using variable X_1. Terminal nodes split the input dataset to subsets t_2, t_3 and t_4. Each terminal node is tagged by major class (c_1 or c_2) in these subsets. Taken from Ref. [92].

For classification, entropy and Gini impurities are mostly used. The thermodynamics-inspired entropy is defined as

$$i_H(t) = -\sum_k p_k(t) \log_2 p_k(t), \tag{2.12}$$

where $p_k(t)$ is a probability of sample in t to belong to class k. Entropy i_H has values in $[0, 1]$, which the algorithm aims to minimize. The shape of the entropy function for various compositions of a two-class set is shown in Fig. 2.7.

Another impurity measure is Gini impurity, defined as

$$i_G(t) = \sum_k p_k(t) \left(1 - p_k(t)\right). \tag{2.13}$$

It can have values from 0 to 0.5.

For regression, one of the commonly used impurities is the variance in the node, defined as

$$i_r(t) = \frac{1}{N_t} \sum_{\boldsymbol{x}, y \in t} (y - y_t)^2, \tag{2.14}$$

where the sum is over all samples in the node t, N_t is the number of samples in the node, y is the training target, and y_t is the tag for the given node (mean value of all y in the node). Variance is zero in the case of a completely homogenous node, achieved by the same target values of the samples in the node.

2.8 Random forest

An ensemble of the models is a good way to generalize the predictions. Various models with different training data or architecture could be connected using some ensemble method. Since every model architecture has strengths and weaknesses, aggregated predictions of multiple well-trained models are usually better than the individual model's prediction.

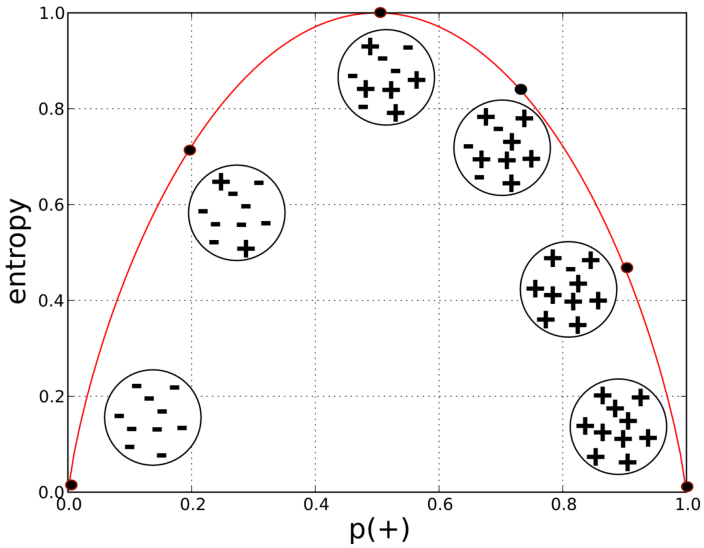

Figure 2.7: Entropy function shape for two-class set as function of probability of one of the classes in the dataset. Taken from Ref. [90].

A single decision tree, presented in the previous section, easily overfits with the increasing depth. Given the binary decisions, it can easily focus only on a small part of the phase space of training data. The solution is the random forest ensemble method that combines multiple, usually shallow, decision trees trained independently. Each decision tree is trained on a slightly different subset of the training set. This subset is constructed by randomly picking samples from the training set with repetitions allowed so that a selection might occur multiple times. The picking stops when the maximum number of samples per subset, usually equal to the size of the training set, is achieved. The number of such generated subsets equals the required number of decision trees.

In the prediction, all trained trees evaluate every feature vector sample. Finally, individual predictions (tags) of individual trees are aggregated to obtain the prediction of the random forest method. The described construction method of the training subsets and their aggregation in the prediction is called bootstrap aggregating (bagging).

There are different ways how to aggregate decisions of the trees. In the case of regression targets, predictions of trees might be just averaged. For the classifiers, every decision tree votes for a class, and the majority of votes is taken as the prediction. A more sophisticated way to combine models in the ensemble is stacked generalization (stacking) [93]. Predictions of models in the ensemble are combined in the higher-level model that calculates the final prediction. For an example of stacking in the random forest, predictions of individual decision trees might be combined in the linear regression to optimize their weights and calculate the final prediction (in the case of a simple average, all of the trees have similar weight equal to one over the number of trees in the ensemble).

2.8.1 Application to the D^0 meson dataset

In our example of D^0 meson reconstruction, scikit-learn [94] random forest implementation is applied. All steps are done separately for described studied scenarios (datasets with different precut selections and p_{T,D^0} intervals). Firstly, input data in all datasets are divided into

training and test sets in the 6:4 ratio, and feature standardization is fitted on the training set and applied on both test and training sets. Then, grid search over multiple combinations of the random forest hyperparameters, such as the number of the decision trees, their maximum depth, and impurity measure, is done separately for studied transverse momentum intervals using 3-fold cross-validation on the training set. The input training set is balanced for all model training, so the same number of samples per class (signal and background) is used in the optimization. Hyperparameters with the best classification performance, evaluated with the AUC, are summarized in Table 2.2. As can be seen, entropy impurity (Eq. 2.12) is selected as the one with the best performance for all datasets. In the scenario where precuts are not applied, optimization selects deeper trees within the ensemble since more complex input space partitioning is needed. Finally, the classifier set with the best hyperparameters is trained over the whole training set and later validated over the test set.

Table 2.2: Optimized parameters (number of trees N_{trees}, maximum tree depth d_{max}, impurity measure) of random forest classifiers for Kπ pair transverse momentum $p_{\text{T,D}^0}$ intervals with and without precuts application. Entropy (E) impurity measure is selected for all input data setups.

	With precuts					Without precuts				
$p_{\text{T,D}^0}$ [GeV/c]	0–1	1–2	2–3	3–5	5–8	0–1	1–2	2–3	3–5	5–8
d_{max}	10	13	12	10	7	15	15	12	12	7
N_{trees}	1200	600	1000	200	200	1200	600	1000	1200	200
Impurity	E	E	E	E	E	E	E	E	E	E

2.9 Boosted decision trees

The random forest method combines decision trees trained independently on a slightly different subset of the training set. Another way to construct an ensemble method is boosting. In the boosting, base models (typically weak learners) are trained consecutively, and input to the training of the individual base model depends on the performance of the previously trained learner.

In the Adaptive Boosting (AdaBoost) method [95], the first base model is trained using all training samples with the same weight. Then, this model's predictions are evaluated, and weights are assigned to each training sample. Higher the model prediction error on the sample, the higher the assigned weight. The following base model is trained using the weighted samples. Thanks to this, the individual base model focuses on the region where the previous one does not perform well, thus improving its prediction. Additionally, weight, calculated from its classification performance, is calculated for each base learner. This weight is used in the application phase of the trained ensemble model, where the base models are aggregated using weighted mean. Generally, the number of boosting iterations depends on the stopping criteria the analyzer sets, e.g., the maximum number of base models or the performance of the last base learner. In the AdaBoost method usage, it is essential to work with well-prepared input data since, for example, outliers may lead to the model focusing on the region of data that does not properly represent the data in the application phase.

Another boosting method is gradient boosting [96]. The first base model is trained using the target values as in AdaBoost. However, every other base model is trained on the residuals of the aggregated predictions of the previous models. Thus each iteration helps to bring

the predictions closer to the target. The residuals are calculated as the gradient of the loss function with respect to the predictions. Base model predictions are added to the ensemble model multiplied by a learning rate coefficient, which impacts the number of iterations the algorithm needs to converge. Extreme gradient boosting (XGBoost) [97] is the extension of gradient boosting that implements multiple methods to prevent overfitting and handling of the missing data in the input dataset and is designed to perform faster. A more detailed summary of the boosting algorithm is in [98].

2.9.1 Application to the D^0 meson dataset

Boosted decision trees (BDT) machine learning algorithm from the Toolkit for Multivariate Data Analysis (TMVA) package [4] is applied to classify signal and background Kπ pairs. This method uses the AdaBoost algorithm. Overfitting is prevented by setting the maximum tree depth to three. Moreover, the decision tree node is not further split if it contains less than 2.5% of the input training samples. Each tree is trained with randomly selected 50 % of the training samples. The split impurity is calculated with Gini (Eq. 2.13).

Data in all $p_{\mathrm{T,D^0}}$ intervals are divided into training and test sets in the 6:4 ratio, in the same way as it was done for the random forest algorithm. Signal and background sets are balanced using the class weights. In the TMVA implementation of the BDT, classifier prediction is calculated as the BDT response value. This value ranges from -1 to 1, and the higher the value, the higher the probability of the sample being the signal. For each base decision tree model, the error fraction is calculated as how much signal training samples have positive BDT response and vice-versa for the background samples. As more trees are trained, their error fraction increases and converges, as shown in Fig. 2.8. The error fraction equal to 0.5 means the classification is similar to random guesses, and such trees are weak classifiers. At first, in all $p_{\mathrm{T,D^0}}$ intervals, BDT with 1000 trees is trained. Error fraction for $1 < p_{\mathrm{T,D^0}} < 2$ GeV/c is displayed in Fig. 2.8, and it is similar also in other intervals. A simple moving average of the error fraction shows that it converges around 300 trained trees. Our study used 500 trees in the BDT model for all intervals.

2.10 Neural networks

The sigmoid function ensures the prediction has a probability value in logistic regression. The single layer of the neural network is a generalization of the logistic regression, where other non-linear functions may replace the sigmoid function. This function is called an activation function and allows the neural network to model more complex relationships between the input features and the output. Such a generalization of logistic regression leads to the definition of the perceptron architecture. Perceptron is the simplest neural network that contains an input layer and an output layer with a single node (neuron). Its architecture is shown in Fig. 2.9. The input layer consists of nodes whose number is equal to the dimensionality of the feature vector. On the way to the output node, weights are assigned to the input features' values, and their linear combinations are summed in the output node. This part is similar to linear regression. Finally, the activation function transforms this sum into the prediction of the perceptron.

The definition of perceptron architecture helps to build a more sophisticated multi-layer perceptron (MLP) neural network with multiple layers. Hidden layers, added between the

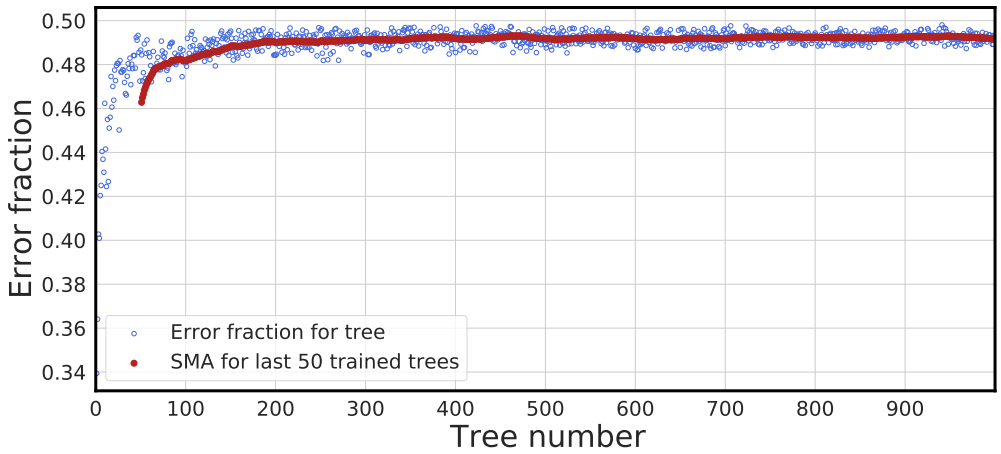

Figure 2.8: Error fraction of gradually trained boosted decision trees and simple moving average (SMA) of error fraction for the last 50 trees for $1 < p_{\mathrm{T,D^0}} < 2$ GeV/c. Taken from Ref. [85].

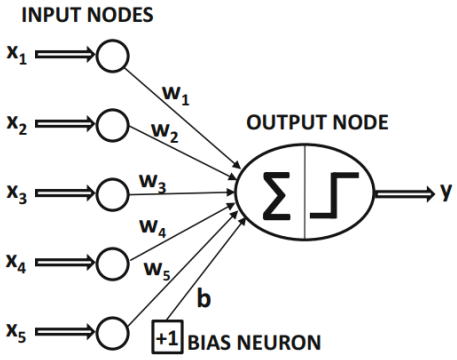

Figure 2.9: Schema of the perceptron, the simplest neural network. Taken from Ref. [89].

input and output layers, help to learn more complicated relations between the features and the targets. Each layer contains multiple nodes, and each node is represented by a single perceptron. Outputs from all the nodes in the layer are passed as the input to the next layer. Hidden layers can have any number of nodes. However, the number of nodes in the output layer equals the expected dimensionality of the prediction. The output of a hidden layer is defined by a vector function

$$\boldsymbol{h_l}(\boldsymbol{z}) = \boldsymbol{a_l}\left(\boldsymbol{W_l}\boldsymbol{z} + \boldsymbol{b_l}\right), \tag{2.15}$$

where $\boldsymbol{z}$ is the vector of inputs, $\boldsymbol{a_l}(\boldsymbol{z})$ is the activation function for given layer, $\boldsymbol{W_l}$ is the weights matrix and $\boldsymbol{b_l}$ is the bias vector. Two different representation schemas of the such network are shown in Fig. 2.10. The left plot shows the scalar representation, where each line reflects a weight given to the output of the single node. The right plot shows the vector form corresponding to Eq. 2.15, where the connector weights are generalized in the matrices. MLP is an example of the most vanilla neural network, but there are various neural networks on the market. A clear review of commonly used neural networks and a comprehensive explanation of various hyperparameters and their setup is in [89]. Further detailed explanation using more mathematical background is in [99].

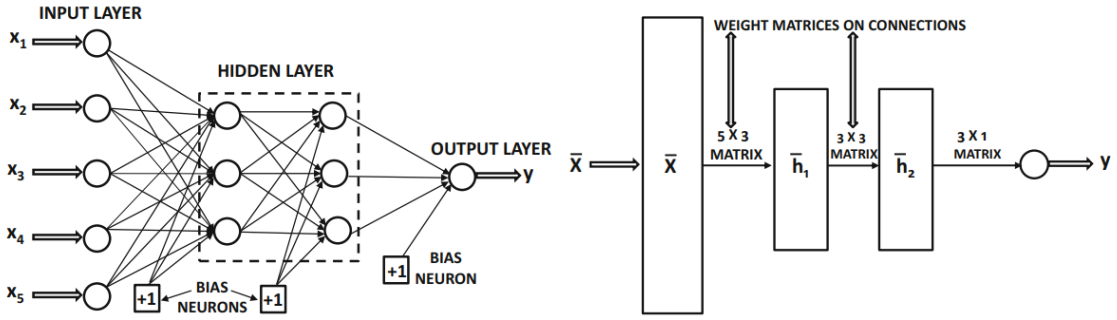

Figure 2.10: General schemas of the multi-layer perceptron neural network architecture. The left schema shows the scalar and the right vector notation. Taken from Ref. [89].

The analyzer defines the neural network's architecture: the number of hidden layers and nodes in them. Additionally, the activation function per layer is defined. If the activation function is linear, the neural network would be linear, and non-linearities in the training data would not be discovered in the optimization. The most commonly used activation functions are tanh,

$$a_{\tanh}(z) = \tanh(z) = \frac{e^z - e^{-z}}{e^z + e^{-z}}, \tag{2.16}$$

and RELU, defined as

$$a_{\mathrm{ReLU}}(z) = \begin{cases} z, & \text{if } z \geq 0 \\ 0, & \text{otherwise} \end{cases} \tag{2.17}$$

The activation function of the output node depends on the target properties. For classification, it is a sigmoid function.

Dropout is one of the techniques used to prevent the neural network from overfitting. In training, after a hidden layer is constructed, the outputs of some random nodes are set to 0, so they are not used. The dropout rate hyperparameter gives the ratio of dropped nodes. An equivalent definition of the dropout rate is the probability of each node being removed. Dropout helps the network to learn more complicated relations in the data and not to rely only on a few strong features.

Another commonly set hyperparameter is batch size. The batch is a subset of the training data with a user-defined size. Weights in the network are recalculated after each batch is processed. In one training epoch, the number of batches is equal to the ratio of the training set size and the size of one batch, defined by the analyzer. The small batch size can lead to a more accurate estimate of the gradients in the optimization but can also result in longer training times.

There are multiple ways for weight initialization in the neural network to ensure smooth convergence and avoid unwanted symmetries. Too small (or too big) initial weights might lead to the significant layer output signal lowering (raising) as it goes through layers, so at the output node, it is significantly out of the target. One option is to choose initial weights from the uniform distribution within some limits. Another is to sample them randomly from the Gaussian distribution with a mean at 0 and some small sigma. The choice of the limits (sigma) is crucial and highly depends on the activation function, the number of inputs n_{in}, and outputs n_{out} of the layer. For example, in He kernel initialization [100], the sigma is $\sqrt{2/n_{\text{in}}}$ and in Lecun initialization [101] it is $\sqrt{1/n_{\text{in}}}$. Xavier initialization [102] considers the number of outputs from the layer. In this case, the sigma is equal to $\sqrt{2/n_{\text{in}} + n_{\text{out}}}$, where n is the number of inputs to the layer. For all mentioned initializations, both uniform and gaussian versions are used. More detailed mathematical explanations of the initializations of the weight are in [102].

2.10.1 Application to the D^0 meson dataset

The neural network to be studied on our example dataset is constructed with the Keras package with the TensorFlow backend [103]. The architecture of the neural network that is tested is shown in Fig. 2.11, with the hyperparameters to be optimized in the grid search written in blue. The input layer contains seven nodes, which corresponds to the number of topological variables. There are four hidden layers and one output node with a sigmoid activation function.

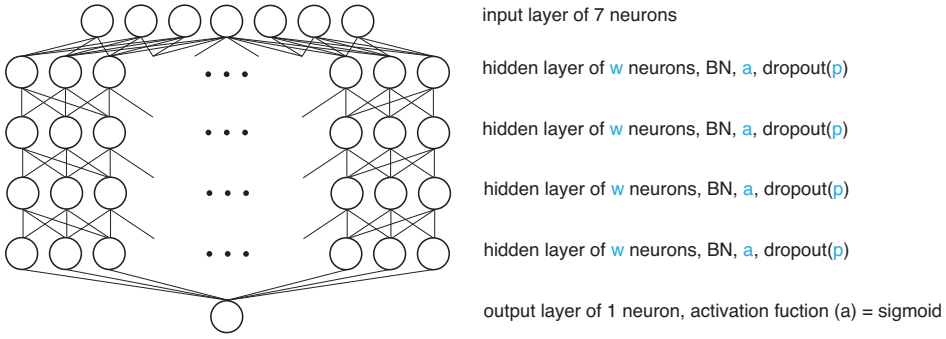

Figure 2.11: Schema of selected neural network architecture with description of the setup of layers. Parameters of hidden layers in blue are left to grid search optimization: number of neurons w, activation function a and dropout rate p. Batch normalization (BN) is applied in all hidden layers. Taken from Ref. [85].

Before entering each hidden layer, batch normalization (BN) is applied, meaning that feature data are normalized according to the sigma and mean calculated in training to accelerate the convergence. The number of nodes w in the hidden layer is left to be optimized in the grid search, together with their activation function a and dropout probability p. Additionally, an

optimizer for minimalization, batch size B, learning rate γ (or its initial value), and type of kernel initialization are optimized. Tested values of hyperparameters are shown in Table 2.3.

Table 2.3: Hyperparameter space for neural network grid search optimization, to classify Kπ pairs in D^0 meson reconstruction. Options for activation function of hidden layers a, learning rate γ, dropout rate in hidden layers p, optimizer, kernel initialization, batch size B, and number of neurons in hidden layers w are shown.

Parameter	a	γ [$\cdot 10^{-5}$]	p	Optimizer	Kernel init.	B	w
Options	ReLU	0.1	0.2	Adam	Lecun uniform	64	64
	tanh	0.5	0.3	SGD	He normal	128	128
		1.0	0.4	AdaMax	He uniform		256

Training data are divided into training, validation, and test sets in the 6:2:2 ratio. For each $p_{\mathrm{T,D^0}}$ interval, balancing of the training set is performed. Before the training, feature standardization is fitted and applied to the training data and then applied to the validation and test sets. After the data are prepared, the best hyperparameter combination is found separately for each $p_{\mathrm{T,D^0}}$ interval with the grid search over parameters in Table 2.3. In the grid search, for each combination of hyperparameters, the model is trained with 70 epochs.

In all cases, $w = 256$ nodes in the hidden layer, batch size $B = 64$, dropout $p = 0.2$ and Adam optimizer starting at initial learning rate $\gamma = 1 \cdot 10^{-5}$ are selected. For data in $5 < p_{\mathrm{T,D^0}} < 8$ GeV/c where precuts are not applied, tanh activation function achieves the best performance. For the rest of the data, ReLU activation is selected. The performance is maximal under He normal kernel initialization for $0 < p_{\mathrm{T,D^0}} < 1$ GeV/c and with Lecun uniform kernel initialization for $p_{\mathrm{T,D^0}} > 2$ GeV/c, when precuts are applied as well as for $p_{\mathrm{T,D^0}} > 1$ GeV/c, when no precuts are used. He uniform kernel initialization results in the best model performance for the data pre-processed with precuts in the $1 < p_{\mathrm{T,D^0}} < 2$ GeV/c interval.

Finally, the training with selected hyperparameters is done. After each epoch, the accuracy is evaluated on the validation set. If it is not significantly improving for the last 60 epochs, training is stopped. The final evaluation of the model performance is done on the test set.

2.11 Performance of the methods on the D^0 meson decay data

In what precedes, the configuration of the random forest from the scikit-learn package, the boosted decision trees from the TMVA, and the neural network implemented with the Keras framework were described. In this section, their performance on the test sets is summarized. Figure 2.12 shows ROC curves for all studied $p_{\mathrm{T,D^0}}$ intervals, methods, and both setups with and without precuts applied. Table 2.4 compares performance in terms of AUC. The AUC ranges from 0.81 to 0.96 throughout all the precut D^0 meson transverse momentum intervals, which is sufficient to carry out any relevant subsequent physical analysis of D^0 mesons.

Machine-learning classification methods benefit from the precut application mainly for $p_{\mathrm{T,D^0}} < 5$ GeV/c. Classification ability naturally increase with $p_{\mathrm{T,D^0}}$, since in this region, D^0 mesons decay later. D^0 mesons with low $p_{\mathrm{T,D^0}}$ decay closer to the primary vertex, resulting in low $\mathrm{DCA_K}$, $\mathrm{DCA_\pi}$, and $\mathrm{DCA_{D0}}$. In such cases, the topological variables' properties of the signal and the combinatorial background are more similar since the tracks created in the primary vertex have low DCA, too.

Table 2.4: Area under receiver operating characteristic (ROC) curve of tested machine learning methods on test samples of datasets in D^0 meson candidate transverse momentum p_{T,D^0} intervals.

	With precuts					Without precuts				
p_{T,D^0} [GeV/c]	0–1	1–2	2–3	3–5	5–8	0–1	1–2	2–3	3–5	5–8
Random forest	**0.81**	**0.87**	**0.94**	**0.95**	**0.96**	**0.73**	**0.79**	0.82	**0.90**	**0.94**
Boosted dec. trees	0.78	0.84	0.90	0.93	0.93	0.70	0.76	**0.83**	0.89	**0.94**
Neural network	0.79	0.83	0.90	0.93	0.91	0.70	0.76	**0.83**	0.89	0.92

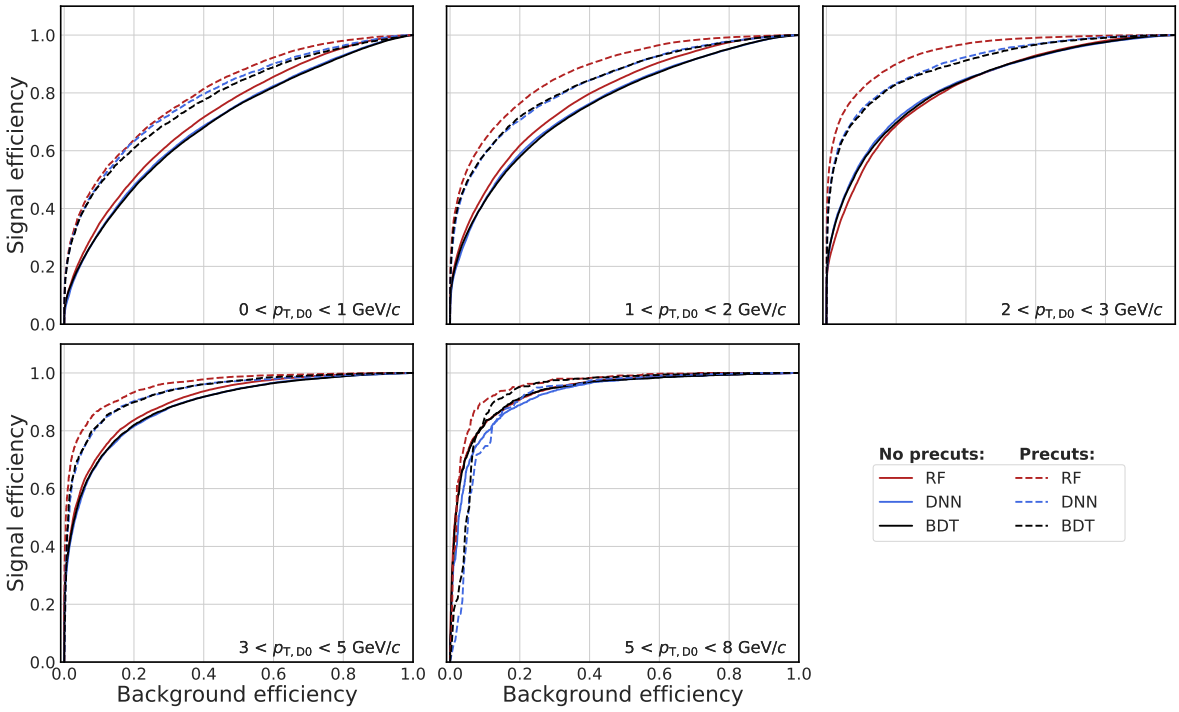

Figure 2.12: The receiver operating characteristic (ROC) curves for random forests (RF), deep neural networks (DNN) and boosted decision trees (BDT) in D^0 meson candidate transverse momentum p_{T,D^0} intervals, with and without precuts application. Taken from Ref. [85].

As can be seen from ROC curves in Fig. 2.12, random forest, not common in high-energy physics, classifies pairs significantly better than other methods for data with precuts applied and $1 < p_{T,D^0} < 5$ GeV/c. In the case of no precuts applied, random forest performance is not significantly better, but it is still slightly more successful. The boosted decision trees and the neural network are similar in terms of both ROC and AUC. In the future, we plan to investigate the performance of studied algorithms for three body decays and, e.g., separation of prompt and non-prompt (coming from B meson decays) D^0 mesons, where the separation of background from a signal is even more difficult with standard analysis methods.

Chapter 3

Experimental setup

3.1 Relativistic Heavy-Ion Collider

The Relativistic Heavy-Ion Collider (RHIC) accelerator is placed at Brookhaven National Laboratory (BNL) in New York. Collisions studied in the primary analysis of this thesis were recorded in 2016 with the Solenoidal Tracker at RHIC (STAR). The schema of the RHIC and its pre-accelerators is shown in Fig. 3.1. Other experiments that measured collisions of beam accelerated at RHIC were the PHOBOS (ended operation in 2005), the Broad RAnge Hadron Magnetic Spectrometers Experiment (BRAHMS, completed operation in 2006), and the Pioneering High Energy Nuclear Interaction eXperiment (PHENIX). In 2023, the sPHENIX detector started to operate, and together with the STAR, it will focus on detailed studies of the QGP.

RHIC is very versatile thanks to its capability to accelerate and collide various nuclei species, such as gold, uranium or copper, protons, and deuterons, all at energies from $\sqrt{s_{\mathrm{NN}}} =$ 7.7 GeV to 200 GeV and for p+p collisions up to $\sqrt{s} = 510$ GeV. Furthermore, it is the only machine able to accelerate and collide beams of polarised protons. Additionally, to achieve very low $\sqrt{s_{\mathrm{NN}}}$, needed to investigate the nuclear matter at the high baryochemical potential region of the QCD phase diagram, the STAR is capable of working in a fixed target regime, in which gold foil is bombarded by gold or aluminum beam, achieving $\sqrt{s_{\mathrm{NN}}}$ down to 3.9 GeV. The summary of all RHIC collisions until 2022, together with their energies and luminosities, is shown in Fig. 3.2. Figure 3.3 shows integrated luminosities and duration of data-taking for these collisions. Among other asymmetric collisions, studied d+Au collisions recorded in 2016 are shown in the right plot. As can be seen, physics data recording took approximately two weeks and achieved integrated luminosity of around 60 pb^{-1}.

The source of various ion beams to the RHIC is the Electron Beam Ion Source (EBIS) [105]. The EBIS is also used as the source of ions for the NASA Space Research Laboratory. The source of low-charge ions is the Laser Ion Source (LION), where the laser irradiation of the solid target generates the ions. Then, the ion beam enters the EBIS, where the electron beam strips electrons from low-charge ions. Optically Pumped Polarised Ion Source (OPPIS) [106] generates polarised proton beams by ionizing the polarised hydrogen atoms. These are created in low-energy collisions of protons and rubidium vapor. Such created low-energy beams are accelerated in the radio frequency quadrupole (RFQ) and the linear accelerator (LINAC). The first circular accelerator on the way to the RHIC is the Alternating Gradient Synchrotron (AGS) Booster [107] with a circumference of 201.78 m. Subsequently, the beam continues into

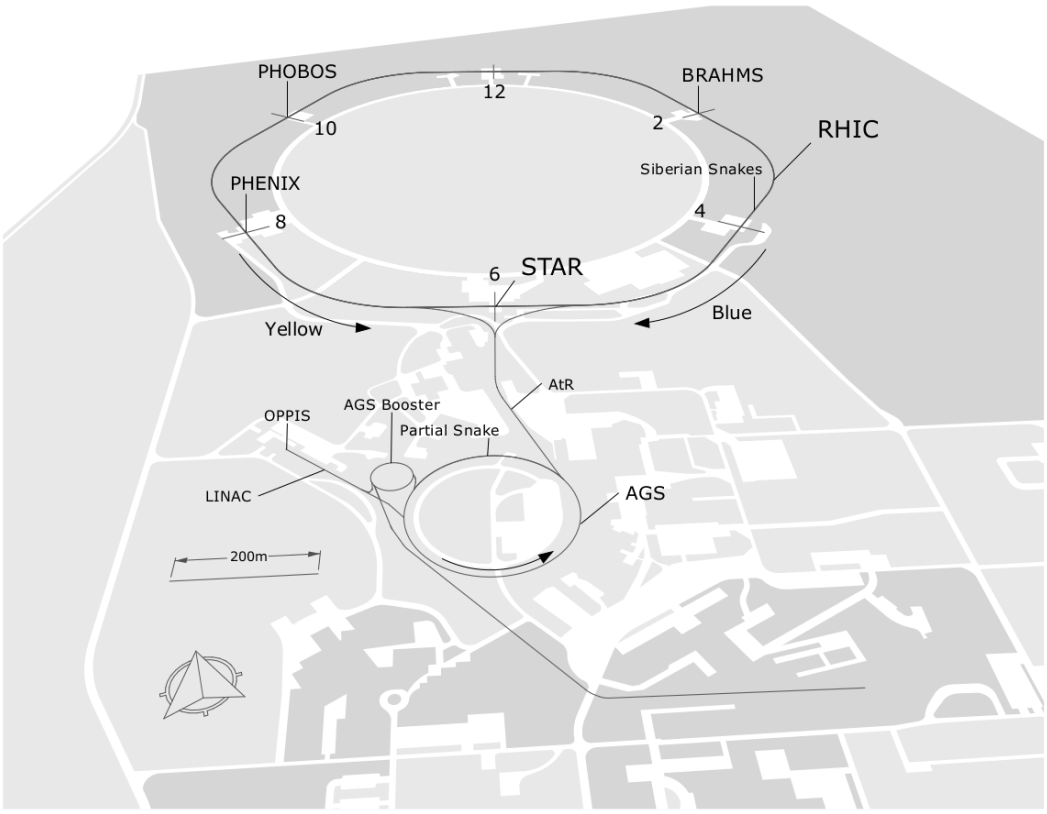

Figure 3.1: Schema of the Relativistic Heavy-Ion Collider (RHIC) accelerator complex.

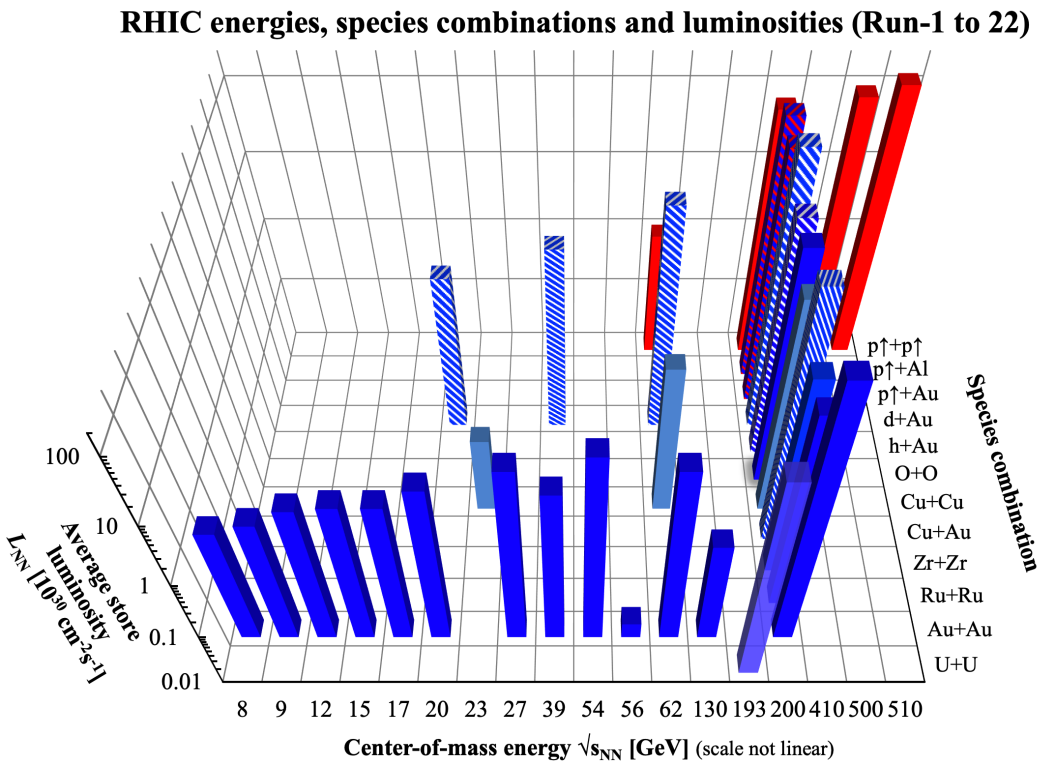

Figure 3.2: Summarry of the collisions at RHIC, recorded till year 2022. Taken from Ref. [104].

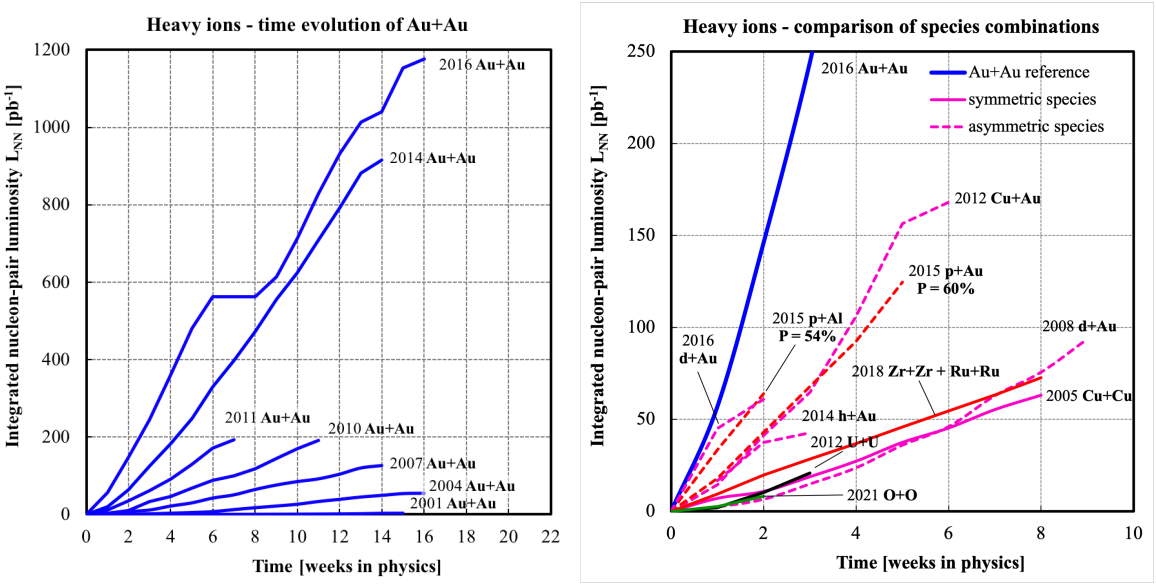

Figure 3.3: Integrated nucleon-pair luminosity of Au+Au collisions (left) and of assymetric collisions and collisions of other ion species (right). Taken from Ref. [104].

the AGS, a circular accelerator with a four-times larger circumference than the AGS Booster, 807.12 m. Finally, a beam is transferred to one of the two RHIC rings via a 770-meter-long AGS-to-RHIC transfer line. The RHIC has a circumference of 3.8 km and six possible interaction points. The beams are bunched, with the bunch crossing rate at the STAR of approximately 9 MHz.

3.2 The Solenoidal Tracker at RHIC

This section describes the STAR detector as it operated from 2014 till 2016, when the analyzed d+Au collisions were recorded. In this period, the STAR detector design focuses mainly on measurements of heavy-ion and polarised protons collisions. It mainly aims to measure tracks produced in the mid-rapidity region. Figure 3.4 shows the STAR schema. Detectors in the central barrel, enclosed in a 0.5 T solenoidal magnetic field, are Heavy Flavor Tracker (HFT), Time Projection Chamber (TPC), Time Of Flight (TOF), Barrel Electromagnetic Calorimeter (BEMC) and Muon Telescope Detector (MTD). The main tracking detectors are the HFT and the TPC, further described in more detail. The TOF measures track velocity and enhances the STAR particle identification capabilities. The BEMC aims to measure and track high transverse momentum electrons. The outermost detector in the central barrel is the MTD which helps mainly with the reconstruction of charmonium and bottomonium decays to muons.

Particles produced in a forward and backward rapidity are detected by Vertex Position Detector (VPD), Beam Beam Counters (BBC), and Zero Degree Calorimeter (ZDC). These detectors have east and west parts, each on the opposite side of the central barrel. The coincidence of the signals in the two parts is used as a trigger for a collision event, and the time difference between signals gives an estimate of the interaction point position. Particle traversing these detectors generates a signal in the scintillators connected to fast photomultiplier tubes. The BBC covers $3.3 < |\eta| < 5.0$, and additionally to the triggering, it helps measure

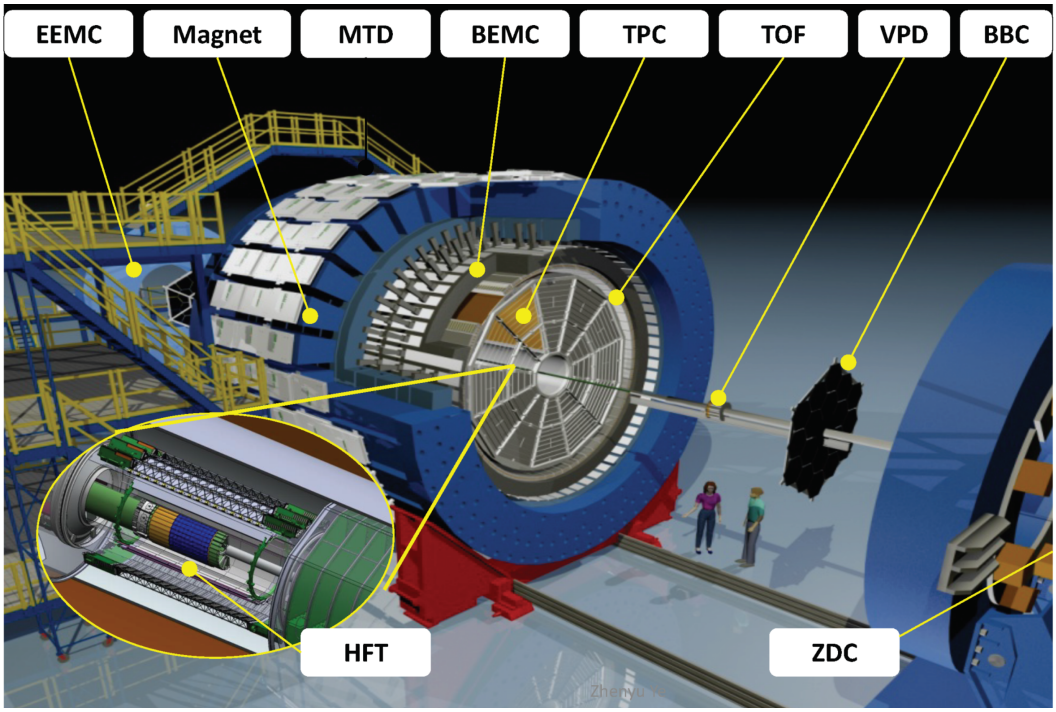

Figure 3.4: The STAR experiment schema with subdetectors denoted.

interaction point position and event-plane shape. The VPD is an essential fast trigger detector with $3.7 < |\eta| < 4.9$. It complements the TOF measurements of the track velocity by a high-precision measurement of the collision start time by detecting the arrival time of prompt photons from π^0 decays. The furthermost detector, placed 18 m from the STAR center, is the ZDC. Thanks to its position, it detects the spectators from the collisions. Additionally, it can measure the luminosity of the beam accelerated in the RHIC.

Endcap Electromagnetic Calorimeter (EEMC) and Forward Meson Spectrometer (FMS) are forward detectors placed only on one side of the STAR and assure continuous coverage of the full azimuth in $1.1 < |\eta| < 4$ region. The EEMC, with $1.1 < |\eta| < 2$, complements the BEMC measurements of the high-energy electrons and photons. It is essential in the spin physics studied in polarised p+p collisions. The FMS covers $2.5 < |\eta| < 4$ in pseudorapidity. Additionally, it helps to measure the event-plane geometry for particle flow studies.

3.2.1 Trigger of the data recording

This section summarizes information about the trigger system at the STAR as it worked till 2018 and is based on the article [108]. Since the TPC, STAR's primary tracking detector is a gaseous detector, it is relatively slow. Thus, like other detectors, it can not detect all collisions provided by the RHIC. However, interactions with a good chance of having valuable physics information should be recorded. The STAR trigger system decides whether a collision has to be saved or not, with inputs from the fast detectors. At STAR, electronics should take this decision in approx. 1.5 μs time window.

In the STAR, there are three different types of trigger algorithms based on measurements of the vertex position, event multiplicity, or jets. The vertex-finding triggers use the ZDC,

the VPD, the BBC, or the MTD. The main idea of vertex triggers is to record only events with a chance of good reconstruction and that have as many as possible tracks in the rapidity acceptance of the detectors. The collision is recorded if the vertex is close enough to the center of the STAR central barrel. Thus, the goal is to use fast information on the collision position. In the case of the ZDC, the BBC, and the VPD, there are two ways to measure the vertex position. Both are based on comparing the coincidence signal in the detectors' east and west side. In the case of p+p collisions, the summed signal of all hits in the towers and the arrival time of the first hit are sent to the trigger electronics from each side. In heavy-ion collisions, the trigger electronics use the mean arrival time of the hits in the detector towers separately for each side. Based on the time differences, fast electronics calculate the interaction point position. In the case of the MTD vertex trigger, time information from the VPD is compared to the time of the first hit in the MTD to trigger using the muons created in the collision. The so-called VPD-5 trigger is used to analyze D^0 meson in d+Au collision. This trigger records only events within ± 5 cm from the STAR center. Such a requirement is common in HFT-based analyses due to the physical dimensions of the HFT. This trigger is also the so-called minimum-bias trigger since, by its definition, it does not explicitly filter out any physics phenomenon (that is the case for the various centrality triggers, jet triggers, etc.).

The multiplicity trigger uses the number of hits in the TOF detector; thus, event selection based on centrality is made. Additionally, the electronics can distinguish the cosmic ray traversing the STAR or the ultra-peripheral collision. The triggering by the jet is done with the STAR calorimeter system. There are multiple jet-triggering setups based on the calorimeter towers with significantly high detected signal ("hot" towers), or high sum of signal in the pre-defined group of calorimeter towers.

3.2.2 Time Projection Chamber

STAR's primary tracking detector is Time Projection Chamber [109], which determines momentum and identifies particles via specific energy loss $\mathrm{d}E/\mathrm{d}x$. An example of such measurement is shown in Fig. 3.5. The schema of the TPC is in Fig. 3.6. Thanks to its cylindrical shape with an inner diameter of 1 m, an outer diameter of 4 m, and a length of 4.2 m, the TPC provides coverage over the full azimuthal angle and has a pseudorapidity acceptance of $|\eta| < 1$.

The TPC is a gaseous detector filled with argon and methane (P10 gas). Traversing charged particles ionizes the gas molecules, and detached electrons drift through the TPC volume into the readout planes, placed in the opposite ends of the TPC. The TPC is split into two parts by the central membrane. It is a cathode with a voltage of -28 kV. Readout planes are segmented into 12 sectors, each having 45 rows of pad planes. Each pad plane is a single multi-wire proportional chamber (MWPC). The MWPC consists of a pad plane and three wire planes. The first plane drifting electrons meet on their way is the gated grid, which works as a shutter and, based on the trigger information, allows the entry of electrons into the MWPC. Then, electrons pass through the shield plane, which blocks positive ions, created in the MWPC from entering the TPC drift volume. Finally, thanks to the anode wire plan, the avalanche of electrons is created, and the pads detect its electric field. The higher the number of electrons entering the MWPC, the higher signal is measured by the pad, which ensures the TPC ability of energy-loss measurement.

The position of the track in the plane transverse to the beam direction is given by the position of the pads that detected its signal. In the beam direction, the position is given by

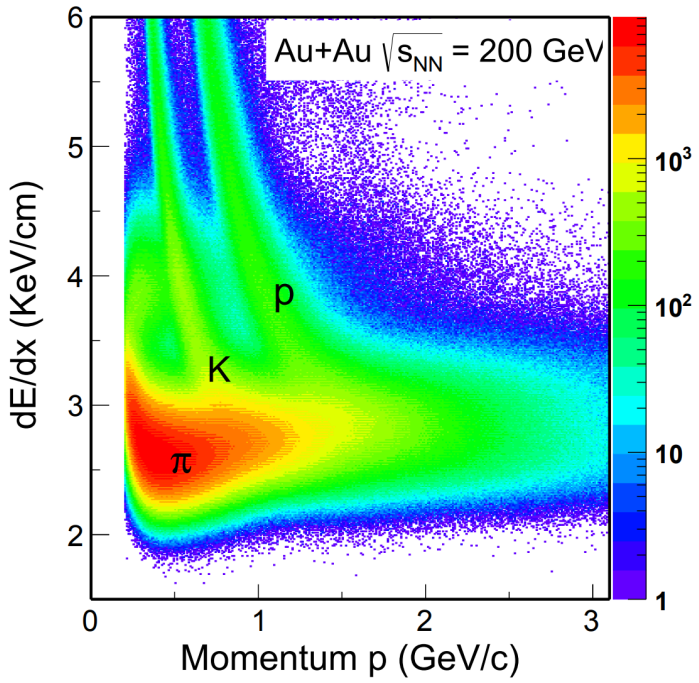

Figure 3.5: The energy loss in the TPC $\mathrm{d}E/\mathrm{d}x$ vs. track momentum p in Au+Au collision at $\sqrt{s_{\mathrm{NN}}} = 200$ GeV. Taken from Ref. [57].

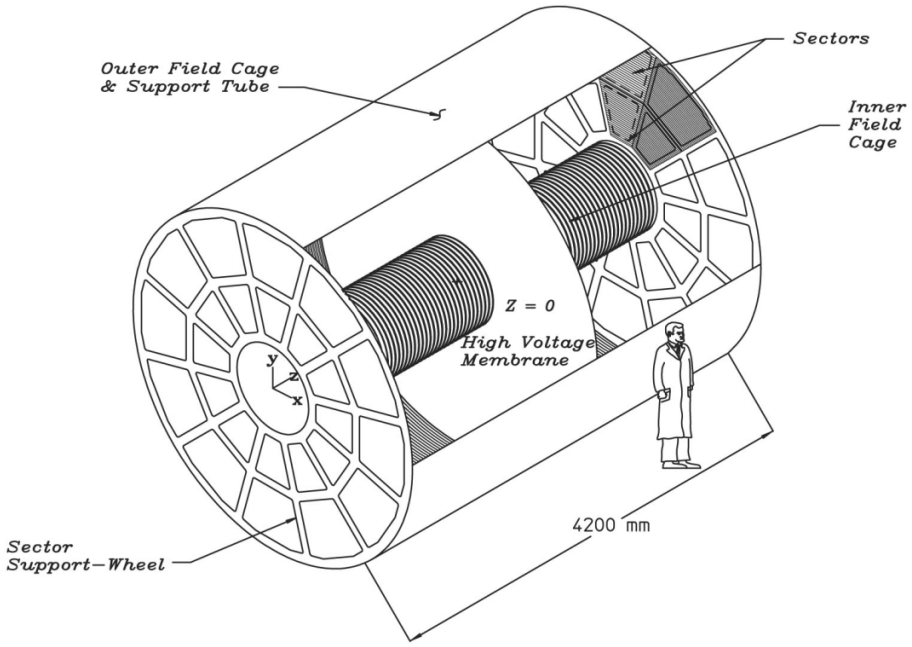

Figure 3.6: Schema of the Time Projection Chamber at STAR. Taken from Ref. [109].

the drifting time of the electrons. The drifting speed of the electrons in the TPC is measured in the calibrations with a laser beam. Depending on the crossing angle of the track in the TPC, the resolution in the transverse plane varies from 0.4 to 2.2 mm (the best resolution is achieved for the track parallel to the readout planes) and in the beam direction from 0.8 to 3.1 mm. The TPC measures track with transverse momentum $p_{\mathrm{T}} > 0.125$ MeV/c.

In the analysis, to identify the track as corresponding to particle X, normalised $\mathrm{d}E/\mathrm{d}x$ is used. It expresses the uncertainty that the reconstructed track is particle X, and it is calculated as

$$n\sigma_{\mathrm{X}}^{\mathrm{d}E/\mathrm{d}x} = \frac{1}{R^{\mathrm{d}E/\mathrm{d}x}} \ln \frac{\mathrm{d}E/\mathrm{d}x}{\langle \mathrm{d}E/\mathrm{d}x \rangle_{\mathrm{X}}}, \tag{3.1}$$

where $R^{\mathrm{d}E/\mathrm{d}x}$ is the TPC resolution and $\langle \mathrm{d}E/\mathrm{d}x \rangle_{\mathrm{X}}$ is the mean value of ionization loss in the TPC for particle X, given by the Bichsel function [110].

3.2.3 Time Of Flight

As seen in Fig. 3.5, for tracks with momentum higher than 1 GeV, particle identification with solely TPC is challenging. Another detector that helps to identify particles is the Time Of Flight [111]. It measures the velocity of the particle β, measuring the time interval that the particle needs to reach it traveling from the interaction point. The time of a collision is determined with the fast VPD, which detect particles produced in the forward directions. The TOF is built from multiple multi-gap resistive plate chambers (MRPC). In MRPC, charged particles ionize the gas, and the high voltage accelerates the resulting electrons to create a detectable avalanche. The TOF time resolution is at the level of 100 ps. Measured $1/\beta$ for tracks in Au+Au collisions at $\sqrt{s_{\mathrm{NN}}} = 200$ GeV is displayed in Fig. 3.7. Particle species can be distinguishable up to a momentum of 3 GeV/c.

Analogically to the TPC, normalised $1/\beta$, noted $\mathrm{n}\sigma_{\mathrm{X}}^{1/\beta}$, is used to identify tracks in the analyses and is defined as

$$\mathrm{n}\sigma_{\mathrm{X}}^{1/\beta} = \frac{\Delta 1/\beta}{R^{1/\beta}} = \frac{\frac{1}{\beta_{\mathrm{meas}}} - \frac{1}{\beta_{\mathrm{teo}}}}{R^{1/\beta}} = \frac{\frac{1}{\beta_{\mathrm{meas}}} - \sqrt{\frac{m_{\mathrm{X}}^2}{p_{\mathrm{X}}^2} + 1}}{R^{1/\beta}}, \tag{3.2}$$

where β_{meas} is measured track velocity, β_{teo} is theoretical (expected) velocity of the track if it corresponds to the particle X, m_{X} is expected mass of a particle X, p_{X} is measured momentum, $R^{1/\beta}$ is the TOF resolution. Sometimes, for TOF particle identification, selection based only on $\Delta 1/\beta$ solely is used.

3.2.4 Heavy Flavor Tracker

The detector closest to the interaction point is the Heavy Flavor Tracker [2], which was installed in the STAR only in years 2014–2016. As the name suggests, its proximity to the beam pipe and the silicon sensors' excellent resolution allow reconstruction of the secondary vertices coming from the heavy-flavor hadron decays. Figure 3.8 displays HFT track-pointing resolution in the plane transverse to the beam direction for protons, kaons, and pions. The resolution of the distance of the closest approach (DCA) at the level of 30 μm for particles with a momentum of 1.5 GeV/c is achieved. A similar resolution is achieved in the beam direction.

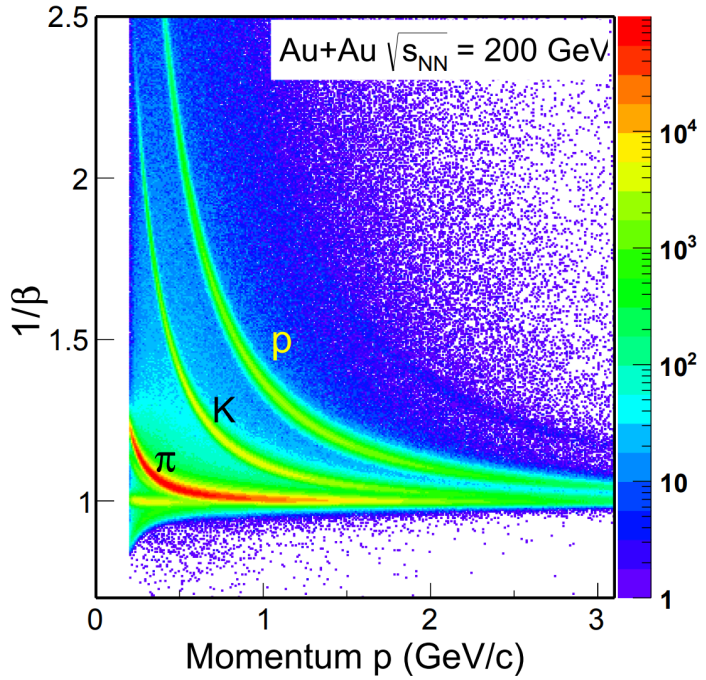

Figure 3.7: The measured inverse velocity $1/\beta$ vs. momentum p for tracks in Au+Au collision at $\sqrt{s_{\mathrm{NN}}} = 200$ GeV. Taken from Ref. [57].

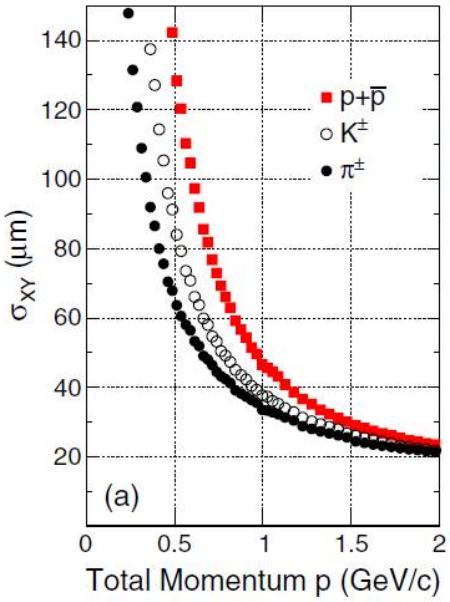

Figure 3.8: Track pointing resolution in the azimuthal direction σ_{xy} as a function of the particle momentum, measured for the overall detector. Taken from Ref. [2].

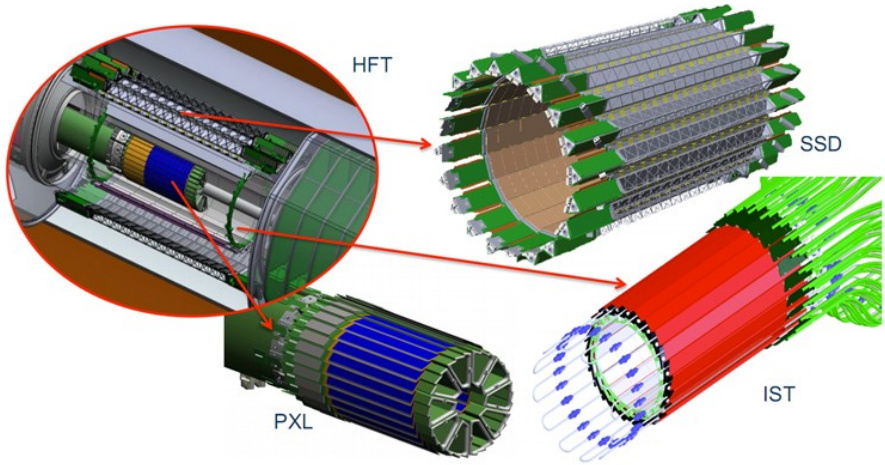

Figure 3.9: Schema of the Heavy Flavor Tracker (HFT) and its subsystems: the PiXeL detector (PXL), the Silicon Strip Detector (SSD) and the Intermediate Silicon Tracker (IST).

The HFT comprises three subsystems, schematically displayed in Fig. 3.9. The PiXeL detector (PXL) consists of two CMOS Monolithic Active Pixel Sensors (MAPS) sensors layers, situated only 2.7 cm and 8 cm from the beam axis. The PXL at STAR was the first time MAPS sensors were employed in a vertex detector at a collider experiment. The pixel size of these sensors is only 20.7×20.7 μm, resulting in a hit spatial resolution of 6 μm, which can be further improved with clustering reconstruction methods [112]. Thanks to their low power dissipation, sensors are operated at room temperature and only air-cooled. Another subdetector is the Intermediate Silicon Tracker (IST), placed at 14 cm from the beam axis. It is a layer of fast, single-sided, silicon strip detectors that filter pile-up events and increase tracking resolution. The outermost layer of the HFT, situated 22 cm from the beam axis, is the Silicon Strip Detector (SSD). It is composed of two-sided silicon drift sensors. In the track reconstruction, requirements on the number of hits in the HFT are used. Typically, track must have hits in both PXL layers since its resolution is crucial for secondary vertices.

3.3 The STAR detector after 2016

In 2017 and 2018, isobar collisions (Ru+Ru and Zr+Zr) were collected to measure chiral magnetic effect [113]). From 2019 to 2021, the Beam Energy Scan program was running, and its primary goal was to study the QCD phase diagram further. Additionally, in 2017 and 2022, beams of polarised protons were colliding to study the proton spin. Main upgrades of the STAR detector are shown in Fig. 3.10. In 2018, BBC was replaced by the Event Plane Detector (EPD) [114]. As the name suggests, it improves the reconstruction of the event planes for flow measurements. It detects particles on the west side of the STAR in $2.1 < |\eta| < 5.1$ acceptance. Additionally, it helps with the triggering and background suppression in the measurements.

In 2019, the TPC was significantly upgraded to track particles in wider pseudorapidity region $|\eta| < 1.5$ and with lower $p_{\mathrm{T}} > 60$ MeV/c. New, more segmented sectors replaced all inner TPC sectors. This upgrade doubled the number of measured hit points per track.

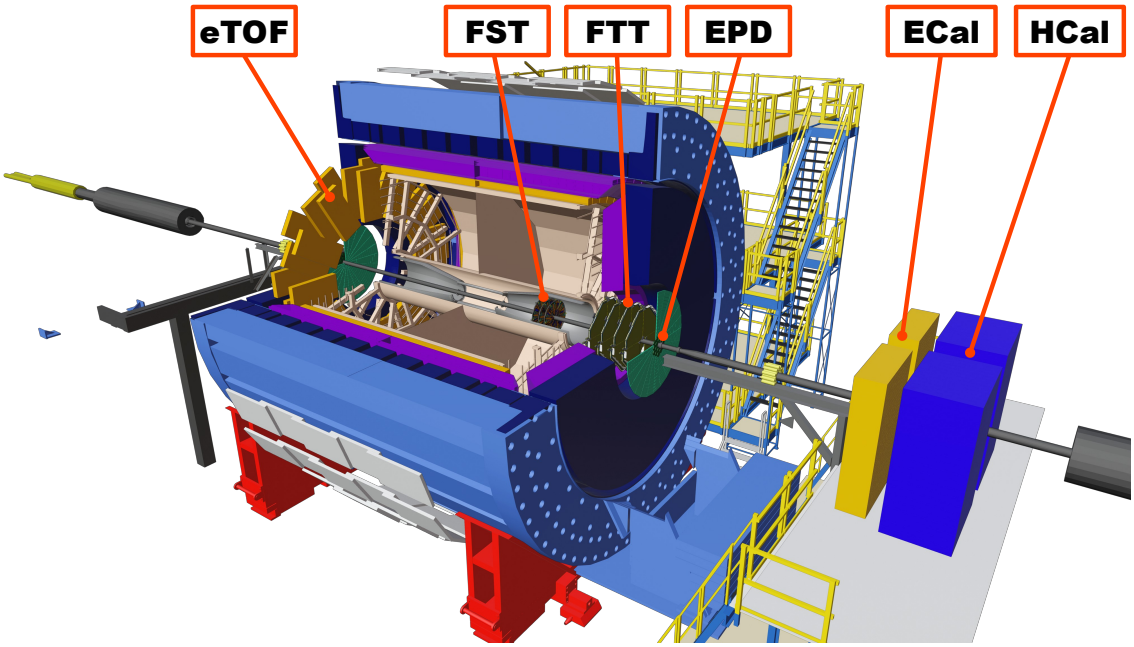

Figure 3.10: The STAR experiment schema with denoted subdetectors, which were upgraded after 2016.

Furthermore, resolution in both momentum and energy loss is approved. More details on the upgrade can be found in [115]. The Endcap Time Of Flight (eTOF) detector was installed in the same year. Situated at the east side of the STAR, the eTOF allows the identification of particles in the forward acceptance of $1.1 < |\eta| < 1.6$. It is especially crucial for particle identification in fixed-target collisions.

The west side of the STAR was upgraded by multiple forward detector systems, displayed in Fig. 3.10. High-precision tracking with relative p_{T} resolution at 20–30% level is enabled by Forward Silicon Tracker (FST) and Forward Small-strip Thin Gap Chambers Tracker (FTT) [116]. Both were installed in the STAR in 2021. The FST consists of three silicon discs situated at 152, 165, and 179 cm from the place of the collision (interaction point). At 307 cm from the interaction point, the first of four FTT disks is placed. There is an 18 cm gap between individual disks, so the last is 361 cm from the interaction point. The forward calorimeter system, installed in 2020, comprises Electromagnetic Calorimeter (ECal) and Hadronic Calorimeter (HCal). These are placed in a platform 7 m from the interaction point.

Chapter 4

D^0 meson production in d+Au collisions at $\sqrt{s_{NN}} = 200$ GeV

4.1 D^0 meson reconstruction strategy

Hadronic decay of D^0 meson to K^- and π^+ with branching ratio 3.89 ± 0.04 % [3] is used for D^0 reconstruction. The observed signal is enhanced by considering both unlike-sign combinations of pion and kaon ($K^-\pi^+$ and $K^+\pi^-$) as correct charge combinations, so $\overline{D^0}$ are reconstructed together with D^0 mesons. In this analysis, the wrong (like-sign) charge combination of pion and kaon ($K^+\pi^+$ and $K^-\pi^-$) are considered as combinatorial background pairs. D^0 mesons are reconstructed and analyzed in three transverse momentum p_{T,D^0} intervals: 1–2, 2–3 and 3–5 GeV/c. Ranges of p_{T,D^0} correspond to the intervals of Kπ pairs transverse momentum $p_{T,K\pi}$.

In the analysis, recorded collision events are checked for their properties and trigger information to analyze those with relevant and reliable detector information. If they pass these requirements, pions and kaons detected in these events are selected with quality and particle identification criteria. Then, for each event, pions and kaons are combined into unlike-sign and like-sign pairs. For each of these pairs, topological variables are calculated. After that, the Boosted Decision Trees classification is trained and applied to find the raw yield of D^0 mesons. Finally, efficiency corrections are applied to the raw yield to calculate invariant yield and nuclear modification factor of D^0 meson in d+Au collisions.

4.2 Simulations used to calculate D^0 meson spectra

4.2.1 Data-driven fast Monte Carlo simulation (FastSim)

Data-driven fast Monte Carlo simulation (FastSim) was developed for STAR heavy-flavor analyzes. It was further modified and set up to analyze the D^0 meson in d+Au collisions. In the FastSim, D^0 meson decay to kaon and pion is simulated with PYTHIA [117]. D^0 mesons are generated in flat transverse momentum range $0 < p_{T,D^0} < 8$ GeV/c and rapidity is taken randomly from flat $|y| < 1$ distributions.

Then, kaon and pions tracks are smeared according to momentum resolution, calculated using the single-particle TPC and HFT embedding (Sec. 4.6.1). Other smearing inputs to the simulation are distributions from recorded data. These data are the same events as those used for D^0 meson reconstruction analysis. They are separated into four vertex positions V_z and six event multiplicity intervals that define 24 event classes together. From each event class, these distributions are extracted separately for kaons and pions:

- DCA_{xy} vs. DCA_z; separately for five track η and 15 track p_T intervals (together 75 distributions for each event class and both track species),
- ratio of HFT tracks to all TPC tracks (HFT ratio) vs. track p_T; separately for 10 η and 11 azimuthal angle intervals to reflect the HFT layout (together 110 distributions for each event class and both track species).

For each D^0 generated in the simulation, the event class is randomly Taken from Ref. V_z and multiplicity distributions for data. DCA of the track is then smeared according to distributions from data for a given event class and smeared track p_T and η. The HFT ratio from data is expected to reflect the efficiency of HFT for tracks that pass the TPC selection criteria. Additionally, it is expected to have better precision than the simulated HFT response since it concerns HFT spatial resolution in the recorded data.

Finally, as done in the recorded collisions, D^0 mesons are reconstructed back from these smeared tracks. These D^0 mesons are expected to have nearly the same distribution of topological properties as the real D^0 mesons, whose daughter particles are detected. The FastSim is used to properly convolute p_T-dependend single particle efficiencies to D^0 meson p_T to calculate total D^0 meson reconstruction efficiency. Additionally, the output from this simulation is taken as a signal sample to train classification methods for finding D^0 meson raw yield.

4.2.2 Full-event simulation

Full-event simulation and embedding to the real data are done to estimate the reconstruction performance in the specific conditions of d+Au collisions. Simulation of the d+Au collisions is done with the HIJING simulator [86] and the detector response is simulated by the GEANT [87] with official STAR software. Such events are then embedded in the so-called zero-bias (events not filtered by any trigger) recorded d+Au collisions to be as close as possible to the real collision environment. Thanks to this full detector simulation, the efficiency of individual event selection cuts and triggers might be tested. Three different samples were produced:

1. minimum-bias (MB) events,
2. events with at least one simulated D^0 meson in the detector acceptance (D^0 events),
3. D^0 events with primary vertex position in beam direction $V_z < 6$ cm.

For the D^0 events, hard scatterings in the initial state are enhanced in the HIJING setup. This simulation is produced to compare specific properties of such collisions with minimum-bias data.

4.3 Event selection

In 2016, approximately 350 million of d+Au collisions at $\sqrt{s_{NN}} = 200$ GeV were recorded. The minimum-bias trigger, which requires coincidence in both VPD East and West detectors,

is used for this analysis. Only events with the reconstructed position of the primary vertex in the beam direction V_z less than 6 cm and events with correlated primary vertices reconstructed with TPC and VPD ($|V_{z,\mathrm{TPC}} - V_{z,\mathrm{VPD}}| < 3\,\mathrm{cm}$) are further analyzed.

Analyzed d+Au collisions suffer from many pileup tracks created in multiple bunch crossing per recorded TPC event. The number of bunch crossings is reflected in the BBC or ZDC detector's coincidence rate at the time of the recorded collision. The HFT detector is turned off for the BBC rate higher than 900 kHz to protect its electronics. Together with the requirements on the tracks, it decreases the pileup effect in the D^0 meson analysis.

All recorded d+Au events are then tested for quality when individual variables and properties are compared and tested for consistency within runs. Those runs, whose variables' averages are out of $\pm 4\sigma$ range from the average overall recorded runs in d+Au, are rejected for further analysis.

Additionally, a cut on the vertex position in the xy-plane, which is perpendicular to the beam direction and where the detector center is at $V_{x,y} = 0$ cm, is applied. Due to the technical conditions, the beam of colliding particles is not going through the exact center of the STAR detector, and its position changes between different runs. However, it had the same position during d+Au collisions data taking. Separate measurement of the beamline position is one of the constraints in the vertex reconstruction at STAR [118], and it helps to improve the resulting primary vertex resolution. Therefore, only primary vertices close to the beamline are used due to the need for good primary vertices for the topological reconstruction of D^0 meson decay. These are selected with cut $-0.25 < V_{x,y} < -0.16$ cm.

In general, 2016 d+Au collisions have good quality since they were recorded after the long Au+Au collisions run. After applying trigger selection, event cuts, and rejecting bad runs, approximately 90 million d+Au events remain for D^0 meson analysis.

4.4 Track selection

Tracks of daughter particles must have at least 15 space points used for track reconstruction in the TPC. In addition, these are required to have hit in both HFT PXL layers and at least one in the IST or SSD layers (such tracks are so-called HFT tracks). Only tracks with pseudorapidity $|\eta| < 1$ and transverse momentum $p_{\mathrm{T}} > 0.15$ GeV/c are used in further analysis.

For TPC particle identification, $|\mathrm{n}\sigma_{\mathrm{X}}^{\mathrm{d}E/\mathrm{d}x}| < 3$ is used for pions, and $|\mathrm{n}\sigma_{\mathrm{X}}^{\mathrm{d}E/\mathrm{d}x}| < 2$ is used for kaons. For TOF identification, the so-called hybrid TOF strategy is used. For both kaons and pions, $\Delta 1/\beta_{\mathrm{TOF}} < 0.03$ cut is required only in the case track has information in the TOF detector. If there is no TOF information, only TPC is used for daughter particle identification.

4.5 Raw yield extraction

Reconstructed kaons and pions that pass selection criteria in the same event are combined into wrong and correct charge pairs. Then, described topological variables described in Sec. 1.4.1 are calculated for all $\mathrm{K}\pi$ pairs. Before training and applying machine-learning classification, relatively wide topological precuts are applied to all pairs to cut-out regions,

where the relevant D^0 signal is not expected. These cuts are listed in Tab. 4.1. Distributions of described topological variables after application of these precuts are displayed in Fig. 4.1 for $1 < p_{T,K\pi} < 2$ GeV/c. Projections for other analyzed $p_{T,K\pi}$ intervals are in App. A. As can be seen, there is no difference between projections from unlike-sign and like-sign Kπ pairs. Since correct charge pairs suffer from the significant combinatorial background and D^0 meson could not be directly observed, the Boosted Decision Trees (BDT) machine learning classification, implemented in the Toolkit for Multivariate Analysis (TMVA) [4] is used. TMVA package is integrated with the ROOT environment and includes multiple algorithms and methods designed for the needs of high-energy physics.

Table 4.1: Sets of preselection cuts applied to topological variables of D^0 meson decay before classification method training and application.

Variable	Min.	Max.
$DCA_{K,\pi}$ [mm]	0.02	2
$DCA_{daughters}$ [mm]	0	0.2
decay length [mm]	0.005	2
DCA_{D0} [mm]	0	0.5
$\cos\theta$ [-]	0.7	1

For the training, the BDT, as a standard machine learning algorithm, requires samples of signal and background D^0 meson pairs. As the signal sample, D^0 meson pairs from FastSim, described in Sec. 4.2.1 are used. The background sample consists of the wrong-sign Kπ pairs from recorded data. Classification training and application are implemented separately for three analyzed $p_{T,K\pi}$ intervals.

Multiple hyperparameters are tested in order to find the set with the best performance. Overtraining is minimized by requiring the maximum tree depth of 3 and the minimum number of training events in the tree leaf 2.5 % of the training events in the $p_{T,K\pi}$ interval. Gini impurity measure is employed to separate tree nodes with an unlimited number of tested cuts on the topological variables in training. Finally, 50 % of randomly selected training sample pairs is used for each tree optimization. The number of trained trees is estimated similarly as shown in Sec. 2.9. For $1 < p_{T,K\pi} < 2$ GeV/c and $2 < p_{T,K\pi} < 3$ GeV/c analysis bins, the final number of trees used is 150, for $3 < p_{T,K\pi} < 5$ GeV/c it is 400.

After the training, BDT response distributions can be displayed for training and test samples, both for signal and background inputs to the training. One of the checks that BDT is not over-trained is that test and training BDT distributions do not have significantly different shapes. Figure 4.2 shows BDT response distributions for three studied $p_{T,K\pi}$ intervals. The signal pairs typically have positive BDT responses. However, their distributions are significantly wider than those for the background. As can be observed, test and train distribution shapes are close to each other.

Classification is done by selecting a value of the BDT response cut that is applied to all pairs. Pairs with calculated BDT response higher than the selected cut are considered a signal, and others are a background. This calculation is done for various BDT response cuts on the Kπ pairs in the BDT training to calculate signal and background efficiencies. Figure 4.3 shows ROC curves (signal vs. background efficiency) for the three $p_{T,K\pi}$ intervals. Every point on the shown curves corresponds to the one BDT response cut.

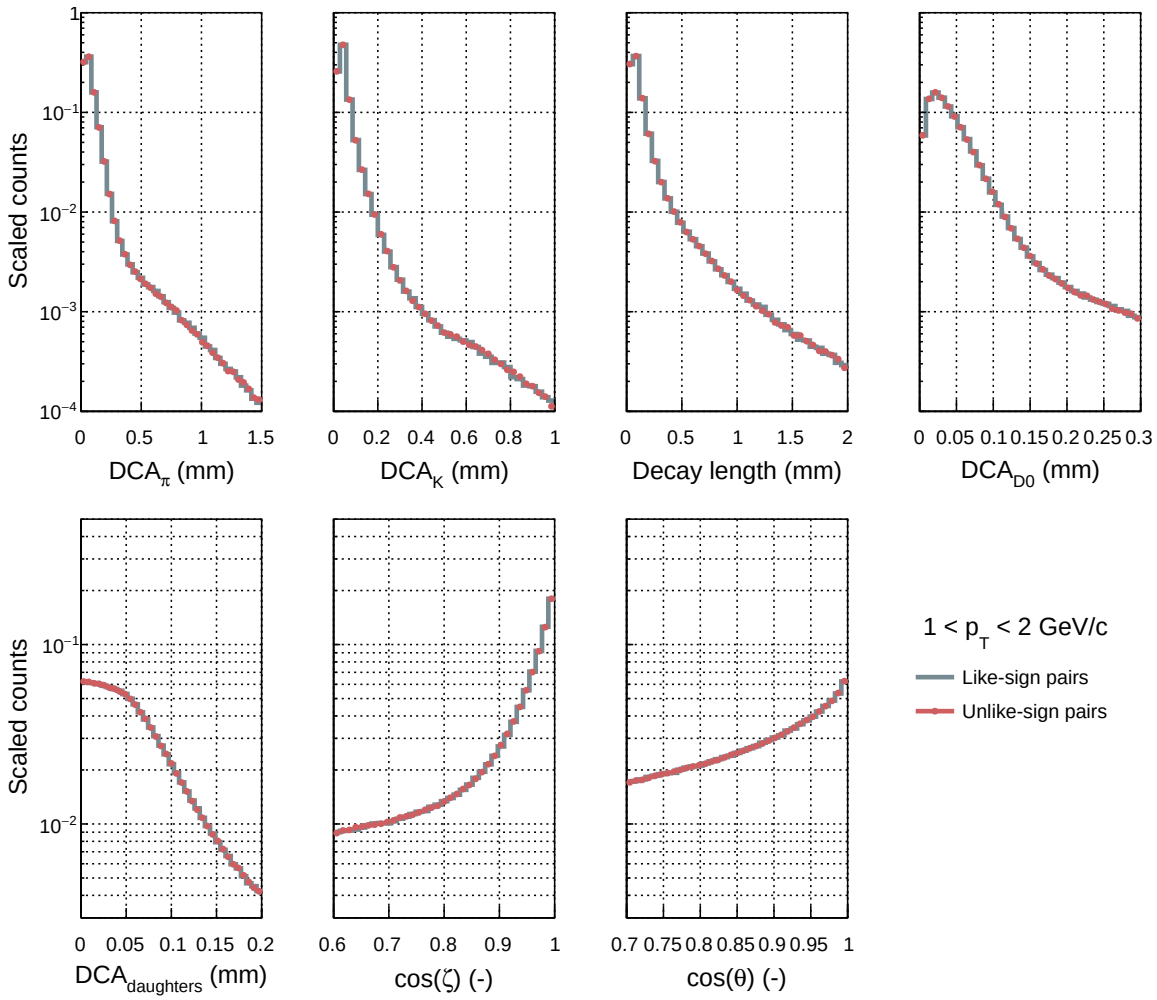

Figure 4.1: Distributions of topological variables for Kπ pairs with invariant mass 1.7–2 GeV/c^2, transverse momentum p_{T} 1–2 GeV/c and after application of precuts shown in Table 4.1.

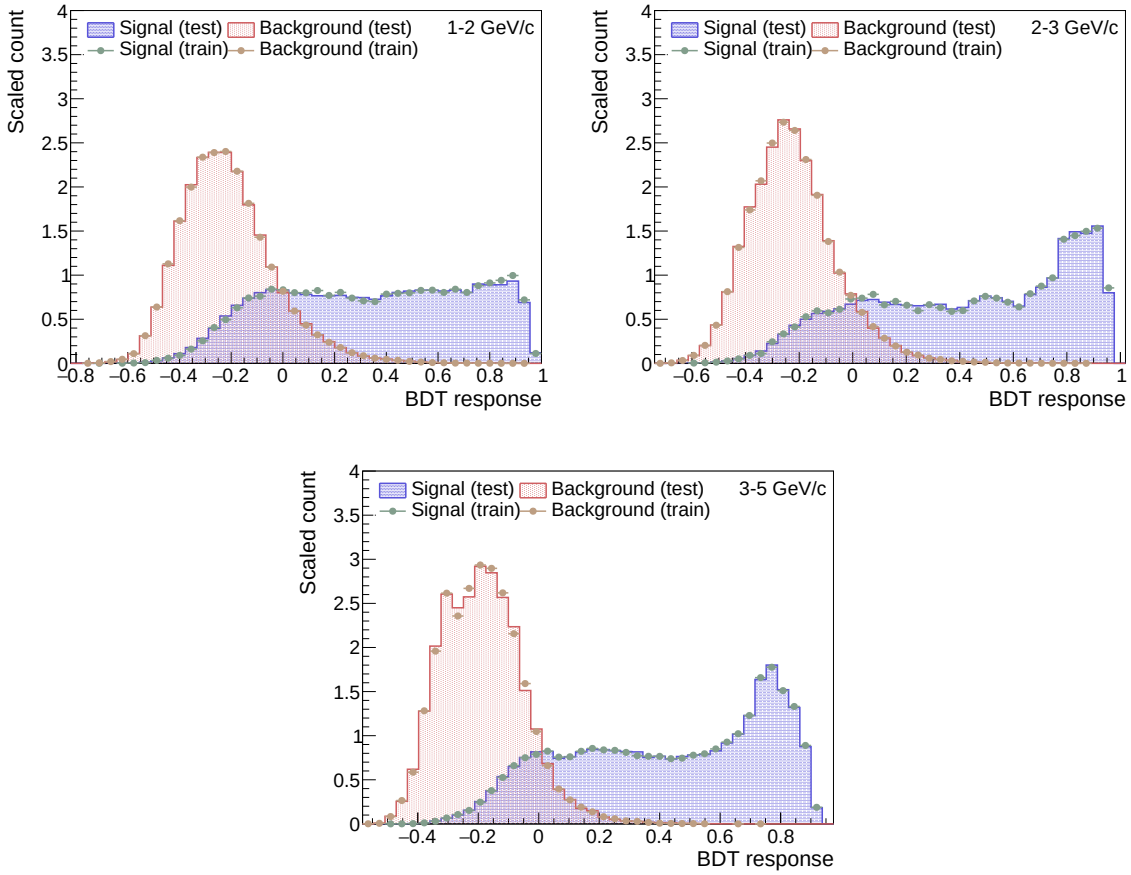

Figure 4.2: Response of the trained Boosted Decision Trees (BDT) for training and test samples, and for both signal and background Kπ pairs in the three analyzed Kπ transverse momentum intervals.

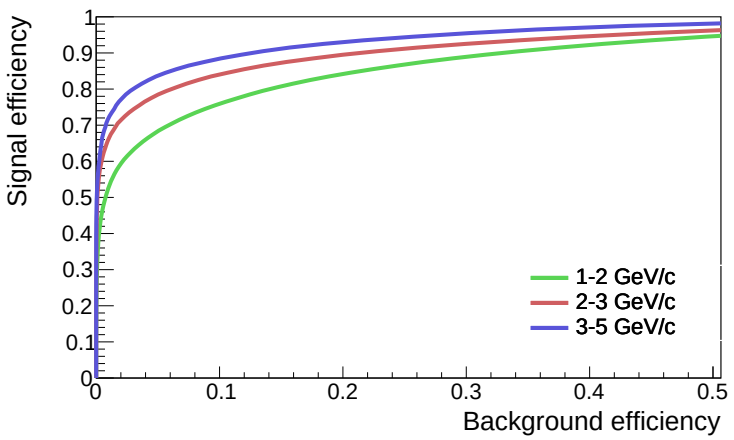

Figure 4.3: Receiver operating characteristic (ROC) curve—signal vs. background efficiency from the BDT training for three analysed Kπ transverse momentum intervals.

BDT response cut to be applied in the recorded data is calculated as the point of the maximum expected significance of the D^0 signal. Expected signal significance is defined as

$$\Sigma(r_{\mathrm{BDT}}) = \frac{N_{\mathrm{S}}\epsilon_{\mathrm{S}}(r_{\mathrm{BDT}})}{\sqrt{N_{\mathrm{S}}\epsilon_{\mathrm{S}}(r_{\mathrm{BDT}}) + N_{\mathrm{B}}\epsilon_{\mathrm{B}}(r_{\mathrm{BDT}})}}, \tag{4.1}$$

where r_{BDT} is the selected BDT response cut, N_{S} and N_{B} are estimates of the number of signal and background pairs in the recorded data before the BDT application, $\epsilon_{\mathrm{S}}(r_{\mathrm{BDT}})$ and $\epsilon_{\mathrm{B}}(r_{\mathrm{BDT}})$ are signal and background efficiencies calculated in the BDT training. N_{S} is estimated using scaled D^0 invariant yield measured in p+p collisions [52] and the estimates of detector efficiencies. N_{B} is evaluated from the number of wrong-sign pairs in the data. Figure 4.4 displays expected significances, together with ingredients for their calculation using Eq. 4.1. Finally, significance is fitted, and the BDT response cut, where this fitted function has maximum, is used for the raw yield extraction. In Fig. 4.4, selected BDT response cuts are shown by the brown vertical line.

Afterward, the trained classifier calculates the BDT response for all unlike-sign (signal) and like-sign (background) pairs from the recorded data. Subsequently, a calculated cut on the minimum BDT response is applied for both signal and background. Pairs that pass this cut are used to calculate the D^0 meson raw yield.

Invariant mass $m_{\mathrm{K}\pi}$ distributions of $\mathrm{K}\pi$ pairs that pass the calculated BDT response cuts are shown in Fig. 4.5 for both unlike-sign and like-sign pairs. From these distributions, D^0 raw yield is extracted by two methods: integration of the fitted functions and bin-counting in the interval defined by fitting. In the first method, unlike-sign pair distributions are fitted by the sum of Gaussian and linear functions for $1.7 < m_{\mathrm{K}\pi} < 2$ GeV/c^2. The linear function describes the combinatorial background, which typically drops with $m_{\mathrm{K}\pi}$, and the Gaussian function describes the D^0 meson signal. Afterward, to obtain the raw yield Y, the Gaussian part of the fit is integrated in $\pm 3\sigma$ interval around its mean. Resulting fits are shown in Fig. 4.6. The resulting significance is calculated as

$$\Sigma_{\mathrm{data}} = \frac{Y}{\sqrt{Y + 2N_{\mathrm{B,data}}}}, \tag{4.2}$$

where $N_{\mathrm{B,data}}$ is the number of background pairs calculated as the integral of the linear part of the fitted function in the same interval as Y is calculated. This method is the default in the analysis, and its results are used to calculate D^0 invariant yield distributions.

The secondary method to extract raw yields uses $m_{\mathrm{K}\pi}$ distributions resulting from the subtraction of like-sign pair $m_{\mathrm{K}\pi}$ distribution from unlike-sign $m_{\mathrm{K}\pi}$ distribution. Resulting distributions are shown in Fig. 4.7 by blue points. Afterward, these are fitted by the sum of Gaussian and linear functions for $1.7 < m_{\mathrm{K}\pi} < 2$ GeV/c^2. The linear part of the fit is considered as the residual background and is subtracted from the distributions, resulting in distributions plotted by grey points in Fig. 4.7. Finally, these cleaned distributions are fitted by the Gaussian function. The Gaussian σ and μ are then used to calculate raw yield Y using bin-counting in the cleaned distributions and in $\pm 3\sigma$ region around fitted μ. In this case, to calculate the significance using Eq. 4.2, $N_{\mathrm{B,data}}$ is calculated by bin-counting in the same interval as the one used for Y. Raw yield results for this method are used for the systematic uncertainty calculation.

As a cross-check of the results of the simulated significance from the BDT training, shown in Fig. 4.4, the significances of the raw yields for multiple BDT cuts are calculated. These

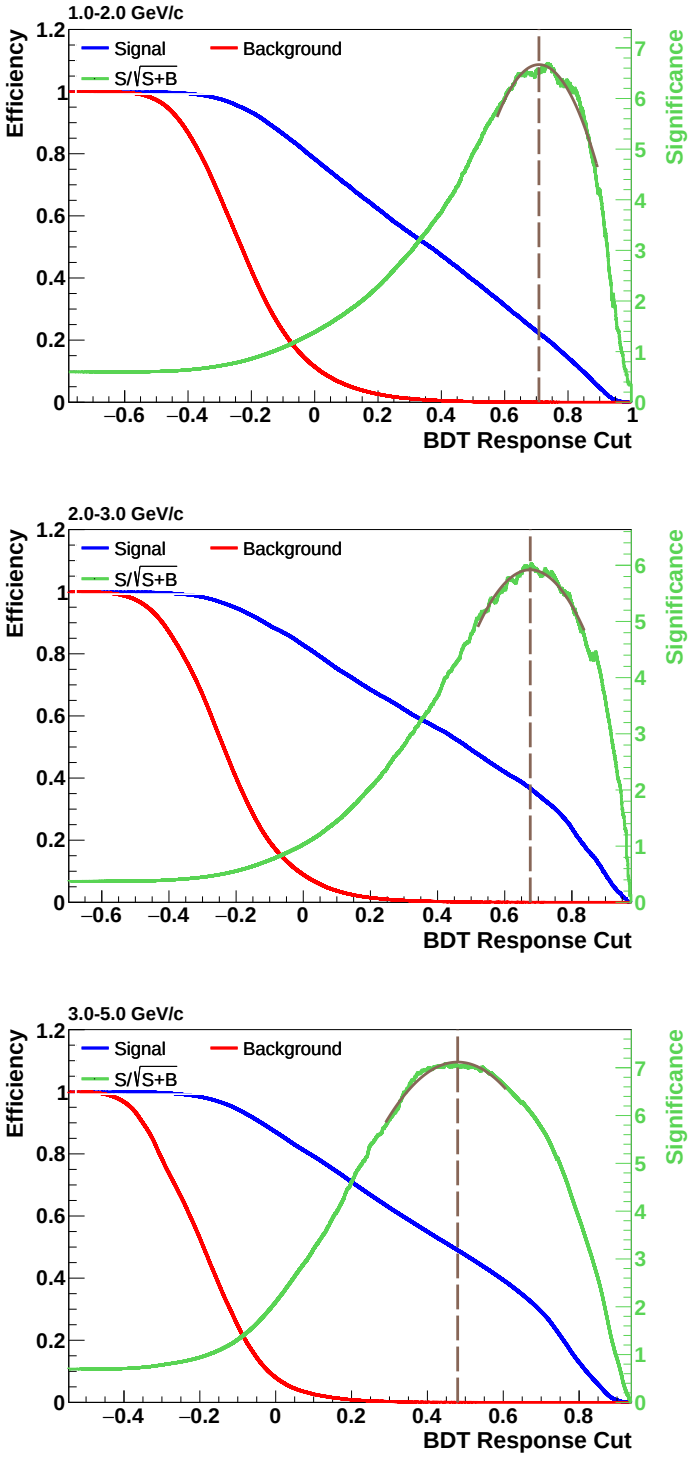

Figure 4.4: The calculation of the optimal BDT response cut that maximizes D^0 meson significance. The blue and red lines show the signal and background efficiencies from the BDT training. The green line is the calculated D^0 meson significance. The full brown lines show the fits around the point of the maximum significance, and the vertical dashed line shows the selected BDT response cut.

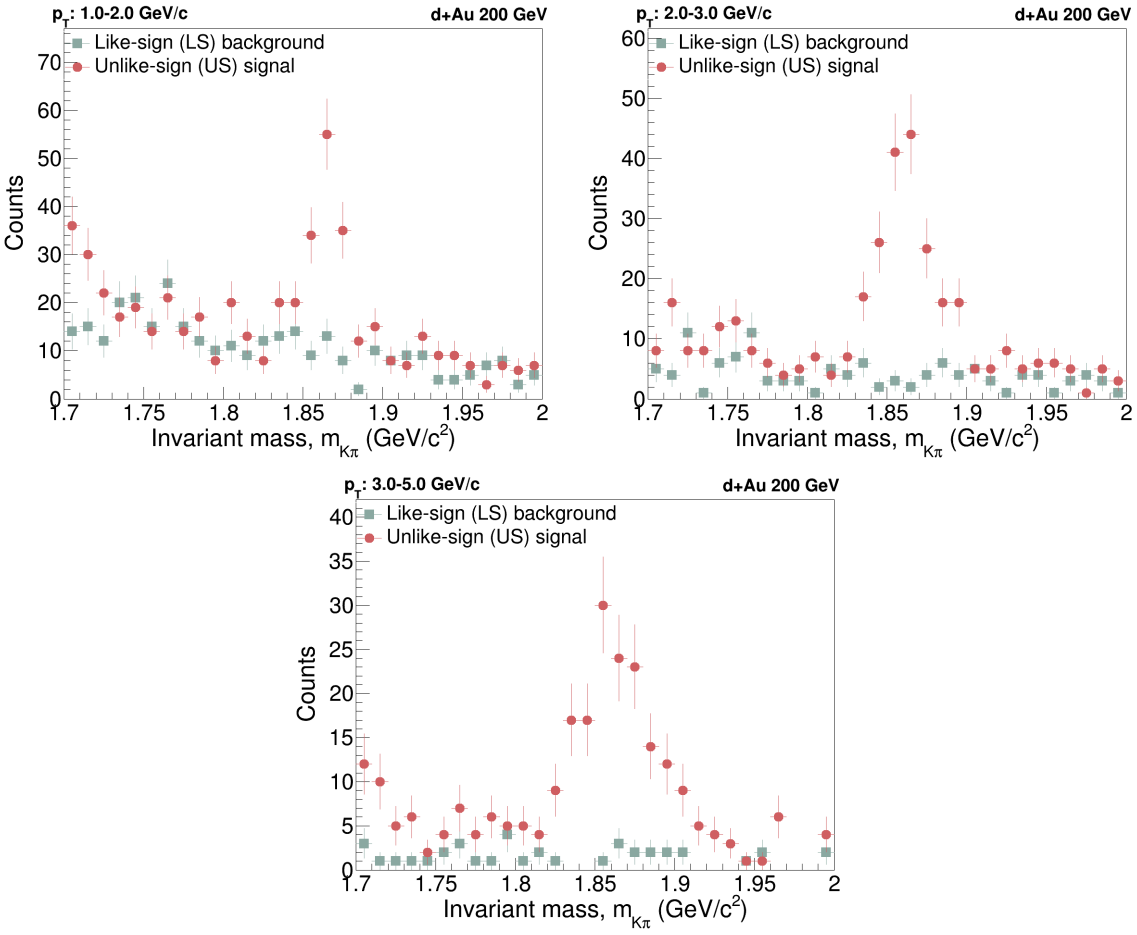

Figure 4.5: Invariant mass $m_{\mathrm{K}\pi}$ distributions for like-sign and unlike-sign Kπ pairs after application of the BDT classifier, in three analysed Kπ transverse momentum p_{T} intervals.

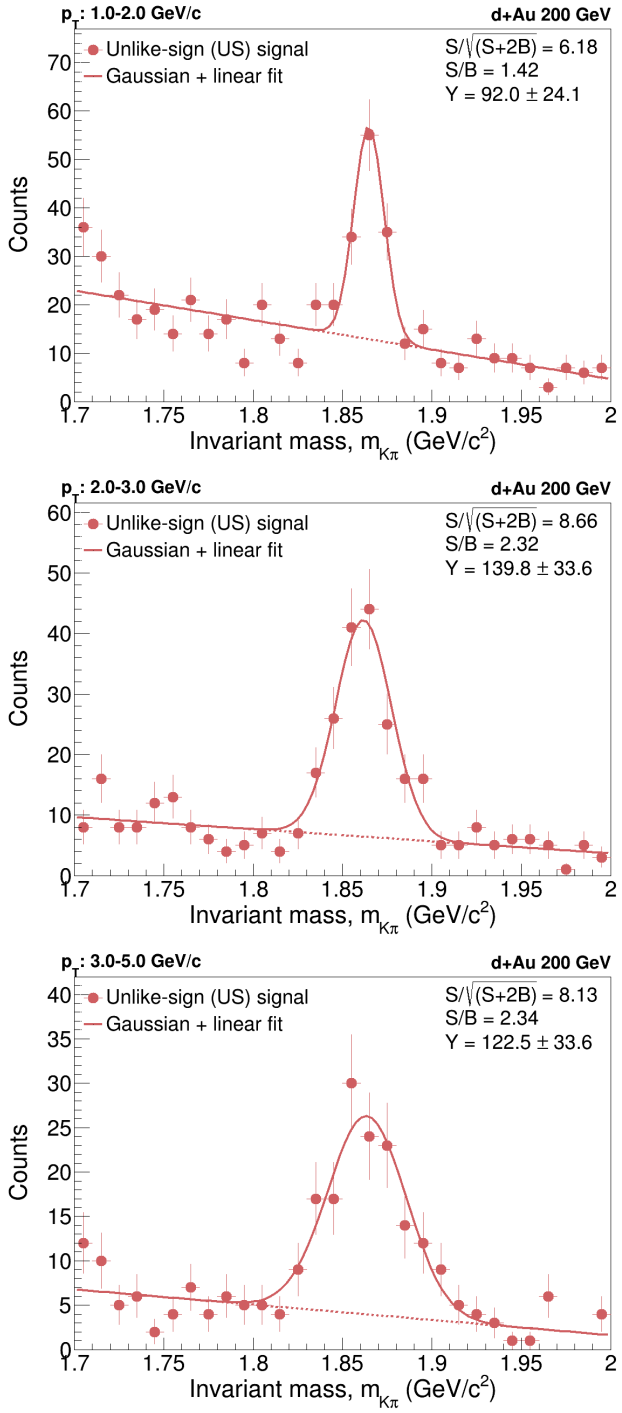

Figure 4.6: D^0 meson signals in the distributions of the invariant mass of unlike-sign $K\pi$ pairs $m_{K\pi}$ and their fits by the sum of Gaussian and linear functions, in analysed $K\pi$ transverse momentum p_T intervals. Calculated raw yields Y, signal over background ratios S/B and significances $S/\sqrt{S+2B}$ from the fit results are displayed on the plots.

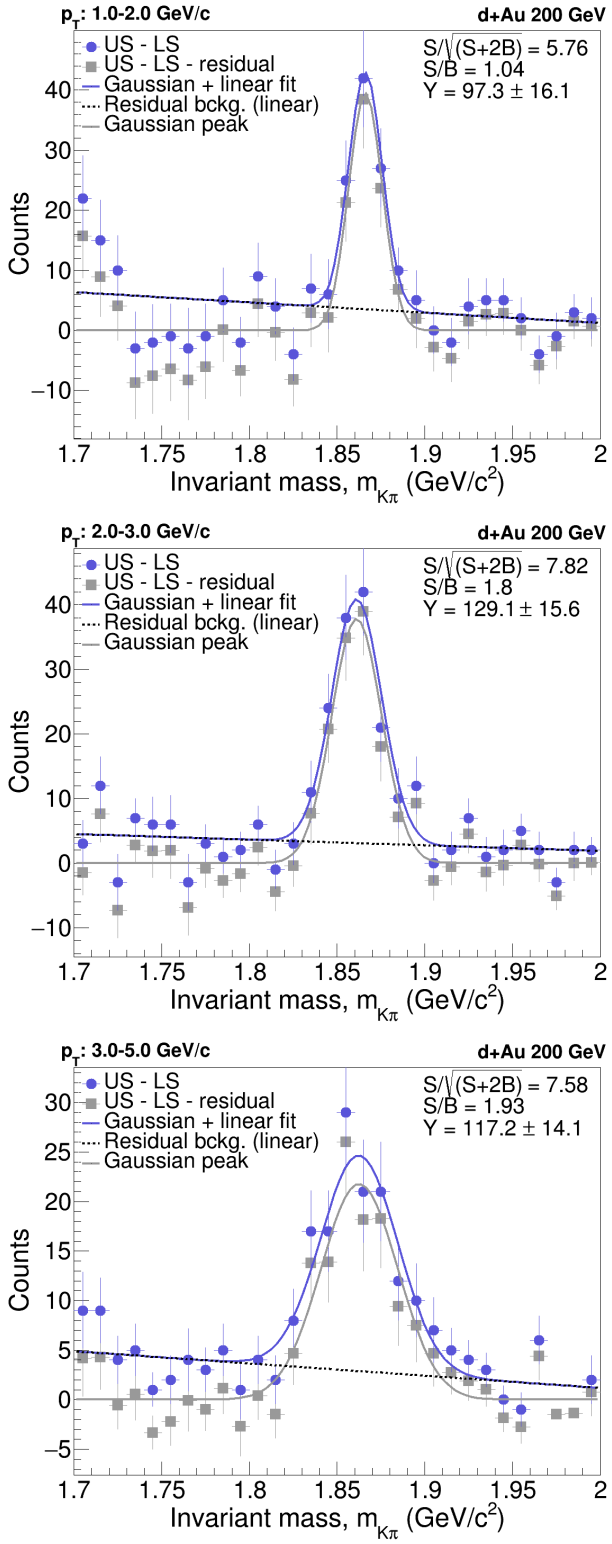

Figure 4.7: D^0 meson signals in the distributions of the invariant mass of Kπ pairs $m_{K\pi}$ and ingredients to the bin-counting raw yield calculation, in analysed Kπ transverse momentum p_T intervals. Blue circles show results from subtraction of like-sign pairs from unlike-sign pairs distributions and blue lines show their Gaussian+linear fits. Grey squares display results from additional subtraction of the fitted residual background (linear part of the fit, showed by dashed grey line). Solid grey line shows the Gaussian part of the fit. Calculated raw yields Y, signal over background ratios S/B and significances $S/\sqrt{S+2B}$ from the fit results are displayed on the plots.

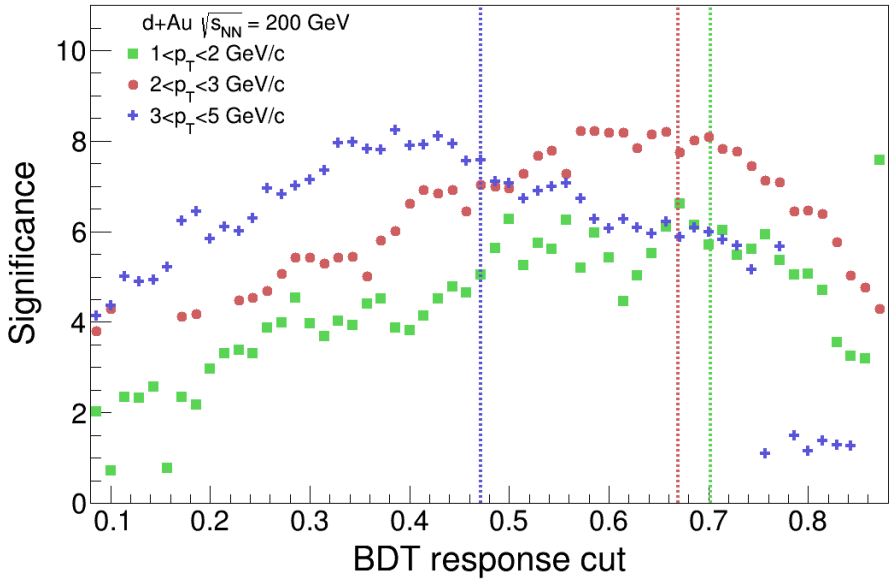

Figure 4.8: D^0 meson raw yield significances for multiple BDT response cuts calculated in recorded data using bin-counting method, and for analyzed $K\pi$ transverse momentum p_T intervals. Vertical lines show optimal BDT cuts calculated in the BDT training and used for the final invariant yield calculations.

significances are calculated using the bin-counting method. Results are shown in Fig. 4.8, where vertical lines show BDT cuts calculated using signal and background efficiencies from the BDT training (the vertical lines in Fig. 4.4). As can be seen, these cuts are close to the significance maxima, which validates the BDT training and the cut selection.

4.6 Efficiency corrections

To calculate the invariant yield of D^0 meson in $|\eta| < 1$, the efficiencies for each step of its reconstruction are estimated:

- trigger bias efficiency, that covers the difference in the event selection for events with and without D^0 meson;
- detector acceptance and tracking efficiencies for the HFT and the TPC detectors;
- TOF matching efficiency;
- particle identification efficiencies for the TPC and the TOF;
- BDT selection efficiency;
- vertex reconstruction efficiency, that corrects the lower efficiency of primary vertex reconstruction in low-multiplicity d+Au collisions with D^0 meson created;
- correction of the double counting, that is caused by the combinatorial construction of $K\pi$ pairs.

All of the single particle efficiencies have to be combined with D^0 meson decay simulation from FastSim (Sec. 4.2.1), in order to properly calculate according D^0 meson efficiency vs. transverse momentum p_{T,D^0}.

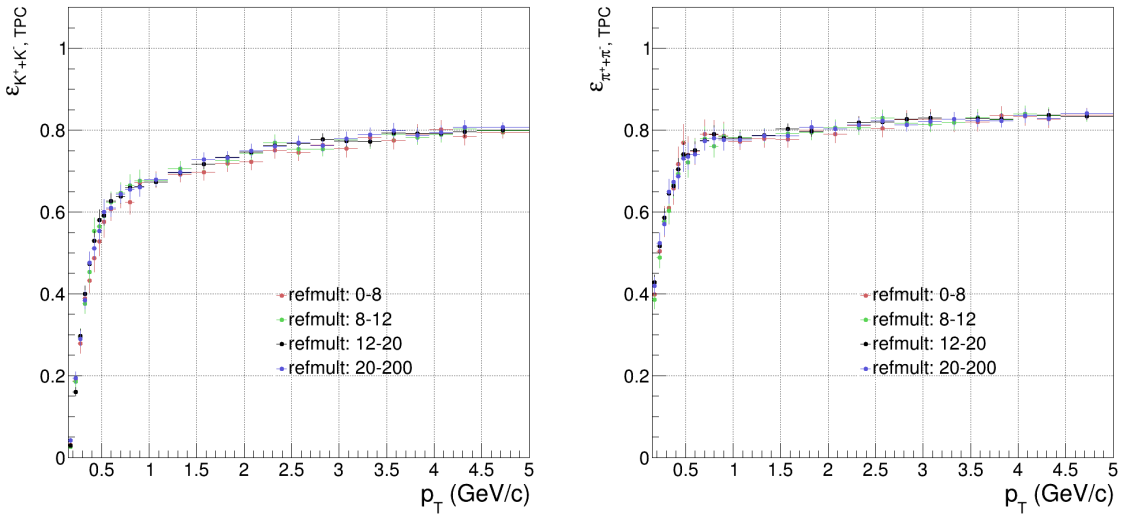

Figure 4.9: Single-particle TPC efficiencies vs. track transverse momentum p_T for kaons (left) and pions (right), calculated in various event multiplicity classes.

4.6.1 HFT and TPC tracking efficiency and momentum resolution

The tracking efficiency of the TPC detector and its momentum resolution is calculated using the single-particle embedding to the real STAR data.[1] In this simulation, 300 thousand of each K^-, K^+, π^+ and π^- tracks are generated using PYTHIA in flat and full η and ϕ distributions, and in flat p_T interval between 0 and 5 GeV/c. Simulated particle tracks enter the simulators of the TPC and HFT detectors. Additionally, these generated tracks are mixed into the recorded collision events (one simulated track per event) to have a data sample similar to the measured data. Thanks to this embedding, track properties are compared at the simulation level and after the detection system smearing.

The simulated track is considered reconstructed by the detector if it has at least ten common hits with some real track and reconstructed $|\eta| < 1$. TPC efficiency is then defined as the ratio of the number of such tracks fulfilling additional analysis cuts (nHitsFit > 15 and reconstructed $\mathrm{DCA_{PV}} < 1$ cm) to the number of all tracks that have simulated $|\eta| < 1$.

To test the TPC performance for different event multiplicities, the resulting efficiencies are compared for four multiplicity classes, as shown in Fig. 4.9. As can be seen, there is no significant difference between efficiencies in shown multiplicity classes. Additionally, efficiency is compared for positively and negatively charged particles (Fig. 4.10). It is observed that efficiencies are similar within particle species.

TPC and HFT momentum resolution is calculated as σ parameter from Gaussian fit of MC tracks relative p_T uncertainty $((p_T^{MC} - p_T^{reco})/p_T^{MC})$ distribution. This resolution is calculated for multiple track p_T intervals, and results are shown in Fig. 4.11 for tracks selected with the same TPC and HFT reconstruction cuts as in the principal analysis.

[1] Embeddings are produced by the Software and Computing group at the STAR experiment according to the requirements of the analyzers.

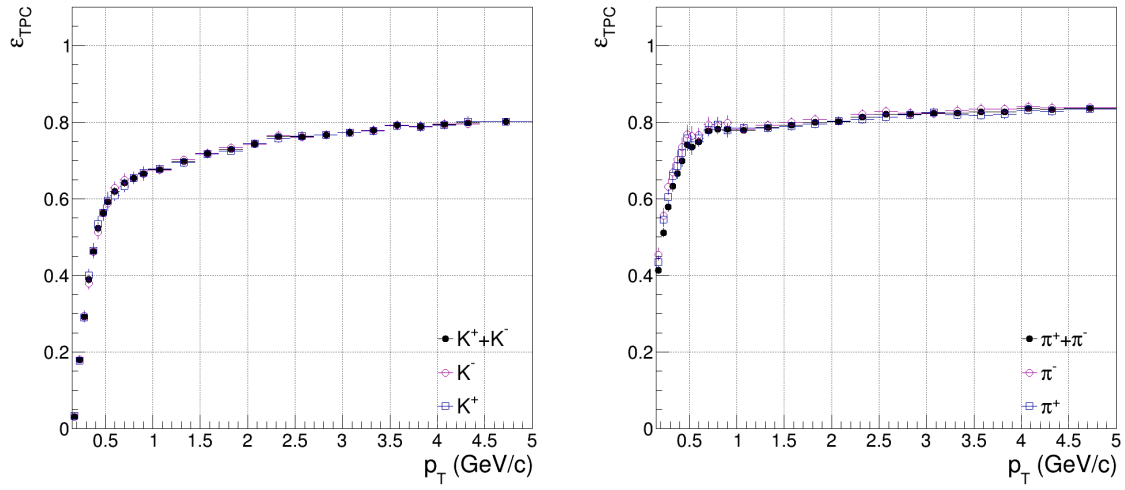

Figure 4.10: Single-particle TPC efficiencies vs. track transverse momentum p_{T} for kaons (left) and pions (right), calculated separately for positively and negatively charged tracks.

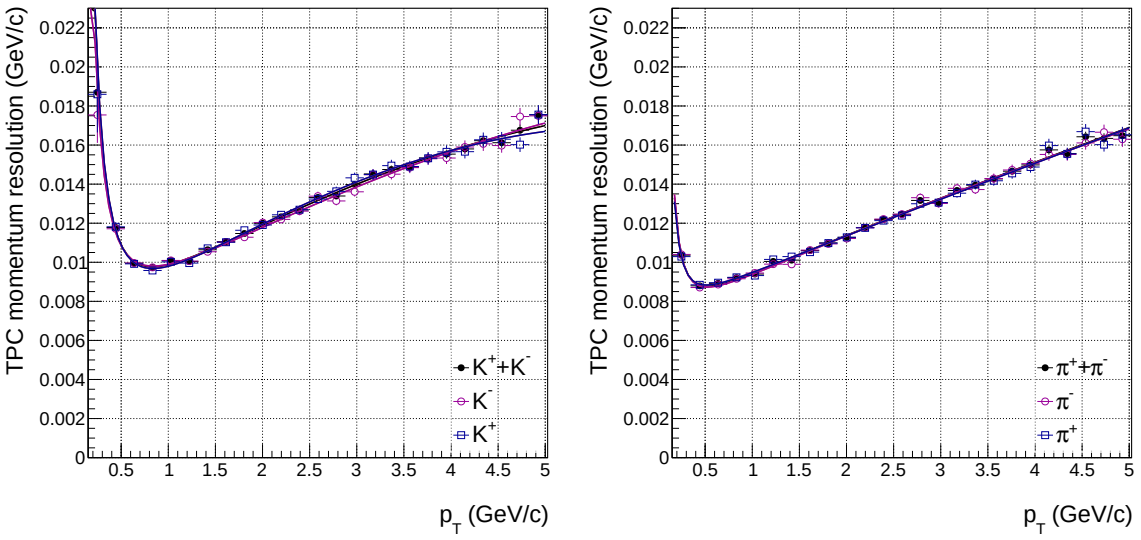

Figure 4.11: TPC and HFT momentum resolution vs. track transverse momentum p_{T} for kaons (left) and pions (right).

4.6.2 TOF matching efficiency

TOF matching efficiency is defined as the probability of a track having any signal (match) in the TOF detector. It is calculated using the recorded events as the ratio of the number of tracks with the TOF signal and all tracks in the given sample. This ratio is calculated separately for K^-, K^+, π^+ and π^-. For tracks used in the main D^0 analysis (nHitsFit > 15, $DCA_{PV} < 1$ cm, HFT tracks), three different TPC identified samples are tested—with $|n\sigma_{TPC}|$ < 1, 2 and 3. Figure 4.12 shows resulting TOF efficiencies. As could be observed, there is no significant difference in the three TPC particle identification cut samples. For the final TOF matching correction, tracks with $|n\sigma_{TPC}| < 1$ are used, to isolate the TOF efficiency from the TPC PID efficiency. However, for p_T between 0.6 and 2 GeV/c, there is a drop caused by hadron contamination in the TPC detector (also observed in the published analysis of D^0 meson in Au+Au collisions), which is worsening particle identification quality. This drop is excluded from the fitting of the TOF matching distributions. Resulting fits are shown in Fig. 4.13 and are further used in the analysis as the TOF matching efficiencies.

4.6.3 Particle identification efficiencies

The TOF and the TPC detectors' particle identification (PID) efficiencies are calculated using the recorded tracks in the same events as those for the central analysis, with an additional requirement to have at least 1 HFT track (to reduce pile-up events). It is essential to isolate samples of "clean" (very high probability of correctly identified) pion and kaon tracks to separate PID efficiency from other detector effects. For this, $K^0_s \to \pi^+\pi^-$ and $\Phi \to K^+K^-$ hadronic decays are used. K^0_s and Φ mesons are reconstructed in the similar way as D^0 meson in the main analysis. Firstly, daughter tracks are selected using the cuts shown in Table 4.2. Then, these tracks are within events combined to $\pi^+\pi^-$ and K^+K^- pairs. Additional topological cuts, shown in Table 4.2, are applied on these pairs. Correct-sign pairs have a total electric charge equal to zero; wrong-sign pairs are the others. Invariant mass distributions of wrong-sign pairs are subtracted from those of correct-sign. Resulting distributions are considered as signal peaks of K^0_s and Φ mesons and are fitted by the sum of Gaussian and linear functions. For further PID efficiency study, pairs with the invariant mass in the $\pm 2\sigma$ region around the fitted Gaussian function mean are used.

The track is used in the final step of the PID efficiency calculation only if its "partner" track in the reconstructed pair pass additional selection criteria to make the pion and the kaon samples even purer. This decision is motivated by the fact that if the $\pi\pi$ (KK) pair passes the topological criteria and if one of the tracks is identified as pion (kaon), there is a high probability that the other track is pion (kaon), too. Three different sets of cuts on the partner track are tested:

- $|n\sigma_{TPC}| < 5$, $\Delta 1/\beta_{TOF} < 0.05$ and $p_T > 0.5$ GeV/c,
- $|n\sigma_{TPC}| < 3$, $\Delta 1/\beta_{TOF} < 0.03$ and $p_T > 0.5$ GeV/c,
- no additional cut on partner the partner track. In this case, both tracks in the pair are further used.

Then, distributions of PID variables ($\Delta 1/\beta_{TOF}$ and $n\sigma_{TPC}$) in multiple tracks p_T intervals are used. In each p_T bin, wrong-sign pairs $\Delta 1/\beta_{TOF}$ distribution is subtracted from the one of correct-sign pairs. The resulting distribution is again fitted by the sum of Gaussian and linear functions. Results of the Gaussian part of the fits are shown in Fig. 4.14. Upper plots show the results for pions, and lower plots are for kaons. The left plots show sigma, and the right

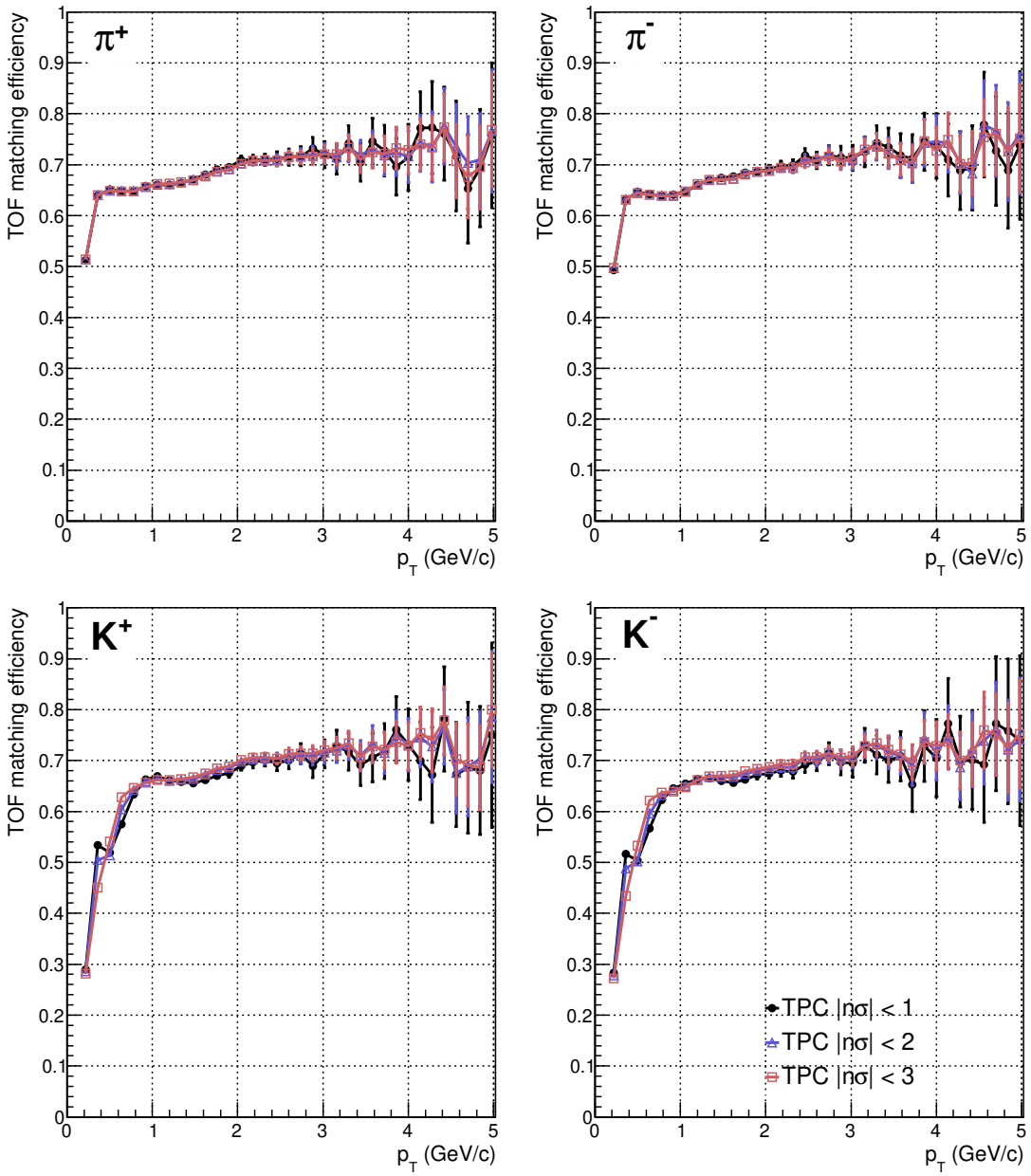

Figure 4.12: The TOF matching efficiency calculated using tracks in the recorded collisions vs. track transverse momentum p_T for three different TPC particle identification cuts. Upper plots show pions, lower plots kaons, left plots are efficiencies for positive and right for negative tracks.

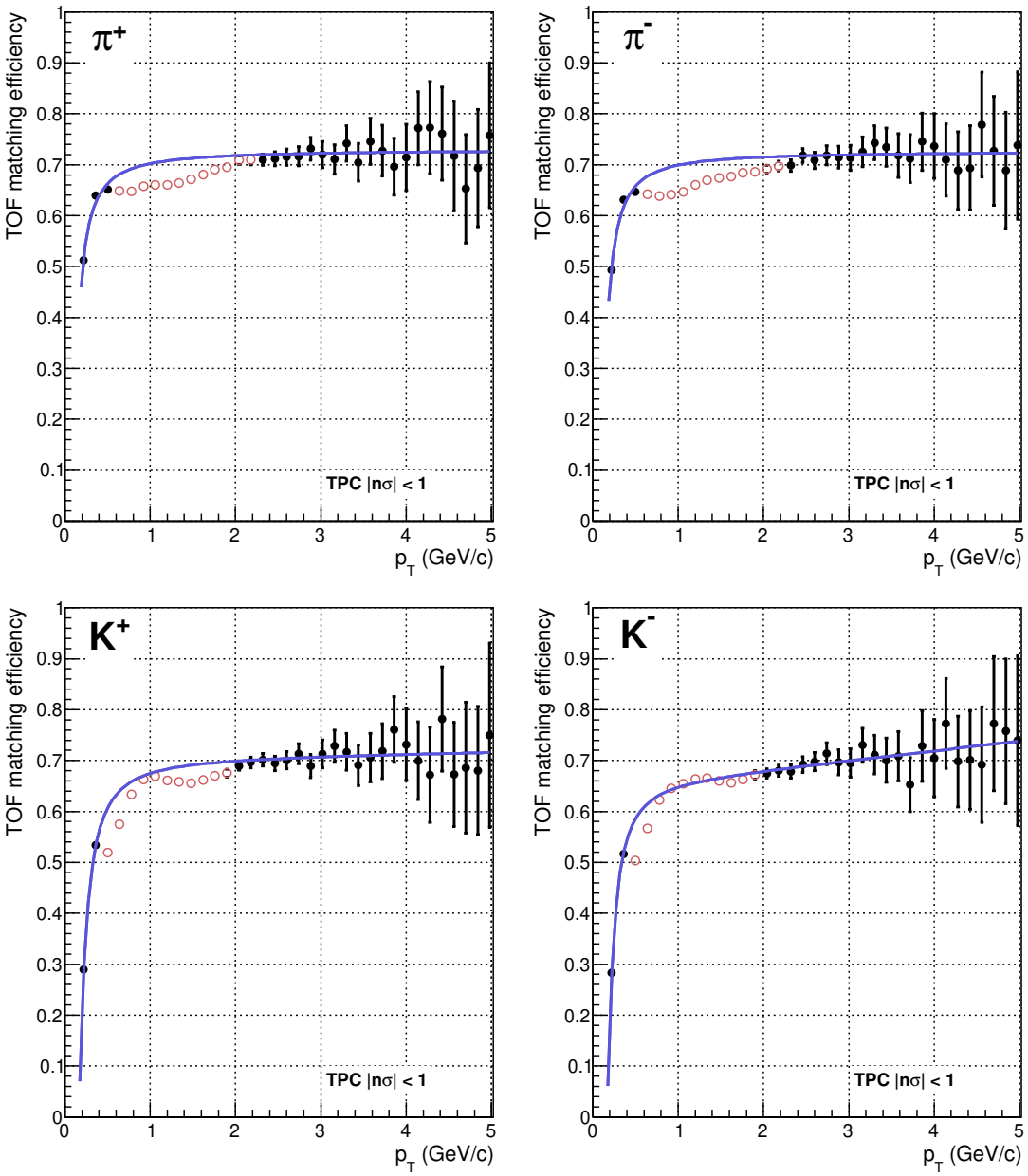

Figure 4.13: Polynomial fits of the transverse momentum (p_{T}) dependent TOF matching efficiencies, for the tracks identified in the TPC with cut $n\sigma < 1$. Only black points are considered in the fits, red circles show region with the strong contamination in the TPC. Upper plots show pions, lower plots kaons, left plots are efficiencies for positive and right for negative tracks.

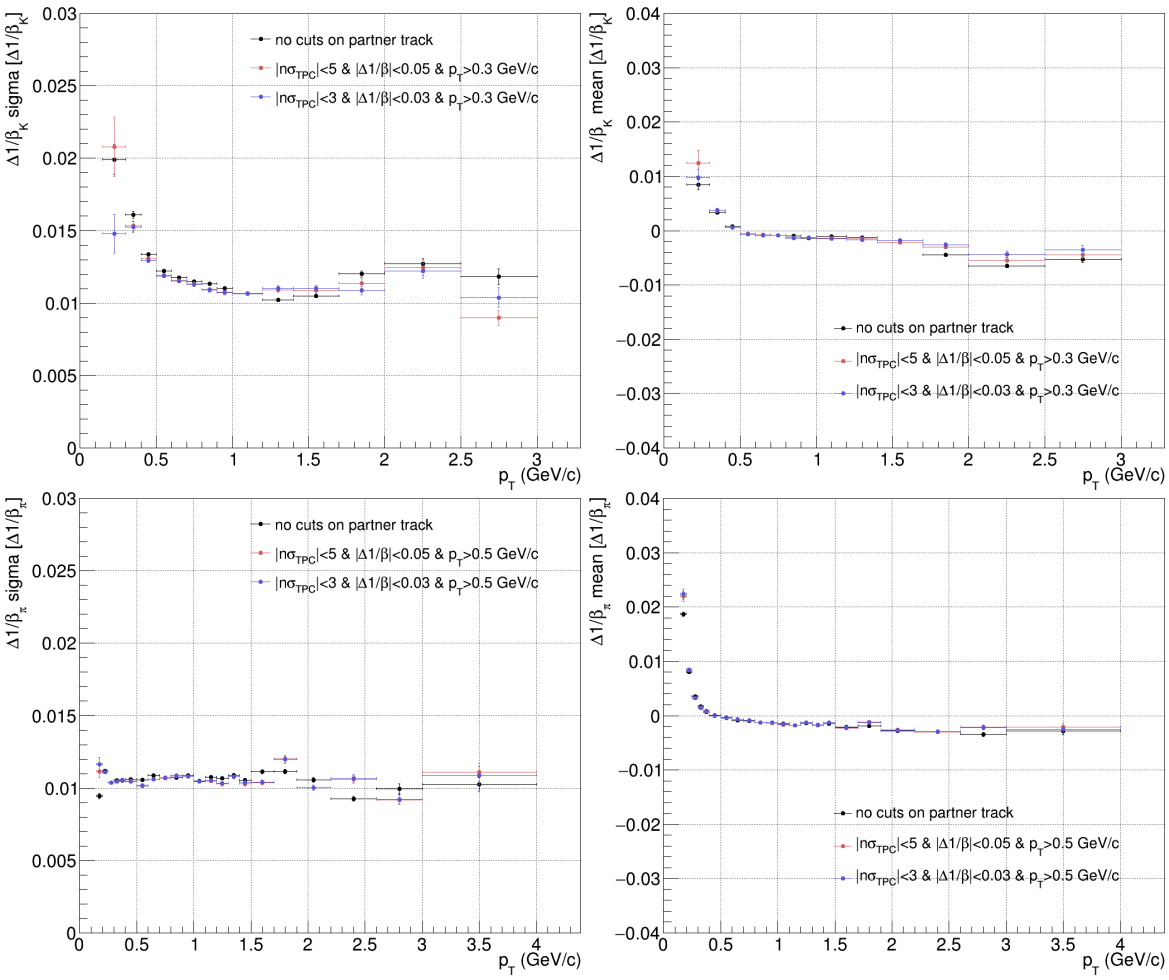

Figure 4.14: Sigma and mean parameters from the Gaussian fits of the TOF PID variable $\Delta 1/\beta_{\mathrm{TOF}}$ vs. track transverse momentum p_{T}, for various cuts on the partner track in the $\pi\pi$ or KK pairs. The upper plots are for kaons, the lower for pions. Left plots show resulting sigmas, right plots display means of the Gaussians.

plots display the mean of Gaussians. PID efficiency is calculated as the ratio of the integral of the fitted function in the PID interval used in the analysis ($-0.03 < \Delta 1/\beta_{\mathrm{TOF}} < 0.03$) to the total integral of the function. The same procedure is done to calculate TPC PID efficiency. Results of the corresponding Gaussian fits of $n\sigma_{\mathrm{TPC}}$ distributions are shown in Fig. 4.15.

Final PID efficiencies are shown in Fig. 4.16 for the TOF and Fig. 4.17 for the TPC. The left column shows efficiencies for three different partner track cuts. Figures in the right column show efficiencies and their fits for the selected data sample (with the most severe cuts on the partner track). These fits are used as the PID efficiency, separately for kaons and pions in the TOF and the TPC.

4.6.4 Reconstruction efficiency

Total reconstruction efficiency is the combined efficiency of the detector acceptance, HFT reconstruction, TPC reconstruction, particle identification, and topological reconstruction efficiencies. These efficiencies are combined in the FastSim (Sec. 4.2.1) to obtain $p_{\mathrm{T,D^0}}$-dependent

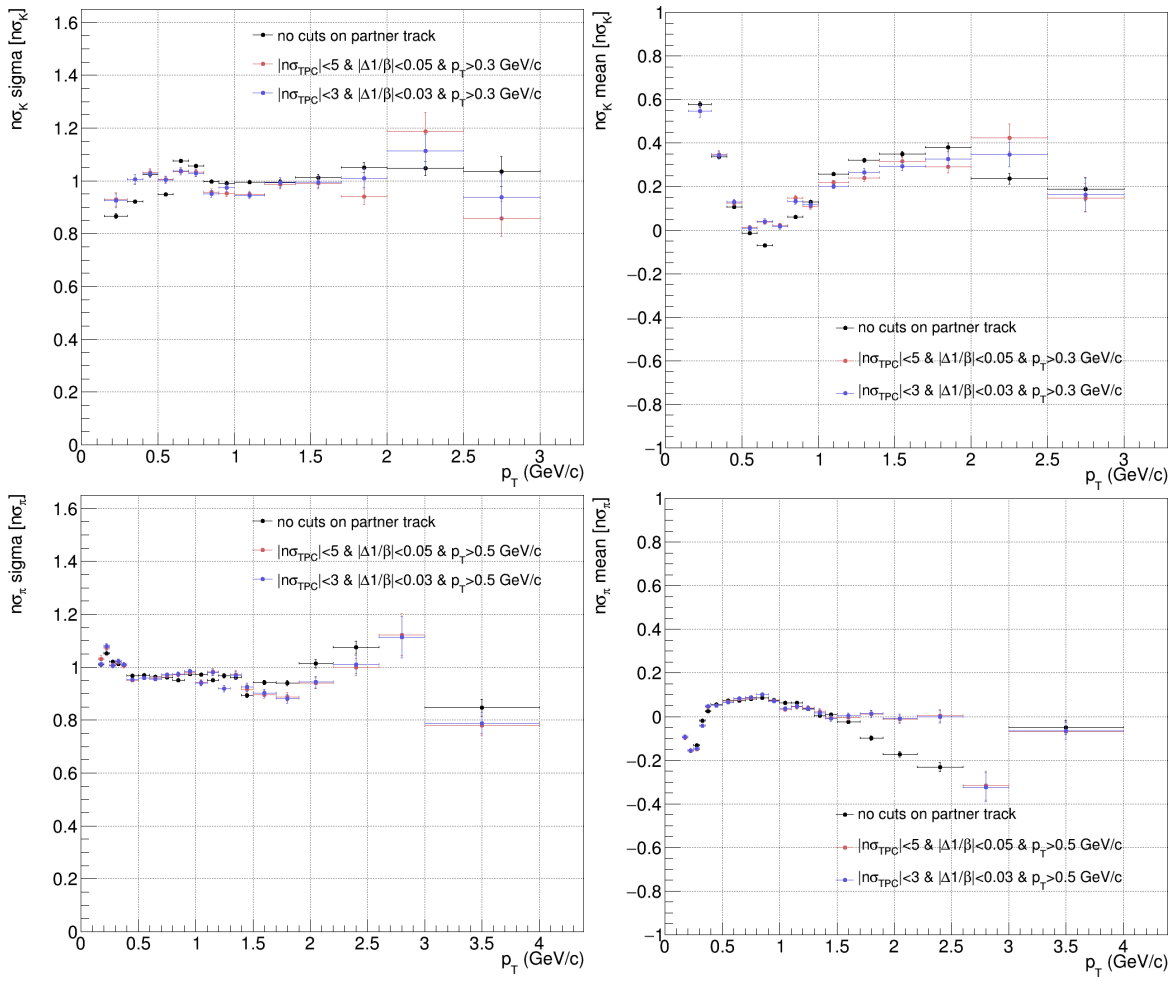

Figure 4.15: Sigma and mean parameters from the Gaussian fits of the TPC PID variable $n\sigma$ vs. track transverse momentum p_{T}, for various cuts on the partner track in the $\pi\pi$ or KK pairs. The upper plots are for kaons, the lower for pions. Left plots show resulting sigmas, right plots display means of the Gaussians.

Table 4.2: Cuts on topological variables used for Φ and $\mathrm{K}^0_{\mathrm{s}}$ meson reconstruction. Topological variables are equivalent to those shown in Fig. 1.6 and described in Sec. 4.5.

Reconstructed decay	$\Phi \to \mathrm{K}^+\mathrm{K}^-$		$\mathrm{K}^0_{\mathrm{s}} \to \pi^+\pi^-$	
Variable	Min.	Max.	Min.	Max.
$\mathrm{DCA}_{\mathrm{K}/\pi}$ [cm]	0	1	0.008	1
Pair p_{T} [GeV/c]	0.2	10	0.5	-
$\mathrm{DCA}_{\mathrm{daughters}}$ [cm]	0	1	0	0.6
$\cos\theta$ [-]	0.85	1	0.7	1
$\mathrm{DCA}_{\Phi/\mathrm{K}^0_{\mathrm{s}}}$ [cm]	0	1	0	0.9
Decay length [cm]	0	25	0.5	6

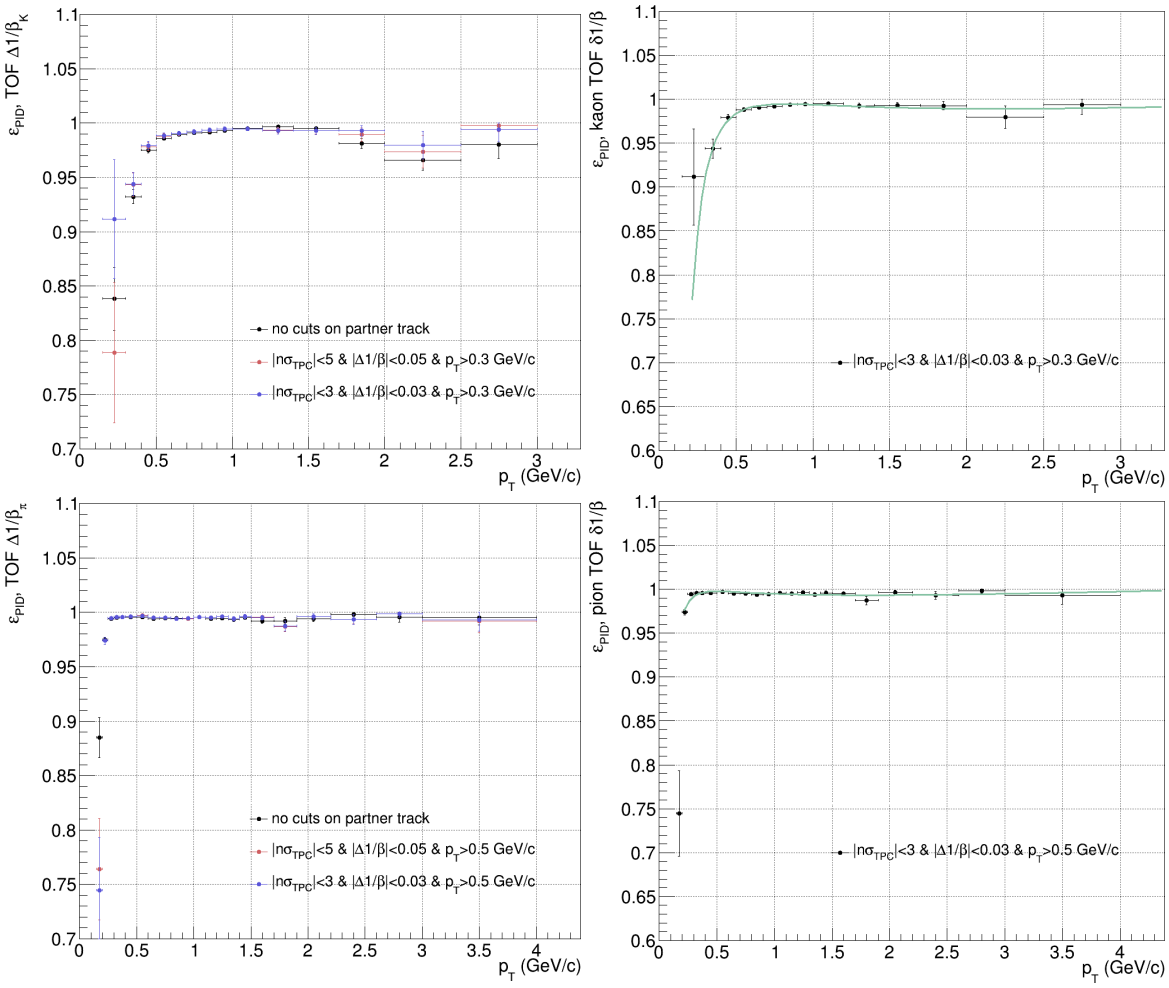

Figure 4.16: The TOF particle identification efficiencies vs. track transverse momentum p_{T}. The upper plots are for kaons, the lower for pions. The left plots results for various cuts on the partner track in the construction of the clean sample of pions or kaons. The right plots show the polynomial fits for the chosen track sample.

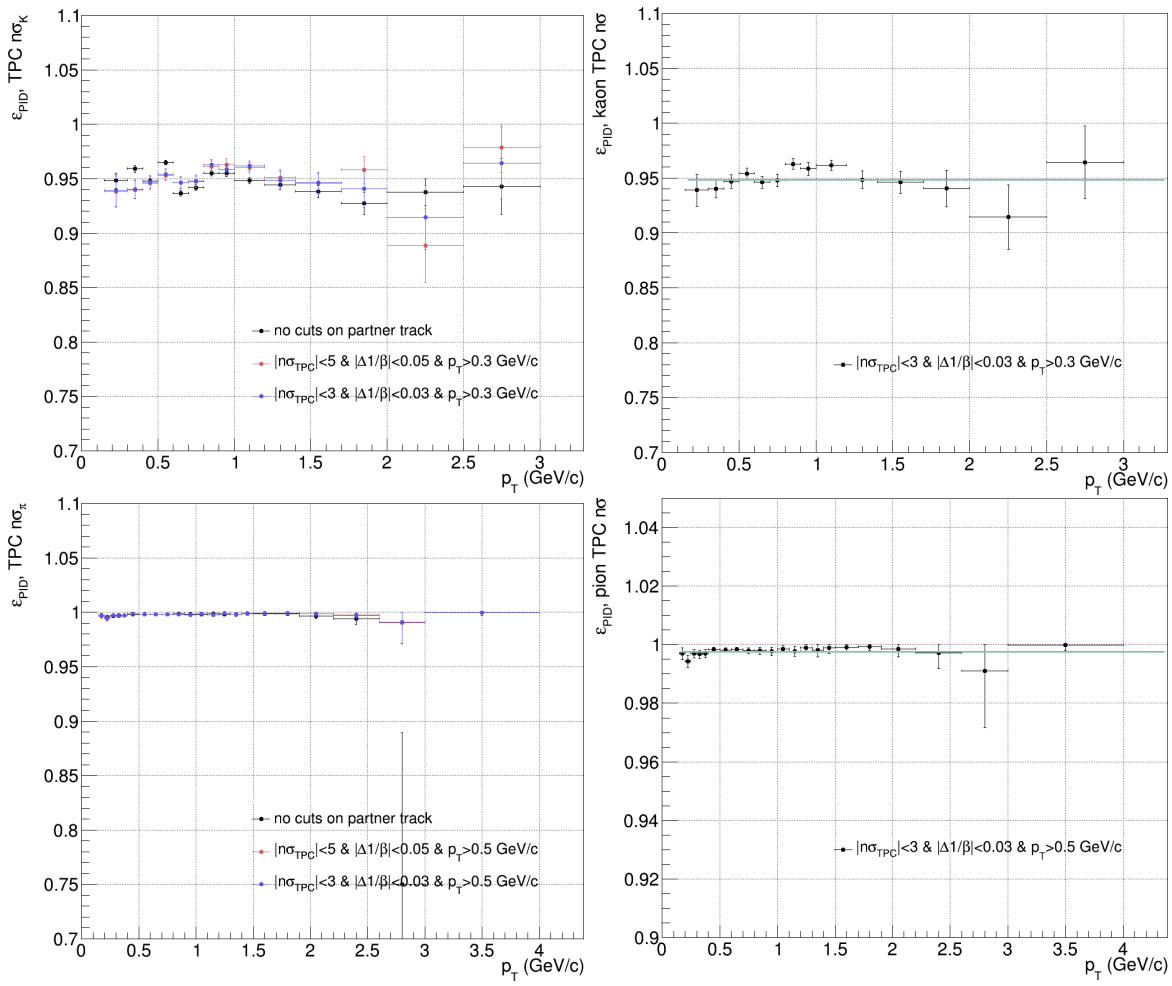

Figure 4.17: The TPC particle identification efficiencies vs. track transverse momentum p_{T}. The upper plots are for kaons, the lower for pions. The left plots results for various cuts on the partner track in the construction of the clean sample of pions or kaons. The right plots show the polynomial fits for the chosen track sample.

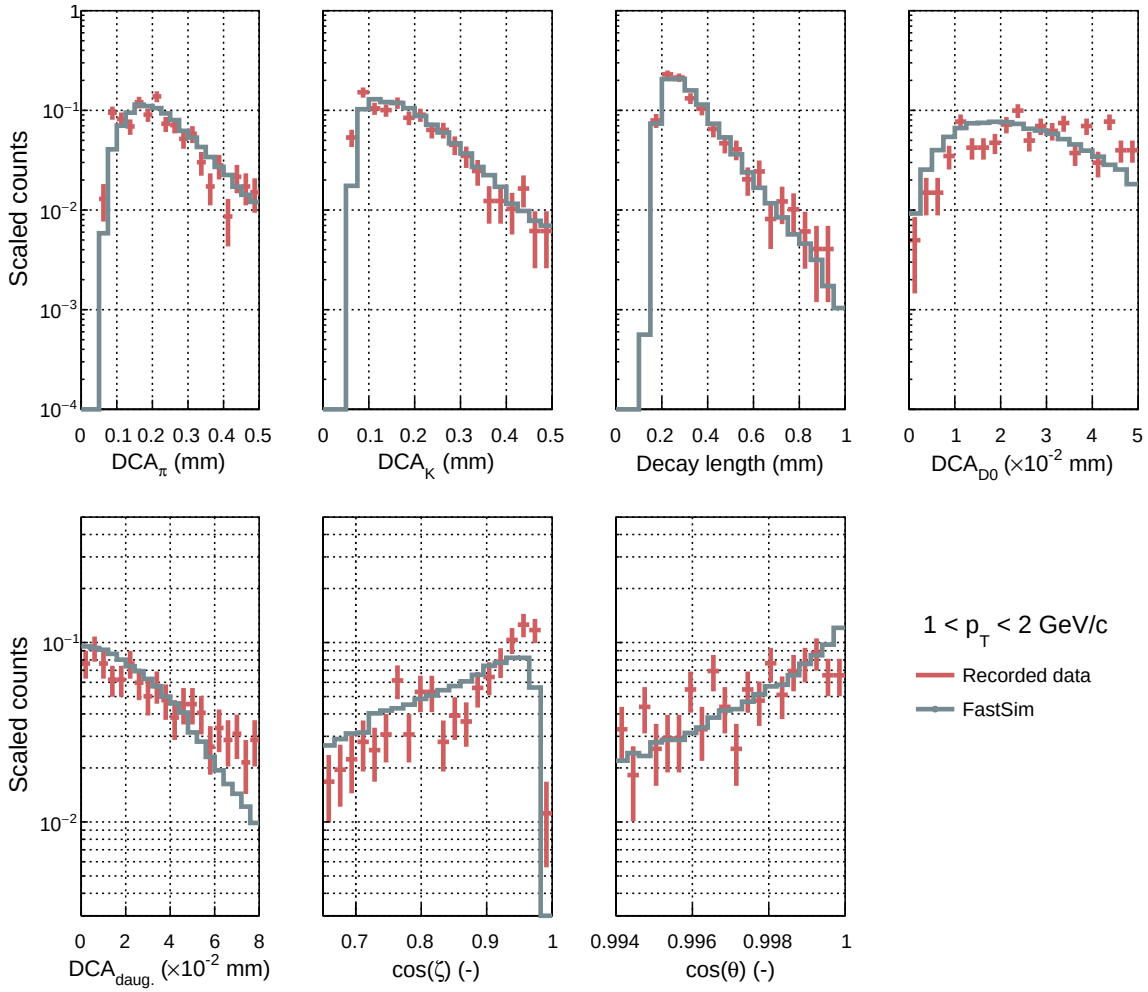

Figure 4.18: Distributions of topological variables for Kπ pairs with invariant mass 1.7–2 GeV/c^2, transverse momentum p_{T} 1–2 GeV/c after application of precuts shown in Table 4.1 and analysis BDT response cut.

D^0 reconstruction efficiency. Distributions of topological variables after application of reconstruction cuts on Kπ pairs in the recorded data and in the FastSim are compared in Fig. 4.18 for $p_{\mathrm{T,K\pi}}$ 1–2 GeV/c. Other studied $p_{\mathrm{T,K\pi}}$ intervals are in App. A. As can be seen, the FastSim successfully simulates the D^0 meson decay.

Detector acceptance is calculated as the ratio of the number of simulated D^0 mesons with reconstructed $|y| < 1$ to the number of D^0 mesons with simulated $|y| < 1$. HFT efficiency is substituted by the HFT ratio from reconstructed data, as described in Sec. 4.2.1. TPC reconstruction efficiency is described in Sec. 4.6.1, and PID efficiencies are explained in Sec. 4.6.3. Topological efficiency is the ratio of the number of simulated D^0 mesons that pass the topological precuts and the BDT response cut selected for the given $p_{\mathrm{T,D^0}}$ interval. A summary of these efficiencies and their gradual combinations are shown in Fig. 4.19. Total D^0 meson reconstruction efficiency in three analyzed $p_{\mathrm{T,D^0}}$ intervals is displayed with black points and lines.

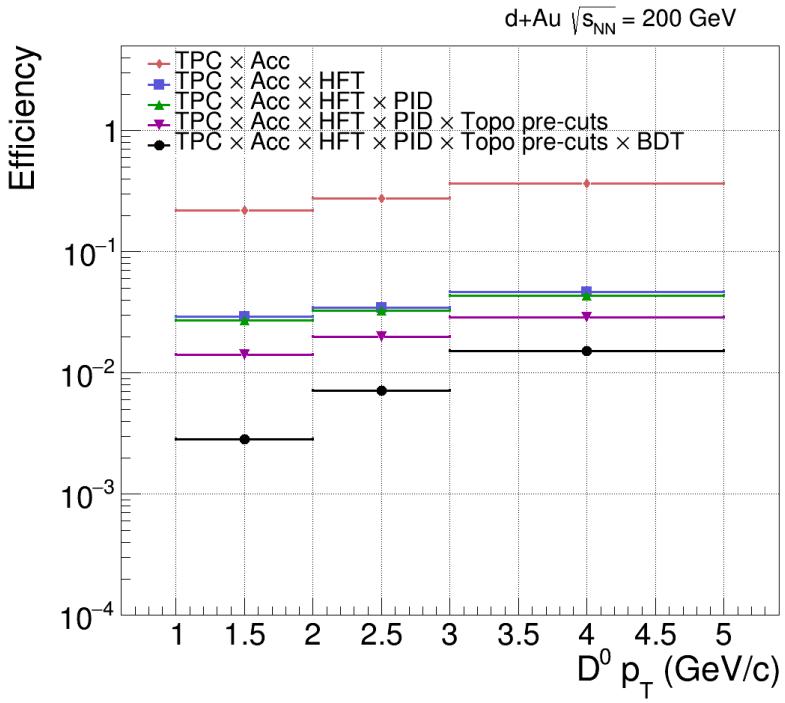

Figure 4.19: D^0 meson reconstruction efficiency vs. transverse momentum p_T. Gradual combinations of the corrections are shown.

4.6.5 Double counting correction

In the analysis of D^0 mesons, all selected kaons and pions in the event are combined into $K\pi$ pairs that are further classified as signal or background. Some reconstructed tracks fulfill PID criteria for both pions and kaons. Pair combinations are constructed from two independently created sets of tracks (one set identified as pions, the other as kaons). If $K\pi$ pair contains pion, which passes PID cuts for kaons as well, and kaon, which satisfies PID cuts for pions, such pair is calculated (analyzed) twice. If the invariant mass of this pair happens to be around the D^0 meson invariant mass, then it influences the measured signal.

This PID misidentification effect is studied with $\pi\pi$ and KK pairs from meson decay described in Sec. 4.6.3. Pairs that meet topological criteria and have invariant mass in $\pm 2\sigma$ region around fitted Gaussian function mean are tested for TPC and TOF double identification. To evaluate this correction for pions in the TOF, additional analysis PID cut ($\Delta 1/\beta^{\pi}_{\mathrm{TOF}} < 0.03$) is applied on pairs from reconstructed K^0_s decay. Then, the $\Delta 1/\beta^{\mathrm{K}}_{\mathrm{TOF}}$ distribution of wrong-sign pairs is subtracted from the distribution of the correct-sign pairs, and the Gaussian function fits the resulting distribution. Fitted distributions for multiple track p_T intervals are shown in Fig. 4.20 lower right. Vertical lines show the analysis cut on kaons, so all the tracks within these two lines are identified as both kaons and pions in the TOF.

The equivalent procedure is done for kaons in the TOF and pions and kaons in the TPC. The resulting fits are shown in Fig. 4.20. Fit results are shown in Fig. 4.21, where the upper row shows sigmas and the lower row means from Gaussian fits vs. track p_T. These distributions are then fitted by polynomial functions. The results for the TPC are fitted in track p_T interval from 0.3 to 2 GeV/c; for the TOF, it is for 0.4 to 3 GeV/c. For track p_T higher than the

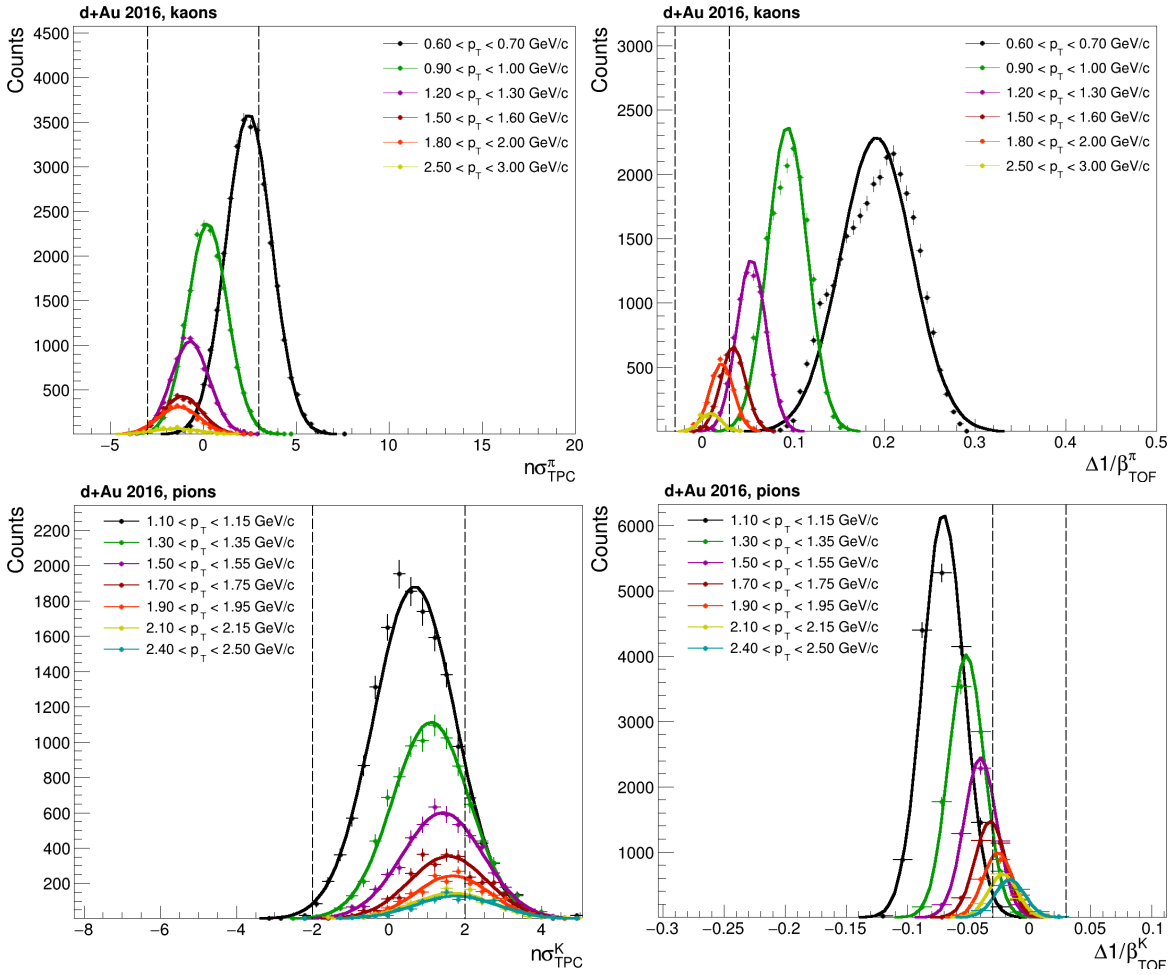

Figure 4.20: Distributions of particle identification variables, $\Delta 1/\beta_{\mathrm{TOF}}$ and $n\sigma_{\mathrm{TPC}}$, in multiple track p_{T} intervals. Pion identification variables ($\Delta 1/\beta^{\pi}_{\mathrm{TOF}}$ and $n\sigma^{\pi}_{\mathrm{TPC}}$) are projected from clean sample of kaons. Kaon identification variables ($\Delta 1/\beta^{\mathrm{K}}_{\mathrm{TOF}}$ and $n\sigma^{\mathrm{K}}_{\mathrm{TPC}}$) are projected from clean sample of pions. Upper plots show results projected from clean sample of kaons, lower are for clean pions. Vertical lines show the variable cuts in the main D^0 meson analysis.

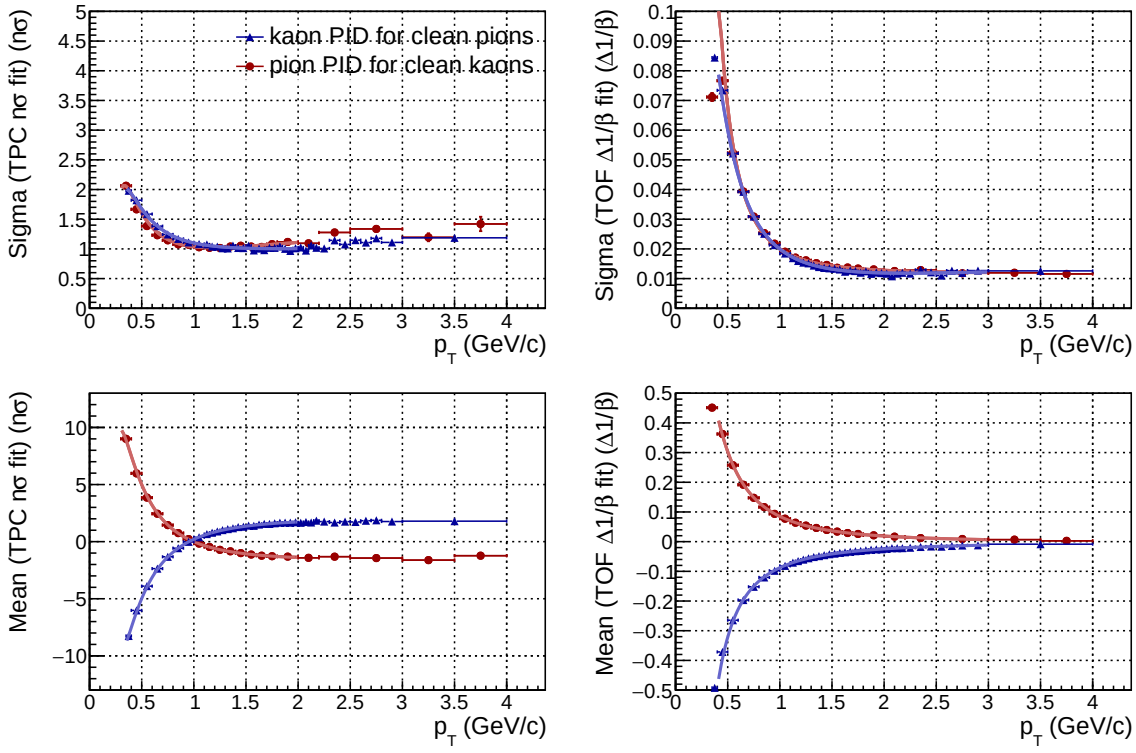

Figure 4.21: Results of the Gaussian fits of the particle identification variables $n\sigma_{\mathrm{TPC}}$ (left column) and $\Delta 1/\beta_{\mathrm{TOF}}$ (right column) vs. track p_{T}. Blue points show results from fitting the variables for kaon identification in the sample of clean pions, red points are for pion identification in the sample of kaons.

maximum of fitted intervals, values in this maximum are used as a constant function.

Gaussian functions with sigmas and means from polynomial fits are constructed using these fits. For multiple track p_{T}, the integral of the Gaussian function within analysis PID cut (also shown by horizontal lines in Fig. 4.20) is divided by the total integral of this function to obtain single track misidentification probability, shown in Fig. 4.22 left. These results are combined with the TOF matching efficiency (Fig. 4.13) to obtain total misidentification probability for kaons and pions identified by the TPC and the hybrid TOF method. Finally, to obtain correction for D^0, single track efficiencies are combined with decay kinematics from FastSim (Sec. 4.2.1). For pairs coming from simulated D^0 meson decay, pions and kaons are tagged as misidentified according to the efficiency shown in Fig. 4.24 left. Figure Fig. 4.22 right shows total resulting misidentification probability for D^0 meson daughter tracks. If both tracks are tagged as misidentified, the invariant mass of $\mathrm{K}\pi$ pair is calculated additionally with swapped invariant masses of pion and kaon. Distributions of such misidentified pairs and the clean signals are shown in Fig. 4.23. These distributions are fitted by Gaussians to obtain their σ and mean. Double counting correction is calculated as the ratio of the count of misidentified to the sum of misidentified and signal pairs in the same invariant mass interval. These estimates are done using the bin-counting method in $\pm 2.5\sigma$, $\pm 3\sigma$, and $\pm 3.5\sigma$ regions around the fitted Gaussian mean. Resulting efficiencies vs. D^0 meson p_{T} are shown in Fig. 4.24. As the final correction to the data, counting in $\pm 3\sigma$ region around D^0 meson invariant mass peaks is used. The difference between this efficiency to the other efficiencies shown in Fig. 4.24 is used as the systematic uncertainty of the method. Raw yield Y is corrected by the displayed double

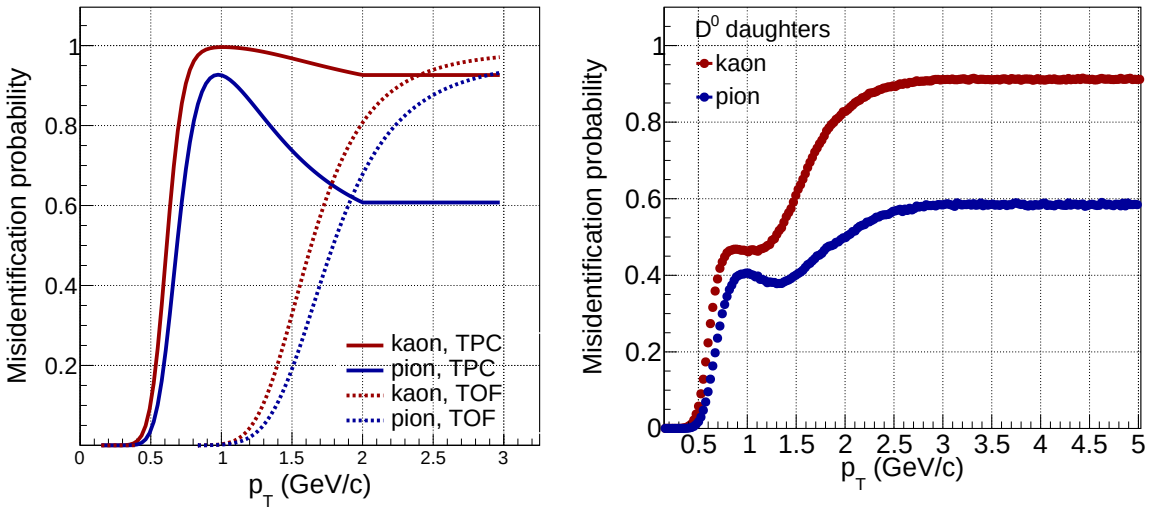

Figure 4.22: Misidentification probabilities for kaons and pions vs. track p_{T}. The left plot displays the single-particle misidentification probabilities coming from the TPC and TOF particle identification methods. After combining them with the TOF matching efficiency and convoluting them to the D^0 meson decay simulation, probabilities for D^0 meson daughter tracks are obtained and displayed on the right figure.

counting ratio r_{dc} as

$$Y_{\mathrm{corr}} = Y(1 - r_{\mathrm{dc}}). \tag{4.3}$$

4.6.6 Vertex reconstruction efficiency

Due to the relatively low number of tracks in d+Au events, it is necessary to consider the effect of lower vertex reconstruction efficiency. Especially for events that contain heavy mesons (such as D^0), the reconstructed vertex might be "pulled" toward the daughter tracks coming from decays of such mesons. In the FastSim (described in Sec. 4.2.1), the inputs from data that partially consider this are DCA distributions of tracks. However, these also contain a contribution from the track reconstruction resolution and are created using all events since, in the recorded data, it is unknown whether D^0 meson is created in the event. To separate the effect of the vertex reconstruction uncertainty, full-event simulation (HIJING, described in Sec. 4.2.2) with the requirement to have at least one simulated D^0 meson in the event and primary vertex placed ± 6 cm in beam direction around the center of the detector is used. Events that pass the same cuts as those in the central D^0 analysis are used. DCA and HFT ratio distributions from these simulated events are extracted and fed to the FastSim. Reconstruction efficiency from this FastSim setup is compared to the one calculated in the full-event simulation.

Figure 4.25 shows the reconstruction efficiency comparison for the two simulations. The left plot shows the combined efficiencies for detector acceptance, TPC and HFT reconstruction, particle identification, and topological precuts. It can be seen that, at this point, there is no significant vertex reconstruction uncertainty effect. However, as shown in the right plot, after applying the BDT response cut, the efficiencies for the two simulations diverge. The effect of the vertex resolution causes the differences from the unity in the ratio on the lower plot.

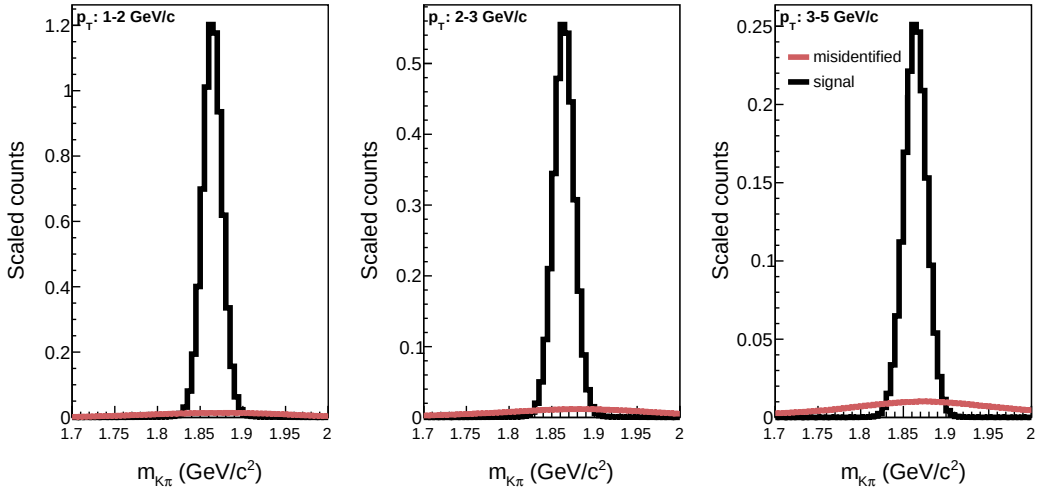

Figure 4.23: Invariant mass $m_{\mathrm{K}\pi}$ distributions for correct-sign signal Kπ pairs and for Kπ pairs made up from misidentified kaons and pions, for three studied D^0 transverse momentum p_{T} intervals.

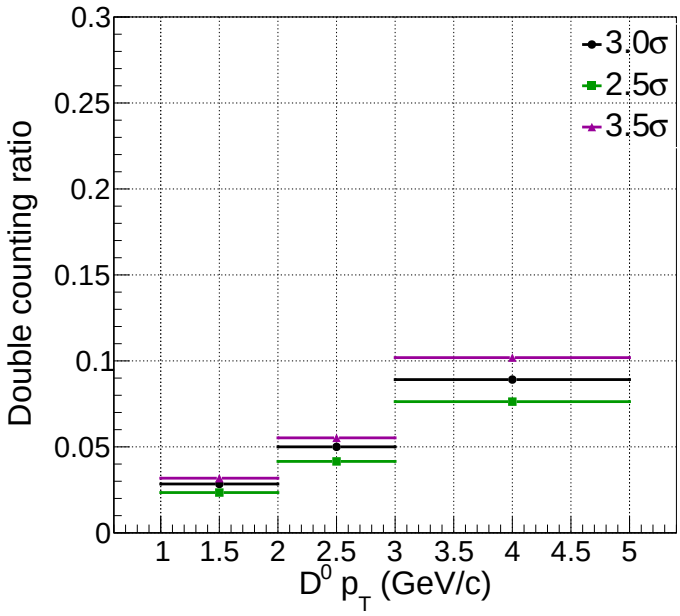

Figure 4.24: Double counting ratio caused by the tracks identified as both kaons and pions vs. D^0 transverse momentum p_{T} for three different bin-counting intervals, used to count the number of misidentified and signal pairs in the D^0 meson signal region.

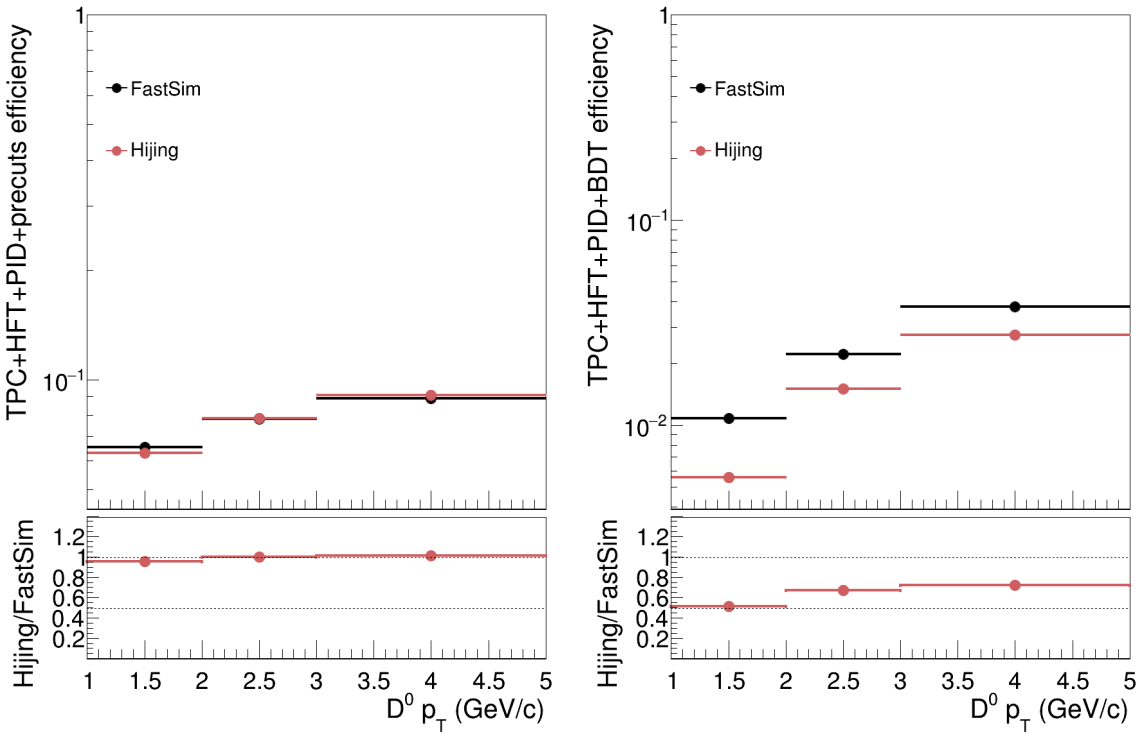

Figure 4.25: The combined reconstruction efficiencies calculated from the FastSim and the full-event HIJING simulations and their ratio as a function of D^0 meson transverse momentum p_T. The right plot shows the total reconstruction efficiency; the left shows the reconstruction efficiency without considering the BDT response cut. The ratio on the bottom of the right plot is the correction for the vertex reconstruction uncertainty.

This p_T-dependent ratio is used to correct D^0 meson spectra. Its statistical uncertainty is considered as vertex reconstruction systematic uncertainty. These results are consistent with the efficiencies calculated for D^0 mesons in peripheral Au+Au collisions (Fig. 17 in Ref. [57]).

4.6.7 Trigger bias correction

Events, where D^0 meson is created, have different spatial (η) distribution of tracks, typically higher multiplicity or more energy in the mid-rapidity region. These differences are caused by the creation of heavy mesons in the initial hard scatterings. These effects influence vertex finding efficiencies and signals in the detectors and thus trigger information. Events with D^0 meson are expected to be more likely to pass event selection criteria than all minimum-bias (MB) events. However, we aim to calculate the production of D^0 meson in the MB events. The described effect is called trigger bias and is evaluated using the full-event simulations described in Sec. 4.2.2.

Figure 4.26 shows the η distributions of tracks in simulated HIJING MB events, then events with at least one simulated D^0 meson and events with one simulated D^0 meson with the additional requirement on vertex V_z position. It can be seen that tracks with D^0 meson have higher multiplicity in the central region. Vertical lines show the acceptance region of the VPD detector, which is used as a trigger in the D^0 analysis.

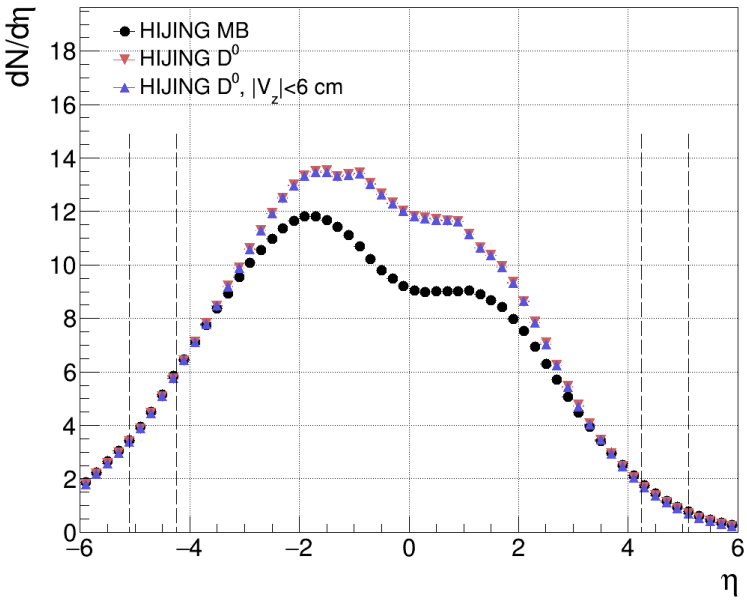

Figure 4.26: Pseudorapidity η distributions of tracks in three different full-event HIJING simulation setups—minimum bias (MB) events, events with at least one D^0 meson, and events with at least one D^0 meson and vertex reconstructed less than 6 cm from the detector centre in the beam direction. Vertical lines show the acceptance of the VPD detector.

In the analysis of the recorded data, event have to pass the criteria described in Sec. 4.3 to be used. In the trigger bias study, equivalent cuts are tested:

- vertex is reconstructed, that means:
  - reconstructed vertex position in the beam direction V_z less than 6 cm from the center of the STAR,
  - difference between simulated and reconstructed vertex position in detector x, y and z directions less than 1.5 cm,
- BBC rate $<$ 900 kHz (for higher event rates, HFT detector is turned off in order to protect electronics),
- hit in both VPD East and VPD West detectors.

In what follows, events with D^0 meson are those, where:

- D^0 daughters have simulated $|\eta| < 1$ (in order to be inside the TPC acceptance),
- D^0 daughters have simulated $p_T > 0.15$ GeV/c,
- D^0 simulated rapidity is $|y| < 1$.

Figure 4.27 shows efficiencies of used event cuts vs. BBC rate for MB events (left) and for events with D^0 (right). As it can be observed, vertex efficiency is smaller for higher BBC rate, thus higher collision rate. However, there is no significant difference in the shape for MB and D^0 events, thus further calculations does not depend on the BBC rate.

The efficiencies for described event cuts are show in Fig. 4.28 left, for both event classes. The final event reconstruction efficiency is shown as "Good event", and it is 0.091 ± 0.001 for MB and 0.115 ± 0.001 for D^0 events. Total trigger bias is the ratio of these two efficiencies. In Fig. 4.28 right, trigger bias is shown for analyzed p_{T,D^0} bins. This efficiency is calculated

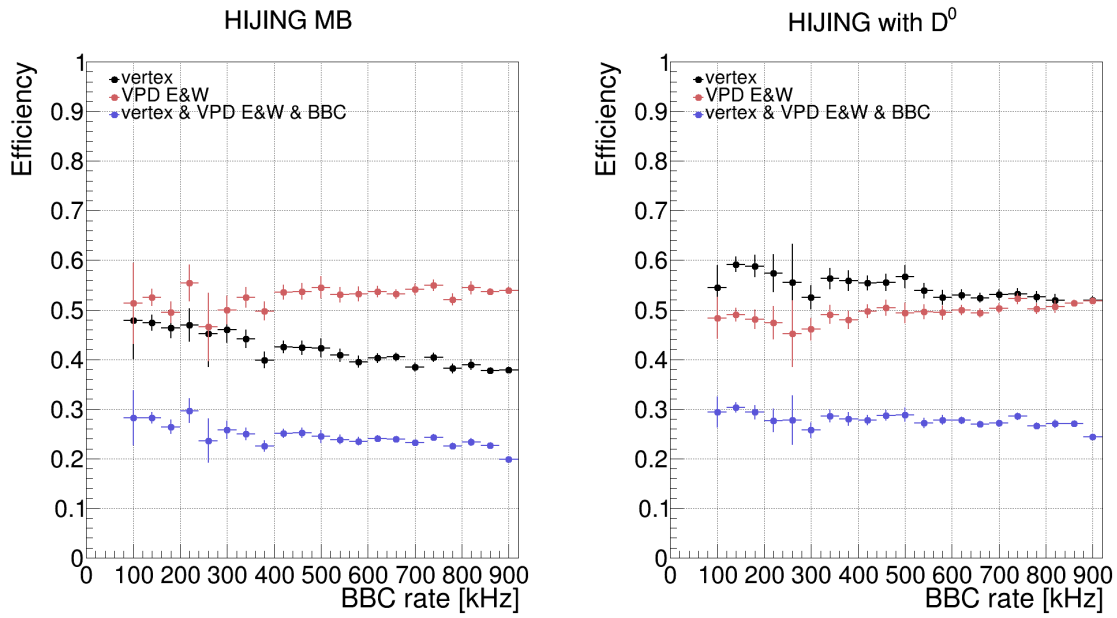

Figure 4.27: Efficiency of event selection vs. BBC rate measured in the event. The total vertex reconstruction, the VPD trigger (hit in both VPD East and West), and the total event efficiencies are compared. Left plot shows results for simulated HIJING minimum-bias events, the right is for HIJING events with at least one D^0 meson reconstructed.

as the ratio of p_{T,D^0}-dependent efficiency in D^0 events and the p_{T,D^0}-constant value of event reconstruction efficiency in MB collisions. This is used as another correction of D^0 meson raw yield and its statistical error is one of the systematic uncertainties.

4.7 Systematic uncertainty

4.7.1 BDT response cut variation

The stability of the BDT response cut is tested by its variation within some range of the signal efficiency output from the BDT training. Figure 4.29 shows the distributions of signal efficiency vs. BDT response cuts for studied $p_{T,K\pi}$ intervals. Red vertical lines show the default BDT cuts used in the analysis, and black lines show BDT cuts where the efficiency is 50 % and 150 % of the default efficiency. Then, D^0 meson invariant yield is calculated for all the points between two black vertical lines using the same calculation as the default cut in the primary analysis. Results are shown in Fig. 4.30, and it could be observed that the results are stable and there are no significant differences compared to the default invariant yield (shown again with red vertical line). Figure 4.31 shows the differences between the individual invariant yields resulting from the efficiency cut variation and the default invariant yield. The purple horizontal line shows these differences' root mean square (RMS) and is used as the BDT reconstruction systematic uncertainty.

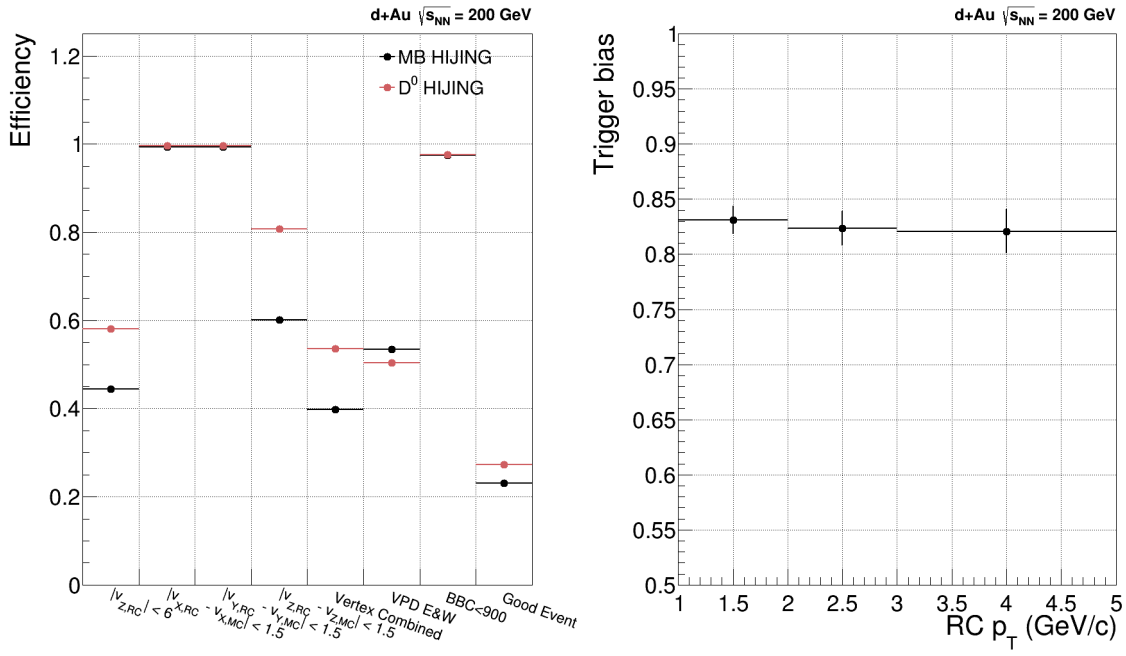

Figure 4.28: Left: Efficiencies of event cuts compared for HIJING simulated minimum-bias events and for events with at least one reconstructed D^0 meson. From left to right, the cuts are: vertex position in the beam direction less than 6 cm from the detector center, distance between reconstructed (RC) and simulated (MC) vertex in x direction less than 1.5 cm, distance between RC and MC vertex in y less than 1.5 cm, distance between RC and MC vertex in z less than 1.5 cm, total vertex reconstruction, the VPD trigger, BBC rate smaller than 900 kHz and total event efficiency. Right: Trigger bias efficiency vs. reconstructed D^0 meson transverse momentum p_T.

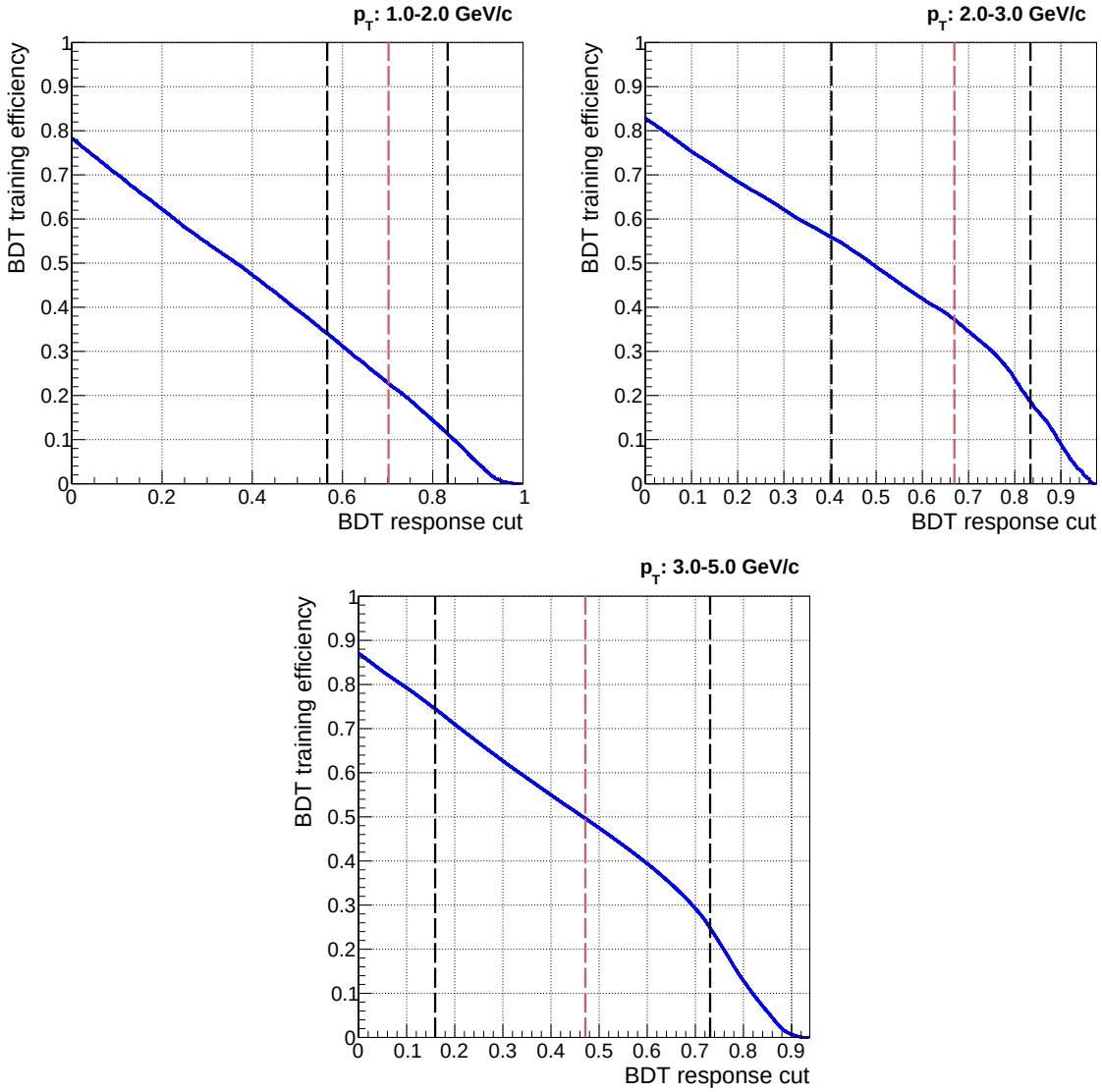

Figure 4.29: Signal efficiency from the BDT training for various BDT response cuts in the studied D^0 meson transverse momentum p_T intervals. The red vertical line shows the BDT cut used in the final analysis, and the black lines show the interval where efficiency is 50–150 % from the final one.

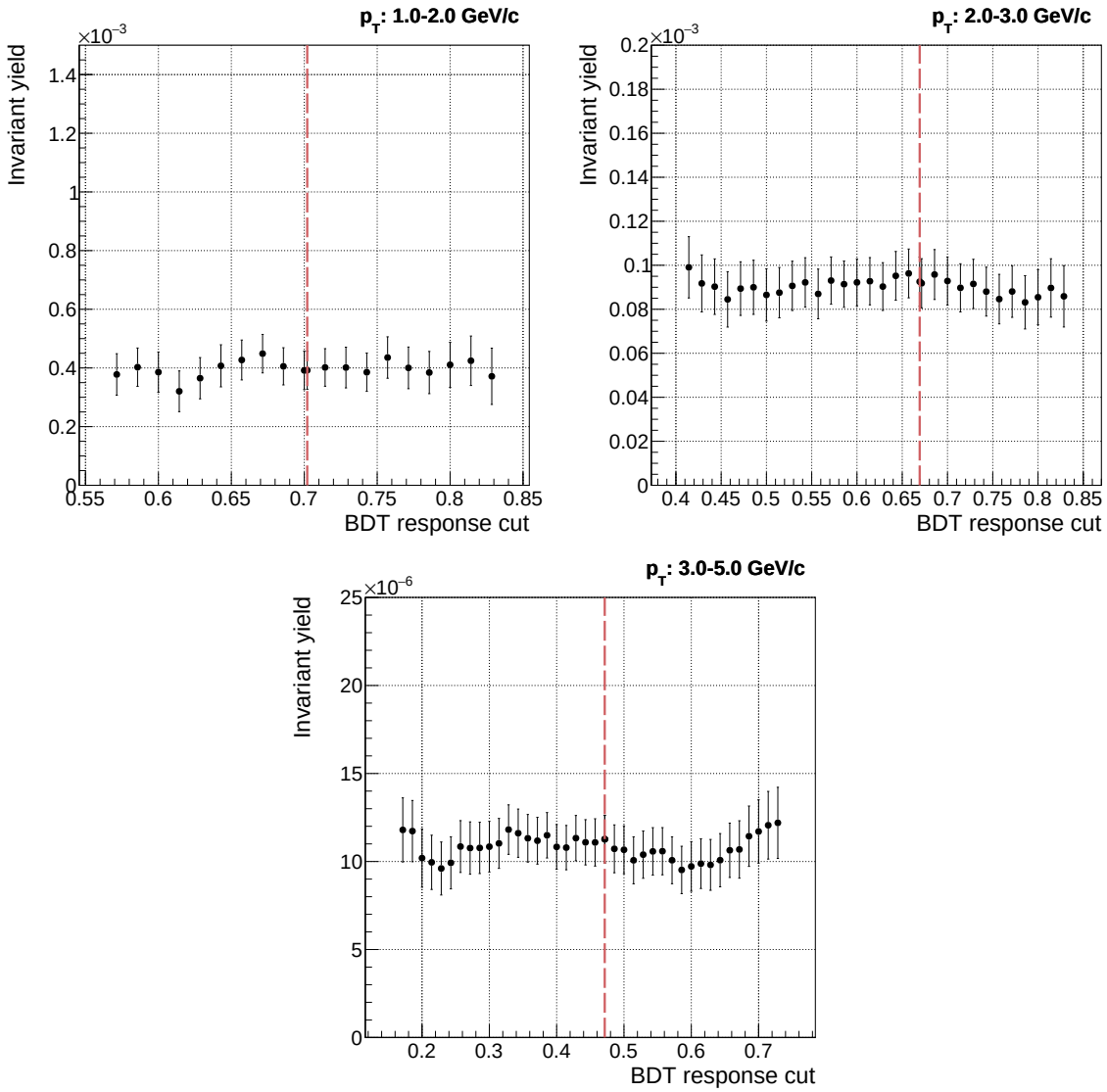

Figure 4.30: D^0 meson invariant yield for various cuts on the BDT response and for the studied D^0 transverse momentum p_T intervals. The red vertical line shows the final analysis BDT cut.

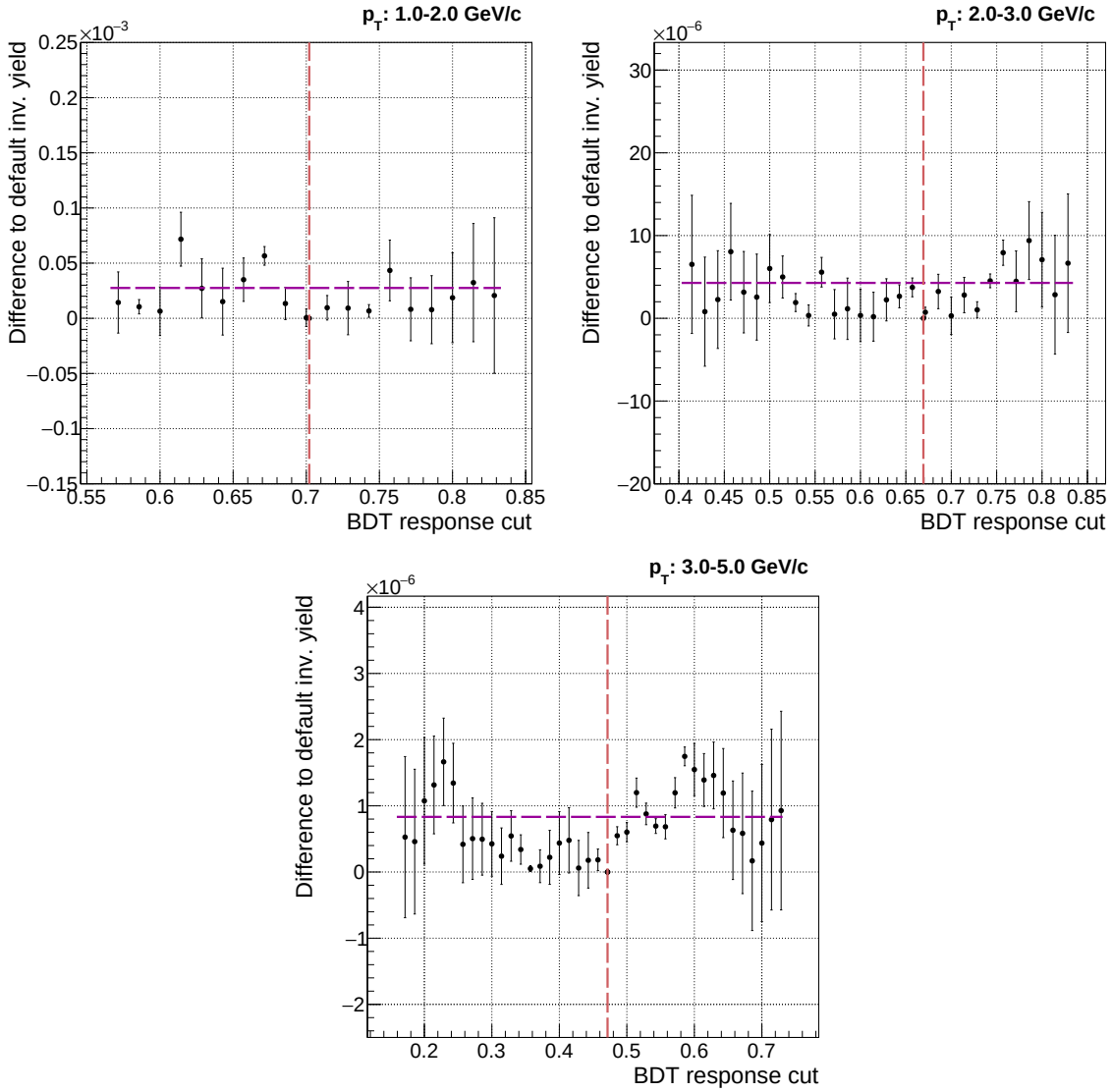

Figure 4.31: Difference of the invariant yields resulting from various BDT response cuts and the default invariant yield, for the studied D^0 transverse momentum p_T intervals. The red vertical line shows the final analysis BDT cut. The purple horizontal line shows the root mean square of the shown values.

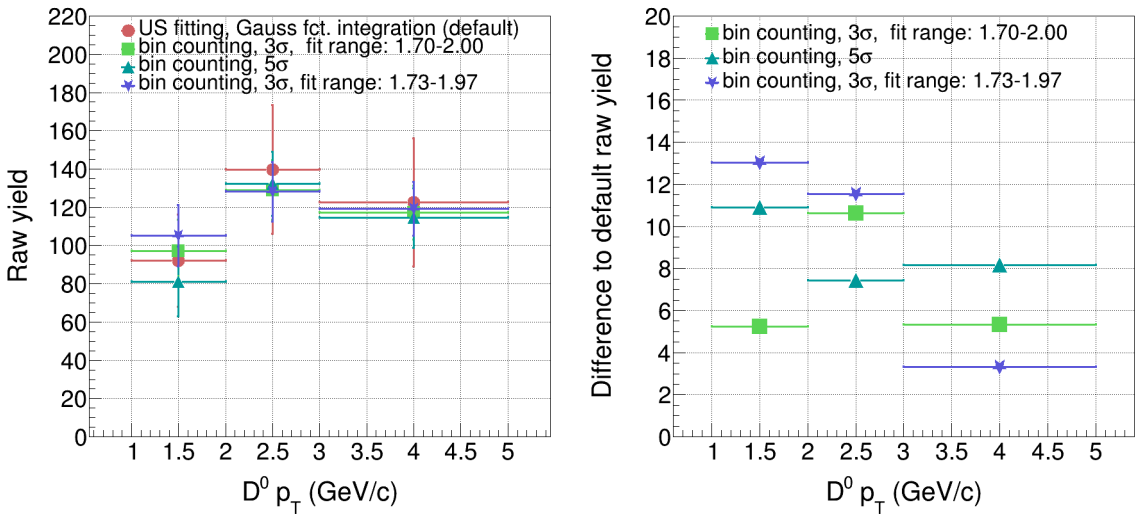

Figure 4.32: Left: Raw yield calculated using different methods vs. D^0 meson transverse momentum p_T. Right: Differences of the raw yield calculated with different method to the default one (from the fitted Gaussian function integration) vs. D^0 transverse momentum p_T.

4.7.2 Raw yield extraction systematics

Raw yield and its uncertainty may vary with the method used for its calculation. In Sec. 4.5, raw yield calculations are described. The method that fits the invariant mass peaks by the sum of Gaussian and linear functions and then integrates the Gaussian part is used as the default in the analysis. Another method integrates the invariant mass distributions to calculate the raw yield (bin-counting). To further estimate the uncertainties, raw yield is calculated with bin-counting within $\pm 5\sigma$ region around the mean of the fitted Gaussian. Finally, bin-counting is again tested, but all of the fits of invariant mass distributions are done for $1.73 < m_{K\pi} < 1.97$ GeV/c^2 (the default is $1.7 < m_{K\pi} < 2$ GeV/c^2).

Raw yields and their uncertainties for all four methods are shown in Fig. 4.32 (left). Figure 4.32 (right) shows differences between the default method and others. The final systematic uncertainty of the raw yield extractions is calculated as RMS of these differences and its ratio to the default raw yield shown in Fig. 4.33.

4.7.3 TPC embedding uncertainty

Another systematic uncertainty comes from the TPC+HFT single-particle embedding and efficiency calculation described in Sec. 4.6.1. DCA and nHitsFit distributions of kaon and pion tracks in multiple track p_T intervals, in both recorded data and embedding, are compared to calculate this uncertainty. Distributions in recorded data are from the HFT tracks that pass the same PID selection criteria as those in the primary analysis. Firstly, for multiple track p_T intervals, integrals of corresponding distributions are calculated for the analysis cut and the reference cut. In the case of nHitsFit uncertainty, the analysis cut is nHitsFit > 15, and the used reference cut is nHitsFit > 20. For DCA, in the analysis, tracks with DCA < 1 cm are used, and the reference cut is DCA < 1.5 cm. Secondly, p_T-dependent ratios are calculated as:

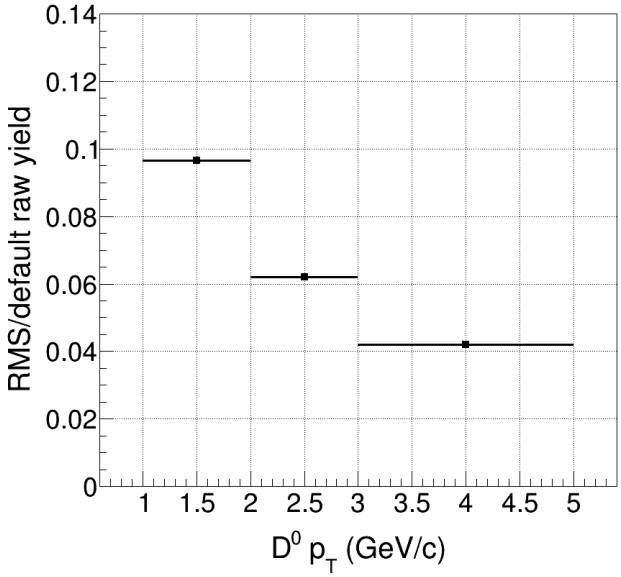

Figure 4.33: Total systematic uncertainty of the raw yield extraction vs. D^0 transverse momentum p_T.

$$r_{\mathrm{DCA}} = \frac{\int_{0\ \mathrm{cm}}^{1\ \mathrm{cm}} h_{\mathrm{DCA}}}{\int_{0\ \mathrm{cm}}^{1.5\ \mathrm{cm}} h_{\mathrm{DCA}}}, \tag{4.4}$$

$$r_{\mathrm{nHitsFit}} = \frac{\int_{20}^{45} h_{\mathrm{nHitsFit}}}{\int_{15}^{45} h_{\mathrm{nHitsFit}}}, \tag{4.5}$$

where h_{DCA} and h_{nHitsFit} are studied distributions of DCA and nHitsFit. Then, these ratios are compared for distributions in the recorded data and the embedding,

$$\delta(p_{\mathrm{T}}) = \frac{r^{\mathrm{data}}(p_{\mathrm{T}})}{r^{\mathrm{embedding}}(p_{\mathrm{T}})}. \tag{4.6}$$

In the ideal case, when the embedding is close to the recorded data, $\delta(p_{\mathrm{T}}) = 1$. In reality, $\delta(p_{\mathrm{T}})$ differs from unity, and this difference is the single-particle systematic uncertainty for simulated DCA and nHitsFit. These ratios are shown in Fig. 4.34 for DCA (left) and nHitsFit (right) distributions for both kaons (up) and pions (down). The upper parts of the plots show ratios $r_{p_{\mathrm{T}}}$ for data and embedding, and the lower parts show $\delta(p_{\mathrm{T}})$. As it can be seen, thanks to the relatively wide nHitsFit cut used in the analysis (>15), $\delta(p_{\mathrm{T}})$ for nHitsFit is close to the unity for both data and embedding. For DCA, the difference between data and embedding is more significant, especially for low track p_{T}. Then, FastSim is used to convolute these single-particle efficiencies to p_{T}-dependent D^0 meson efficiency. This is done separately for kaons and pions, DCA, and nHitsFit. D^0 meson efficiency for the individual variable is calculated as the sum of the results of these convolutions for the kaon and the pion daughter track. Results of such convolution are shown in Fig. 4.35, for DCA (left) and nHitsFit (right).

Finally, the total embedding efficiency (relative uncertainty) is calculated as

$$\epsilon^{\mathrm{D}^0}_{\mathrm{sys,TPC}} = \sqrt{\left(\epsilon^{\mathrm{D}^0}_{\mathrm{sys,nHitsFit}}\right)^2 + \left(\epsilon^{\mathrm{D}^0}_{\mathrm{sys,DCA}}\right)^2}. \tag{4.7}$$

Table 4.3: Summary of the systematical uncertainties of D^0 meson reconstruction in d+Au collisions at $\sqrt{s_{NN}} = 200$ GeV for studied D^0 transverse momentum p_{T,D^0} intervals.

p_{T,D^0} [GeV/c]	1–2	2–3	3–5
Trigger bias [%]	1.52	1.93	2.45
Vertex reconstruction [%]	4.51	3.61	3.43
Raw yield extraction [%]	9.66	6.21	4.20
BDT topological reconstruction [%]	7.01	4.62	7.39
TPC embedding [%]	0.98	1.17	1.30
Double counting [%]	0.45	0.78	1.54
Total [%]	12.9	8.9	9.7

Figure 4.36 shows the final relative single-particle embedding systematic uncertainty. As can be seen, this systematic is small, mainly thanks to the high quality of the HFT tracks used in the analysis.

4.7.4 Summary of D^0 meson reconstruction systematic uncertainties

Trigger bias and vertex reconstruction efficiency statistical uncertainties are additional contributions to the D^0 meson reconstruction systematics. Total relative systematic uncertainty is calculated as

$$\sigma_{\text{total sys.}} = \sqrt{\sum_i \epsilon_i^2}, \tag{4.8}$$

where ϵ are individual systematic uncertainty contributions. All systematics are summarized and shown in Fig. 4.37 and in Table 4.3. As can be seen, due to the relatively low significance of D^0 meson signal, the biggest contribution to systematics is from the raw yield extraction and BDT topological reconstruction.

4.8 Invariant yield and nuclear modification factor of D^0 meson

The invariant yield of D^0 meson in d+Au collisions is calculated using all described ingredients as

$$\frac{\mathrm{d}^2N}{2\pi p_T \mathrm{d}p_T \mathrm{d}y} = \frac{1}{\epsilon\,\mathrm{BR}} \frac{Y}{N_{\text{evt}} 2\pi p_T \Delta p_T \Delta y}, \tag{4.9}$$

where ϵ is the total efficiency of the raw yield extraction, BR is the branching ratio of D^0 meson decay to Kπ (3.89 ± 0.04 % [3]), Y is the D^0 meson raw yield for the transverse momentum interval with center at p_T and width Δp_T, Δy is the studied rapidity window ($|y| < 1$, so $\Delta y = 2$). Values of used variables and efficiencies are in Table 4.4.

The resulting invariant yield is shown in Fig. 4.38, with the invariant yield measured in data recorded in 2003 [84] and the reference from p+p collisions scaled by the number of binary nucleon+nucleon collisions in d+Au collisions. This reference is calculated from the measurements of $c\bar{c}$ cross-section, inferred from D^0 and D^* production measurements [52]. This cross-section is scaled by the scaling factor $f(c \to D^0)/\sigma_{pp}^{\text{inel}}$, where fragmentation function

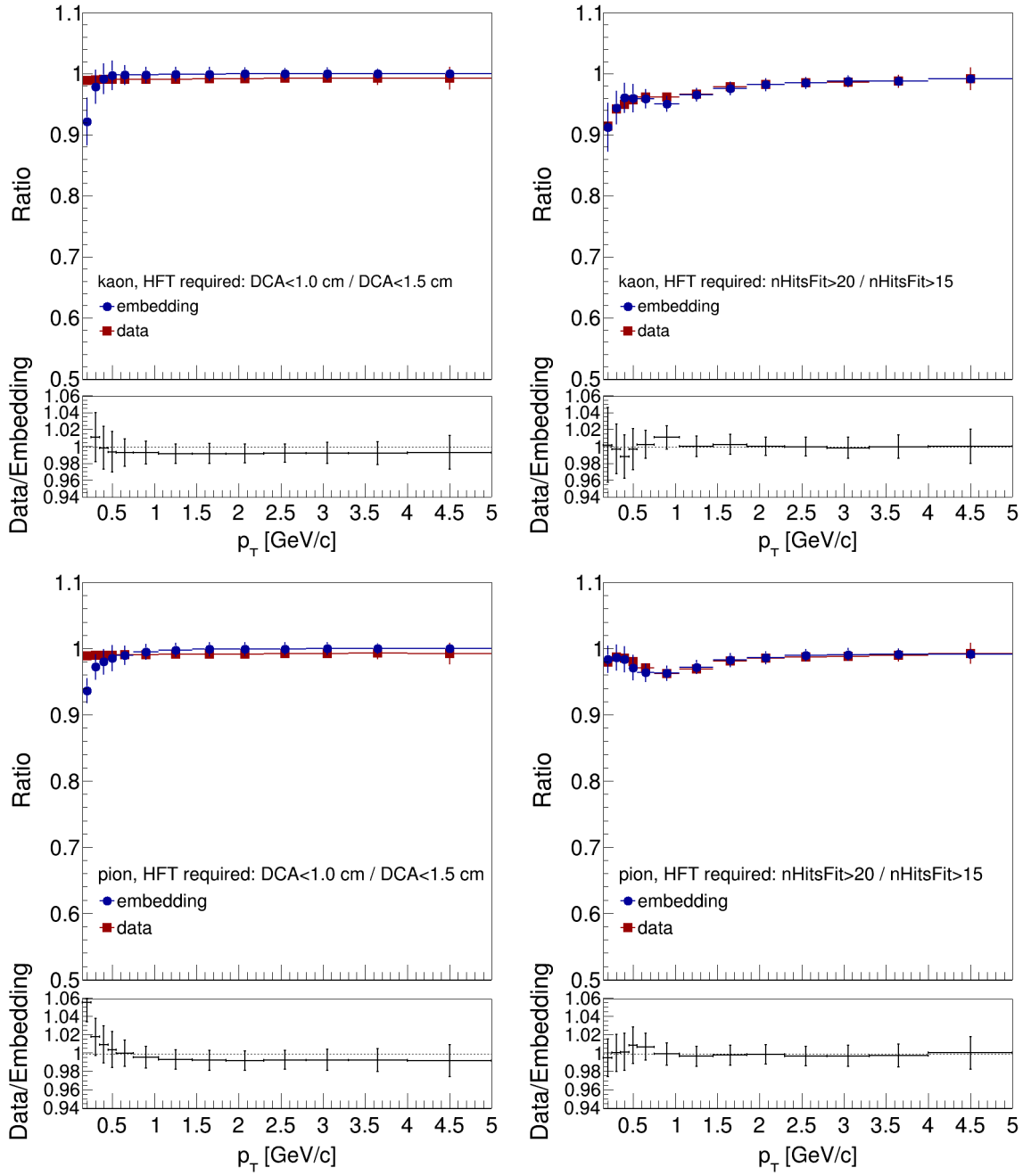

Figure 4.34: Ratios of DCA and nHitsFit distributions integrals for the analysis and the reference cuts (defined in Eq. 4.4 and Eq. 4.5), calculated in the recorded data and in the single-particle embedding, together with their ratio (defined in Eq. 4.6).

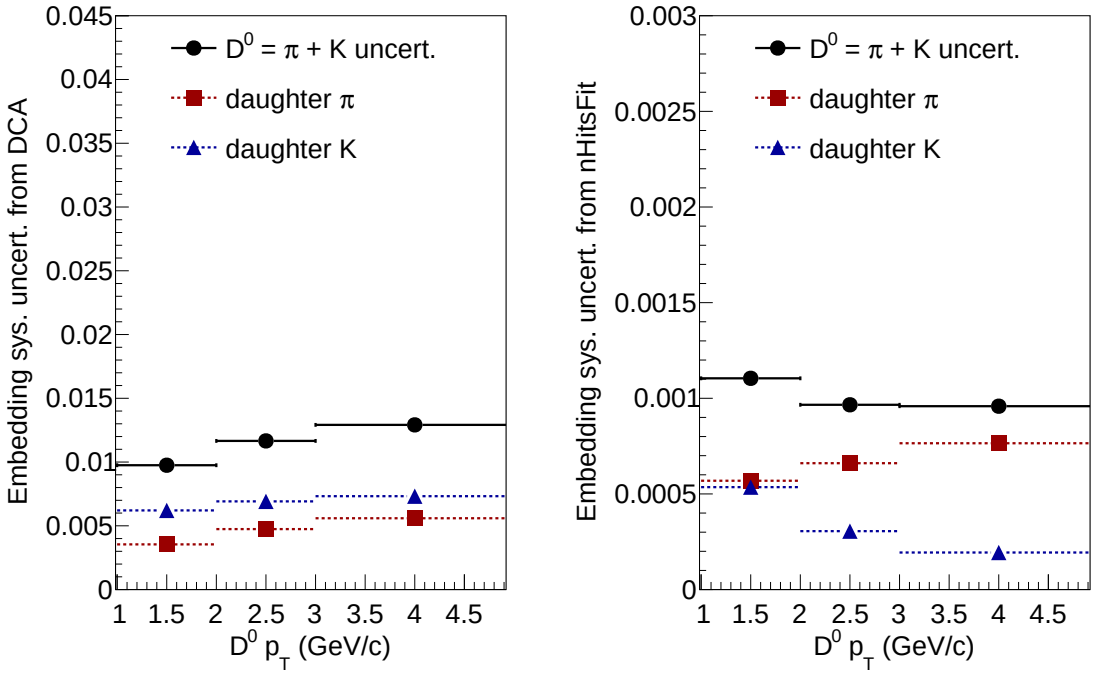

Figure 4.35: Relative systematic uncertainty of the single-particle embedding for kaons and pions, convoluted to D^0 transverse momentum p_T, and their sum vs. D^0 transverse momentum p_T, for DCA (left) and nHitsFit (right).

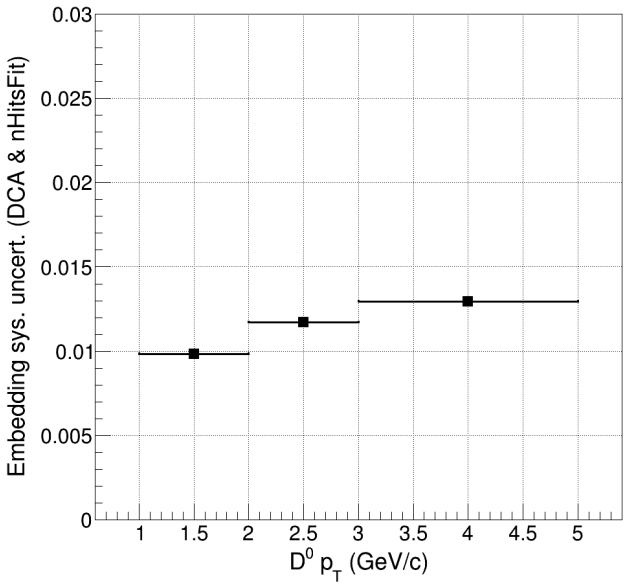

Figure 4.36: Total relative systematic uncertainty of the single-particle embedding calculated with DCA and nHitsFit distributions vs. D^0 meson transverse momentum p_T.

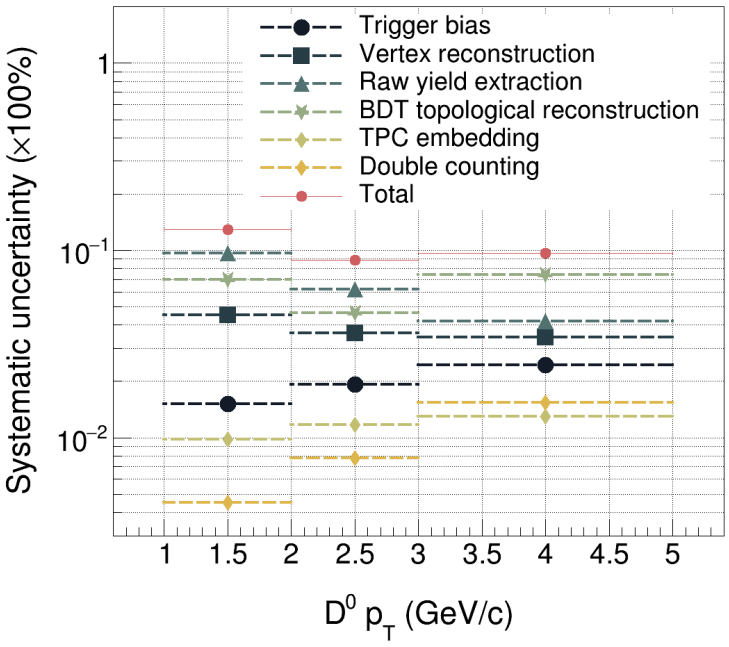

Figure 4.37: Summary of systematic uncertainty sources, together with the total relative systematic uncertainty vs. D^0 transverse momentum p_T.

$f(c \to D^0) = 0.6086$ and the total inelastic p+p cross-section σ_{pp}^{inel} is 42 mb. The mean number of binary collisions in d+Au collisions N_{bin} is 7.5±0.4 [119]. Binned results are shown together with their fits by the Levy function. Due to the low number of fitted points, the precision of the resulting fit parameters could be more satisfying, and resulting functions are not further used. However, this fits lead eye on where the bin width correction would place the unbinned data points. As can be observed, the results presented in this thesis have significantly smaller uncertainties than those measured in 2003.

Finally, the nuclear modification factor R_{dAu} is calculated using the presented invariant yield spectra and the p+p reference. Calculated R_{dAu} is shown in Fig. 4.39, together with results for charged hadrons [119] and various light hadron species [120]. Global uncertainty for d+Au collisions is the relative uncertainty of N_{bin}. For p+p collisions, the global uncertainty is caused by the different binning and coverage of the p+p reference. The study for this uncertainty is done in the published results of D^0 meson measurements in Au+Au collisions [57]. The vertical lines represent the statistical (raw yield) uncertainty; the brackets are the systematics uncertainties. The grey boxes are the uncertainties coming from the significant uncertainty of the p+p references. All of the plotted results and uncertainties for D^0 meson R_{dAu} are in Table 4.4, too.

Figure 4.40 (left) shows the comparison of the studied D^0 meson R_{dAu} with D^0 nuclear modification factor in peripheral (40–80% centrality) and central (0–10% centrality) Au+Au collision at the same collision energy measured by the STAR experiment [57]. As can be seen, for low p_T up to 3 GeV/c the Cronin peak shape in all collisions systems is similar.

In Fig. 4.40 (right), d+Au results are compared to the ALICE results of nuclear modification factor in p+Pb collisions at $\sqrt{s_{NN}} = 5.02$ TeV [78]. The ALICE averaged results for D meson species are shown by the light red triangles, and the dark red triangles show prompt

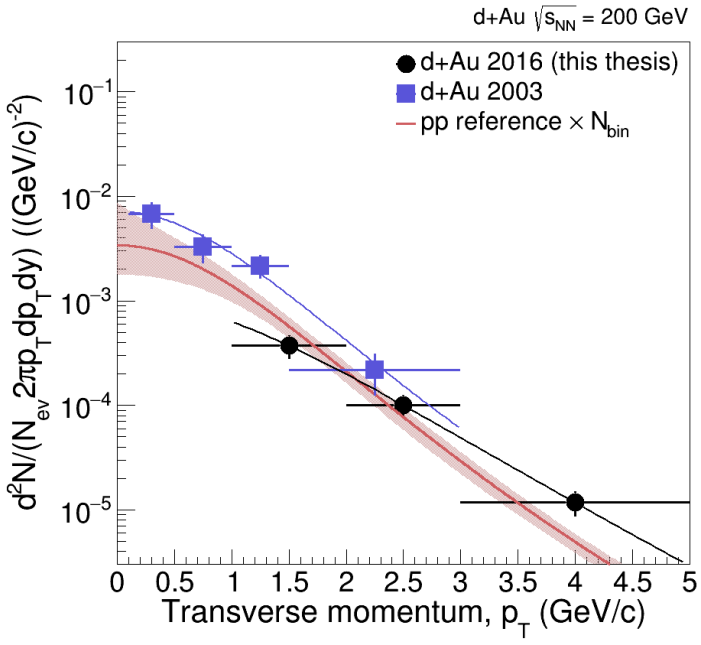

Figure 4.38: Invariant yield spectra of D^0 mesons measured in d+Au collisions at $\sqrt{s_{NN}}$ = 200 GeV. Results presented in this thesis (d+Au 2016) are compared to the published results from data recorded in 2003 (d+Au 2003) and data from p+p collisions [52] scaled by the number of binary nucleon+nucleon collisions in d+Au collisions [119]. Lines show Levy fits to the data.

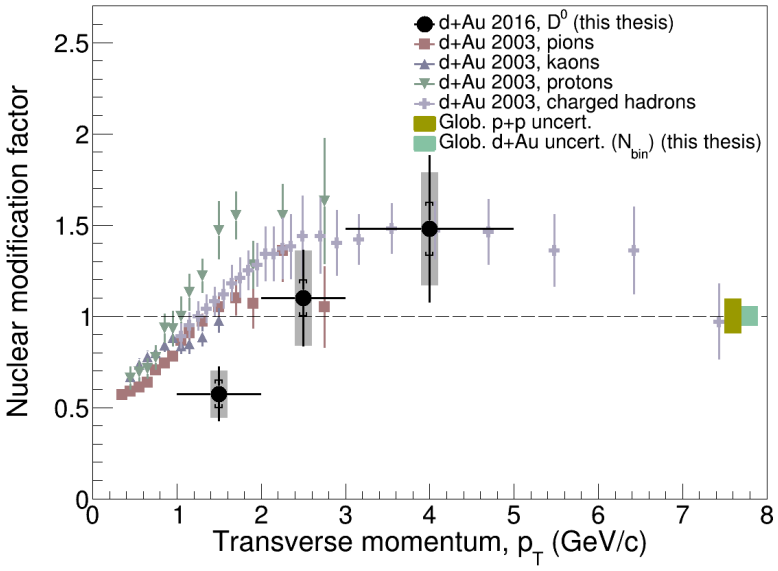

Figure 4.39: Nuclear modification factor R_{dAu} of D^0 meson in d+Au collisions at $\sqrt{s_{NN}}$ = 200 GeV. The grey boxes are uncertainties coming from the p+p reference, the vertical lines are statistical and the brackets are systematical uncertainties. The brown box shows the global p+p uncertainty and the green is uncertainty of number of binary collisions in d+Au collisions at $\sqrt{s_{NN}}$ = 200 GeV. R_{dAu} is also shown for charged hadrons [119], pions, kaons and protons [120].

Table 4.4: Summary of all ingredients to the final D^0 meson invariant yield and nuclear modification factor R_{dAu} in d+Au collisions at $\sqrt{s_{NN}} = 200$ GeV, together with their results.

D^0 p_T [GeV/c]	1–2	2–3	3–5
Raw yield	92.0	139.8	122.5
Raw yield relative statistical uncert.	0.26	0.24	0.27
Reconstruction efficiency ϵ_{reco}	0.00285	0.00720	0.0152
Double counting correction ϵ_{double}	0.972	0.950	0.911
Vertex reconstruction efficiency ϵ_{vtx}	0.505	0.656	0.692
Trigger bias correction ϵ_{TB}	0.831	0.823	0.821
Total efficiency ϵ	0.00116	0.00369	0.00787
Branching ratio [%]	3.89 ± 0.04		
Invariant yield [$\times 10^{-5}$(GeV/c)$^{-2}$]	37.17	10.00	1.17
Invariant yield statistical uncert. [$\times 10^{-5}$ (GeV/c)$^{-2}$]	9.72	2.40	0.32
Invariant yield systematical uncert. [$\times 10^{-5}$ (GeV/c)$^{-2}$]	4.80	0.89	0.11
Number of binary collisions N_{bin}	7.5 ± 0.4		
N_{bin} uncert. [%]	5.3		
R_{dAu}	0.57	1.10	1.48
R_{dAu} statistical uncert.	0.15	0.26	0.41
R_{dAu} systematical uncert.	0.07	0.10	0.14
R_{dAu} p+p ref. systematical uncert.	0.13	0.26	0.31
R_{dAu} global p+p uncert. [%]	9.6		

D^0 meson results separately. Higher collisional energy at the ALICE causes a nearly constant nuclear modification factor equal to the unity. However, the STAR measurements at the lower energies explore a region with lower quark momentum fraction x and thus the Cronin peak might be observed.

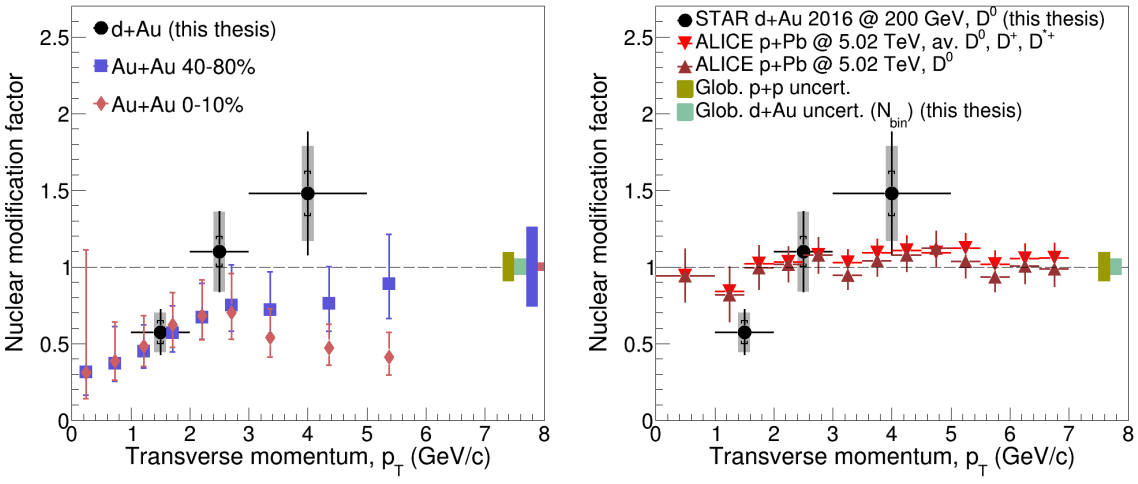

Figure 4.40: Nuclear modification factor of D^0 mesons in d+Au collisions at $\sqrt{s_{NN}} = 200$ GeV compared to the STAR results of D^0 in peripheral (40–80%) and central (0–10%) Au+Au collisions at the same $\sqrt{s_{NN}}$ [57] (left) and the ALICE results of prompt D mesons in p+Pb collisions at $\sqrt{s_{NN}} = 5.02$ TeV [78] (right). For d+Au results, the grey boxes are uncertainties coming from the p+p reference, the vertical lines are statistical and the brackets are systematical uncertainties. The brown box shows the global p+p uncertainty (common for d+Au and Au+Au). The green, the blue and the red boxes are the uncertainties of number of binary collisions (N_{bin}) in d+Au, Au+Au peripheral and Au+Au central collisions, respectively.

Summary and outlook

Charm and beauty quarks are excellent probes of the hot and dense nuclear matter created in heavy-ion collisions. They are created mainly in the initial stages of the collisions. Thus, they probe their whole evolution. Measurements of heavy-flavor production allow exploiting various QGP properties, such as the transport coefficient of the QGP, dependency of the quark energy loss in the medium on its mass, or hadronization of quarks and gluons. Furthermore, heavy-flavor mesons probe not only QGP but can also be used to investigate a wide range of CNM effects. The CNM effects comprise mainly the impact of the heavy nuclei in the initial stages of collisions and the dense environment after hadronization occurs. Experiments at the LHC and the RHIC record asymmetric p+Pb, p+Au, and d+Au collisions to exploit these effects. However, data so far do not allow quantitative favor or reject of specific theoretical models based on nuclear PDF, parton saturation, or initial parton energy loss. Furthermore, it is crucial to separate the CNM effects from the QGP ones to properly study the energy loss of heavy mesons in heavy-ion collisions.

The HFT, silicon vertex and tracking detector, was installed at STAR in 2014–2016. The detailed study of charm quark production in Au+Au collisions at $\sqrt{s_{\mathrm{NN}}} = 200$ GeV was done using data recorded in this period. The total charm production per binary (nucleon-nucleon) collisions was found to be similar to the one in p+p collisions at the same energy. However, D mesons suppression in central Au+Au collisions measured via nuclear modification factor points to the different charm hadronization in heavy-ion and p+p collisions. Moreover, this suppression induces strong interactions of charm with the created hot medium. Furthermore, indications of less suppression of beauty-decayed than charm-decayed electrons were measured in Au+Au collisions. Results from the charm elliptic flow measurements show that charm quarks achieve local thermal equilibrium in the QGP. In Au+Au collisions, the directed flow of D^0 meson is significantly larger than for light hadrons, which constrains the geometric and transport parameters of the hot QCD medium.

To further study QGP properties in heavy-ion collisions and quantify CNM effects, STAR measured d+Au collisions at $\sqrt{s_{\mathrm{NN}}} = 200$ GeV in 2016 with the HFT detector installed. Reconstruction of D^0 meson in these collisions is the primary goal of this thesis. The CNM effects on heavy-flavor quark production at STAR were measured only for J/Ψ in p+Au collisions at $\sqrt{s_{\mathrm{NN}}} = 200$ GeV. D^0 measurements in d+Au collisions recorded in 2016 follow up the D^0 meson production measurement done in 2003 in the same collisions.

Analysis of D^0 meson production in d+Au collisions measured in 2016 is completed, and all the reconstruction and correction steps were presented in the last chapter of this thesis. Hadronic decay channel $\mathrm{D}^0(\overline{\mathrm{D}^0}) \to \mathrm{K}^-\pi^+(\mathrm{K}^+\pi^-)$ was used. Firstly, in the events recorded by the selected minimum-bias trigger, kaon and pion tracks were selected using a selection that assures the high quality of these input data. Then, these tracks were combined for each event

to the like-sign charge and unlike-sign charge Kπ pairs. Further analysis was done separately in three Kπ transverse momentum $p_{\mathrm{T,K}\pi}$ bins, 1–2, 2–3 and 3–5 GeV/c.

The distance of the closest approach to the primary vertex was calculated for each track. Also, D^0 meson decay topological properties were calculated for each Kπ pair. These are DCA between kaon and pion, decay length, DCA of the reconstructed D^0 meson candidate to the place of the collision, the angle between reconstructed Kπ pair momentum and decay length, and the angle between reconstructed Kπ pair momentum and kaon momentum. The mentioned topological variables were used in the machine-learning classification model to separate the signal from the background in the correct charge (unlike-sign) Kπ pairs.

We exploited the boosted decision trees method from the Toolkit for Multivariate Data Analysis, random forest from scikit-learn package, and deep neural network from the Keras package. Detailed descriptions of individual steps for the machine-learning algorithm application on the data were published and further described in this thesis. A similar setup of the studied algorithms might be used in future analyses. To further exploit the machine learning capabilities, it might be beneficial to generate the simulation of D^0 mesons with properties more similar to the recorded D^0 meson candidate Kπ pairs. The better the simulation is, the better the algorithm identifies low-probability combinations of decay properties as the signal ones. Furthermore, constructing the model ensemble, consisting of the studied model algorithms, could benefit from combining the individual model qualities. On the simulated data, the performance of the three algorithms was close, and, mainly due to their growing popularity in high-energy physics, the BDT algorithm was selected. In D^0 meson reconstruction, a machine-learning classifier was trained on the simulated unlike-sign signal pairs and recorded like-sign Kπ pairs. Despite the relatively low number of recorded events, D^0 meson peak significance around six was achieved for $1 < p_{\mathrm{T,K}\pi} < 2$ GeV/c. The significance goes up to eight for $2 < p_{\mathrm{T,K}\pi} < 5$ GeV/c.

The efficiency of all selection criteria was calculated. Single particle efficiencies were combined with the PYTHIA D^0 meson decay simulation to correctly calculate the D^0 meson efficiency in all studied $p_{\mathrm{T,D^0}}$ intervals. Kaon and pion tracking efficiencies and momentum resolution in the HFT and the TPC detector were estimated using the single-particle embedding to the zero-bias data. The TOF matching efficiency was estimated in the recorded data. The recorded data were also used for TPC and TOF particle identification efficiencies. To calculate these efficiencies, clean samples of kaons and pions, selected with the reconstruction of hadronic decays $\mathrm{K}^0_{\mathrm{s}} \to \pi^+\pi^-$ and $\Phi \to \mathrm{K}^+\mathrm{K}^-$, were used. Generally, particle identification efficiency at STAR is at a very high level. Clean samples of kaons and pions were also used to estimate D^0 meson double counting frequency. Double counting occurs when both tracks in Kπ pair are identified as kaons and pions. Such a pair would be counted twice to the signal. As importantly, reconstruction efficiency was calculated by estimating the ratio of D^0 mesons that fulfill the topological and the BDT selection criteria.

Due to the relatively low multiplicity in d+Au collisions, the creation of D^0 meson influences the rapidity distribution of the created tracks. Thus, the trigger detectors' signal in forward and backward rapidity differs. Trigger bias correction was calculated using the full d+Au collision HIJING simulation embedded in the zero-bias data. Furthermore, D^0 meson in the low-multiplicity event significantly influences the primary vertex reconstruction resolution. Two simulations were compared to estimate this effect. One of them is the mentioned full-event HIJING simulation embedded in the recorded data. The other is the fast simulation, where DCA of kaon and pion tracks from D^0 meson decay simulated in PYTHIA are smeared according to the response of detectors in the mentioned full-event simulation.

Systematic uncertainties of the BDT selection, raw yield extraction method, single particle simulation, trigger bias, primary vertex reconstruction, and double counting are combined. The raw yield extraction and BDT selection are the highest contributions to the systematics. The reconstruction method selection does not primarily cause these high contributions from the peak reconstruction, but it is mainly due to the relatively low statics in the reconstructed D^0 meson peaks.

After all the corrections were applied, the invariant yield of D^0 meson in d+Au collisions and its statistical and systematical uncertainties were calculated. D^0 meson invariant yield in d+Au was compared to the p+p reference to calculate the nuclear modification factor R_{dAu}. In the first $p_{\mathrm{T,D^0}}$ interval, 1–2 GeV/c, it is 0.57±0.15(stat.)±0.07(sys.). For $2 < p_{\mathrm{T,D^0}} < 3$ GeV/c, R_{dAu} central value is above unity, resulting in $R_{\mathrm{dAu}} = 1.10 \pm 0.26(\mathrm{stat.}) \pm 0.10(\mathrm{sys.})$. In the highest measured $p_{\mathrm{T,D^0}}$ interval, 3–5 GeV/c, R_{dAu} goes up to $1.48 \pm 0.41(\mathrm{stat.}) \pm 0.14(\mathrm{sys.})$. Further uncertainties are from the number of binary collisions in d+Au collision and p+p reference measurements. The suppression for $p_{\mathrm{T,D^0}} < 2$ GeV/c is similar with the result in both central and peripheral Au+Au collisions. Thus, the CNM could explain the R_{AuAu} for low p_{T}. As can be seen in Fig. 4.39, despite the limited statistics, it could be observed that the nuclear modification factor of D^0 mesons in d+Au collisions follows a similar trend as the one for light hadrons. A more detailed study of the CNM will be enabled in 2024 when p+Au collisions at $\sqrt{s_{\mathrm{NN}}} = 200$ GeV is requested at the RHIC. Both sPHENIX and STAR detectors will record those.

Bibliography

[1] Z.-W. Lin and M. Gyulassy, *Open charm as a probe of preequilibrium dynamics in nuclear collisions*, *Phys. Rev. C* **51** (1995) 2177.

[2] G. Contin et al., *The STAR MAPS-based PiXeL detector*, *Nucl. Instrum. Meth. A* **907** (2018) 60 [1710.02176].

[3] Particle Data Group collaboration, *Review of Particle Physics*, *Phys. Rev. D* **98** (2018) 030001.

[4] A. Hocker et al., *TMVA - Toolkit for Multivariate Data Analysis*, *CERN-OPEN-2007-007* (2007) .

[5] T. Truhlář, *Optimalization of charm hadrons reconstruction in d/p+Au collisions*, bachelor's thesis, Czech Technical University in Prague, 2018.

[6] Z. Moravcová, *Methods of optimalization of charm hadrons reconstruction*, bachelor's thesis, Czech Technical University in Prague, 2017.

[7] Z. Moravcová, *Production of charm mesons in STAR experiment*, master's thesis, Czech Technical University in Prague, 2019.

[8] R. Líčeník, *Study of D meson production in 200 GeV Au+Au collisions at the STAR experiment*, master's thesis, Czech Technical University in Prague, 2019.

[9] P. A. R. Ade, N. Aghanim, M. Arnaud, M. Ashdown, J. Aumont, C. Baccigalupi et al., *Planck2015 results*, *Astronomy and Astrophysics* **594** (2016) A13.

[10] Super-Kamiokande collaboration, *Evidence for oscillation of atmospheric neutrinos*, *Phys. Rev. Lett.* **81** (1998) 1562 [hep-ex/9807003].

[11] SNO collaboration, *Direct evidence for neutrino flavor transformation from neutral current interactions in the Sudbury Neutrino Observatory*, *Phys. Rev. Lett.* **89** (2002) 011301 [nucl-ex/0204008].

[12] FCC collaboration, *FCC Physics Opportunities*, *Eur. Phys. J.* **C79** (2019) 474.

[13] ATLAS, CMS collaboration, *Combined Measurement of the Higgs Boson Mass in pp Collisions at $\sqrt{s} = 7$ and 8 TeV with the ATLAS and CMS Experiments*, *Phys. Rev. Lett.* **114** (2015) 191803 [1503.07589].

[14] ATLAS collaboration, *Measurement of the Higgs boson mass with $H \to \gamma\gamma$ decays in 140 fb^{-1} of $\sqrt{s} = 13$ TeV pp collisions with the ATLAS detector*, 2308.07216.

[15] S. P. Martin, *A Supersymmetry primer*, *Adv. Ser. Direct. High Energy Phys.* **18** (1998) 1 [hep-ph/9709356].

[16] L. S. Sparke and J. S. Gallagher, *Galaxies in the Universe - An Introduction.* Cambridge, 2007.

[17] A. Einstein, *Näherungsweise Integration der Feldgleichungen der Gravitation*, *Sitzungsber. K. Preuss. Akad. Wiss. 1* (1916) 688.

[18] LIGO Scientific, Virgo collaboration, *Observation of Gravitational Waves from a Binary Black Hole Merger*, *Phys. Rev. Lett.* **116** (2016) 061102 [1602.03837].

[19] J. H. Christenson, J. W. Cronin, V. L. Fitch and R. Turlay, *Evidence for the 2π decay of the K_2^0 meson*, *Phys. Rev. Lett.* **13** (1964) 138.

[20] R. Hagedorn and J. Ranft, *Inclusive single particle spectra and the strong thermodynamic bootstrap solution*, *Nucl. Phys. B* **48** (1972) 157.

[21] NA35 collaboration, *Strange particle production in nuclear collisions at 200 GeV per nucleon*, *Zeitschrift für Physik C Particles and Fields* **64** (1994) 195.

[22] H. Bial·kowska, M. Gaździcki, W. Retyk and E. Skrzypczak, *Strangeness enhancement and strangeness suppression in nuclear collisions at 200 GeV/N*, *Zeitschrift für Physik C Particles and Fields* **55** (1992) 491.

[23] CERN collaboration, "New state of matter created at CERN." https://home.web.cern.ch/news/press-release/cern/new-state-matter-created-cern [Accessed: 11 November 2023], 2000.

[24] J. Adams et al., *Experimental and theoretical challenges in the search for the quark–gluon plasma: The star collaboration's critical assessment of the evidence from rhic collisions*, *Nuclear Physics A* **757** (2005) 102.

[25] B. Back et al., *The PHOBOS perspective on discoveries at RHIC*, *Nuclear Physics A* **757** (2005) 28.

[26] K. Adcox et al., *Formation of dense partonic matter in relativistic nucleus–nucleus collisions at RHIC: Experimental evaluation by the PHENIX collaboration*, *Nuclear Physics A* **757** (2005) 184.

[27] I. Arsene et al., *Quark–gluon plasma and color glass condensate at RHIC? The perspective from the BRAHMS experiment*, *Nuclear Physics A* **757** (2005) 1.

[28] ATLAS collaboration, *Observation of a Centrality-Dependent Dijet Asymmetry in Lead-Lead Collisions at $\sqrt{s_{NN}} = 2.77$ TeV with the ATLAS Detector at the LHC*, *Phys. Rev. Lett.* **105** (2010) 252303 [1011.6182].

[29] STAR collaboration, *Dijet imbalance measurements in $Au + Au$ and pp collisions at $\sqrt{s_{NN}} = 200$ GeV at STAR*, *Phys. Rev. Lett.* **119** (2017) 062301 [1609.03878].

[30] T. Matsui and H. Satz, *J/ψ Suppression by Quark-Gluon Plasma Formation*, *Phys. Lett. B* **178** (1986) 416.

[31] H. Caines, *The search for critical behavior and other features of the qcd phase diagram – current status and future prospects*, *Nuclear Physics A* **967** (2017) 121 .

[32] M. G. Alford, A. Schmitt, K. Rajagopal and T. Schäfer, *Color superconductivity in dense quark matter*, *Rev. Mod. Phys.* **80** (2008) 1455 [0709.4635].

[33] MILC collaboration, *QCD thermodynamics with three flavors of improved staggered quarks*, *Phys. Rev. D* **71** (2005) 034504 [hep-lat/0405029].

[34] J. Berges and K. Rajagopal, *Color superconductivity and chiral symmetry restoration at nonzero baryon density and temperature*, *Nucl. Phys. B* **538** (1999) 215 [hep-ph/9804233].

[35] HotQCD collaboration, *Equation of state in (2+1)-flavor QCD*, *Phys. Rev. D* **90** (2014) 094503 [1407.6387].

[36] STAR collaboration, *Bulk Properties of the Medium Produced in Relativistic Heavy-Ion Collisions from the Beam Energy Scan Program*, *Phys. Rev. C* **96** (2017) 044904 [1701.07065].

[37] STAR collaboration, *The STAR detector upgrades for the BES II and beyond physics program*, *Nucl. Phys. A* **1005** (2021) 121758.

[38] K. J. Eskola, H. Paukkunen and C. A. Salgado, *EPS09: A New Generation of NLO and LO Nuclear Parton Distribution Functions*, *JHEP* **04** (2009) 065.

[39] N. Armesto, *Nuclear shadowing*, *J. Phys. G* **32** (2006) R367 [hep-ph/0604108].

[40] E. Iancu, A. Leonidov and L. D. McLerran, *The Renormalization group equation for the color glass condensate*, *Phys. Lett. B* **510** (2001) 133 [hep-ph/0102009].

[41] J. W. Cronin, H. J. Frisch, M. J. Shochet, J. P. Boymond, P. A. Piroué and R. L. Sumner, *Production of hadrons at large transverse momentum at 200, 300, and 400 GeV*, *Phys. Rev. D* **11** (1975) 3105.

[42] D. McGlinchey, A. D. Frawley and R. Vogt, *Impact-parameter dependence of the nuclear modification of J/ψ production in d+Au collisions at $\sqrt{s_{NN}} = 200$ GeV*, *Phys. Rev. C* **87** (2013) 054910.

[43] M. L. Miller, K. Reygers, S. J. Sanders and P. Steinberg, *Glauber modeling in high energy nuclear collisions*, *Ann. Rev. Nucl. Part. Sci.* **57** (2007) 205 [nucl-ex/0701025].

[44] STAR collaboration, *Evidence from d+Au measurements for final state suppression of high-p_T hadrons in Au+Au collisions at RHIC*, *Phys. Rev. Lett.* **91** (2003) 072304 [nucl-ex/0306024].

[45] PHENIX collaboration, *Scaling properties of proton and anti-proton production in 200-GeV Au+Au collisions*, *Phys. Rev. Lett.* **91** (2003) 172301 [nucl-ex/0305036].

[46] PHENIX collaboration, *Spectra and ratios of identified particles in Au+Au and d+Au collisions at $\sqrt{s_{NN}} = 200$ GeV*, *Phys. Rev. C* **88** (2013) 024906 [1304.3410].

[47] Y. L. Dokshitzer and D. E. Kharzeev, *Heavy quark colorimetry of QCD matter*, *Phys. Lett. B* **519** (2001) 199 [hep-ph/0106202].

[48] SLAC-SP-017 collaboration, *Discovery of a Narrow Resonance in e^+e^- Annihilation*, *Phys. Rev. Lett.* **33** (1974) 1406.

[49] E598 collaboration, *Experimental Observation of a Heavy Particle J*, *Phys. Rev. Lett.* **33** (1974) 1404.

[50] I. Peruzzi et al., *Observation of a Narrow Charged State at 1876 MeV/c^2 Decaying to an Exotic Combination of $K\pi\pi$*, *Phys. Rev. Lett.* **37** (1976) 569.

[51] G. Goldhaber et al., *Observation in e^+e^- Annihilation of a Narrow State at 1865 MeV/c^2 Decaying to $K\pi$ and $K\pi\pi\pi$*, *Phys. Rev. Lett.* **37** (1976) 255.

[52] STAR collaboration, *Measurements of D^0 and D^* production in p+p collisions at $\sqrt{s}$ = 200 GeV*, *Phys. Rev. D* **86** (2012) 072013.

[53] M. Cacciari, P. Nason and R. Vogt, *QCD predictions for charm and bottom production at RHIC*, *Phys. Rev. Lett.* **95** (2005) 122001 [hep-ph/0502203].

[54] D. Tlustý, *A Study of Open Charm Production in p+p Collisions at STAR*, Ph.D. thesis, Czech Technical University in Prague, 2014.

[55] STAR collaboration, *High p_T non-photonic electron production in $p+p$ collisions at $\sqrt{s}$ = 200 GeV*, *Phys. Rev. D* **83** (2011) 052006 [1102.2611].

[56] STAR collaboration, *Measurements of open heavy-flavor hadrons in Au+Au collisions at $\sqrt{s_{NN}}$ = 200 GeV with the STAR experiment*, *PoS* **ICHEP2020** (2021) 546.

[57] STAR collaboration, *Centrality and transverse momentum dependence of D^0-meson production at mid-rapidity in Au+Au collisions at $\sqrt{s_{\rm NN}} = 200\,\text{GeV}$*, *Phys. Rev. C* **99** (2019) 034908 [1812.10224].

[58] J. Vaněk, *Measurement of open-charm mesons in heavy-ion collisions by the STAR experiment*, Ph.D. thesis, Czech Technical University in Prague, 2022.

[59] S. Cao, G.-Y. Qin and S. A. Bass, *Energy loss, hadronization, and hadronic interactions of heavy flavors in relativistic heavy-ion collisions*, *Phys. Rev. C* **92** (2015) 024907.

[60] S. Cao, T. Luo, G.-Y. Qin and X.-N. Wang, *Linearized boltzmann transport model for jet propagation in the quark-gluon plasma: Heavy quark evolution*, *Phys. Rev. C* **94** (2016) 014909.

[61] W. Cassing and E. L. Bratkovskaya, *Parton transport and hadronization from the dynamical quasiparticle point of view*, *Phys. Rev. C* **78** (2008) 034919 [0808.0022].

[62] W. Cassing and E. L. Bratkovskaya, *Parton-Hadron-String Dynamics: an off-shell transport approach for relativistic energies*, *Nucl. Phys. A* **831** (2009) 215 [0907.5331].

[63] STAR collaboration, *Evidence of Mass Ordering of Charm and Bottom Quark Energy Loss in Au+Au Collisions at RHIC*, *Eur. Phys. J. C* **82** (2022) 1150 [2111.14615].

[64] STAR collaboration, *First observation of the directed flow of D^0 and $\overline{D^0}$ in $Au+Au$ collisions at $\sqrt{s_{NN}}$ = 200 GeV*, *Phys. Rev. Lett.* **123** (2019) 162301.

[65] A. M. Poskanzer and S. A. Voloshin, *Methods for analyzing anisotropic flow in relativistic nuclear collisions*, *Phys. Rev. C* **58** (1998) 1671 [nucl-ex/9805001].

[66] ALICE collaboration, *Directed Flow of Charged Particles at Midrapidity Relative to the Spectator Plane in Pb-Pb Collisions at $\sqrt{s_{NN}}$ = 2.76 TeV*, *Phys. Rev. Lett.* **111** (2013) 232302 [1306.4145].

[67] STAR collaboration, *Measurement of D^0 Azimuthal Anisotropy at Midrapidity in Au+Au Collisions at $\sqrt{s_{NN}}$ = 200 GeV*, *Phys. Rev. Lett.* **118** (2017) 212301.

[68] STAR collaboration, *First measurement of Λ_c baryon production in au+au collisions at $\sqrt{s_{NN}}$ = 200 GeV*, *Phys. Rev. Lett.* **124** (2020) 172301.

[69] S. Plumari, V. Minissale, S. K. Das, G. Coci and V. Greco, *Charmed hadrons from coalescence plus fragmentation in relativistic nucleus-nucleus collisions at RHIC and LHC*, *Eur. Phys. J. C* **78** (2018) 348.

[70] STAR collaboration, *Observation of $D_s^{\pm}/D^0$ enhancement in Au+Au collisions at $\sqrt{s_{NN}}$ = 200 GeV*, *Phys. Rev. Lett.* **127** (2021) 092301 [2101.11793].

[71] ALICE collaboration, *Measurement of D-meson production at mid-rapidity in pp collisions at $\sqrt{s}$ = 7 TeV*, *Eur. Phys. J. C* **77** (2017) 550.

[72] ALICE collaboration, *Measurement of D^0, D^+, D^{*+} and D_s^+ production in Pb-Pb collisions at $\sqrt{s_{NN}}$ = 5.02 TeV*, *JHEP* **10** (2018) 174.

[73] CMS collaboration, *Nuclear modification factor of D^0 mesons in PbPb collisions at $\sqrt{s_{NN}}$ = 5.02 TeV*, *Phys. Lett.* **B782** (2018) 474.

[74] ALICE collaboration, *Transverse momentum dependence of D-meson production in Pb-Pb collisions at $\sqrt{s_{NN}}$ = 2.76 TeV*, *JHEP* **03** (2016) 081.

[75] ATLAS collaboration, *D meson production and long-range azimuthal correlation in 8.16 TeV p+Pb collisions with ATLAS*, *ATLAS-CONF-2017-073* (2017) .

[76] LHCb collaboration, *Study of prompt D^0 meson production in pPb collisions at $\sqrt{s_{NN}}$ = 5 TeV*, *JHEP* **10** (2017) 090 [1707.02750].

[77] CMS collaboration, *Elliptic flow of charm and strange hadrons in high-multiplicity pPb collisions at $\sqrt{s_{NN}}$ = 8.16 TeV*, *Phys. Rev. Lett.* **121** (2018) 082301.

[78] ALICE collaboration, *Measurement of prompt D^0, D^+, D^{*+}, and D_S^+ production in p–Pb collisions at $\sqrt{s_{NN}}$ = 5.02 TeV*, *JHEP* **12** (2019) 092 [1906.03425].

[79] A. Andronic et al., *Heavy-flavour and quarkonium production in the LHC era: from proton-proton to heavy-ion collisions*, *Eur. Phys. J.* **C76** (2016) 107.

[80] ALICE collaboration, *Measurement of electrons from beauty-hadron decays in p-Pb collisions at $\sqrt{s_{NN}}$ = 5.02 TeV and Pb-Pb collisions at $\sqrt{s_{NN}}$ = 2.76 TeV*, *JHEP* **07** (2017) 052.

[81] E. Ferreiro, *Excited charmonium suppression in proton–nucleus collisions as a consequence of comovers*, *Physics Letters B* **749** (2015) 98.

[82] X. Du and R. Rapp, *In-Medium Charmonium Production in Proton-Nucleus Collisions*, *JHEP* **03** (2019) 015 [1808.10014].

[83] STAR collaboration, *Measurement of cold nuclear matter effects for inclusive J/ψ in p+Au collisions at $\sqrt{s_{NN}}$ = 200 GeV*, *Phys. Lett. B* **825** (2022) 136865 [2110.09666].

[84] STAR collaboration, *Open charm yields in d+Au collisions at $\sqrt{s_{NN}}$ = 200 GeV*, *Phys. Rev. Lett.* **94** (2005) 062301 [nucl-ex/0407006].

[85] J. Bielčík, K. Hladká, L. Kramárik and V. Kůs, *Machine learning classification for D^0 meson signal extraction in d+Au collisions*, *Journal of Instrumentation* **17** (2022) P02017.

[86] M. Gyulassy and X.-N. Wang, *Hijing 1.0: A monte carlo program for parton and particle production in high energy hadronic and nuclear collisions*, *Computer Physics Communications* **83** (1994) 307.

[87] R. Brun, F. Bruyant, F. Carminati, S. Giani, M. Maire, A. McPherson et al., *GEANT: Detector Description and Simulation Tool; Oct 1994*, CERN Program Library. CERN, Geneva, 1993, 10.17181/CERN.MUHF.DMJ1.

[88] D. P. Kingma and J. Ba, *Adam: A method for stochastic optimization*, *arXiv preprint arXiv:1412.6980* (2014) .

[89] C. Aggarwal, *Neural Networks and Deep Learning: A Textbook*. Springer International Publishing, Cham, 2018, 10.1007/978-3-319-94463-0.

[90] F. Provost and T. Fawcett, *Data Science for Business: What You Need to Know about Data Mining and Data-Analytic Thinking*. O'Reilly Media, 1st ed., 2013.

[91] I. Goodfellow, Y. Bengio and A. Courville, *Deep Learning*. MIT Press, 2016.

[92] G. Louppe, *Understanding Random Forests: From Theory to Practice*, Ph.D. thesis, University of Liège, 10, 2014. 10.13140/2.1.1570.5928.

[93] D. H. Wolpert, *Stacked generalization*, *Neural Networks* **5** (1992) 241.

[94] F. Pedregosa, G. Varoquaux, A. Gramfort, V. Michel, B. Thirion, O. Grisel et al., *Scikit-learn: Machine learning in python*, *J. Mach. Learn. Res.* **12** (2011) 2825–2830 [1201.0490].

[95] Y. Freund and R. E. Schapire, *A decision-theoretic generalization of on-line learning and an application to boosting*, *Journal of computer and system sciences* **55** (1997) 119.

[96] J. H. Friedman, *Greedy function approximation: A gradient boosting machine*, *The Annals of Statistics* **29** (2001) 1189.

[97] T. Chen and C. Guestrin, *Xgboost: A scalable tree boosting system*, in *Proceedings of the 22nd ACM SIGKDD International Conference on Knowledge Discovery and Data Mining*, pp. 785–794, ACM, 2016.

[98] R. E. Schapire and Y. Freund, *Boosting: Foundations and Algorithms*. MIT press, 1998.

[99] C. M. Bishop, *Pattern Recognition and Machine Learning*. Springer, 2006.

[100] K. He, X. Zhang, S. Ren and J. Sun, *Delving deep into rectifiers: Surpassing human-level performance on imagenet classification*, in *Proceedings of the IEEE International Conference on Computer Vision*, pp. 1026–1034, IEEE, 2015, https://ieeexplore.ieee.org/abstract/document/7410480.

[101] Y. LeCun, L. Bottou, G. B. Orr and K.-R. Müller, *Efficient backprop*, in *Neural Networks: Tricks of the Trade*, pp. 9–50, Springer, (1998), https://link.springer.com/chapter/10.1007/3-540-49430-8_2.

[102] X. Glorot and Y. Bengio, *Understanding the difficulty of training deep feedforward neural networks*, in *International conference on artificial intelligence and statistics*, pp. 249–256, 2010.

[103] F. Chollet et al., "Keras." `https://keras.io`, 2015.

[104] "RHIC Runs." `https://www.agsrhichome.bnl.gov/RHIC/Runs/`.

[105] J. G. Alessi, D. Barton, E. Beebe, S. Bellavia, O. Gould, A. Kponou et al., *The Brookhaven National Laboratory electron beam ion source for RHIC*, *Review of Scientific Instruments* **81** (2010) .

[106] A. Zelenski, J. Alessi, B. Briscoe, G. Dutto, H. Huang, A. Kponou et al., *Optically pumped polarized H ion source for RHIC spin physics*, *Review of Scientific Instruments* **73** (2002) 888.

[107] W. Weng and Y. Lee, *Bnl–41030*, Tech. Rep. BNL–41030, Brookhaven National Laboratory, United States, 1988.

[108] E. Judd, L. Bland, H. Crawford, J. Engelage, J. Landgraf, W. Llope et al., *The evolution of the star trigger system*, *Nuclear Instruments and Methods in Physics Research Section A: Accelerators, Spectrometers, Detectors and Associated Equipment* **902** (2018) 228.

[109] STAR collaboration, *The Star time projection chamber: A Unique tool for studying high multiplicity events at RHIC*, *Nucl. Instrum. Meth.* **A499** (2003) 659.

[110] H. Bichsel, *A method to improve tracking and particle identification in TPCs and silicon detectors*, *Nucl. Instrum. Meth.* **A562** (2006) 154.

[111] W. J. Llope et al., *The TOFp / pVPD time-of-flight system for STAR*, *Nucl. Instrum. Meth.* **A522** (2004) 252.

[112] G. Contin, E. Anderssen, L. Greiner, J. Schambach, J. Silber, T. Stezelberger et al., *The STAR Heavy Flavor Tracker (HFT): focus on the MAPS based PXL detector*, *Nuclear and Particle Physics Proceedings* **273-275** (2016) 1155.

[113] STAR collaboration, *Search for the chiral magnetic effect with isobar collisions at* $\sqrt{s_{NN}}$ *= 200 GeV by the STAR Collaboration at the BNL Relativistic Heavy Ion Collider*, *Phys. Rev. C* **105** (2022) 014901 [2109.00131].

[114] J. Adams et al., *The STAR Event Plane Detector*, *Nucl. Instrum. Meth. A* **968** (2020) 163970 [1912.05243].

[115] F. Shen, S. Wang, F. Kong, S. Bai, C. Li, F. Videbæk et al., *MWPC prototyping and performance test for the STAR inner TPC upgrade*, *Nucl. Instrum. Meth.* **A896** (2018) 90.

[116] STAR collaboration, *The sTGC prototyping and performance test for the STAR forward upgrade*, *JINST* **15** (2020) C09021.

[117] T. Sjostrand, S. Mrenna and P. Z. Skands, *PYTHIA 6.4 Physics and Manual*, *JHEP* **05** (2006) 026.

[118] D. Smirnov, J. Lauret, V. Perevoztchikov, G. V. Buren and J. Webb, *Vertex reconstruction at STAR: Overview and performance evaluation*, *Journal of Physics: Conference Series* **898** (2017) 042058.

[119] STAR collaboration, *Evidence from d+Au Measurements for final-state suppression of high-p_T hadrons in Au+Au Collisions at RHIC*, *Phys. Rev. Lett.* **91** (2003) 072304.

[120] STAR collaboration, *Pion, kaon, proton and anti-proton transverse momentum distributions from p+p and d+Au collisions at $\sqrt{s_{NN}} = 200$ GeV*, *Phys. Lett. B* **616** (2005) 8 [nucl-ex/0309012].

Appendix A

Projections of topological variables

This Appendix complements distributions of topological properties used for D^0 meson reconstruction with projections for Kπ transverse momentum $p_{T,K\pi}$ intervals 2–3 GeV/c and 3–5 GeV/c. Distributions for $p_{T,K\pi}$ interval 1–2 GeV/c are shown in Sec. 4.5 and Sec. 4.6.4. Only pairs with invariant mass 1.7–2 GeV/c^2 are considered. Schema of the D^0 meson decay and the corresponding topological variables is shown n Fig. 1.6 and described at the beginning of Sec. 4.5.

Figures A.1 and A.2 display projections for like-sign and unlike-sign pairs in the recorded data after applying precuts shown in Table 4.1. In Fig. A.3 and A.4, distributions in recorded data and FastSim, with additional application of BDT response cut, are compared.

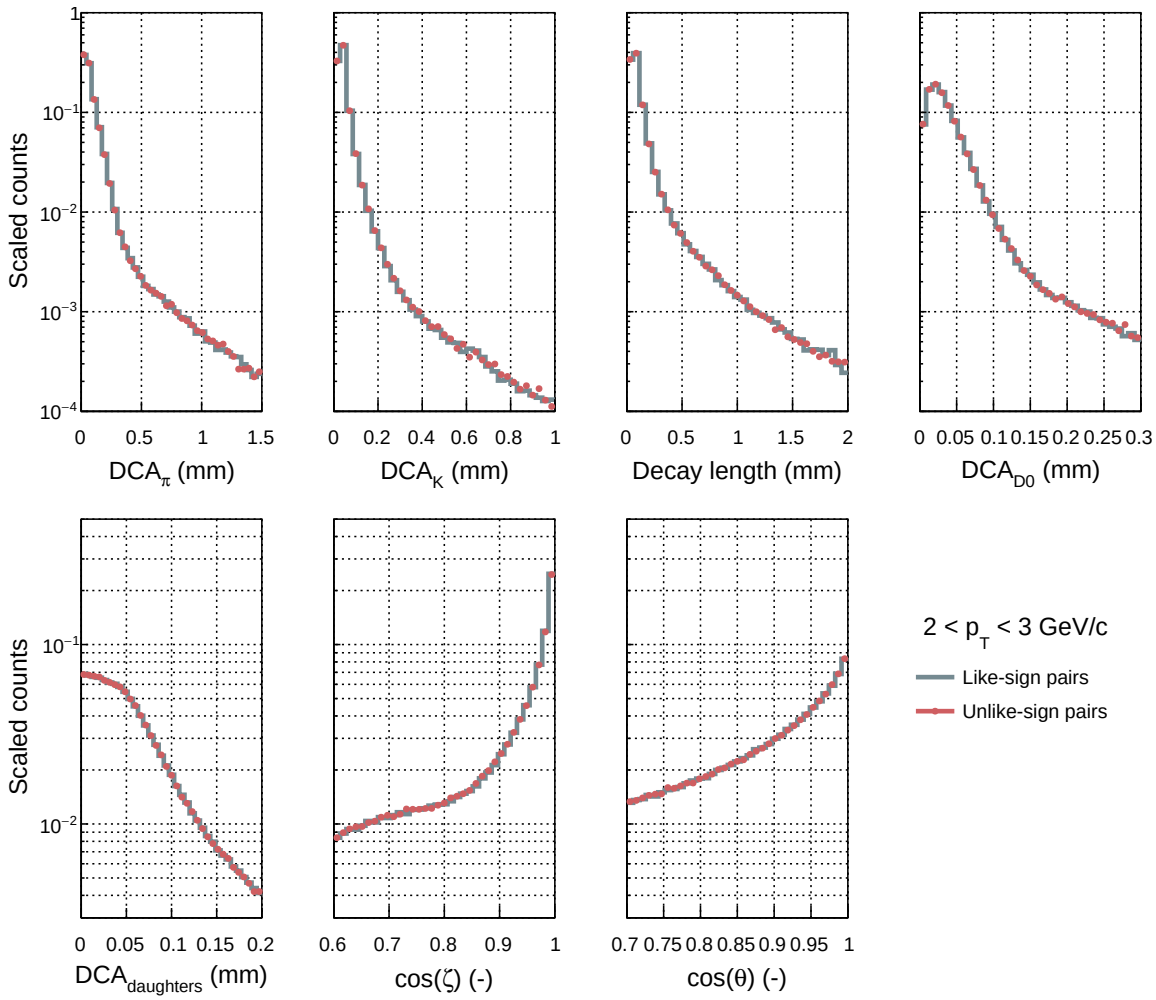

Figure A.1: Distributions of topological variables for Kπ pairs with invariant mass 1.7–2 GeV/c^2, transverse momentum p_{T} 2–3 GeV/c and after application of precuts shown in Table 4.1.

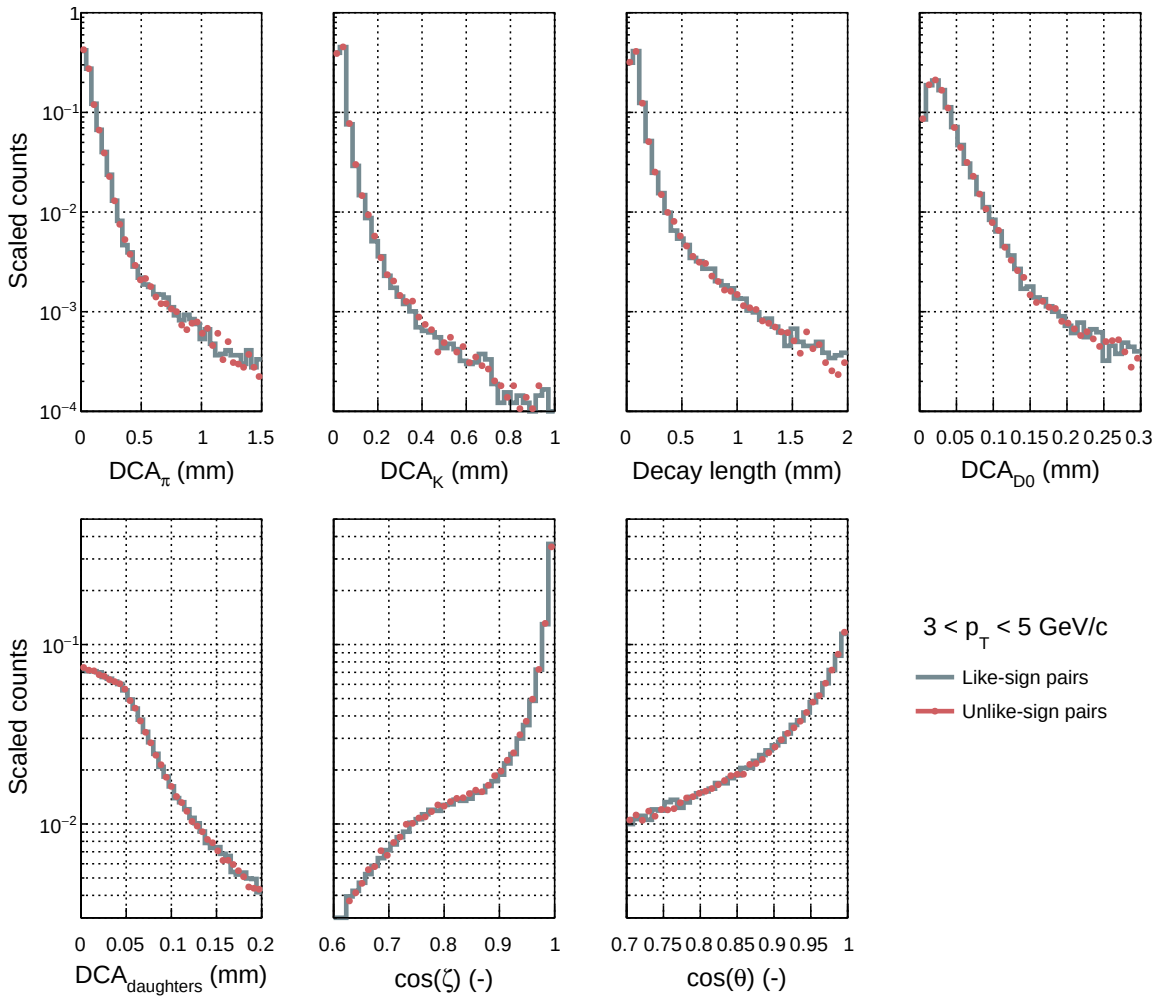

Figure A.2: Distributions of topological variables for Kπ pairs with invariant mass 1.7–2 GeV/c^2, transverse momentum p_{T} 3–5 GeV/c and after application of precuts shown in Table 4.1.

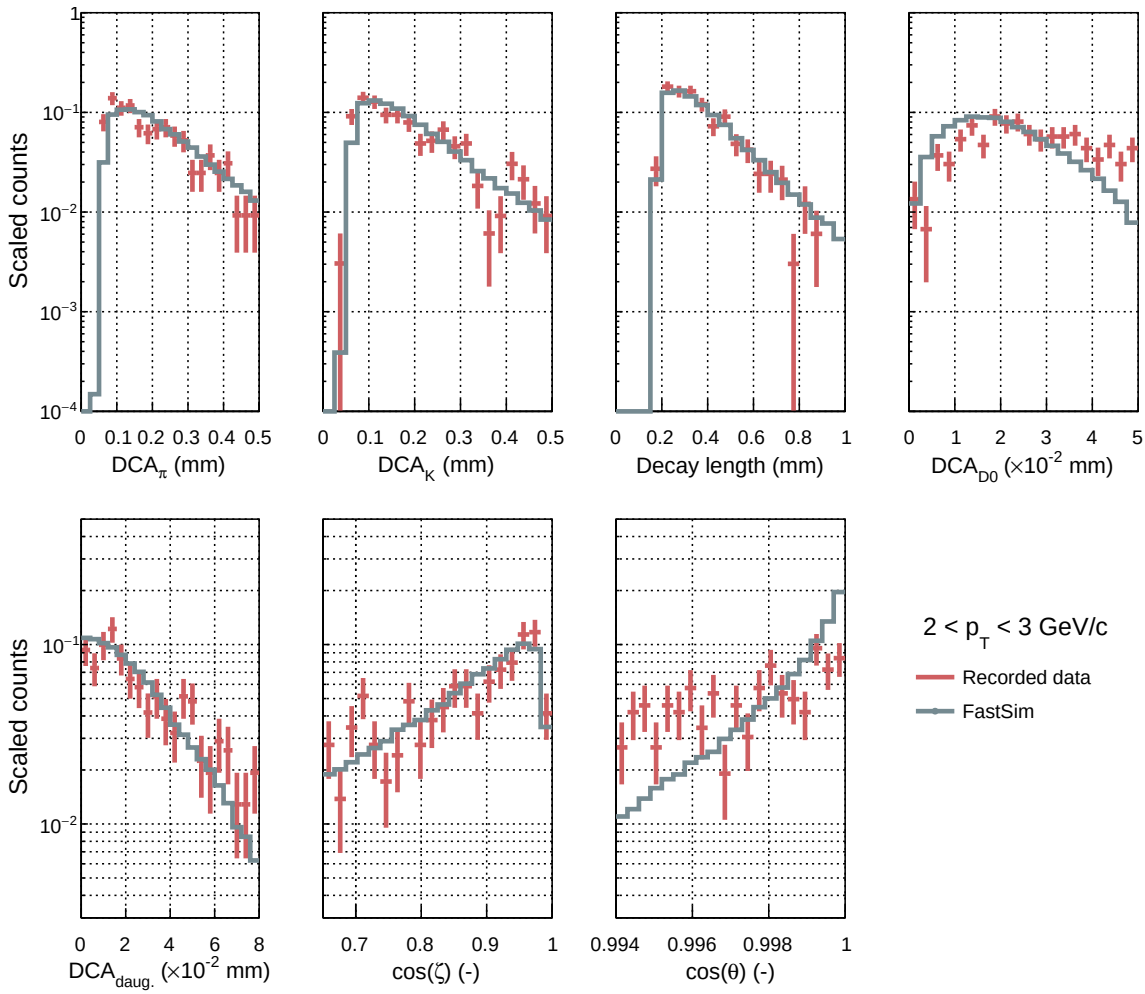

Figure A.3: Distributions of topological variables for Kπ pairs with invariant mass 1.7–2 GeV/c^2, transverse momentum p_{T} 2–3 GeV/c after application of precuts shown in Table 4.1 and analysis BDT response cut.

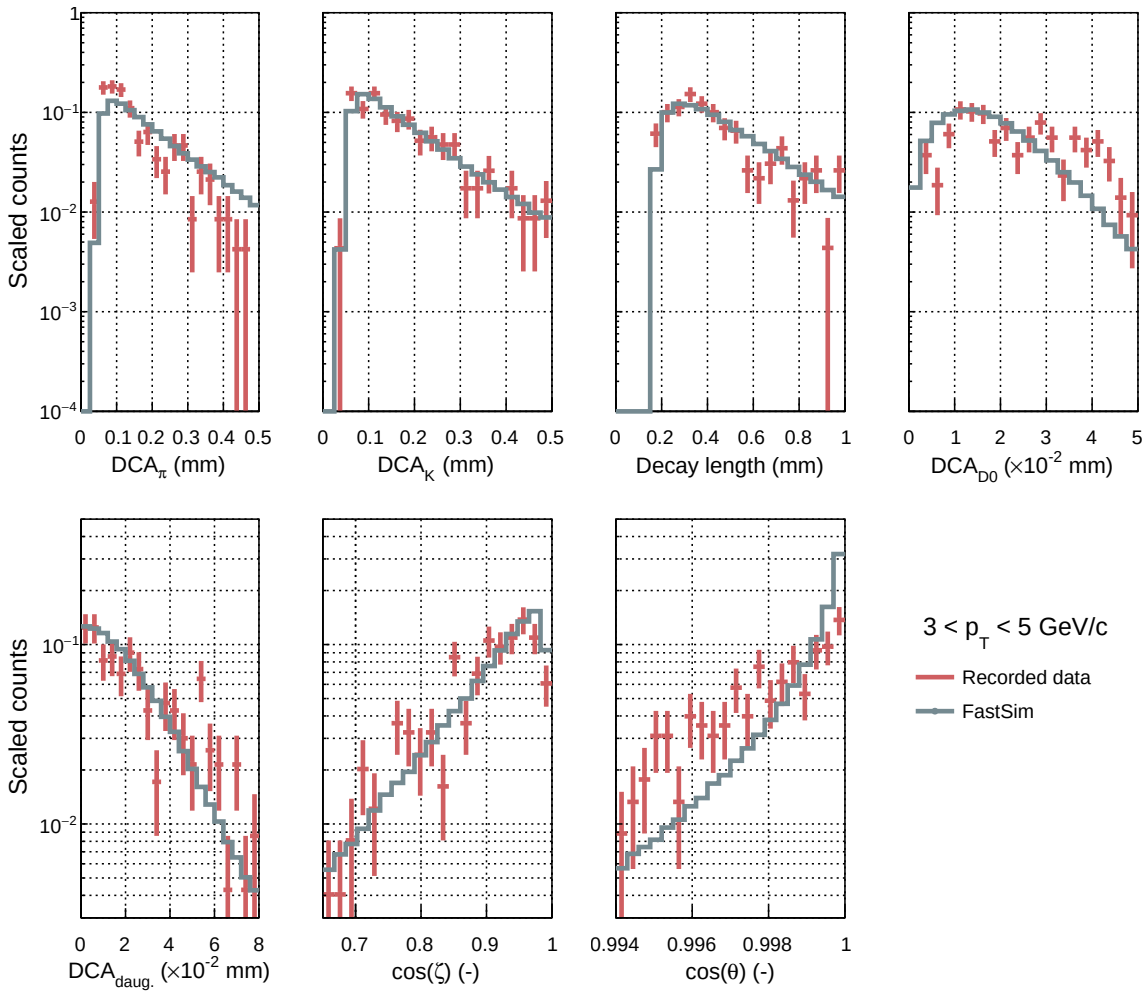

Figure A.4: Distributions of topological variables for Kπ pairs with invariant mass 1.7–2 GeV/c^2, transverse momentum p_{T} 3–5 GeV/c after application of precuts shown in Table 4.1 and analysis BDT response cut.

Appendix B

List of public presentations and posters

Public presentations:

- L. Kramárik, for the STAR Collaboration, *Measurements of open heavy-flavor hadrons in Au+Au collisions at $\sqrt{s_{NN}}$ = 200 GeV with the STAR experiment*, 40th International Conference on High Energy Physics, virtual conference, 28 July–6 August 2020.
- L. Kramárik, for the STAR Collaboration, *Measurements of D^0 production in d+Au collisions at $\sqrt{s_{NN}}$ = 200 GeV by the STAR experiment*, poster presentation, 28th International Conference on Ultrarelativistic Nucleus-Nucleus Collision, Wuhan, China, 4–9 November 2019.
- L. Kramárik, for the STAR Collaboration, *Reconstruction of D^0 mesons in d+Au collisions at $\sqrt{s_{NN}}$ = 200 GeV by the STAR experiment*, poster presentation, 8th International Conference on New Frontiers in Physics, Kolymbari, Greece, 21–29 August 2019.
- L. Kramárik, for the STAR Collaboration, *Measurements of D^0 production in d+Au collisions at $\sqrt{s_{NN}}$ = 200 GeV by the STAR experiment*, poster presentation, 27th International Conference on Ultrarelativistic Nucleus-Nucleus Collision, Venice, Italy, 13–19 May 2018.
- L. Kramárik, for the STAR Collaboration, *Measurements of charm meson production in Au+Au collisions at $\sqrt{s_{NN}}$ = 200 GeV by the STAR experiment*, 19th Conference of Czech and Slovak Physicists, Prešov, Slovakia, 4–7 September 2017.
- L. Kramárik, for the STAR Collaboration, *Measurements of charm meson production in p+p and Au+Au collisions by the STAR experiment*, poster presentation, EPS Conference on High Energy Physics, Venice, Italy, 5–12 July 2017.
- L. Kramárik, *Open heavy-flavour at RHIC and LHC*, poster presentation, 53rd Karpacz Winter School of Theoretical Physics, Karpacz, Poland, 26 February–4 March 2017.

Publications:

- J. Bielčík, K. Hladká, L. Kramárik and V. Kůs, *Machine learning classification for D^0 meson signal extraction in d+Au collisions*, JINST 17 (2022) 02, P02017.
- L. Kramárik, for the STAR Collaboration, *Measurements of open heavy-flavor hadrons in Au+Au collisions at 200 GeV with the STAR experiment*, PoS ICHEP2020 (2021) 546.

- L. Kramárik, for the STAR Collaboration, *Reconstruction of D^0 meson in d+Au collisions at 200 GeV by the STAR experiment*, 2020 Phys. Scr. 95 074010.
- L. Kramárik, for the STAR Collaboration, *Measurements of charm meson production in p+p, p+Au and Au+Au collisions by the STAR experiment*, PoS EPS-HEP2017 (2017) 650.

Published by IOP Publishing for Sissa Medialab

Received: *October 25, 2021*
Revised: *December 20, 2021*
Accepted: *January 21, 2022*
Published: *February 9, 2022*

Machine learning classification for D^0 meson signal extraction in d+Au collisions

J. Bielčík, K. Hladká, L. Kramárik* and V. Kůs

Faculty of Nuclear Sciences and Physical Engineering, Czech Technical University in Prague, Břehová 7, Prague, Czech Republic

E-mail: lukas.kramarik@fjfi.cvut.cz

Abstract: In heavy-ion collisions at large particle colliders, such as LHC or RHIC, heavy-flavour (charm and beauty) quarks are produced mainly through initial hard scatterings. Therefore, they can serve as the probes of properties of the hot medium created in such collisions. Additionally, in small collision systems, such as d/p+Au collisions, cold nuclear matter effects can also affect the charm quark production with respect to p+p collisions.

Hadrons, that contain heavy-flavour quarks, could not be directly detected, thus they are measured via reconstruction of their decay products. However, due to a large number of particles produced in such collisions, separation of the decay products from combinatorial background is challenging and advanced statistical analysis is needed.

In this article, we exploit $D^0(\overline{D^0}) \rightarrow K^-\pi^+(K^+\pi^-)$ decay in order to investigate performance of several machine learning algorithms with different implementation approaches to find the most effective way how to separate signal from random combinatorial background. For this study, we use HIJING and STAR detector simulation of d+Au collisions at $\sqrt{s_{NN}} = 200$ GeV embedded to the collisions recorded with the STAR. In this paper we compare deep neural network implemented using Keras with TensorFlow backend, random forest model implemented using scikit-learn and boosted decision trees implemented by means of the Toolkit for Multivariate Data Analysis with ROOT. Described methods might be applied on reconstruction of any two-body decay in high-energy physics experiments.

Keywords: Analysis and statistical methods; Data processing methods; Particle identification methods; Performance of High Energy Physics Detectors

*Corresponding author.

https://doi.org/10.1088/1748-0221/17/02/P02017

2022 JINST 17 P02017

Contents

2022 JINST 17 P02017

1 Motivation

In high-energy physics, the reconstruction of particle decays is a common step to search for signals of particles, that could not be directly observed in detector systems. In order to extend our knowledge in physics, recorded data need to be exploited as much as possible, thus rare particle decays are analyzed and all the recorded datasets of collisions are used. These decays represent only a small fraction of the recorded particles, which leads to the very low signal-to-background ratio in the analyses [1]. Therefore they could not be identified on an event-by-event basis and consequent statistical analysis of the complete set of recorded collisions needs to be done.

For the signal from background separation, mainly rectangular cuts on decay properties, such as the distance from the place of collisions or the angle between decay products, are used [2–4]. In recent years the data analyzers started applying machine learning (ML) algorithms in order to optimize the signal and background separation. The particular application of the algorithm is often motivated by practical arguments such as the existence of an implementation in the Toolkit for Multivariate Data Analysis (TMVA) package [5], but the comparison of the performance of various algorithms is missing. Especially the application of the boosted decision trees (BDT) machine learning algorithm from the TMVA is currently popular [6–11]. Other classification machine learning algorithms, such as the random forest (RF) of independent trees not linked via boosting, and, on the contrary, more complex deep neural networks (DNN) are not overall common for signal classification in high-energy physics. However, their current implementation in scikit-learn [12] and Keras [13] packages enables their suitable use in wide ranges of problems across numerous research and business fields. When dealing with specific problems it is difficult to select an appropriate ML algorithm, because of multidimensionality of the feature space (number of input variables) and impossibility to see it

as a whole. This causes a priori the selection of appropriate classification algorithm challenging. The most suitable algorithm is typically identified a posteriori only after a number of optimized algorithms are applied to the specific data sample and their performance is evaluated.

In this article, we present the step-by-step setup and performance comparisons of the RF, BDT and DNN algorithms in the search for D^0 meson signal using simulated deuteron-gold (d+Au) collisions at $\sqrt{s_{NN}} = 200$ GeV from the Solenoidal Tracker at RHIC (STAR) experiment. Performance of these algorithms is compared using the receiver operating characteristic (ROC) curves, that show dependency of signal efficiency on background efficiency for different threshold on output classifications.

D^0 meson measurement is challenging due to its short mean lifetime of $\tau = (410.1 \pm 1.5) \times 10^{-15}$ s, that corresponds to $c\tau = 122.90 \pm 0.45$ µm [14]. In order to determine the yield of D^0 meson produced in collisions, the invariant mass distribution of pairs of daughter particles is used, where a signal peak, around the invariant mass of the D^0 meson (1864.83 ± 0.05 MeV/c^2 [14]), is expected to be observed above the background.[1] Without any selection criteria, the signal peak has low significance because only a small fraction of these pairs is from the D^0 meson signal.[2]

The D^0 meson contains a charm quark, which is relatively heavy when compared to the scale of strong interactions given by Λ_{QCD}. Therefore, in heavy-ion collisions, such as gold-gold (Au+Au) at the STAR experiment, it probes evolution of the collisions and mainly the quark-gluon plasma, hot nuclear matter created in such collisions. To separate effects of the hot medium from those induced by the large number of nucleons present in the collision (so-called Cold Nuclear Matter effects), asymmetric small-systems collisions are studied. At the Relativistic Heavy-Ion Collider (RHIC), these are p+Au and d+Au collisions.

2 Data for the analysis

Simulation of collisions is used to generate approximately 3 million of collision events similar to the real recorded data, but with the additional information on the particles created in the early stage of collisions that could not be directly detected. For the purpose of this study, d+Au collisions at $\sqrt{s_{NN}} = 200$ GeV and tracks in the final state are generated by the HIJING [15] simulator. It is required that at least one D^0 meson per collision with daughter tracks (kaon and pion) in the STAR detector acceptance is produced. All the simulated tracks enter the GEANT [16] simulation of the STAR detector response. Additionally, these generated data are mixed with the real events recorded by STAR in 2016 in order to have a data sample similar to the measured data. Thanks to this full detector simulation, simulated data are analysed in the same way as done for measured data and tracks are reconstructed back from hits registered in the detectors. Reconstructed tracks in this simulation are used to train and test studied machine learning algorithms. All simulations are produced using the STAR collaboration infrastructure.

The D^0 meson signal is analysed using the topological reconstruction of the hadronic decay $D^0 \to K^-\pi^+$ with branching ratio of 3.89 ± 0.04 % [14]. The signal is enhanced by combining D^0

[1] Invariant mass M of combined particles in natural units is defined as $M^2 = (\sum_i E_i)^2 - \|\sum_i \mathbf{p}_i\|^2$, where E_i are energies and $\mathbf{p}_i$ momentum vectors of particles.

[2] Significance is defined as $S/\sqrt{S+2B}$, where S and B are number of signal and background in the observed region, respectively.

2022 JINST 17 P02017

and $\overline{\mathrm{D}^0}$ mesons, thus both unlike-sign charge combinations ($\mathrm{K}^-\pi^+$ and $\mathrm{K}^+\pi^-$) are considered to be correct charge pairs.

Firstly, tracks reconstructed by the detector are identified and selected in the same way, as it is done in the real data analysis. The STAR consists of multiple subdetectors able to track and identify charged particles down to very low transverse momentum p_{T} at mid-rapidity ($|\eta| < 1$) with full azimuthal coverage.[3] In this analysis, tracks with p_{T} larger than 0.15 GeV/c and in the full space covered by the STAR detector are used.

Information from the Time Projection Chamber (TPC) [17], the Time of Flight (TOF) [18], and the Heavy Flavor Tracker (HFT) [19] detectors are used to select kaons and pions that are then combined to pairs. The TPC is used for both tracking and particle identification using the specific energy loss $\mathrm{d}E/\mathrm{d}x$ deposited inside the detector. Kaons and pions selected for the analysis are required to have at least 15 measured points in the TPC out of a maximum equal to 45. To identify tracks, the deviation of the measured $\mathrm{d}E/\mathrm{d}x|_{\mathrm{meas}}$ from the expected $\mathrm{d}E/\mathrm{d}x|_{\mathrm{exp}}$ is calculated as

$$n\sigma = \frac{1}{R} \ln \frac{\mathrm{d}E/\mathrm{d}x|_{\mathrm{meas}}}{\mathrm{d}E/\mathrm{d}x|_{\mathrm{exp}}}, \tag{2.1}$$

where R is the $\ln(\mathrm{d}E/\mathrm{d}x)$ resolution of the TPC [17]. Pions are selected with the condition $|n\sigma| < 3$ and kaons $|n\sigma| < 2$.

Particle identification is further improved with the TOF detector that measures the track velocity β. If the track has hit in this detector, the measured velocity β_{meas} is compared to the expected β_{exp} and is required to fulfill $|1/\beta_{\mathrm{meas}} - 1/\beta_{\mathrm{exp}}| < 0.03$ in order to be used in the D^0 meson reconstruction.

At STAR, the HFT is the crucial detector for the measurements of open heavy-flavor particles with short lifetimes thanks to its fine track pointing and vertex resolution. It is made up of four layers of silicon sensors forming three detection systems. The systems ordered from the closest to the furthest from the place of the collision are: the PIXEL, containing two layers of Monolithic Active Pixel Sensors, the Intermediate Silicon Tracker (IST), and the Silicon Strip Detector (SSD). In this analysis, tracks are required to have hits in both layers of PIXEL detector and at least one hit in IST or SSD layers of the HFT.

3 Inputs to the classification

After passing all of the described selection criteria, the tracks are combined to like-sign and unlike-sign $\mathrm{K}\pi$ pairs. Only the pairs with invariant mass in the region from 1.7 GeV/c^2 to 2 GeV/c^2 are selected and further analyzed.

Then, topological variables specific for two-particle decays are calculated. Figure 1 shows the schema for reconstructed D^0 meson decay into kaon and pion. Observed topological variables are smeared due to the finite detector resolution, thus selection criteria or classifier algorithm are needed to select $\mathrm{K}\pi$ pairs coming from D^0 decays. The primary vertex (PV) is the reconstructed position of d+Au collision, whereas the secondary vertex (SV) is the reconstructed point of the D^0 meson decay. It is calculated as the midpoint of the line corresponding to the distance of the

[3] $p_{\mathrm{T}} = \sqrt{p_{\mathrm{x}}^2 + p_{\mathrm{y}}^2}$, where particle momentum vector $\mathbf{p} = (p_{\mathrm{x}}, p_{\mathrm{y}}, p_{\mathrm{z}})$, while p_{z} denotes momentum in the direction of beam (colliding nucleons).

2022 JINST 17 P02017

closest approach (DCA) between kaon and pion tracks, $DCA_{daughters}$. Then, the decay length of reconstructed D^0 meson is the distance between the PV and the SV. DCA of D^0 meson to the PV (DCA_{D0}) is calculated using the vector of reconstructed D^0 momentum. The cosine of an angle between D^0 momentum and the decay length vector, θ, and the cosine of an angle between D^0 momentum and kaon momentum, ζ, both calculated in the laboratory frame, are other variables used for classification.

Since the origins of kaon and pion tracks coming from D^0 meson decay are expected to be shifted from the PV, their DCA to the PV, DCA_K and DCA_π, are as well expected to have significant classification power.

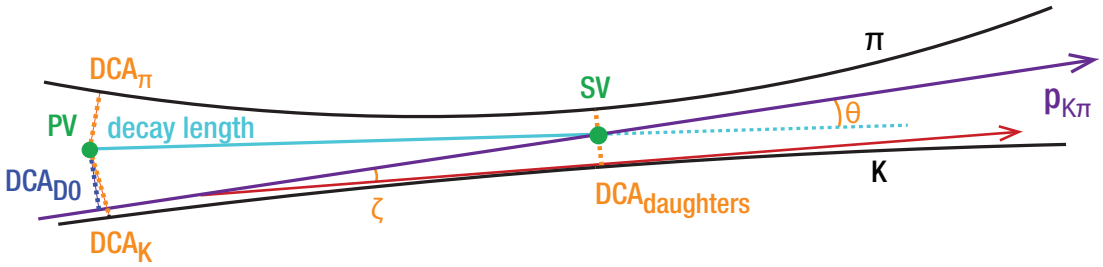

Figure 1. Schematic representation of $D^0(\overline{D^0}) \rightarrow K^-\pi^+(K^+\pi^-)$ decay and its topological properties. Curvatures of K and π tracks are exaggerated.

Additionally, each reconstructed correct-charge Kπ pair is associated to the tracks in the HIJING simulation in order to identify those coming from the real D^0 meson decay. Those tagged as D^0 meson daughters enter as signal sample to the classification training, other correct-charge pairs are considered to be the background. For testing phase of the methods, combined signal and background correct-charge pairs are used. In the analysis of real data, the combinatorial background left after classification is usually estimated by wrong-charge (like-sign) pairs and statistically subtracted from the distributions classified as signal in correct-charge pairs. Figure 2 shows distributions of topological variables for correct-charge and wrong-charge pairs with transverse momentum $1 < p_{T,K\pi} < 2\,\mathrm{GeV}/c$. As it could be observed, there is a difference between correct-charge signal and background distributions, from which the consequent classification algorithm might benefit. However, in the real data, signal distribution is unknown and there is only a small fraction of signal pairs in the correct-charge pairs, causing nearly similar shape of correct-charge and wrong-charge pairs distributions. Furthermore, as it could be observed from shown background ratios, there is no significant distributional difference between correct-charge background pairs, that are not coming from D^0 meson decay in our data, and wrong-charge pairs.

All classification methods are independently trained and tested in the five D^0 meson transverse momentum p_{T,D^0} intervals: 0–1, 1–2, 2–3, 3–5, and 5–8 GeV/c. These intervals reflect typical p_{T,D^0} range measured by the STAR experiment and rapidly falling D^0 meson spectra [3, 20, 21]. Ranges of p_{T,D^0} correspond to the subdivisions of the data according to $p_{T,K\pi}$ with the same intervals.

Since the signal-to-background ratio in real collisions is typically very low, preselection of pairs is done before training and application of the classification methods. Main goal is to cut-out regions, where a massive portion of the good signals of the studied particle is not expected or might be hardly

2022 JINST 17 P02017

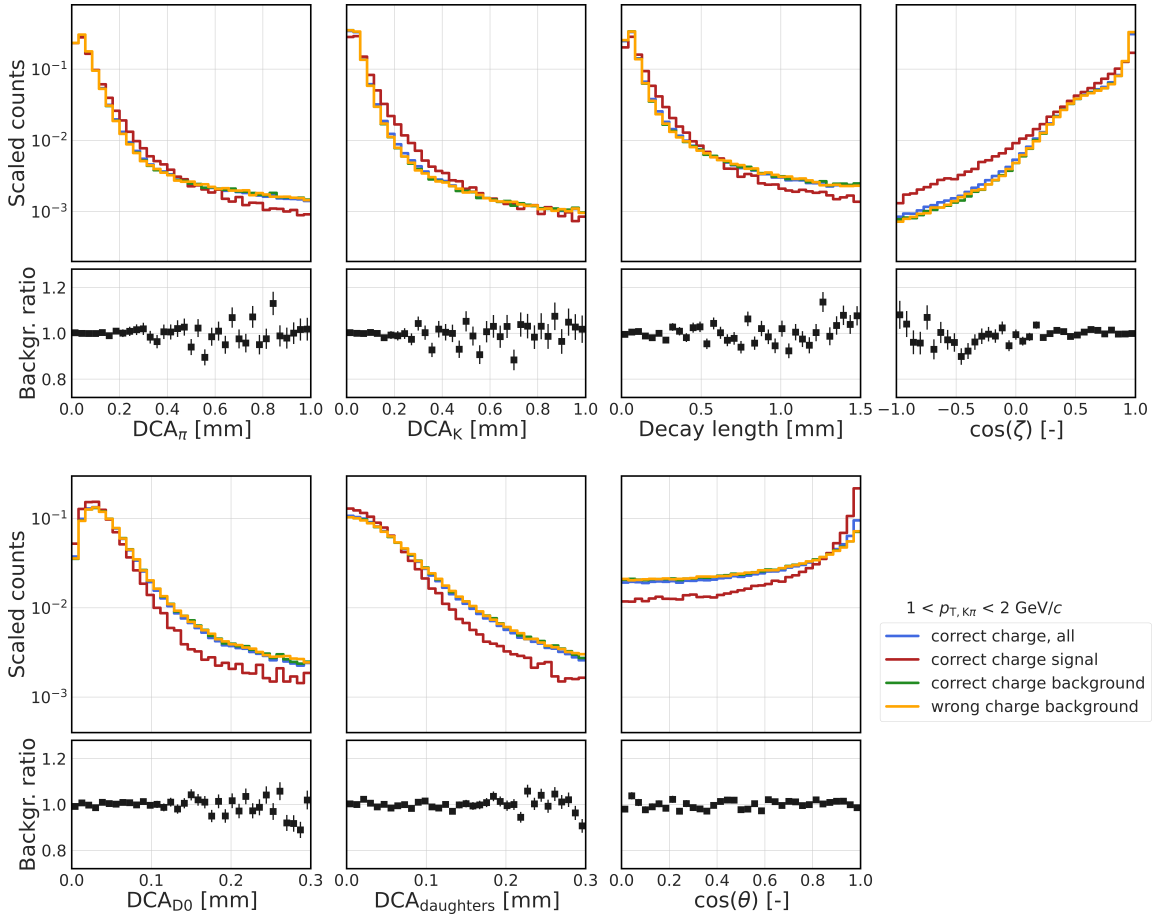

Figure 2. Distributions of topological variables for Kπ pair transverse momentum $1 < p_{\mathrm{T,K}\pi} < 2\,\mathrm{GeV}/c$ and for correct-charge and wrong-charge Kπ pairs, together with corresponding ratios of correct-charge and wrong-charge backgrounds Kπ pairs distributions.

distinguishable from background due to its significant distortion caused by the detection system. The goal is to find such preselection that suppress background more than signal. In this analysis, preselection efficiency is tested with three sets of rectangular cuts on D^0 meson decay properties. These cuts are similar in all $p_{\mathrm{T,D}^0}$ intervals. The cuts are listed in table 1 and resulting efficiencies in studied $p_{\mathrm{T,D}^0}$ intervals are plotted in figure 3. Signal efficiency is defined as the ratio between the number of signal pairs, after cut application, and the number of all signal pairs, background efficiency is defined analogically. As it can be seen, the background efficiencies of loose cuts are nearly similar to the signal ones', however, tighter cuts suppress background significantly more than the signal. For the study of machine learning algorithms performance, we decided to compare tight cut preselection and the option with no preselection criteria applied. By cutting out the area with low signal density, algorithms are forced to focus on the region, where the signal density is high on the one hand, but on the other hand hard to be set apart from the background. Using this approach we expect to obtain algorithms precise in high signal density region. To summarize, all three supervised machine learning algorithms are trained over every train set separately resulting in 30 final classifiers (three types of classification algorithms, five $p_{\mathrm{T,D}^0}$ intervals, with and without precut application).

2022 JINST 17 P02017

Table 1. Sets of preselection cuts applied to topological variables of D^0 meson decay before classification methods have been trained.

	Loose cuts		Intermediate cuts		Tight cuts	
Variable	Min.	Max.	Min.	Max.	Min.	Max.
$DCA_{K,\pi}$ [mm]	0.0	10.0	0.0	1.0	0.002	2.0
$DCA_{daughters}$ [mm]	0.0	5.0	0.0	0.3	0.0	0.2
decay length [mm]	0.0	5.0	0.0	1.5	0.005	2.0
DCA_{D0} [mm]	0.0	5.0	0.0	0.3	0.0	0.5
$\cos\theta$ [-]	−1.0	1.0	0.0	1.0	0.7	1.0

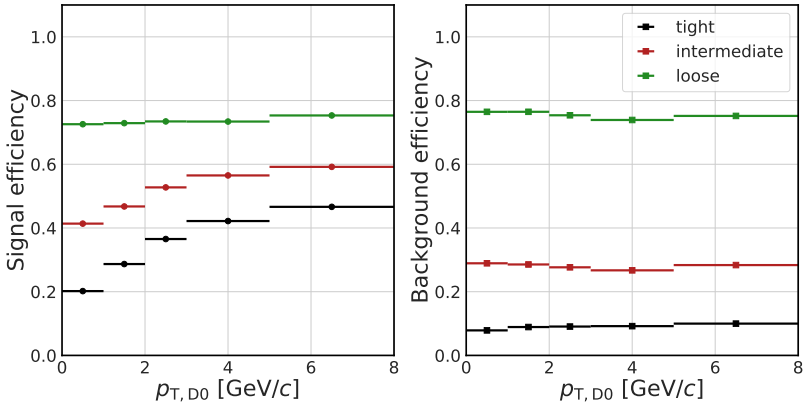

Figure 3. Signal (left) and background (right) efficiencies vs. reconstructed transverse momentum of Kπ pairs (D^0 meson candidates) p_{T,D^0} for selection cuts listed in table 1.

4 Machine learning algorithms setup and training

4.1 Random Forest

RF is an interpretable robust machine learning algorithm based on the ensemble of decision trees [22]. Additionally, training and optimization of RF is relatively fast compared to DNN. However, for such classes that can not be separated using linear partitioning, the depth of individual trees of the ensemble may increase dramatically. The trees, tied up together using bootstrap aggregating algorithm, ensure partitioning of the observation space and assign class labels to these partitions. In this study, scikit-learn [12] RF implementation is applied.

Firstly, input data in all p_{T,D^0} intervals are divided into training and test sets in 6:4 ratio. For the setup with precuts, this division is done after their application. For each p_{T,D^0} interval, feature-wise standardization is fitted for all topological variables over training data and both training and test sets are transformed by it.[4]

Next, optimized random forest is trained over balanced training set in terms of number of samples per class. The corresponding hyper-parameter space for optimization of the classifier is given in table 2 and is the same for all p_{T,D^0} intervals. In order to enhance the RF classification

[4]In machine learning, feature-wise standardization rescales the features to have zero mean and standard deviation equal to one in order to align feature ranges.

2022 JINST 17 P02017

performance, Gini (G) and Entropy (E) impurity measures for evaluation and selection of possible sample split inside the tree's node are tested. We aim to the partitioning of the feature space as much as possible for sufficient class distinction. However, too fine partitioning results in model overfitting. Therefore, classification quality dependency on maximum depth of trees d_{max} is explored as well. Sufficient information exploitation of all features is ensured with increasing number of trees N_{trees}. Nevertheless, for the larger values of N_{trees}, the classification quality improvement may not be noticeable while the computational complexity is increasing dramatically. During the training phase, 3-fold cross-validation is used to train the RF model taking each combination of hyper-parameters over each $p_{\text{T,D}^0}$ interval (grid search). The set of hyper-parameters producing trained classifier with the highest average area value under the ROC curve (AUC) is refitted over the whole training set and later validated over test set.

The parameters of the optimized classifier resulting from the grid search are presented in table 3. Entropy is the optimal impurity measure for each scenario. There seemed to be no trend with respect to $p_{\text{T,D}^0}$ values in selection of N_{trees} and d_{max} of the ensemble. In the scenario, where precuts are not applied, optimization selects deeper trees within the ensemble since more complex input space partitioning is needed.

Table 2. Hyper-parameter space for random forest optimization — tested options of maximum depth of trees d_{max}, number of trees N_{trees}, impurity measure.

Parameter	Options						
d_{max}	20	17	15	12	10	7	5
N_{trees}	1200	1000	800	600	400	200	
Impurity measure	Gini (G)	Entropy (E)					

Table 3. Optimized parameters (number of trees N_{trees}, maximum tree depth d_{max}, impurity measure) of random forest classifiers for Kπ pair transverse momentum $p_{\text{T,D}^0}$ intervals with and without precuts application. Entropy (E) impurity measure is selected for all input data setups.

	With precuts					Without precuts				
$p_{\text{T,D}^0}$ [GeV/c]	0–1	1–2	2–3	3–5	5–8	0–1	1–2	2–3	3–5	5–8
d_{max}	10	13	12	10	7	15	15	12	12	7
N_{trees}	1200	600	1000	200	200	1200	600	1000	1200	200
Impurity measure	E	E	E	E	E	E	E	E	E	E

4.2 Boosted Decision Trees

BDT machine learning algorithm from the Toolkit for Multivariate Data Analysis (TMVA) package [5] is applied in this analysis. Data in all $p_{\text{T,D}^0}$ intervals are divided into training and test set in 6:4 ratio, in the same way as it was done for RF algorithm. Signal and background sets are balanced using the class weights.

In the BDT, compared to the RF method, individual trees are not independent, but boosting is applied, i.e., data misclassified by a tree have higher weight in the training of the next tree. Calculation of this weight depends on the chosen boosting algorithm and classification error fraction of the

2022 JINST 17 P02017

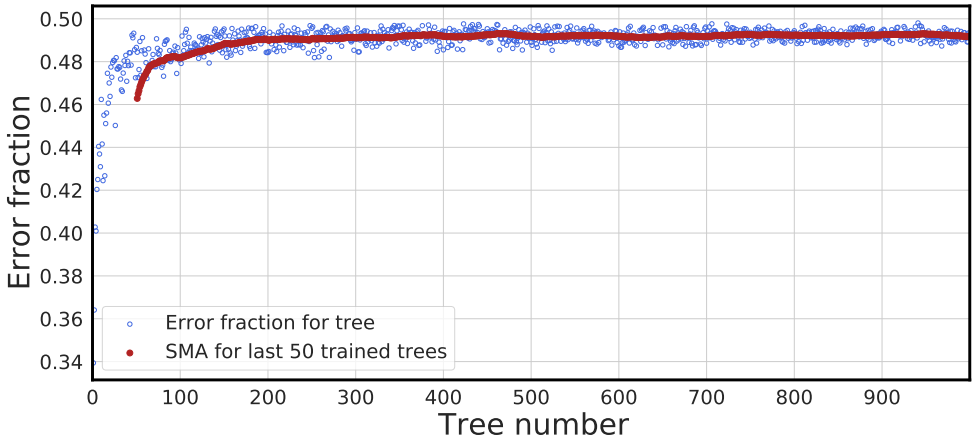

Figure 4. Error fraction of gradually trained boosted decision trees and simple moving average (SMA) of error fraction for the last 50 trees for $1 < p_{\mathrm{T,D^0}} < 2\,\mathrm{GeV}/c$.

tree. For boosting, adaptive boosting algorithm (AdaBoost) is chosen. Error fraction of every tree is determined by calculating how much signal events have positive BDT response (defined in $[-1, 1]$ range) and vice-versa for the background. As more trees are trained, their error fraction is getting higher and converges, as it is shown in figure 4. The trees with error fraction close to 0.5 are very weak classifiers and thus does not significantly help to classify the data. At first, in all $p_{\mathrm{T,D^0}}$ intervals, BDT with 1000 trees is trained. Error fraction for $1 < p_{\mathrm{T,D^0}} < 2\,\mathrm{GeV}/c$ is displayed in figure 4 and it is similar also in other intervals. Simple moving average of the error fraction shows that it converges around 300th tree. Finally, to be on the safe side, we decided to train final models with 500 trees.

Other BDT parameters are set in a usual way in high-energy physics [5]. To minimize overtraining, maximum tree depth is set to 3 and minimum number of training events required in the tree leaf is 2.5 % of the training events in the $p_{\mathrm{T,D^0}}$ interval. Gini impurity measure is employed to separate nodes with not limited number of test cuts on variable in the training sample. Finally, bagging is applied to minimize overtraining further, so for each tree training, 50 % of randomly selected training sample pairs is used.

4.3 Deep Neural Networks

To explore more complex machine learning method, DNN's [23] are tested for the classification of $\mathrm{D^0}$ meson signal, too. DNN are able to perform non-linear transformations of input space. Hence, DNN may address complex classification problems more effectively when optimized properly. Additionally, usage of DNN reduces the need of extensive feature engineering. However, DNN decision process is not easily interpretable. Both training and optimization require large amount of CPU time, computational power and training data.

To implement the method, Keras with TensorFlow backend is used [13]. Basic architecture of the model is derived empirically, however, other model's attributes are left to be optimized. Model architecture is visualized in figure 5. Blue color shows the parameters to be optimized: size of the hidden layer w, activation function of hidden layers a, and dropout rate p. Data are fed to

2022 JINST 17 P02017

the input layer with 7 neurons, corresponding to the 7 D^0 meson topological decay variables, and transferred using the network connections (weights) through the hidden layers to the final (output) layer. For hidden layers, batch normalization (BN) is applied. Outputs of inner and final layers are not only scaled using the network weights, but also using activation functions. Since the desired network output is the probability of the sample being signal or background, activation function of the output layer is set to a sigmoid and the loss function, used for optimization, is binary-crossentropy. Additionally, common DNN parameters, such as optimizer, batch size B, learning rate γ (or its initial value) and type of kernel initialization are optimized. Range of the hyper-parameter space is presented in table 4 and it is the same for all $p_{\mathrm{T,D^0}}$ intervals.

Data are divided into three subsets: training, validation and test in 6:2:2 ratio. For each $p_{\mathrm{T,D^0}}$ interval, balancing of the training set is performed. Firstly, feature-wise standardization is fitted and applied to the training data and then applied to the corresponding validation and test sets. Then, the training phase over given $p_{\mathrm{T,D^0}}$ interval is performed in two steps. In the first step, for all combinations of hyper-parameters in table 4, DNN model is trained for 70 epochs. The parameters of the classification model with the highest AUC are used to perform the second step, where the training of the model starts all over again with fixed values of parameters. Training is stopped when the validation accuracy is not improved during the last 60 epochs (early stopping rule). Since the validation set is already used for hyper-parameters selection thus it influences the classifier training, binary classification metrics are evaluated over the test set only. Iterative algorithms (optimizers), such as stochastic gradient descent, are used to find neural network weights that minimize loss function. To enhance ability of neural network's convergence, the optimizers with adaptive learning rate (Adam, AdaMax) are tested as well. Adaptive change of learning rate γ in the training process enables the optimizer to recognize and escape local minima of the loss function more efficiently. Appropriate kernel initializer may further help optimizer to converge smoothly. Therefore, Lecun uniform, He normal and He uniform initializers of weight values are explored when searching for optimal hyper-parameter combination of the DNN model. Dropout is used as generalization technique and it is tested at different rates p. Additionaly, trade-off between generalization and computational speed is examined by training the models for several values of batch size B. Unlike RF, more consistent parameter combinations are selected as optimal for given $p_{\mathrm{T,D^0}}$ intervals and pre-processing types.

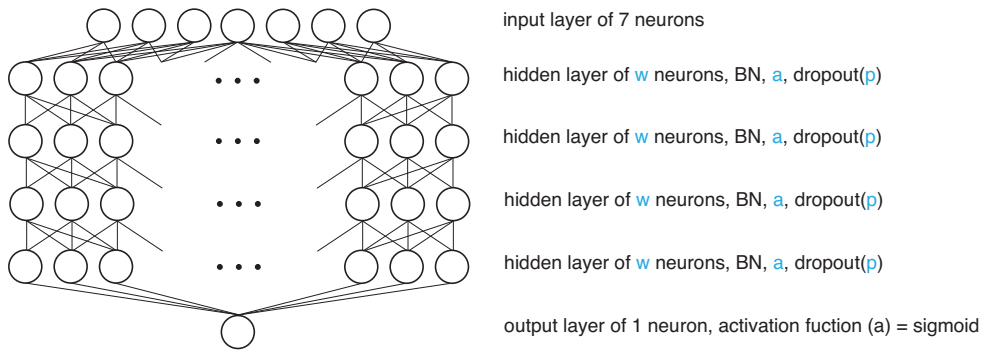

Figure 5. Schema of deep neural network architecture with description of the setup of layers. Parameters of hidden layers in blue are left to optimization: number of neurons w, activation function a and dropout rate p. Batch normalization (BN) is applied in all hidden layers.

2022 JINST 17 P02017

In all cases, $w = 256$ neurons is selected as the optimal width of the inner layer. The training performs the best at batch size value $B = 64$. Activation function ReLU together with dropout $p = 0.2$ and Adam optimizer starting at initial learning rate $\gamma = 1 \cdot 10^{-5}$ are chosen as the optimal parameters in all scenarios except interval $5 < p_{\mathrm{T,D^0}} < 8\,\mathrm{GeV}/c$, where precuts were not applied. In this case tanh activation function achieves better performance. The classification quality is maximal under He normal kernel initialization for $0 < p_{\mathrm{T,D^0}} < 1\,\mathrm{GeV}/c$ and with Lecun uniform kernel initialization for $p_{\mathrm{T,D^0}} > 2\,\mathrm{GeV}/c$, when precuts are applied, as well as for $p_{\mathrm{T,D^0}} > 1\,\mathrm{GeV}/c$, when no precuts are used. He uniform kernel initialization results in the best model performance for the data pre-processed with precuts in the $1 < p_{\mathrm{T,D^0}} < 2\,\mathrm{GeV}/c$ interval.

Table 4. Hyper-parameter space for deep neural network setup optimization — options for activation function of hidden layers a, learning rate γ, dropout rate in hidden layers p, optimizer, kernel initialization, batch size B, number of neurons in hidden layers w.

Parameter	a	γ [$\cdot 10^{-5}$]	p	Optimizer	Kernel init.	B	w
	ReLU	0.1	0.2	Adam	Lecun uniform (LU)	64	64
Options	tanh	0.5	0.3	Stochastic grad. descent	He normal (HN)	128	128
		1.0	0.4	AdaMax	He uniform (HU)		256

5 Performance evaluation and comparisons

Machine learning classification methods are compared using the ROC curves, that are shown in figure 6 for data with and without precut application. Resulting AUC's are in table 5.

Generally, classification ability increases with higher $p_{\mathrm{T,D^0}}$. This might be caused by physical properties of the studied decay. D^0 meson with low $p_{\mathrm{T,D^0}}$ decays closer to the primary vertex, which leads to low $\mathrm{DCA_K}$, DCA_π and $\mathrm{DCA_{D0}}$. Therefore, these are hardly distinguishable from the combinatorial background composed mainly from particle coming from PV, thus having low $\mathrm{DCA_K}$ and DCA_π, too. With higher $p_{\mathrm{T,D^0}}$, D^0 meson decays later and its topological properties are in the region with less similar combinatorial background pairs.

For $p_{\mathrm{T,D^0}} < 5\,\mathrm{GeV}/c$, classifiers trained over the data after precut application achieve higher AUC values than those trained without precuts application. This is caused by significant background suppression under precuts. In this case, the total signal efficiency is also additionally decreased by the one plotted in figure 3. For $5 < p_{\mathrm{T,D^0}} < 8\,\mathrm{GeV}/c$ the difference in AUC between precut data and no precut data is relatively small compared to other $p_{\mathrm{T,D^0}}$ intervals, that might be caused by the described properties of D^0 meson with high $p_{\mathrm{T,D^0}}$.

As it can be seen from ROC curves in figure 6, for data with precuts inside $1 < p_{\mathrm{T,D^0}} < 5\,\mathrm{GeV}/c$, the RF classification has significantly better performance than other methods. For data without precuts application, the RF could not extract significantly more information and it is slightly more successful compared to the BDT and the DNN. This gain is more significant for data with precuts in p_{T} intervals $1 < p_{\mathrm{T,D^0}} < 2\,\mathrm{GeV}/c$ and $2 < p_{\mathrm{T,D^0}} < 3\,\mathrm{GeV}/c$, where maximal possible result in signal separation is achieved thanks to the RF procedure. On the other hand, the BDT and DNN are almost similar in terms of ROC and AUC.

2022 JINST 17 P02017

Table 5. Area under receiver operating characteristic (ROC) curve of tested machine learning methods on test samples of datasets in D^0 meson candidate transverse momentum p_{T,D^0} intervals.

	With precuts					Without precuts				
p_{T,D^0} [GeV/c]	0–1	1–2	2–3	3–5	5–8	0–1	1–2	2–3	3–5	5–8
Random forest	**0.81**	**0.87**	**0.94**	**0.95**	**0.96**	**0.73**	**0.79**	0.82	**0.90**	**0.94**
Boosted decision trees	0.78	0.84	0.90	0.93	0.93	0.70	0.76	**0.83**	0.89	**0.94**
Deep neural network	0.79	0.83	0.90	0.93	0.91	0.70	0.76	**0.83**	0.89	0.92

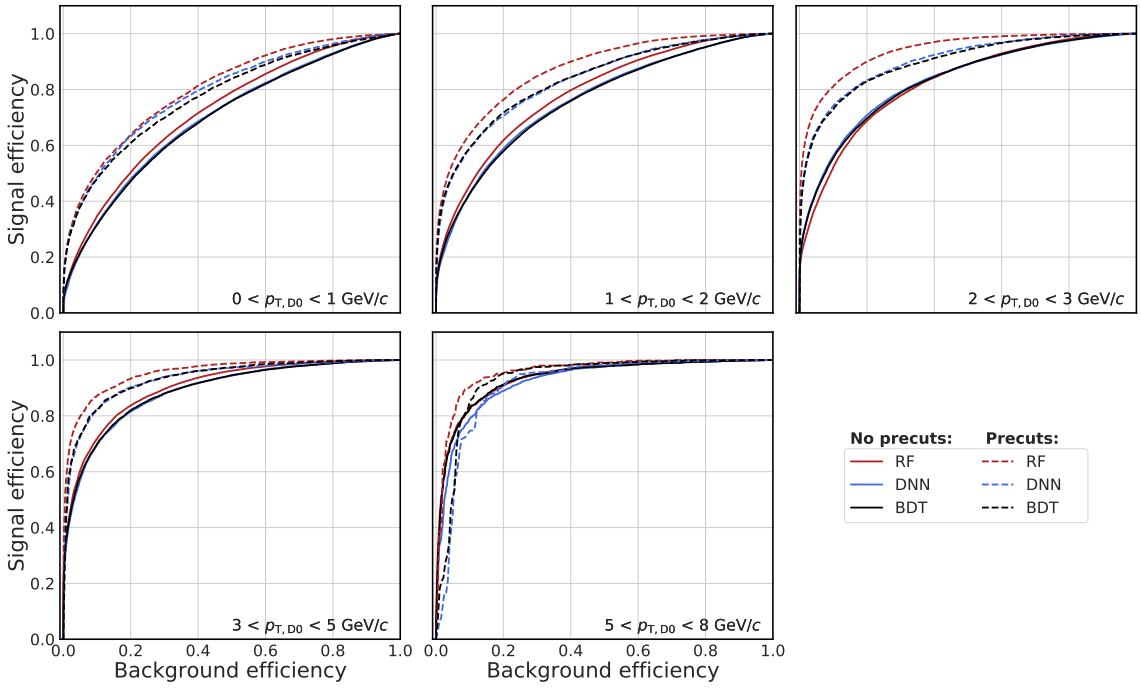

Figure 6. The receiver operating characteristic (ROC) curves for random forests (RF), deep neural networks (DNN) and boosted decision trees (BDT) in D^0 meson candidate transverse momentum p_{T,D^0} intervals, with and without precuts application.

6 Conclusions

Performance study of the machine learning classification methods for signal extraction in two-body decay analysis is reported. Simulated d+Au collisions at $\sqrt{s_{NN}} = 200$ GeV with the STAR experiment are used to study reconstruction of D^0 meson. In order to select D^0 meson decay candidates from $K\pi$ pairs, we test several machine learning classifiers with different implementation approaches: DNN from Keras, RF from scikit-learn and BDT from TMVA package.

To train classifier with the most efficient separation ability, multistep data pre-processing approach is used. Precuts application to the data is tested and it significantly improves classification power of the algorithms. The RF and DNN setup with the best performance is found with grid search over multiple setups of corresponding machine learning parameters. The overall classification rates ranges from 0.81 to 0.96 throughout all the precut D^0 meson transverse momentum intervals which is quite sufficient to carry out any relevant subsequent physical analysis of D^0 mesons.

2022 JINST 17 P02017

Despite the fact that RF method is not common in high-energy physics, it shows notable enhancement of signal efficiency compared to the other presented algorithms. Deep neural networks does not show significant improvement compared to the widely used BDT. However, their performance is close and the DNN might help to improve signal significance in similar analyses. In future we plan to investigate the performance of studied algorithms for three body decays and, e.g., separation of prompt and non-prompt (coming from B meson decays) D^0 mesons, where the separation of background from a signal is even more difficult with standard analysis methods.

Acknowledgments

The work was supported from European Regional Development Fund-Project "Center of Advanced Applied Science" No. CZ.02.1.01/0.0/0.0/16-019/0000778 and by the grants LTT18002, LTT18001, LM2018113 and LM2018109 of Ministry of Education, Youth and Sports of the Czech Republic. We thank the STAR collaboration, SDCC at BNL and the NERSC Center at LBNL for providing d+Au collision simulation, resources and support.

References

[1] ATLAS collaboration, *Observation of a new particle in the search for the Standard Model Higgs boson with the ATLAS detector at the LHC*, *Phys. Lett. B* **716** (2012) 1 [arXiv:1207.7214].

[2] ALICE collaboration, *Measurement of D^0, D^+, D^{*+} and D_s^+ production in Pb-Pb collisions at $\sqrt{s_{NN}}$ = 5.02 TeV*, *JHEP* **10** (2018) 174 [arXiv:1804.09083].

[3] STAR collaboration, *Centrality and transverse momentum dependence of D^0-meson production at mid-rapidity in Au+Au collisions at $\sqrt{s_{NN}}$ = 200 textGeV*, *Phys. Rev. C* **99** (2019) 034908 [arXiv:1812.10224].

[4] STAR collaboration, *First Observation of the Directed Flow of D^0 and $\overline{D^0}$ in Au+Au Collisions at $\sqrt{s_{NN}}$ = 200 GeV*, *Phys. Rev. Lett.* **123** (2019) 162301 [arXiv:1905.02052].

[5] H. Voss, A. Hocker, J. Stelzer and F. Tegenfeldt, *TMVA, the Toolkit for Multivariate Data Analysis with ROOT*, *PoS* **ACAT** (2007) 040.

[6] CMS collaboration, *Observation of a New Boson at a Mass of 125 GeV with the CMS Experiment at the LHC*, *Phys. Lett. B* **716** (2012) 30 [arXiv:1207.7235].

[7] ALICE collaboration, *Λ_c^+ production in pp and in p-Pb collisions at $\sqrt{s_{NN}}$ = 5.02 TeV*, *Phys. Rev. C* **104** (2021) 054905 [arXiv:2011.06079].

[8] STAR collaboration, *First measurement of Λ_c baryon production in Au+Au collisions at $\sqrt{s_{NN}}$ = 200 GeV*, *Phys. Rev. Lett.* **124** (2020) 172301 [arXiv:1910.14628].

[9] LHCb collaboration, *Measurement of the $B_s^0 \to \mu^+\mu^-$ branching fraction and effective lifetime and search for $B^0 \to \mu^+\mu^-$ decays*, *Phys. Rev. Lett.* **118** (2017) 191801 [arXiv:1703.05747].

[10] STAR collaboration, *Observation of $D_s^\pm/D^0$ enhancement in Au+Au collisions at $\sqrt{s_{NN}}$ = 200 GeV*, *Phys. Rev. Lett.* **127** (2021) 092301 [arXiv:2101.11793].

[11] STAR collaboration, *Measurement of D^0 Azimuthal Anisotropy at Midrapidity in Au+Au Collisions at $\sqrt{s_{NN}}$=200 GeV*, *Phys. Rev. Lett.* **118** (2017) 212301 [arXiv:1701.06060].

[12] F. Pedregosa et al., *Scikit-learn: Machine Learning in Python*, *J. Machine Learning Res.* **12** (2011) 2825 [arXiv:1201.0490].

2022 JINST 17 P02017

[13] F. Chollet et al., *Keras*, https://keras.io, 2015

[14] Particle Data Group collaboration, *Review of Particle Physics*, *PTEP* **2020** (2020) 083C01.

[15] M. Gyulassy and X.-N. Wang, *HIJING 1.0: A Monte Carlo program for parton and particle production in high-energy hadronic and nuclear collisions*, *Comput. Phys. Commun.* **83** (1994) 307 [nucl-th/9502021].

[16] R. Brun, F. Bruyant, F. Carminati, S. Giani, M. Maire, A. McPherson et al., *GEANT: Detector Description and Simulation Tool; Oct 1994*, CERN Program Library, CERN, Geneva, 1993, 10.17181/CERN.MUHF.DMJ1.

[17] M. Anderson et al., *The Star time projection chamber: A Unique tool for studying high multiplicity events at RHIC*, *Nucl. Instrum. Meth. A* **499** (2003) 659 [nucl-ex/0301015].

[18] W.J. Llope et al., *The TOFp/pVPD time-of-flight system for STAR*, *Nucl. Instrum. Meth. A* **522** (2004) 252 [nucl-ex/0308022].

[19] STAR collaboration, *STAR heavy flavor tracker*, *Nucl. Phys. A* **931** (2014) 1141.

[20] STAR collaboration, *Open charm yields in d + Au collisions at* $\sqrt{s_{NN}}$ = 200-*GeV*, *Phys. Rev. Lett.* **94** (2005) 062301 [nucl-ex/0407006].

[21] STAR collaboration, *Measurements of* D^0 *and* D^* *Production in* $p + p$ *Collisions at* $\sqrt{s} = 200$ *GeV*, *Phys. Rev. D* **86** (2012) 072013 [arXiv:1204.4244].

[22] G. Louppe, *Understanding Random Forests: From Theory to Practice*, Ph.D. thesis, University of Liège (2014), DOI: https:doi.org/10.13140/2.1.1570.5928 [arXiv:1407.7502].

[23] C.C. Aggarwal, *Neural Networks and Deep Learning*, Springer, Cham (2008), DOI: 10.1007/978-3-319-94463-0.

2022 JINST 17 P02017

PROCEEDINGS OF SCIENCE

Measurements of open heavy-flavor hadrons in Au+Au collisions at $\sqrt{s_{NN}}$ = 200 GeV with the STAR experiment

Lukáš Kramárik, for the STAR collaboration*

Department of Physics
Faculty of Nuclear Sciences and Physical Engineering
Czech Technical University in Prague
Břehová 7, 115 19 Prague 1, Czech Republic

E-mail: lukas.kramarik@fjfi.cvut.cz

At RHIC energies, heavy-flavor quarks are primarily produced in hard partonic scatterings in the early stages of ultra-relativistic heavy-ion collisions. This makes them an excellent probe of the quark-gluon plasma (QGP) since they experience the whole evolution of the hot and dense medium. The STAR experiment allows studying the production of charm quarks and their interaction with the QGP through direct reconstruction of hadronic decays of open charm hadrons and the topological separation of electrons originating from bottom and charm hadron decays. This is possible thanks to the excellent track pointing resolution provided by the Heavy Flavor Tracker.

In these proceedings, the most recent results on open heavy-flavor hadron production in Au+Au collisions at $\sqrt{s_{NN}}$ = 200 GeV from the STAR experiment are shown. In particular, we will discuss the nuclear modification factor of D^0 meson, D_s^+/D^0 and Λ_c^+/D^0 yield ratios as a function of transverse momentum and collision centrality. Additionally, charm- and bottom- hadron decay electron elliptic flow (v_2) are presented. Finally, rapidity-dependent directed flow (v_1) of D^0 meson and charm-hadron decay electrons are reported.

40th International Conference on High Energy physics - ICHEP2020
July 28 - August 6, 2020
Prague, Czech Republic (virtual meeting)

*Speaker

PoS(ICHEP2020)546

1. Introduction

The quark-gluon plasma (QGP) is the hot and dense nuclear matter of deconfined quarks and gluons that is formed in ultrarelativistic collisions of heavy ions [1]. Heavy-flavor (HF, charm and bottom) quarks are produced primarily in the early stages of collisions [2] and thus experience the entire evolution of the medium. Directed flow of HF mesons allows us to study the initial conditions of heavy-ion collisions, such as the tilt of the QGP medium [3] and the initial electromagnetic (EM) field [4]. Furthermore, understanding the sensitivity of HF quarks to the collective motion of the system, reflected in the elliptic flow of HF mesons, can provide information on the degree of the HF quark thermalization in the QGP and help to constrain the HF-quark diffusion coefficient. Study of open-charm meson yields probes not only the quark mass dependence of energy loss in the QGP, but also its hadronization in the heavy-ion collisions.

The STAR experiment at the Relativistic Heavy Ion Collider (RHIC) performed extensive studies of HF-hadron production. The results from Au+Au collisions at $\sqrt{s_{\rm NN}}$ = 200 GeV presented in these proceedings were obtained thanks mainly to the presence of Heavy Flavor Tracker (HFT) [5], the high-precision silicon vertex detector installed at the center of the STAR apparatus for data taking in years 2014–2016. It greatly improves the track pointing resolution and enables the topological reconstruction of the secondary vertices of open charm hadron decays through the hadronic channels, such as $D^0 \to K^-\pi^+$, $\Lambda_c^+ \to K^-\pi^+p$ or $D_s \to \phi\pi^+ \to K^-K^+\pi^+$. In addition, the HFT enables the measurement of electrons from charm and bottom hadron decays with great precision. HF decay electron fractions are extracted using template fits to distributions of the 3D distance of closest approach of a track to the collision vertex.

2. Heavy-flavor production in Au+Au collisions

Particle production in Au+Au collisions can be studied using the nuclear modification factor $R_{\rm AA}$, defined as the ratio of the invariant particle yields measured in Au+Au and p+p collisions (where no QGP is expected to be created), scaled by the average number of binary nucleon-nucleon collisions in the investigated Au+Au collision centrality interval. The D^0 meson $R_{\rm AA}$ measured in three collision centrality intervals is shown in Fig. 1 (left) [6]. At high transverse momentum, $p_{\rm T}$, the yields are greatly suppressed in central collisions, indicating that charm quarks lose a significant amount of energy in the QGP. Towards more peripheral collisions, this suppression at high $p_{\rm T}$ decreases. However, at low $p_{\rm T}$, $R_{\rm AA}$ has no significant centrality dependence.

Figure 1 (right) shows the charm and bottom decay electron $R_{\rm AA}$. The data are consistent with the DUKE model prediction [7] which contains the mass dependence of energy loss. Furthermore, bottom decay electron suppression is smaller than that of charm decay electron with a significance larger than 3σ. This suggests a quark mass dependence of the energy loss in the QGP.

In order to understand hadronization of charm quarks, the Λ_c^+/D^0 yield ratio is measured [8] and results are shown in Fig. 2. In Fig. 2 (left), it can be seen that in the measured $p_{\rm T}$ interval, the Λ_c^+/D^0 ratio is comparable to the baryon-to-meson ratios of strange and light flavor hadrons. Additionally, the data are compared to model calculations including different charm quark hadronization mechanisms and QGP medium properties. The data, as well as those calculations that include coalescence hadronization of charm quarks show significant enhancements compared to the PYTHIA

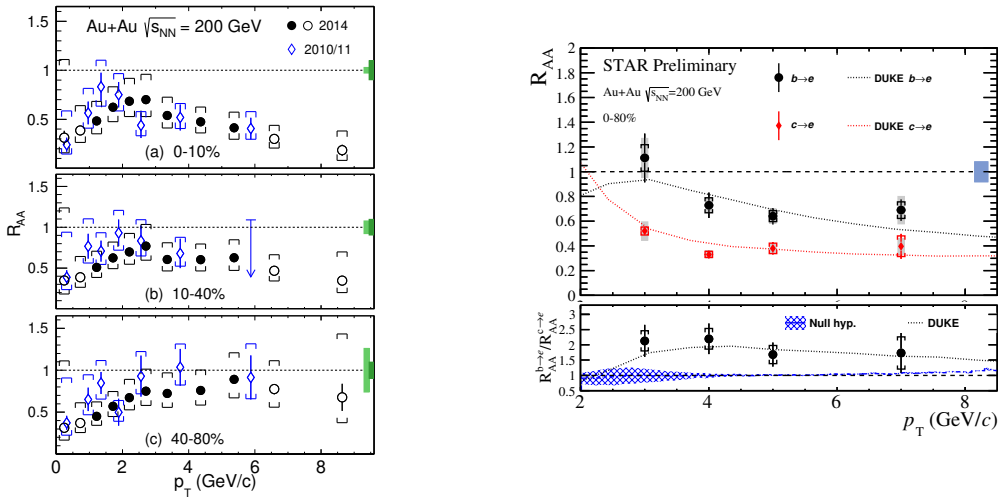

Figure 1: Left: the $R_{\rm AA}$ of $\rm D^0$ meson as a function of $p_{\rm T}$ in different centrality classes measured with (year 2014) and without (years 2010/11) the HFT detector installed [6]. Right: the $R_{\rm AA}$ of charm and bottom decay electron (top) and their ratio (bottom), compared to the DUKE model prediction [7].

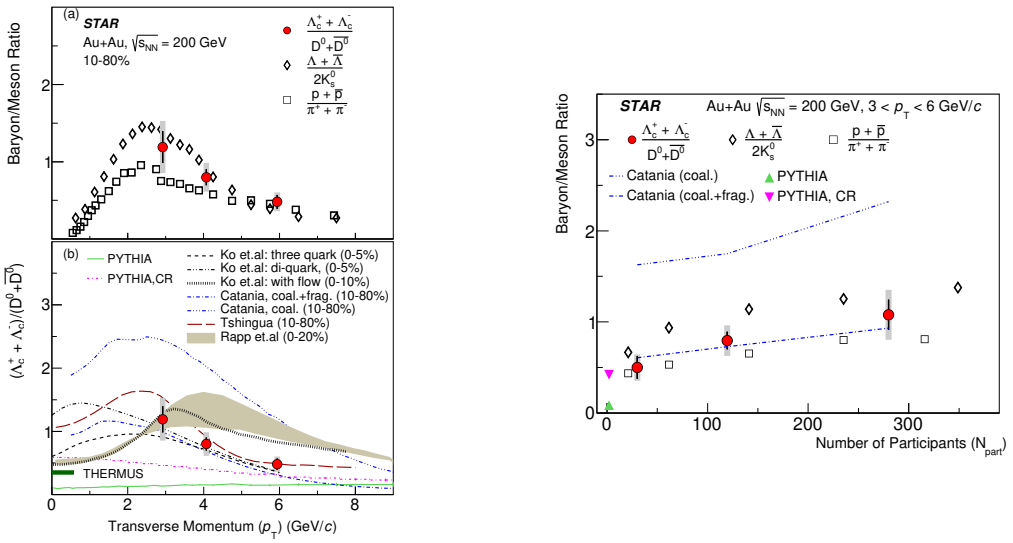

Figure 2: Left: $\Lambda_c^+/\rm D^0$ yield ratio as a function of $p_{\rm T}$ compared to light-hadron results (top) and different model calculations (bottom). Right: $\Lambda_c^+/\rm D^0$ yield ratio vs number of participants $N_{\rm part}$, compared to light-hadron results, PYTHIA calculation with and without color reconnection and the Catania model incorporating coalescence and fragmentation hadronization of the charm quarks [8].

calculations. As displayed in Fig. 2 (right), the centrality dependence of $\Lambda_c^+/\rm D^0$ yield ratio shows a similar trend as that of light flavor and strange hadron yield ratios. The data are consistent with the Catania model calculation incorporating coalescence and fragmentation hadronization of charm quarks [9].

STAR also measured the $\rm D_s^+/D^0$ yield ratio, which probes both strangeness enhancement and coalescence of charm quarks with strange quarks in the QGP. Figure 3 (top left) shows that this ratio

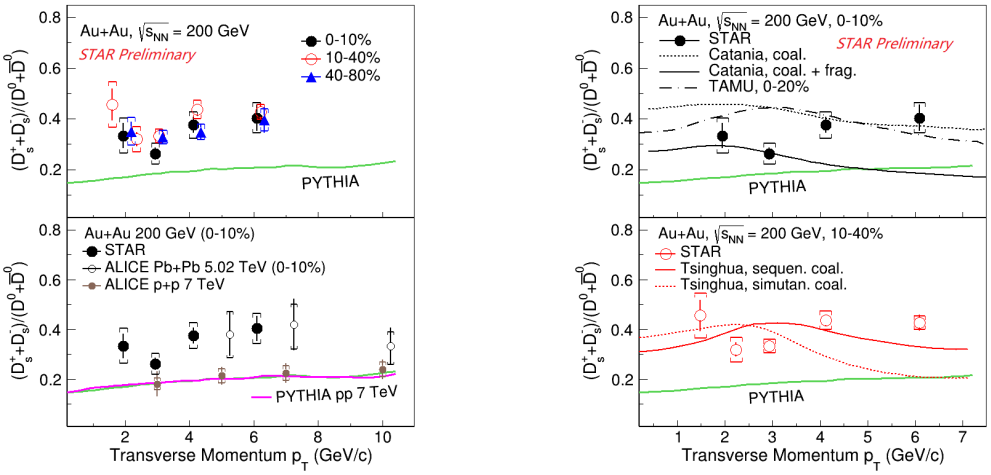

Figure 3: D_s^+/D^0 yield ratio as a function of p_T in different centralities of Au+Au collisions compared to PYTHIA p+p calculations and to an ALICE measurement [10, 11] (left) and to various models incorporating coalescence and fragmentation hadronization of charm quarks [9, 12, 13] (right).

has no significant centrality dependence and is significantly larger than the fragmentation baseline, represented by a PYTHIA8 calculation. In Fig. 3 (bottom left), STAR results in central Au+Au collisions are compared to the ALICE result in central Pb+Pb collisions at $\sqrt{s_{NN}}$ = 5.02 TeV. The results are consistent in the overlapping region. Additionally, ALICE p+p data at $\sqrt{s}$ = 7 TeV are consistent with a PYTHIA calculation at the same energy.

Figure 3 (right) shows the comparison of the STAR results in central (top right) and semi-central collisions (bottom right) with model calculations. The Catania model calculation with only coalescence hadronization describes data for $p_T > 4$ GeV/c, while the Catania model calculation with both coalescence and fragmentation hadronization describes data for lower p_T. Furthermore, the Tsinghua model with sequential coalescence hadronization of charm quarks qualitatively describes data in 10–40% semi-central collisions.

3. Anisotropic flow of heavy-flavor decay electrons

To quantify the transport properties of the hot medium produced in heavy-ion collisions, the collective motion of partons is studied via the measurement of the elliptic flow v_2 of produced particles [14]. This is the second coefficient of the Fourier decomposition of the azimuthal distribution of the particle yield with respect to the event plane. The D^0 meson v_2 measured by STAR in Au+Au collisions was found to follow the number-of-constituent-quark scaling [15].

Figure 4 shows the HF decay electron v_2. In this analysis, non-flow effects are calculated using electron-hadron correlations with electrons from semileptonic charm and bottom decays simulated with PYTHIA. Charm decay electron v_2, shown in Fig. 4 (left) is consistent with the D^0 v_2 [15] folded to account for decay-kinematic effects and the Duke model [7]. For bottom decay electron v_2, shown in Fig. 4 (right), two approaches for the event plane reconstruction are compared. One of them uses tracks reconstructed in the Time Projection Chamber (TPC) in the pseudorapidity range of $|\eta| < 1$, the latter one uses hits in the Forward Meson Spectrometer (FMS) in $-2.5 < \eta < 4$. The

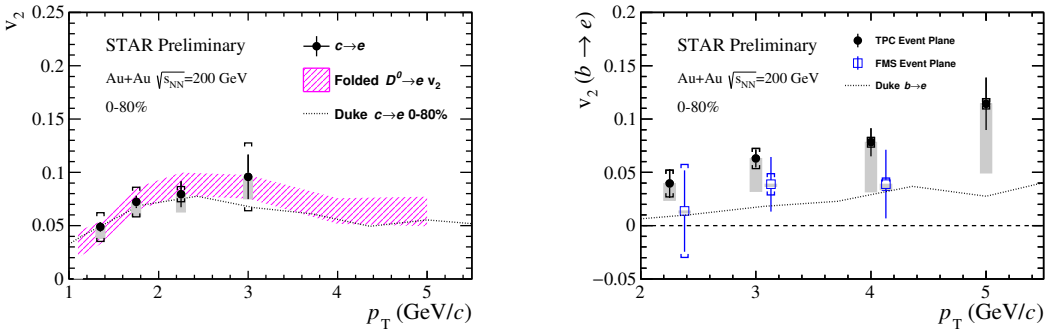

Figure 4: Elliptic flow v_2 of charm decay (left) and bottom decay electrons (right) as a function of p_T, compared to folded D^0 meson v_2 [15] and DUKE model calculations [7]. Gray boxes show the estimated non-flow contributions.

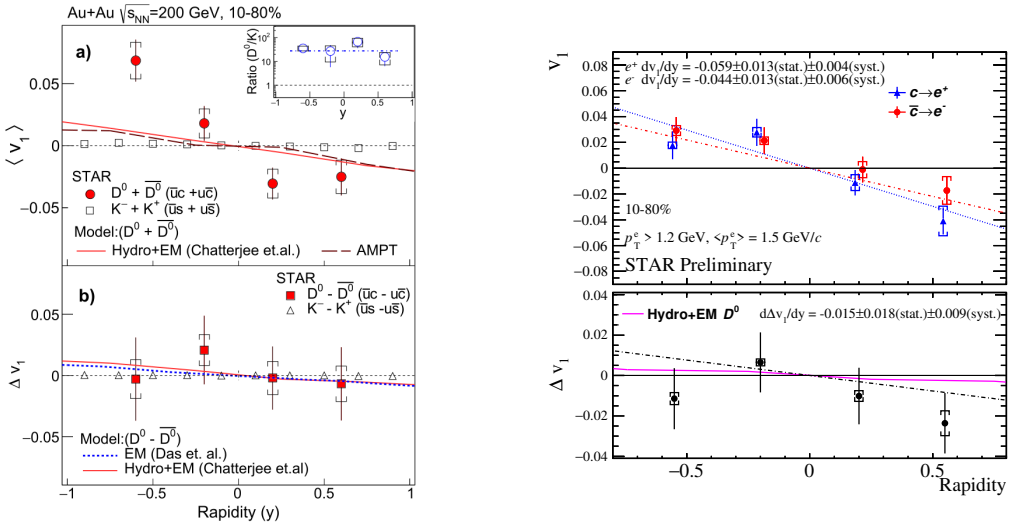

Figure 5: Directed flow v_1 of D^0 and $\overline{D^0}$ for $p_T > 1.5$ GeV/c compared to that of kaons for $p_T > 0.2$ GeV/c [16] (left) and v_1 of charm decay positrons and anti-charm decay electron for $p_T > 1.2$ GeV/c as a function of rapidity in 10–80% central Au+Au collisions compared to model calculations (right).

TPC event plane measurement with non-flow subtraction results in non-zero v_2 of bottom decay electrons with a significance of 3.4σ. The usage of the FMS significantly reduces the non-flow contribution to 0.5%. However, this measurement has a larger uncertainty due to the poorer event-plane resolution and smaller statistics analyzed because the FMS being present only in part of the data recorded.

The initial conditions of heavy-ion collisions could be accessed via measurement of directed flow, v_1, whose magnitude is affected by the initial tilt of the QGP bulk and viscous drag on charm quarks. Furthermore, the initial EM field is predicted to induce larger v_1 for charm quarks than for light flavor quarks due to the early production of charm quarks and gives opposite contributions to charm and anti-charm quarks.

Figure 5 (left) shows the v_1 of combined D^0 and $\overline{D^0}$ (top) and the difference between D^0 and $\overline{D^0}$ v_1 (bottom) [16]. A separate measurement of D^0 and $\overline{D^0}$ is done via topological reconstruction

of decays $D^0 \to K^-\pi^+$ and $\overline{D^0} \to K^+\pi^-$. The absolute value of the D^0 v_1 is observed to be about 25 times larger than that of the kaons with a 3.4σ significance. Model calculations with a tilted source predict the correct sign of dv_1/dy, but the v_1 magnitudes are lower than in data. Study of the initial EM field induced splitting for charm decay electrons is shown in Fig. 5 (right). The v_1 for charm and anti-charm is accessed by separate measurements of charm decay e^+ and anti-charm decay e^-. Within the uncertainties, no splitting due to EM field is observed in both measurements.

4. Summary

The STAR experiment, thanks to the HFT detector, measured open heavy-flavor production in Au+Au collisions at $\sqrt{s_{NN}}$ = 200 GeV via the topological reconstruction of charmed hadrons and extraction of HF decay electrons. The results on the open-charm hadron production suggest that charm quarks hadronize via coalescence with light quarks in the QGP and strongly interact with the created medium. Additionally, measurements of charm and beauty decay electron R_{AA} suggest that parton energy loss in the QGP depends on quark mass. Charm decay electron v_2, consistent with D^0 v_2, indicate that charm quarks gain significant flow in the QGP. Firstly observed non-zero bottom decay electron v_2 is consistent with the Duke model incorporating bottom quark transport in the QGP. The predicted charm and anti-charm splitting due to the initial EM field is not observed in measured v_1 of D^0 and $\overline{D^0}$, as well as charm (anti-charm) decay e^+ (e^-).

Acknowledgments

The work was supported from European Regional Development Fund-Project "Center of Advanced Applied Science" No. CZ.02.1.01/0.0/0.0/16-019/0000778 and by the grant LTT18002 of Ministry of Education, Youth and Sports of the Czech Republic.

References

[1] STAR collaboration, *Nucl. Phys. A* **757** (2005) 102.
[2] Z.-W. Lin and M. Gyulassy, *Phys. Rev. C* **51** (1995) 2177.
[3] S. Chatterjee and P. Bożek, *Phys. Rev. Lett.* **120** (2018) 192301.
[4] S.K. Das, S. Plumari, S. Chatterjee et al., *Phys. Lett. B* **768** (2017) 260.
[5] STAR collaboration, *Nucl. Phys. A* **931** (2014) 1141.
[6] STAR collaboration, *Phys. Rev. C* **99** (2019) 034908.
[7] S. Cao, G.-Y. Qin and S.A. Bass, *Phys. Rev. C* **92** (2015) 024907.
[8] STAR collaboration, *Phys. Rev. Lett.* **124** (2020) 172301.
[9] S. Plumari, V. Minissale, S.K. Das et al., *Eur. Phys. J. C* **78** (2018) 348.
[10] ALICE collaboration, *Eur. Phys. J. C* **77** (2017) 550.
[11] ALICE collaboration, *JHEP* **10** (2018) 174.
[12] M. He, R.J. Fries and R. Rapp, *Phys. Rev. Lett.* **110** (2013) 112301.
[13] J. Zhao, S. Shi, N. Xu et al., 1805.10858.
[14] A.M. Poskanzer and S.A. Voloshin, *Phys. Rev. C* **58** (1998) 1671.
[15] STAR collaboration, *Phys. Rev. Lett.* **118** (2017) 212301.
[16] STAR collaboration, *Phys. Rev. Lett.* **123** (2019) 162301.

IOP Publishing Physica Scripta
Phys. Scr. **95** (2020) 074010 (4pp) https://doi.org/10.1088/1402-4896/ab9034

Reconstruction of D^0 meson in d+Au collisions at $\sqrt{s_{NN}} = 200$ GeV by the STAR experiment

Lukáš Kramárik for the STAR collaboration*

Department of Physics Faculty of Nuclear Sciences and Physical Engineering Czech Technical University in Prague Břehová 7, 115 19 Prague 1, Czech Republic

E-mail: lukas.kramarik@fjfi.cvut.cz

Received 19 March 2020, revised 28 April 2020
Accepted for publication 5 May 2020
Published 29 May 2020

Abstract

Owing to their large masses, charm quarks are predominantly produced through initial hard scatterings in heavy-ion collisions. Therefore, they can serve as penetrating probes to study the intrinsic properties of the hot medium created in heavy-ion collisions. However, Cold Nuclear Matter effects can also affect the charm quark production in nuclear collisions with respect to p + p collisions. These effects can be measured in small collision systems such as d/p+Au. In these proceedings, D^0 meson reconstruction in d+Au collisions at $\sqrt{s_{NN}} = 200$ GeV at the STAR experiment is described. Thanks to the excellent impact parameter resolution provided by the Heavy Flavor Tracker detector, $D^0(\overline{D^0})$ mesons are topologically reconstructed from their hadronic decay channel D^0 ($\overline{D^0}$) $\rightarrow K^-\pi^+$ ($K^+\pi^-$). The Boosted Decision Trees machine learning algorithm from the TMVA package is applied in order to improve signal/background separation.

Keywords: cold nuclear matter effects, STAR, BNL, Boosted Decision Trees, D^0 meson

(Some figures may appear in colour only in the online journal)

1. Introduction

In ultrarelativistic collisions of heavy ions, hot and dense nuclear matter, quark-gluon plasma (QGP), could be created [1]. Since heavy-flavor (charm and beauty) quarks are produced in hard scatterings at the early stage of such collisions [2], they experience the entire evolution of the system including the QGP phase. At Relativistic Heavy Ion Collider (RHIC), strong suppression of open charm mesons at high transverse momentum (p_T) in the 0%–10% most central gold-gold (Au+Au) collisions was measured [3], indicating substantial energy loss of charm quarks in the hot medium. In addition, it was measured that charm quarks exhibit collective behavior [4] that reflects the degree of thermalization of charm quarks in the medium and carries information about the transport properties of the QGP.

However, for more detailed study of the QGP effects on produced particles, quantitative understanding of the effects of the heavy nuclei in the initial stages of collisions is needed. These so-called Cold Nuclear Matter effects include mainly modification of parton distribution functions of nucleons in colliding nuclei [5, 6], multiple scatterings of the partons by the dense target and parton scatterings in the nucleus, resulting in their energy loss and to the broadening of the transverse momentum distribution (Cronin effect) [7, 8].

CNM effects are investigated in the asymmetric collisions of protons or deuterons with nuclei. At Large Hadron Collider (LHC) in CERN, CNM effects on D^0 production were studied in proton-lead (p+Pb) collisions. ALICE experiment measured that D^0 production in such events is not significantly modified compared to proton-proton collisions [9]. However, CMS collaboration measured significant collective behavior (large elliptic flow v_2) of D^0 mesons in p+Pb collisions at $\sqrt{s_{NN}} = 8.16$ TeV [10]. At RHIC, CNM effects are accessible via proton-gold (p+Au) and deuteron-gold (d+Au) collisions. In such collisions, creation of thermalized medium is not expected, nevertheless the dense nuclear environment alters colliding nucleons.

* On behalf of the STAR collaboration, see https://www.star.bnl.gov/central/collaboration/authors/authorList.php.

Reconstruction of open charm D^0 mesons described in these proceedings was done in data from d+Au collisions at $\sqrt{s_{NN}} = 200$ GeV. These were measured by the Solenoidal Tracker at RHIC (STAR) situated in Brookhaven National Laboratory (BNL) in the USA. Topological reconstruction of the hadronic decay of D^0 meson to K^- and π^+ with branching ratio 3.89 ± 0.04 % [11] is used. Shown results are for combined D^0 and $\overline{D^0}$ mesons, thus both unlike-sign combinations of pion and kaon ($K^-\pi^+$ and $K^+\pi^-$) are considered to be correct charge combinations. Furthermore, the Boosted Decision Trees (BDT) machine learning algorithm from the Toolkit for Multivariate Data Analysis (TMVA) package [12] is applied in order to improve separation of signal and background $K\pi$ pairs.

2. Experimental setup - STAR detector

STAR consists of multiple subdetectors that are able to track and identify charged particles down to very low p_T at mid-rapidity ($|\eta| < 1$) with the full azimuthal coverage. STAR's main tracking sub-system is the Time Projection Chamber (TPC) [13], a gaseous detector that identifies charged particles via specific energy loss in it and determines momentum from the curvature of their trajectories in the 0.5 Tesla solenoidal field.

Another detector that was developed to improve the particle identification capability for tracks with momenta between 0.6 and 3 GeV/c, is the Time of Flight (TOF) [14]. It measures the velocity of a particle, β, by measuring the time interval that the particle needs to reach the TOF from the point of the collision. Time of a collision is detected with fast Vertex Position Detectors (VPD) [15], that detects particles produced in forward directions.

For the analysis presented in these proceedings, the Heavy Flavor Tracker (HFT) [16] detector has a great importance. It is the high-precision silicon vertex detector installed at the center of the STAR for data taking in years 2014–2016. It greatly improves the track pointing resolution and enables the topological reconstruction of the secondary vertices of open charm hadron decays through hadronic channels. It consists of three silicon detectors - the PIXEL made of two layers of Monolithic Active Pixel Sensors, Intermediate Silicon Tracker (IST) and Silicon Strip Detector (SSD). The HFT achieves excellent resolution for distance of the closest approach (DCA), e.g. 30 μm for kaons at transverse momentum $p_T = 1.5$GeV/c [16].

3. Event and track selection

In 2016, approximately 350 million of d+Au minimum bias collisions at $\sqrt{s_{NN}} = 200$ GeV were recorded. Only events that are well reconstructed in the HFT geometric acceptance are accepted for this analysis. This is assured by requiring that the distance of reconstructed position of the primary vertex in the beam direction from the center of detector (V_z) is less than 6 cm. To reduce pile-up from multiple events, only events with correlated primary vertices reconstructed by the TPC and by the VPD ($|V_{z,\mathrm{TPC}} - V_{z,\mathrm{VPD}}| < 6$ cm) are further analyzed.

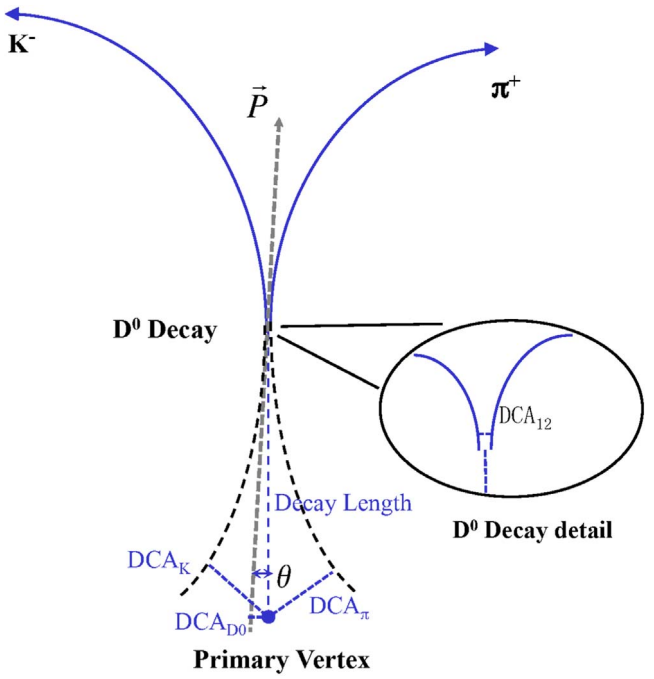

Figure 1. Schematic representation of D^0 meson decay and its topological variables [3]: distances of the closest approach of kaon and pion to primary vertex (DCA_K and DCA_π) and between them (DCA_{12}), D^0 meson DCA to primary vertex (DCA_{D0}) and pointing angle θ between reconstructed D^0 momentum ($\vec{P}$) and decay length vector. Reprinted figure with permission from [3], Copyright (2019) by the American Physical Society.

For this analysis, reconstructed tracks with pseudorapidity $|\eta| < 1$ and $p_T > 0.15$ GeV/c are used. They are also required to have at least 15 measured points in the TPC out of maximum 45, hits in both layers of PIXEL detector and at least one hit in IST or SSD layers of the HFT. Particles are identified using the specific energy loss $\mathrm{d}E/\mathrm{d}x$ in the TPC. Deviation of the measured energy loss $\mathrm{d}E/\mathrm{d}x|_{\mathrm{meas}}$ from the expected $\mathrm{d}E/\mathrm{d}x|_{\mathrm{exp}}$ is calculated for each track as

$$n\sigma = \frac{1}{R} \ln \frac{\mathrm{d}E/\mathrm{d}x|_{\mathrm{meas}}}{\mathrm{d}E/\mathrm{d}x|_{\mathrm{exp}}}, \quad (1)$$

where R is the $\ln(\mathrm{d}E/\mathrm{d}x)$ resolution of the TPC. Pions are selected with the condition $|n\sigma| < 3$ and kaons $|n\sigma| < 2$. Furthermore, if a track has a matched hit in the TOF, its measured velocity β_{meas} is compared to the expected β_{exp} and the track is required to fulfill $|1/\beta_{\mathrm{meas}} - 1/\beta_{\mathrm{exp}}| < 0.03$ in order to be used in the analysis.

4. Topological reconstruction of open charm mesons

STAR equipped with the HFT is able to track charged particles with great precision and thanks to this, topological properties of D^0 meson decay are used in its reconstruction. In the analysis, firstly all pions and kaons are combined into pairs. Then, properties of these pairs are studied in order to study whether they come from D^0 meson decay. Figure 1 shows schematic decay of D^0 meson together with topological variables. D^0 is created in the place of collision, primary

vertex, and decays in the secondary vertex into the pair of daughter particles (kaon and pion). Position of the secondary vertex is calculated as the point of the closest approach of these daughter tracks. Topological variables used in this analysis are:

- DCA between reconstructed daughter particles (DCA_{12}),
- decay length of D^0 meson candidate, calculated as distance between primary and secondary vertex,
- kaon and pion DCA to the primary vertex (DCA_K and DCA_π),
- D^0 meson DCA to the primary vertex (DCA_{D0}),
- pointing angle θ between reconstructed D^0 momentum and decay length vector,
- angle between reconstructed D^0 momentum and kaon momentum.

5. Machine learning algorithm training

Topological properties of the pairs are used in the Boosted Decision Trees algorithm to isolate D^0 candidates in data. In this machine learning algorithm classifiers are not individual variables, but a set of binary structured decision trees constructed in the training phase of the algorithm. In the algorithm application phase, every pair is tested by the set of trees in order to classify it as signal or background. The decision of trees is then projected to the individual number - BDT response that has values from -1 (background-like) to 1 (signal-like). In the presented analysis, BDT is trained separately in three pair (D^0) p_T intervals: 1–2, 2–3, 3–5 GeV/c.

For the algorithm training, the samples of signal and background pairs are needed as the input. Signal sample are D^0 decays generated with PYTHIA. Momenta and DCA of daughter particles from these decays are smeared in accordance with the detector response. Background sample for training are wrong(like)-sign pairs of kaons and pions ($K^-\pi^-$ and $K^+\pi^+$) from recorded data. In the training part of the algorithm, input pairs are divided to training and test samples. After the algorithm is trained and decisions trees are constructed, BDT response is calculated for all training and test pairs. Its distribution is shown in figure 2. It can be seen that the signal and background are clearly separated. In addition, since the shapes of BDT response for training and test samples are the same, the algorithm is not overtrained.

Signal and background efficiencies (ϵ_S, ϵ_B respectively) together with their purities and signal significance Σ after application of different cuts on the BDT response for pairs with $2 < p_T < 3$ GeV/c are shown in figure 3. Signal significance is defined as

$$\Sigma = \frac{N_S \epsilon_S}{\sqrt{N_S \epsilon_S + N_B \epsilon_B}}, \quad (2)$$

where N_S and N_B are estimates of number of signal and background pairs before BDT application. N_S is estimated using D^0 invariant yield measured in p + p collisions [17] and the detector reconstruction efficiency. N_B is evaluated

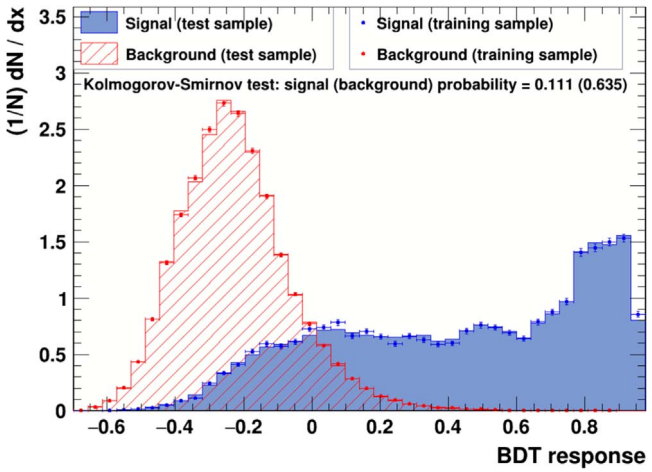

Figure 2. Boosted Decision Trees response distributions for signal and background pairs with transverse momentum $2 < p_T < 3$ GeV/c, for both test and training samples.

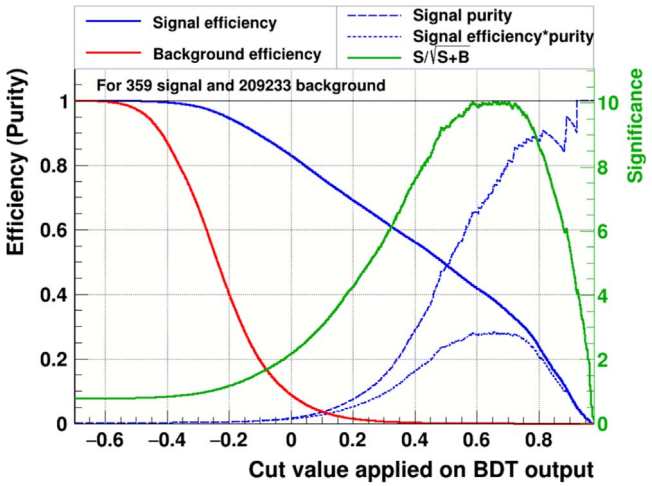

Figure 3. Evaluation of BDT response cuts performance for pairs with transverse momentum $2 < p_T < 3$ GeV/c.

from the number of wrong(like)-sign pairs in the data. Signal efficiency ϵ_S is used as one of the corrections on D^0 raw yield, extracted by applying trained BDT on data.

6. BDT application on data

After the machine learning method is trained, it is applied on both correct(unlike)-sign pairs and wrong(like)-sign pairs from the data and BDT response is calculated for every pair. Unweighted invariant mass distributions for pairs that fulfill the cut on BDT response are further used to evaluate the significance of signal in data. Background ($N_{B,data}$) is estimated via wrong-sign pairs and then subtracted from the correct-sign combinations. Resulting invariant mass distributions of correct-sign pairs are fitted by the combination of a Gaussian function for signal and a linear function for the residual background. D^0 raw yield (Y) is extracted using the bin-counting method in the $\pm 3\sigma$ region around the mean of the fitted Gaussian function with residual background

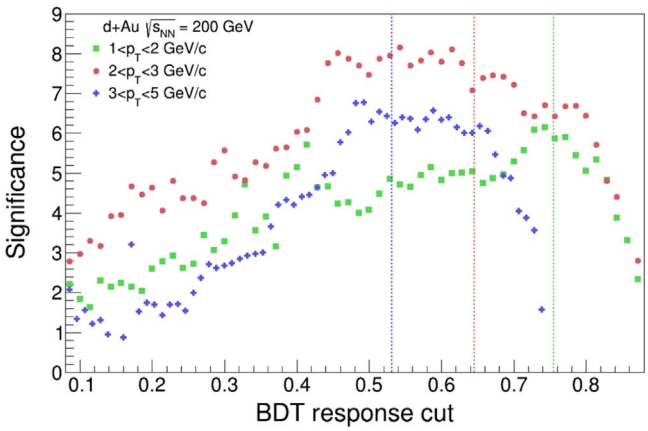

Figure 4. Significance scan of cut on BDT response on data. Vertical lines show BDT response cuts with maximum significance calculated from BDT training.

subtracted. Finally, signal significance in data Σ_{data} is calculated as

$$\Sigma_{\text{data}} = \frac{Y}{\sqrt{Y + 2N_{\text{B,data}}}}. \quad (3)$$

Multiple BDT response cuts are applied on data and significances are calculated for all of them. Resulting distributions for all tested pair p_{T} intervals are in figure 4. In this plot, vertical lines show the BDT response cuts where significance calculated from BDT training (equation (2)) is maximal in three tested D^0 p_{T} bins. It can be seen, that the BDT response cuts with maximum significance in data are consistent with those calculated in the BDT algorithm training (figure 3). Finally, signal significance higher than 6 is achieved in all of the tested p_{T} intervals.

7. Summary

Measurements of open charm mesons are important not only in heavy-ion collision where QGP is created, but also in the asymmetric small systems, such as d+Au collisions where CNM effects are investigated.

At STAR, D^0 mesons are reconstructed in d+Au collisions at $\sqrt{s_{\text{NN}}} = 200$ GeV. Thanks to the HFT, topological reconstruction of hadronic decay channel is used. Furthermore, extraction of the D^0 signal has been optimized using the TMVA Boosted Decision Trees method. This machine learning method significantly helps to improve the D^0 meson measurement.

Evaluations of the efficiency corrections on D^0 raw yields and systematic uncertainties are under way, to determine the invariant yield and nuclear modification factor of D^0 mesons in d+Au collisions.

Acknowledgments

This work was supported by the grants LM2015054 and LTT18002 of Ministry of Education, Youth and Sports of the Czech Republic.

References

[1] Adams J *et al* (STAR Collaboration) 2005 *Nucl. Phys.* A **757** 102–83
[2] Lin Z and Gyulassy M 1995 *Phys. Rev.* C **51** 2177
Lin Z and Gyulassy M 1995 *Phys. Rev.* C **52** 440
[3] Adam J *et al* (STAR Collaboration) 2019 *Phys. Rev.* C **99** 034908
[4] Adamczyk L *et al* (STAR Collaboration) 2017 *Phys. Rev. Lett.* **118** 212301
[5] Noble J V 1981 *Phys. Rev. Lett.* **46** 412–5
[6] Aubert J *et al* 1983 *Phys. Lett.* B **123** 275–8
[7] Vitev I, Goldman J T, Johnson M and Qiu J 2006 *Phys. Rev.* D **74** 054010
[8] Vitev I 2007 *Phys. Rev.* C **75** 064906
[9] Adam J *et al* (ALICE Collaboration) 2016 *Phys. Rev.* C **94** 054908
[10] Adamczyk L *et al* (CMS Collaboration) 2019 *CMS-PAS-HIN-19–009* (http://cds.cern.ch/record/2699456)
[11] Tanabashi M *et al* (Particle Data Group) 2018 *Phys. Rev.* D **98** 030001
[12] Voss H, Hocker A, Stelzer J and Tegenfeldt F 2007 *PoS (ACAT)* **050**
[13] Anderson M *et al* 2003 *Nucl. Instrum. Methods* A **499** 659–78
[14] Llope W J *et al* (STAR Collaboration) 2012 *Nucl. Instrum. Methods* A **661** S110–3
[15] Llope W J *et al* 2014 *Nucl. Instrum. Methods* A **759** 23–8
[16] Qiu H *et al* (STAR Collaboration) 2014 *Nucl. Phys.* A **931** 1141–6
[17] Adamczyk L *et al* (STAR Collaboration) 2012 *Phys. Rev.* D **86** 072013

PROCEEDINGS OF SCIENCE

Measurements of charm meson production in p+p and Au+Au collisions by the STAR experiment

Lukáš Kramárik* **for the STAR collaboration**
Department of Physics
Faculty of Nuclear Sciences and Physical Engineering
Czech Technical University in Prague
Břehová 7, 115 19 Prague 1, Czech Republic
E-mail: lukas.kramarik@fjfi.cvut.cz

Charm quarks possess a large mass and thus they are expected to be primarily produced during the initial stages of heavy-ion collisions. Hot and dense nuclear matter, usually referred to as the Quark-Gluon Plasma (QGP), can also be created in these collisions. Therefore, properties of the QGP can be studied via the energy loss and anisotropy of charm quarks, which is closely related to the nature of interactions between charm quarks and the medium.
In these proceedings, we will report the most recent measurements of D^0, $D^{\pm}$ and D_s production in Au+Au collisions at $\sqrt{s_{NN}} = 200$ GeV. These open charm mesons are reconstructed via their hadronic decay channels, where the daughter particles are tracked and identified with excellent precision by the STAR experiment at RHIC. At high transverse momentum region and in central Au+Au collisions, D meson production is strongly suppressed compared to that in p+p collisions, indicating substantial energy loss of charm quarks in the medium. In addition, measurements of elliptic and triangular anisotropies of D meson azimuthal distributions indicate that charm quarks have gained significant flow in the QGP. These results are compared to those of light hadrons as well as theoretical calculations. Moreover, charm quarks participate in coalescence hadronization in the QGP as suggested by the enhanced D_s to D^0 yield ratio in Au+Au collisions compared to that in p+p collisions.

The European Physical Society Conference on High Energy Physics
5-12 July
Venice, Italy

*Speaker.

PoS(EPS-HEP2017)650

1. Introduction

Quark-Gluon Plasma (QGP) is a state of hot and dense nuclear matter composed of deconfined quarks and gluons. This matter is expected to be present in the early universe and can be currently created in relativistic heavy-ion collisions at both the Relativistic Heavy Ion Collider (RHIC) and the Large Hadron Collider (LHC).

Charm quarks are created mainly in the initial stages of heavy-ion collisions and subsequently travel through the hot, dense matter. Thus they are excellent probes of the properties of the QGP. Measurements of charm meson production in heavy-ion collisions provide a great opportunity to study the charm quark energy loss in the hot medium, which is directly related to the transport coefficients of the QGP. Furthermore, collective behavior of charm quarks in the QGP is sensitive to the degree of thermalization in the medium, and can be used to constrain the heavy-flavour quark spatial diffusion coefficient.

2. Experimental setup

Results on open charm meson production in Au+Au collisions at $\sqrt{s_{\mathrm{NN}}} = 200$ GeV, with comparison to that in p+p collisions at $\sqrt{s} = 200$ GeV, are presented in these proceedings. These were measured by the Solenoidal Tracker at RHIC (STAR) experiment designed to study the strongly interacting matter created in heavy-ion collisions. Charged particles emerging from these collisions are tracked and identified with great precision at STAR. Main sub-systems used for particle reconstruction and identification are the Time Projection Chamber [1], the Time-Of-Flight detector [2] and the Heavy Flavor Tracker (HFT) [3]. In particular, HFT, the high-precision silicon vertex detector installed at the center of STAR for data taking in years 2014-2016, was of pivotal importance for the analyses presented in these proceedings. It greatly improves the track pointing resolution and enables the topological reconstruction of the secondary vertices of open charm meson decays through hadronic channels.

3. Energy loss of open charm mesons in Au+Au collisions

A mass and color charge ordering of the parton energy loss in the hot medium is predicted, i.e. heavy-flavour quarks are expected to lose less energy than light-flavour quarks and gluons. Such energy losses can be quantitatively studied by using the nuclear modification factor R_{AA}, defined as the ratio between the invariant particle yields measured in Au+Au and p+p collisions (where no QGP is expected to be created), scaled by the average number of binary collisions in the investigated centrality interval.

The nuclear modification factors of open charm mesons in the 0-10% most central Au+Au collisions are shown in figure 1 [4], and compared to theoretical predictions. The R_{AA} of D^0 and $\mathrm{D}^{\pm}$ are in agreement with each other and can be qualitatively described by the displayed theoretical predictions, which include strong interactions of the charm quark with the medium. As can be seen, D^0 and $\mathrm{D}^{\pm}$ are strongly suppressed at high transverse momenta (p_{T}) and this suppression decreases towards lower p_{T}.

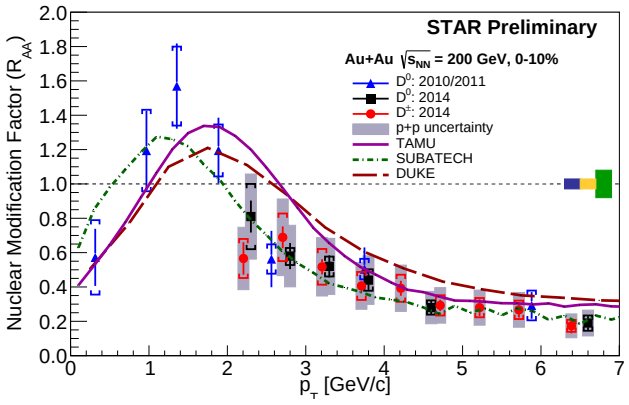

Figure 1: The D^0 and $D^\pm$ R_{AA} in the 0-10% most central Au+Au collisions at $\sqrt{s_{NN}} = 200$ GeV compared to theoretical calculations. Data from 2010/2011 and theoretical predictions are taken from Ref. [4].

4. Elliptic and triangular anisotropies of open charm mesons

In order to study the collective behavior of partons in the QGP, elliptic (v_2) and triangular (v_3) anisotropies of hadrons are measured. These are the second and the third coefficients of the Fourier decomposition of the azimuthal distribution of the particle yield with respect to the event plane. They are sensitive to the hydrodynamic properties of the hot medium.

In figure 2, D^0 meson v_2 (left) and v_3 (right) in Au+Au collisions are shown as a function of p_T, and compared to those of light hadrons. Both of them are non-zero, indicating that charm quarks have gained significant flow in the QGP via strong interactions with the medium. Additionally, v_2 shows a mass ordering for $p_T < 2$ GeV/c and is consistent between open charm mesons and light mesons for $p_T > 2$ GeV/c.

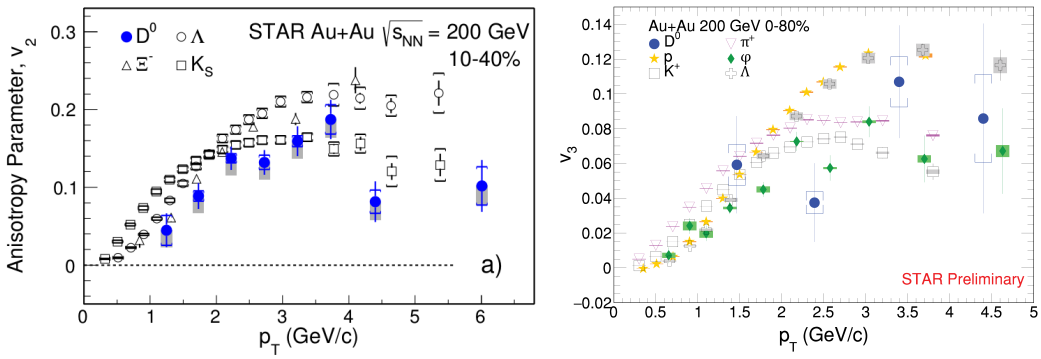

Figure 2: The elliptic anisotropy v_2 in the 10-40% central Au+Au collisions at $\sqrt{s_{NN}} = 200$ GeV [5] (left) and triangular anisotropy v_3 in the 0-80% central Au+Au collisions at $\sqrt{s_{NN}} = 200$ GeV (right) as a function of p_T for D^0 compared to those of light hadrons.

5. Strangeness enhancement for charm mesons

Due to their earlier freeze-out, strange-charm mesons (D_s) are more sensitive to the proper-

ties of the QGP than non-strange charm mesons (D^0). Enhancement of the D_s to D^0 yield ratio in Au+Au collisions compared to that in p+p collisions is expected if the quark coalescence mechanism plays an important role in the charm quark hadronization.

Figure 3 shows the yield ratios of D_s to D^0 in 0-10% and 10-40% central Au+Au collisions as a function of p_T, compared to the world-data average of the charm quark fragmentation ratio (0.132) in elementary collisions [6] and model predictions. Results in the two centrality intervals are comparable within uncertainties. The PYTHIA prediction and the fragmentation ratio in elementary collisions are significantly lower than the Au+Au results in both centrality intervals. The Statistical Hadronization Model (SHM) [7] is consistent with data, predicting an enhanced yield ratio of about 0.338. The measurement in the 10-40% centrality interval for $p_T < 4$ GeV/c is underestimated by the TAMU model calculation [8], which includes the coalescence mechanism.

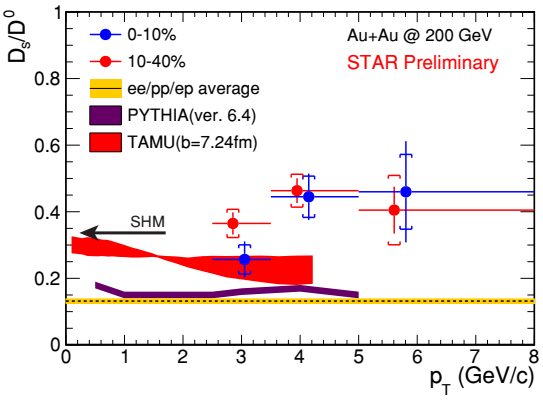

Figure 3: The yield ratios of D_s to D^0 in the 0-10% and 10-40% most central Au+Au collisions at $\sqrt{s_{NN}} = 200$ GeV as a function of p_T, compared to fragmentation baseline [6], PYTHIA, Statistical Hadronization Model (SHM) [7] and TAMU [8] predictions.

6. Summary

Open charm mesons are reconstructed via their hadronic decay channels thanks to the excellent track pointing resolution provided by the HFT at the STAR experiment. Results on the nuclear modification factor in 0-10% central Au+Au collisions show strong suppression of D meson production at high p_T compared to that in p+p collisions, indicating substantial energy loss due to strong parton-medium interactions. Comparison of v_2 and v_3 between D^0 and light hadrons suggests that charm quarks have gained significant flow when traversing the medium. The enhancement of the D_s to D^0 yield ratio implies that charm quarks participate in coalescence hadronization in the QGP.

Acknowledgments

This work is supported by the grants CZ.02.1.01/0.0/0.0/16_013/0001569, LG15001, LM2015054 (Brookhaven National Laboratory - participation of the Czech Republic) and LM2015058 (Research Infrastructure for Experiments at CERN) of Ministry of Education, Youth and Sports of the Czech Republic.

References

[1] M. Anderson et al., Nucl. Instrum. Meth. A499, 659 (2003).

[2] W. J. Llope (STAR), Nucl. Instrum. Meth. A661, S110 (2012).

[3] H. Qiu (STAR), Nucl. Phys. A931, 1141 (2014).

[4] L. Adamczyk et al. (STAR), Phys. Rev. Lett. 113, 142301 (2014).

[5] L. Adamczyk et al. (STAR), Phys. Rev. Lett. 118, 212301 (2017).

[6] M. Lisovyi et al., Eur. Phys. J. C 76 no.7, 397 (2016).

[7] A. Andronic et al., Phys. Lett. B 571, 36 (2003).

[8] H. Min et al., Phys. Rev. Lett. 110, 112301 (2013).

Measurements of D^0 Production in d+Au Collisions at $\sqrt{s_{NN}}$ = 200 GeV by the STAR Experiment

Lukáš Kramárik, *for the STAR Collaboration*

Faculty of Nuclear Sciences and Physical Engineering

Czech Technical University in Prague

ABSTRACT

Owing to their large mass, charm quarks are predominantly produced through initial hard scatterings in heavy-ion collisions. Therefore, they can serve as penetrating probes to study the intrinsic properties of the hot medium created in heavy-ion collisions. However, Cold Nuclear Matter (CNM) effects can also affect the charm quark production in nuclear collisions with respect to p+p collisions. These effects can be measured in small systems such as d+Au collisions. In this poster, we report on the first measurement of D^0 production in d+Au collisions at $\sqrt{s_{NN}}$ = 200 GeV by the STAR experiment taking advantage of its high-precision Heavy Flavor Tracker detector. D^0 ($\bar{D}^0$) mesons were topologically reconstructed from their hadronic decay channel D^0 ($\bar{D}^0$) → $K^-\pi^+$ ($K^+\pi^-$). In order to further improve the signal significance, a supervised machine learning algorithm (Boosted Decision Trees) was used.

MOTIVATION

- Heavy-flavor quarks are produced in hard scatterings at the early stage of nuclear collisions, therefore they experience the entire evolution of the system including the **quark-gluon plasma (QGP)** phase.
- Open charm mesons at RHIC exhibit strong suppression at high p_T in the 0–10% most central Au+Au collisions, indicating substantial energy loss of charm quarks in the medium.
- The collective behavior of charm quarks reflects **the degree of thermalization** of charm quarks in the medium and carries information about the bulk properties of the QGP.
- For quantitative studies of the QGP properties (e.g. charm transport coefficients), understanding of the **cold nuclear matter effects**, accessible via proton-nucleus or deuteron-nucleus collisions, is required.

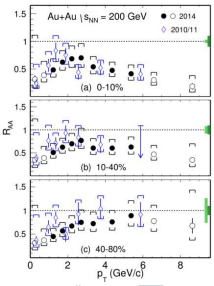

D^0 R_{AA} in Au+Au collisions at $\sqrt{s_{NN}}$ = 200 GeV [1]

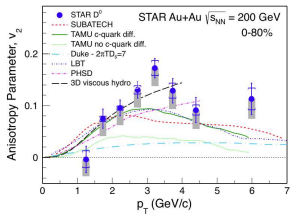

Elliptic anisotropy v_2 for D^0 mesons in Au+Au collisions at $\sqrt{s_{NN}}$ = 200 GeV, compared to theoretical calculations [2]

STAR DETECTOR

- STAR has excellent tracking and charged particles identification at mid-rapidity ($|\eta| < 1$) with full azimuthal coverage.
- Most of the subsystems are immersed in a 0.5 T solenoidal magnetic field.

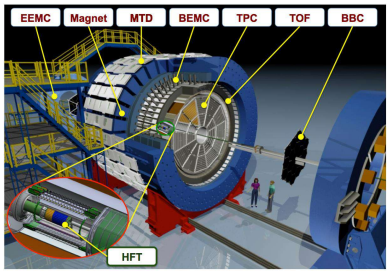

Time Projection Chamber (TPC):
- main tracking detector, momentum determination, particle identification via ionization energy loss (d*E*/d*x*).

Time Of Flight (TOF):
- particle identification via velocity (β).

Heavy Flavor Tracker (HFT):
- inner tracking system composed of three silicon detectors – the PIXEL made of two layers of Monolithic Active Pixel Sensors, Intermediate Silicon Tracker (IST) and Silicon Strip Detector (SSD),
- excellent DCA_{xy} and DCA_z resolution: **30 μm for kaons at p_T = 1.5 GeV/*c***,
- installed for data taking in years 2014–2016.

ANALYSIS METHOD

- About 350 million d+Au events at $\sqrt{s_{NN}}$ = 200 GeV recorded in 2016 are used for this analysis.
- $\bar{D}^0 \rightarrow K^+\pi^-$, $D^0 \rightarrow K^-\pi^+$ decay channels with BR = (3.95 ± 0.03) %.

Event selection:
- Pile-up rejection through requirement of correlation of primary vertex reconstructed using TPC and Vertex Position Detector (VPD) $|V_{z,VPD} - V_{z,TPC}| < 6$ cm
- Vertex position in beam direction $|V_z| < 6$ cm → HFT coverage

Track selection:
- At least 15 space points in the TPC for track reconstruction
- Track pseudorapidity $|\eta| < 1$
- Daughter $p_T > 0.15$ GeV/*c*
- Requirement of hits in both PIXEL layers and at least one of the IST or SSD layer

Particle identification:
- TPC d*E*/d*x*: $|n\sigma_\pi| < 3$, $|n\sigma_K| < 2$
- TOF used only for tracks which have valid TOF information: $|1/\beta_{theo.} - 1/\beta_{meas.}| < 0.03$

Topological cuts for D^0 reconstruction:
- Used topological properties of D^0 decays are:
  1. decay length
  2. daughter $DCA_{K,\pi}$ to primary vertex (PV)
  3. DCA_{12} between daughter kaon and pion
  4. reconstructed D^0 candidate DCA_{D0} to primary vertex
  5. pointing angle θ between reconstructed D^0 momentum and decay length vector
- Signal and background separation is optimized with the **Toolkit for Multivariate Data Analysis** (TMVA) package [3].

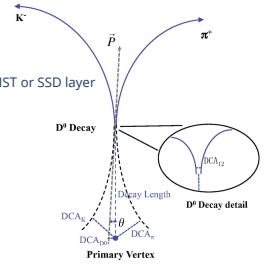

MACHINE LEARNING ALGORITHM TRAINING

- The TMVA - **Boosted Decision Trees** (BDT) method was used.
  - Classifier is a binary structured decision tree.

Signal sample for training:
- D^0 decay is simulated using PYTHIA.
- Momenta and DCA of daughter particles are smeared in accordance to the detector response.

Background sample for training:
- wrong(like)-sign pairs at the D^0 mass region taken directly from data.

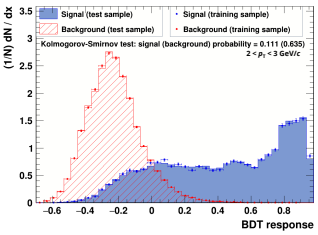

Classifier output distributions
- Both signal and background input pairs are divided to training and test samples of equal size.
- The trained BDT is applied on both samples.
- Overtraining check: if distributions obtained from training and test samples are consistent, BDT is not overtrained.

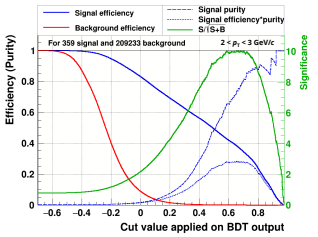

Classifier cut efficiencies
- In order to find the cut with the maximum signal significance, estimates of **number of signal** (N_S) and **background** (N_B) before BDT application are needed.
- N_S is estimated using D^0 invariant yield measured in p+p collisions and the detector reconstruction efficiency.
- N_B is evaluated from the number of wrong(like)-sign pairs in the data.

BDT APPLICATION ON DATA

- BDT is applied **on both correct(unlike)-sign pairs and wrong(like)-sign** pairs from the data.
- Distribution of invariant mass of pairs that fulfill the **cut on BDT response** is used for significance calculation.
- Background from **wrong(like)-sign** combinations of daughter particles ($K^+\pi^+$, $K^-\pi^-$) is subtracted from the **correct(unlike)-sign** combinations.

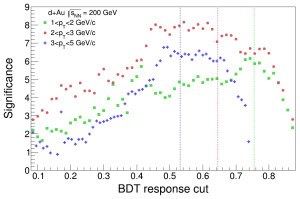

Scan of cut on BDT response on data
- Intervals of pair p_T used for analysis:
  - 1–2, 2–3, 3–5 GeV/*c*.
- BDT is trained separately in these intervals.
- Lines shows the cuts with maximum significances calculated using classifier cut efficiencies and estimates of N_S and N_B.

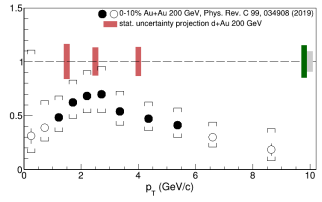

Statistical error projection of R_{dAu}
- Green box: uncertainty in determining N_{bin} in d+Au collisions.
- Grey box: global p+p uncertainty.

CONCLUSIONS AND OUTLOOK

- D^0 mesons are reconstructed via their hadronic decay channels in d+Au collisions thanks to excellent precision of the **Heavy Flavor Tracker at the STAR experiment**.
- Extraction of D^0 signal from d+Au data has been optimized using the TMVA Boosted Decision Trees method in different intervals of p_T bins.
- Evaluations of the efficiency corrections on D^0 raw yields and systematic uncertainties are under way, to determine the invariant yield and **nuclear modification factor** R_{dAu} in d+Au collisions.

REFERENCES

[1] J. Adam et al. (STAR Collaboration), Phys.Rev. C99 (2019) no.3, 034908.
[2] L. Adamczyk et al. (STAR Collaboration), PRL 118 (2017) 212301.
[3] A. Hocker et al., PoS ACAT, 040 (2007).

ACKNOWLEDGEMENT

Supported by the Centre of Advanced Applied Sciences, the project number CZ.02.1.01/0.0/0.0/16-019/0000778 that is co-financed by European Union.

EUROPEAN UNION
European Structural and Investment Funds
Operational Programme Research, Development and Education

MINISTRY OF EDUCATION, YOUTH AND SPORTS

The STAR Collaboration
drupal.star.bnl.gov/STAR/presentations

In part supported by
U.S. DEPARTMENT OF ENERGY | Office of Science

FACULTY OF NUCLEAR SCIENCES AND PHYSICAL ENGINEERING CTU IN PRAGUE

Measurements of D^0 Production in d+Au Collisions at $\sqrt{s_{NN}}$ = 200 GeV by the STAR Experiment

Lukáš Kramárik, *for the STAR Collaboration*

Faculty of Nuclear Sciences and Physical Engineering

Czech Technical University in Prague

Abstract

Charm quarks possess large masses, and thus can serve as penetrating probes to study the intrinsic properties of the hot medium created in heavy-ion collisions. However, Cold Nuclear Matter (CNM) effects, such as the change in the parton distribution function between a free nucleon and a nucleus, also affect the charm quark production in nuclear collisions with respect to p+p collisions. These effects can be measured in small systems such as p+A and d+A collisions, where only the CNM effects are present. Furthermore, a sizable azimuthal anisotropy (v_2) has been observed in both nucleus-nucleus collisions and small-system collisions of high multiplicities. To better understand the origin of the flow-like signal in small-system collisions, it is important to study charm quark azimuthal anisotropy in these systems.

In this poster, we report on the first measurements of D^0 production with the Heavy Flavor Tracker in d+Au collisions at $\sqrt{s_{NN}}$ = 200 GeV.

Motivation

- **A mass ordering** of the parton energy loss in the hot medium is predicted, i.e. heavy-flavor quarks are expected to lose less energy than light-flavor quarks.
  - The nuclear modification factor R_{AA} of open charm mesons exhibits **strong suppression at high p_T in Au+Au collisions**, indicating substantial energy loss of charm quarks in the medium.
- The collective behavior of charm quarks reflects **the degree of thermalization of charm quarks** in the medium, and is related to the bulk properties of the QGP.
- For quantitative studies of the QGP properties (e.g. charm transport coefficients), understanding of the **cold nuclear matter (CNM) effects**, accessed via proton-nucleus or deuteron-nucleus collisions, is required.

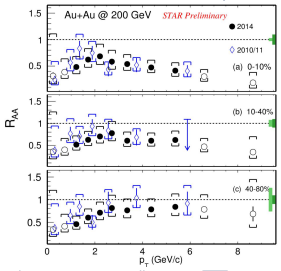

The D^0 R_{AA} in Au+Au collisions at $\sqrt{s_{NN}}$ = 200 GeV

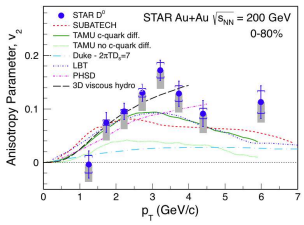

The elliptic anisotropy v_2 for D^0 mesons in Au+Au collisions at $\sqrt{s_{NN}}$ = 200 GeV, compared to theoretical calculations [1]

STAR Detector

- STAR has excellent tracking and charged particles identification at mid-rapidity ($|\eta| < 1$) with full azimuthal coverage.
- Most of the subsystems are immersed in a 0.5 T solenoidal magnetic field.

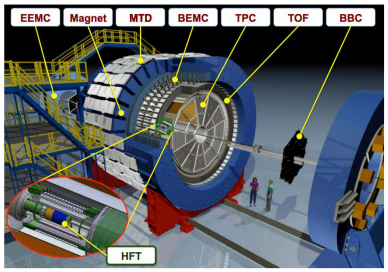

Time Projection Chamber (TPC):
- main tracking device, momentum determination, particle identification via energy loss (d*E*/d*x*)

Time Of Flight (TOF):
- particle identification via velocity (β)

Heavy Flavor Tracker (HFT):
- inner tracking system composed of three silicon detectors – the PIXEL made of two layers of Monolithic Active Pixel Sensors, Intermediate Silicon Tracker (IST) and Silicon Strip Detector (SSD)
- excellent DCA_{xy} and DCA_z resolution: **30 μm at p_T = 1.5 GeV/*c***
- installed for data taking in years 2014-2016

Analysis Method

- About 350 million d+Au events at $\sqrt{s_{NN}}$ = 200 GeV recorded in 2016 are used for this analysis.
- Hadronic decay channels are used for D^0 reconstruction ($\overline{D^0} \rightarrow K^+\pi^-$, $D^0 \rightarrow K^-\pi^+$), whose branching ratio is (3.89 ± 0.04) %.
- **Event selection:**
  - Vertex position in beam direction $|V_z| < 6$ cm
  - Correlation of primary vertices reconstructed using TPC and VPD $|V_{z,VPD} - V_{z,TPC}| < 3$ cm
- **Track selection:**
  - Hits in both PIXEL layers and at least one of the IST or SSD layer
  - At least 15 space points in the TPC for track reconstruction
  - Track pseudorapidity $|\eta| < 1$
- **Particle identification:**
  - Daughter $p_T > 0.15$ GeV/*c*
  - TPC: $|n\sigma_\pi| < 3$, $|n\sigma_K| < 2$
  - TOF: matching for pions, $|1/\beta_{theo.} - 1/\beta_{meas.}| < 0.03$ for kaons
- **Topological cuts for D^0 reconstruction:**
  - Optimized separately for different p_T intervals using Toolkit for Multivariate Data Analysis package [2].
  - Used topological properties of D^0 decays are:
    1. decay length
    2. daughter $DCA_{K,\pi}$ to primary vertex (PV)
    3. DCA_{12} between daughter particles
    4. pointing angle θ between reconstructed D^0 momentum and decay length vector
    5. reconstructed D^0 candidate DCA_{v0ToPV} to primary vertex

Tuning Topological Cuts

- The TMVA - **Rectangular Cut** optimization was used.
  - This mode randomly samples different cut combinations and selects the one with the largest background rejection for a given signal efficiency.
- Cuts with the greatest significance $S/\sqrt{S+B}$ are used for raw yield extraction.
- **Signal sample for training:**
  - D^0 decay is simulated using PYTHIA
  - Momenta and DCA of daughter particles are smeared in accordance to the detector response.
- **Background sample for training** is taken directly from data:
  - wrong (like) sign pairs at the D^0 mass region,
  - correct (unlike) sign pairs outside of the D^0 mass region.

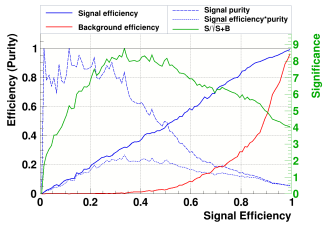

D^0 Raw Yields

- Background is estimated via **wrong (like) sign** combinations of daughter particles ($K^-\pi^-$, $K^+\pi^+$) and is subtracted from the **correct (unlike) sign** combinations.
- Invariant mass distribution of unlike-sign pairs after background subtraction is fitted by the combination of a Gaussian function for signal and a linear function for the residual background.
- Yield is extracted using the **bin-counting method** in the ±3 σ region around the mean of the fitted Gaussian function with residual background subtracted.
- Intervals of pair p_T used for analysis:
  - 1–2, 2–3, 3–5 GeV/*c*
- Significance larger than 5 is achieved in all p_T bins.

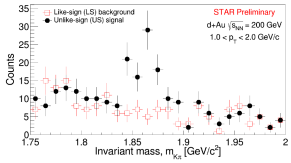

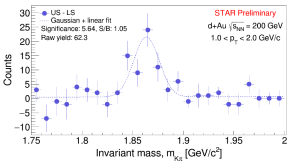

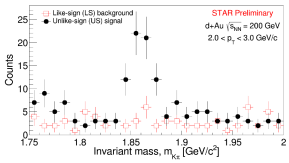

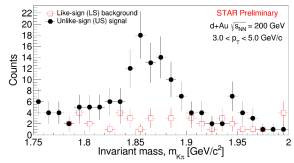

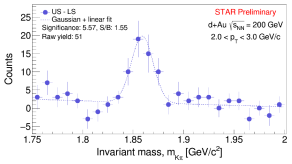

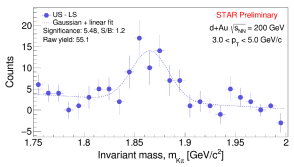

Conclusions and Outlook

- D^0 mesons are reconstructed via their hadronic decay channels in d+Au collisions with excellent precision thanks to the Heavy Flavor Tracker at the STAR experiment.
- Evaluations of the efficiency correction on D^0 raw yield and systematic uncertainties are under way, to determine the **nuclear modification factor** R_{dAu} and the **elliptic anisotropy** v_2 in d+Au collisions.

References

[1] L. Adamczyk et al. (STAR Collaboration), PRL 118 (2017) 212301.

[2] A. Hocker et al., PoS ACAT, 040 (2007).

Acknowledgement

This work was also supported by the grants LM2015054 and CZ.02.1.01/0.0/0.0/16_013/0001569 (Brookhaven National Laboratory - participation of the Czech Republic) of Ministry of Education, Youth and Sports of the Czech Republic.